Multi-scale Imaging and Modelling of Bone

Bailiang CHEN

University College London

Department of Medical Physics and Bioengineering

London, U.K.

A Thesis Submitted to University College London for

the degree of Doctor of Philosophy

April, 2012

Declaration

I, Bailiang CHEN, confirm that the work presented in this thesis is my own. Where information has been derived from other sources, I confirm that this has been indicated in the thesis.

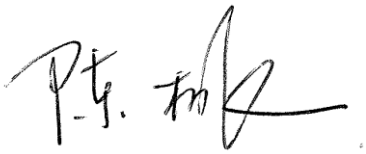

27th April, 2012

Abstract

The multi-level organization of bone facilitates the exploitation of *in-vivo* micro-scale information which is currently lacking for clinical applications. The information at finer scales is important and provides valuable insights complementing the understanding at a single scale. The three sub-projects presented in this thesis investigate the human skeletal system at multiple scales using magnetic resonance imaging (MRI) with the aim of providing new techniques for extracting finer scale information *in-vivo*.

At the whole organ level, human knee joint kinematics was studied using a combined MRI strategy. This new strategy enables the *in-vivo* investigation of tibiofemoral locomotion under body weight-bearing conditions by modelling the knee flexion angle as a function of the femur and tibia cartilage surfaces in contact. The resultant "contact" trajectory may potentially be used to understand the mechanical cause of cartilage degeneration and as a biomarker to detect abnormalities in the lower limb.

At the molecular level, *in-vivo* MR diffusion tensor imaging (DTI) has been performed for the first time in the human tibia epiphysis. By tracking the water molecules inside the red marrow, the organization of trabecular bone network may be understood as the streamlines formed by anisotropic diffusion trajectories. This sub-project aims to understand the organization of trabecular bone networks non-invasively, which is usually performed *ex-vivo* through biopsies. The feasibility and reproducibility of DTI is studied.

Finally, a new MR imaging protocol named multi-directional sub-pixel enhancement (mSPENT) is proposed and developed to quantify the trabecular bone structural arrangement at the meso-scale. By modulating a dephasing gradient to manipulate the underlying spin system inside each voxel, the resulting mSPENT image contrast varies with gradient at different directions based on the magnetization at the corresponding voxel. A tensor-based method is further developed to model this contrast change, leading to a localized quantification of tissue structural orientation beyond the conventional MR imaging resolution.

Acknowledgements

Before continuing further, I would like to express my sincere thanks to all those who have supported and are supporting me all the way along.

I would not have started this PhD, if it were not for my supervisor, Prof. Andrew Todd-Pokropek. It is he who got me to know medical imaging and computing, resuming my interest in physics and allowing me to switch from a purely computer science field to medical physics. Without his explanation in the MSc course on medical scientific computer, I would not have made up my mind of dealing with black-and-white images, instead of colourful digital arts. For his interesting lectures, ideas, patience, I will always be grateful.

I also have to acknowledge my funding body, Marie-Curie Training Network of European Commission. As an early stage researcher under this program, I worked with researchers from the other 7 institutes across Europe and multiple fields on the project called "3D Anatomical Human" (project number: MRTN-CT-2006-035763), which brought me the great opportunity to work with MRI, not only the images but also the physics behind.

I have also been fortunate enough to be surrounded by a great number of people who have given their time and assistance over the past years. My secondary supervisor Dr. Martin Fry has helped me a lot with science, and my English writings. In the quantitative medical imaging group of CMIC, Dr. Tryphon Lambrou has never complained about my bothersome questions, requests and poorly written reports and is always to offer me help. I went to conferences and summer schools with my PhD fellows, Peter Del-Manso and Sofia Michopoulou. The discussions and the great companies made me go through the panic time before various deadlines. My external supervisor, Dr. Amaka Offiah, has always been encouraging me on my work. Every time I talked to her, I felt very energetic to face those difficulties in work. I would also like to mention the nice office-mates in room 220 on the second floor at Malet Place Engineering Building. Their serious attitude towards work always inspired me.

Being a computer science student previously, entering the world of medical imaging, especially MR physics was not easy, not only the physics itself, but also the terminology in physics. I have to thank all the MR physicists who have helped me to open the door of this world. I must sincerely thank Prof. Roger Ordidge for his great help on MR knowledge and my PhD, as well as his kindness, great ideas, patience and enthusiasm all the time. He is as another supervisor. It was his explanation on the principle of Ultrashort TE sequence which made me start to understand MR better, and it was his introducing SPENT that had broadened my sights. I must also particularly mention two names for the work of SPENT, Dr. David Carmichael and Dr. Bernard Siow, for their great support on SPENT, the theory and the data acquisition. I would also like to thank Dr. David Atkinson for all his wise and kind advice on my work. I have to acknowledge the support from IADI, INSERM U947, France for allowing me to perform the *in-vivo* diffusion study on human knee joints, especially Prof. Jacques Felblinger and Dr. Pierre-Andre Vuissoz.

In the end, a special mention must go to my parents, and my grandparents for their love and support for all the past years on my way exploring the world of science, and to Freddy for everything: it was this PhD study that made me find you and it was you who held my hands and took me through the difficulties!

Table of Contents

Abbreviations

ACF	autocorrelation function
ACL	anterior cruciform ligament
ADC	apparent diffusion coefficient
BA	Bland-Altman
BMD	bone mineral density
BVF	bone volume fraction
CP	contact point
CRAZED	correlated spectroscopy revamped by asymmetric z gradient echo detection
CT	Computer tomography
DEXA	dual-energy X–ray absorptiometry
DDF	distant dipolar field
DDIF	Decay of diffusion in the internal field
DoF	degree-of-freedom
DTA	digital topological analysis
DTI	Diffusion tensor imaging
FA	Fractional anisotropy
FE	finite element
FMA	femur median axis
FoV	field of view
FSPGR	Fast Spoiled Gradient Echo
FT	Fourier transform
iMQC	intermolecular multiple-quantum coherences
LSGA	line skeleton graph analysis
MC	Monte Carlo
MD	Mean (apparent) diffusion coefficient
MERGE	Multiple-echo recombined gradient echo
MI	mean inhomogeniety
MIL	Mean intercept length
ML	mid-lateral
MM	Mid-medial
MSE	multiple spin echo
mSPENT	multi-directional SPENT
MRI	magnetic resonance imaging
MTPD	mean trabecular plate density
MTPT	mean trabecular plate thickness
MTPS	mean trabecular plate separation
MTV	Mean trabecular volume
NEX	Number of excitation
Nd.Nd	node to node
Nd.Tm	terminus number
N.Nd	node number
N.Nd/N.tm	node-to-terminus ratio
OA	Osteoarthritis
OI	Osteogenesis imperfecta
PCL	posterior cruciform ligament
PET	Positron emission tomography
PEV	principal eigenvalues
PFG	pulsed field gradient
PGSE	pulsed gradient spin echo
PGSTE	pulsed gradient stimulated spin echo
PIT	inter-trabecular space
pQCT	peripheral quantitative computed tomography
PSF	point spread function
PURE	Phased array UnifoRmity enhancement
RA	Relative anisotropy
r.f.	radiofrequency
ROI	region of interst
RSA	Roentgen stereophotogrammetric analysis
RVE	representative volume element
SEM	Scanning electron microscope
SMI	Structure model index
SNR	Signal to noise ratio
SPENT	sub-pixel enhancement for non-uniform tissue
SR	synchrotron radiation
STD	Standard deviation
SV/LD	Star volume/line distribution
SWIFT	Sweep imaging with Fourier transform (sequence)
TB	trabecular bone

Tb.N	trabecular bone number	Tb.Th	trabecular bone thickness
TBPf	trabecular bone pattern factor	TEM	transmission electron microscope
Tb.Sp	trabecular bone separation	VO	Volume orientation

List of Figures

List of Tables

Chapter 1. Introduction

"The whole is to some degree constrained by the parts (upward causation), but at the same time the parts are to some degree constrained by the whole (downward causation)."

---- *Donald T. Campbell, on hierarchically organised biological systems 1974 [1]*

The length and time scales in biological systems such as bone vary over many orders of magnitude as a result of the structural hierarchy and the diverse phenomena occurring on various time scales. These distinct physical levels are closely linked with each other: the status and appearance of biological components at each level are either the outputs or inputs of certain physiological processes at the successive finer scale or the next coarser scale. Taking bone as an example, its anisotropic internal trabecular bone network is the result of organ level functional loading regulating the bone cellular level remodelling. This kind of recursive hierarchical relation (e.g. Figure 1) suggests the demand of integrating techniques originally for a single scale into an ensemble system linking several scales in order to comprehend the bio-complexity not only on the morphology but also on the causes and influences, i.e. functional, which are related to the current morphology at a certain scale [2]. Such kind of multi-scale methods could be particular helpful for understanding pathologies, detecting it at an early stage, and preventing it from going worth [3]. To achieve this, on one hand, proper integrative computational models to describe physiology and to predict the possible functional changes need to be developed, in which scale bridging and meso-scale models may be potentially challenging; on the other hand, meaningful measurements from various physical sensors indicating *in-vivo* information from all scales are also critical for the successful construction and utilization of those proposed computational models, in which *in-vivo* fine scale information acquisition is difficult to obtain [4].

1.1 Motivation and scope

Although appearing to be homogeneously rigid at the macro-scale, bone is actually far more complicated [4], with its apparent material properties being distinct from macro-level to nano-level [5]. Figure 1 shows the whole 7 level organization of the bone inner structure,

ranging from molecular level (of the order of nanometres) to the whole bone level (of the order of centimetres) [5]. This organization is highly coupled between scales, to ensure the metabolic balance inside the bone. Perturbations at any level would cause abnormality and also be amplified to coarser scales. On the other side, if such abnormal features could be captured at a finer scale, especially *in-vivo*, when the resulting effects are still tiny at the macro-scale (hardly detectable), these sensitive abnormality probes could play a significant role in early stage diagnosis and more accurate treatment evaluation.

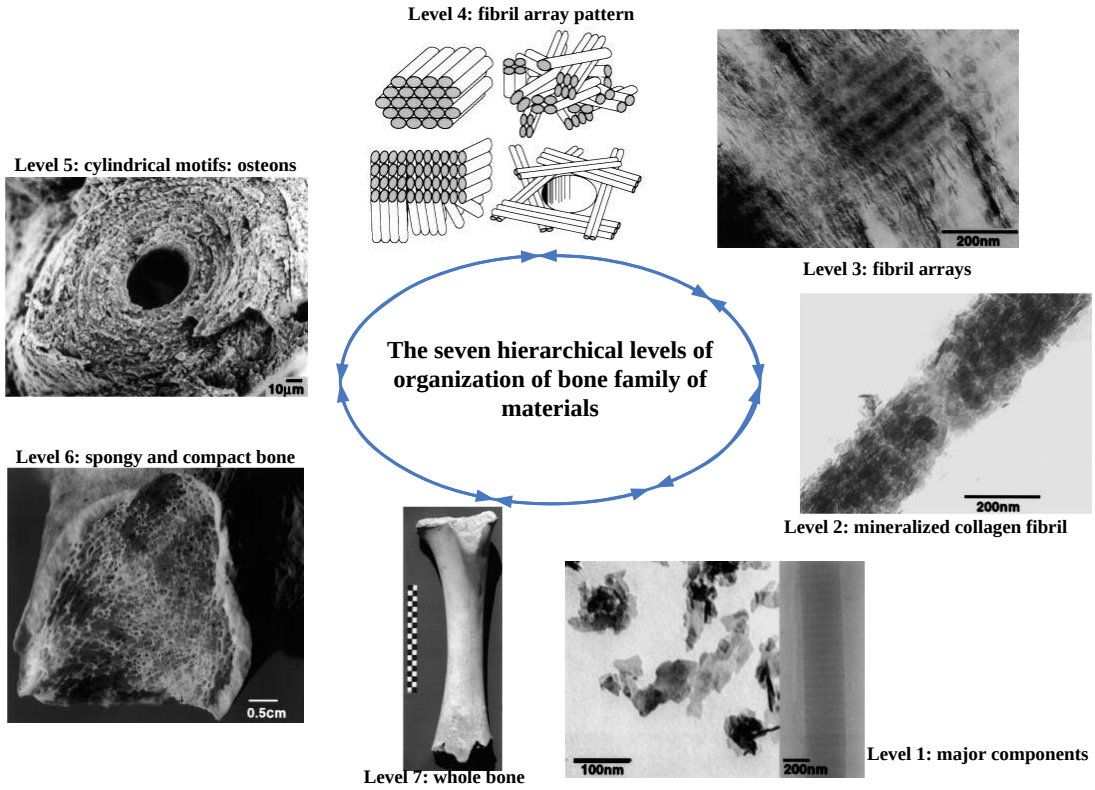

Figure 1. The 7 hierarchical levels of organization of the bone family of materials. Level 1: Isolated crystals from human bone (left side) and part of an unmineralized and unstained collagen fibril from turkey tendon observed in vitreous ice in the TEM (right side). Level 2: TEM micrograph of a mineralized collagen fibril from turkey tendon. Level 3: TEM micrograph of a thin section of mineralized turkey tendon. Level 4: Four fibril array patterns of organization found in the bone family of materials. Level 5: SEM micrograph of a single osteon from human bone. Level 6: Light micrograph of a fractured section through a fossilized (about 5500 years old) human femur. Level 7: Whole bovine bone (scale: 10 *cm*). [5]

In the case of bone, while many computational models have been proposed to describe and predict its remodelling and mechanical competence [6, 7], these models are mostly constrained to ex-vivo data with very high resolution not achievable in the clinical settings, before mentioning its super demand of computational time. The feasibility of applying these models clinically has been degraded. Since resolution is an essential requirement to extract parameters for bone mechanical competence evaluation [7], in this study we focus on *in-vivo* imaging techniques for finer scale information extraction in order to improve bone mechanical competence evaluation.

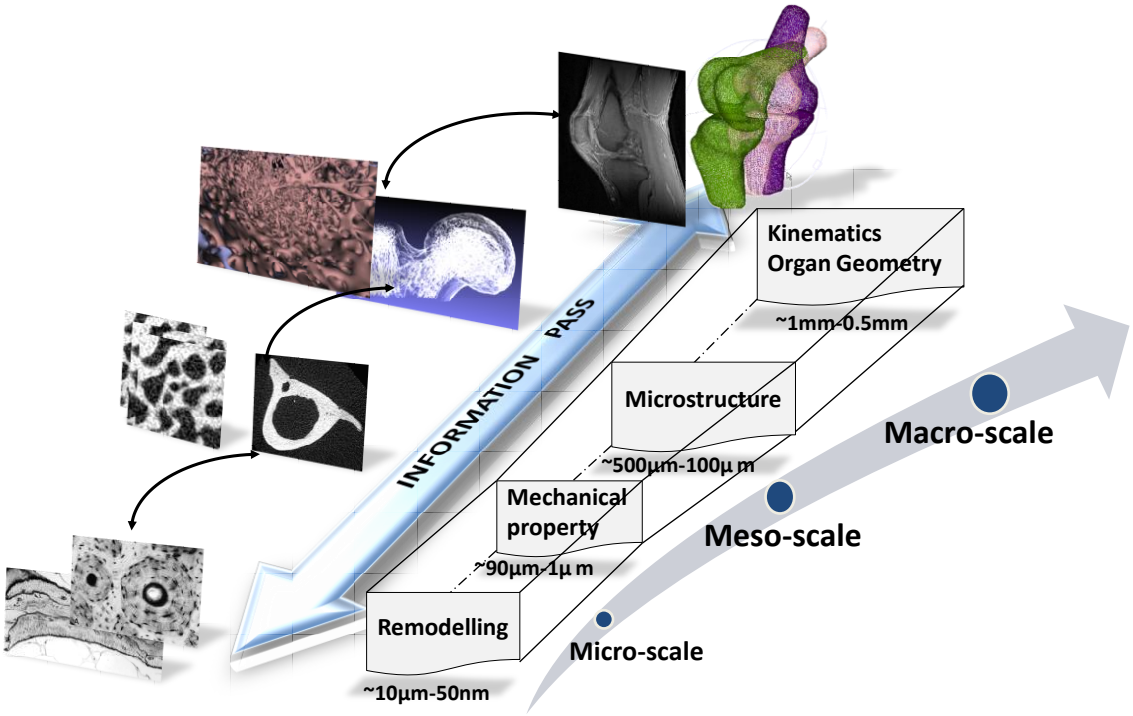

Figure 2. Illustration of the multi-scale method. Information is passed as measured parameters between scales. The scales are bridged with models that are suitable for the corresponding scale.

1.2 A multi-scale approach

An analogy can be made between multi-scale problems and inverse problems. Knowing the tissue morphological or physiological information at the finest scale, the macro-scale appearance might be understood as averaging this information up to the coarser scales, just

like calculating the output of an averaging filter that down-samples the input with certain criteria. The corresponding inverse problem would then be: given the output of the filtering procedure and possible averaging filter, what the input is at finer scales. The "averaging filter" in this scenario can be as a physics model of the imaging devices (when we are observing the spatial scales) or a biological process of the bone remodelling (when we are observing the temporal scales). Ideally, we would like to solve this inverse problem. That is to "reconstruct" the "lost" fine scale information from the coarser scale. This inverse problem is different from the traditional ones, for its initial conditions or its boundary conditions are the solutions of another inverse problem, whose corresponding space is on another order.

Figure 2 illustrates a multi-scale framework of bone study. Multi-scale methods consider the activities (e.g. morphology, tissue features) at each level are interconnected with information modelled as parameters passing between scales. In the traditional research paradigm, individual problems are studied separately at different scales; however scales are not isolated, they are closely coupled. At macro-scale, the kinematics of the whole organs and its geometry are commonly studied. The locomotion of the whole organ and its apparent mechanical properties (i.e. the knee joint) are determined by the underlying cortical bone and trabecular bone tissue. At meso-scale, the mechanical properties and the bone micro-architecture are of main concern. The cause of such arrangements is the underlying cells and molecules at the micro-scale from which the bone is formed and remodelled. Such remodelling process is stimulated and influenced by the forces applied on the whole organ [8, 9]. From macro-scale down to the micro-scale, the size of the objects to be studied varies from around one cm to tens of nanometres. This broad range of physical scale restricts the utilization of many imaging modalities for zooming into the finer scale of the hierarchy, especially for the current clinical imaging modality. The gap between micro-scale imaging (*ex-vivo/in-vitro*) and macro-/meso- scale *in-vivo* is most obvious. For example, the highest in-plane resolution of an *in-vivo* MRI that can be achieved clinically is around $150\times150\,\mu m^2$ while the single trabecula thickness is around 80-200 μm [7]. Therefore, to detect the crack of one trabecula, histology data are needed with sample removed from the living hosting body. The cross-talk between the two may be realized by

model based approaches, which is still challenging and remains as an open question at present. Novel in-vivo clinical imaging techniques targeting at finer scale are still lacking, which we believe is an essential issue to bridge the macro- and micro-scales.

1.3 Objectives

By incorporating finer-scale information obtained from *in-vivo* bone imaging, we hypothesize that new insights and improved diagnosis, as well as prognosis, can be achieved for skeletal diseases, such as osteoporosis and osteoarthritis (OA). The ultimate objective of this research is to model subject-specific information across various physical levels of bone *in-vivo*. With such a model-based approach, we aim to improve the early detection of bone abnormality and the prognosis of skeletal diseases. In particular, this study focuses on developing new MR-based imaging methods suitable for clinical scenarios to quantify the trabecular bone micro-structural anisotropy (i.e. orientation) *in-vivo*, in order to achieve an improved estimation of the mechanical competence of bone by combining the bone volume fraction and anisotropic measurements together. It is composed of three sub-projects, ranging from the whole organ at tens of centimetres, down to the basic element level of trabecular bone network at tens of micrometres.

The objectives of each sub-project are as below:

1) At the whole bone organ level, the objective is to develop a MR based method to study and model the knee joint kinematics under body-weight-bearing conditions *in-vivo* so that the everyday loading conditions can be quantified. This method needs to enable the subject-specific investigation of how the femur and the tibia contact with each other during a natural movement, which indicates the forces (i.e. the directions, the applied locations and possibly the strength) that a person endures in the everyday life.

2) At the micro-scale organ level, the objective is to investigate the feasibility of exploiting diffusion tensor MR imaging (DTI) to characterize the trabecular bone network anisotropy *in-vivo* with the clinical scenarios. DTI is commonly used in studying the brain micro-structures or muscle fibre directions, but is rarely used in bone if ever. The established

protocol needs to be further investigated in terms of the reproducibility and robustness before being applied to study diseased groups.

3) At meso-scale which bridges the bone tissue-level and the whole bone level, the objective is to develop a novel MR imaging sequence which could evaluate the mechanical competence of the trabecular bone network with bone volume fraction and its orientation at the same time. It needs to resolve the resolution penalty (due to the tiny size of each trabecular bone) of the conventional MR imaging methods and to seek a solution for an improved evaluation of bone mechanical competence from the raw MR data instead of commonly-used post-processing method.

The long-term objective is to develop a model based approach that extracts information from all scales of bone for the diagnosis and treatment evaluation of the skeletal system diseases such as osteoporosis, osteoarthritis, and osteogenesis imperfecta (OI). OI is a genetic disease affecting bone and other connective tissues. It is life-long and sometimes fatal. This genetic defect leads to the morphological abnormalities in tissues as it alters the formation of bone cells. Both diseases alter the trabecular bone network as the underlying bone remodelling process is disturbed. Thus to this end, the final aim of this project is to provide MR methods that enable the *in-vivo* investigation of bone at multiple scales and to improve the sensitivity and specificity of osteoporosis and OI diagnosis with gains from finer scale information extraction.

1.4 Summary and Thesis organization

In this work, the human skeletal system, in particular the knee joints, were investigated *in-vivo* via a MR based multi-scale approach by bridging information at distinct physical scales, in order to go beyond the current scanner imaging resolution penalty and to provide a potentially more accurate evaluation for bone mechanical competence. The detailed contributions of this work include the following points. A combined MR imaging strategy was designed and demonstrated on six volunteers for a more thorough analysis of *in-vivo* human tibiofemoral articulation contact mechanism under body-weight bearing conditions,

which lead to a subject-specific 3D functional knee joint model to understand the everyday force direction applied onto the knee joint. A clinically achievable diffusion tensor imaging protocol to measure knee joint trabecular bone network orientation was proposed and performed on three healthy volunteers. The feasibility of *in-vivo* DTI imaging of human trabecular bone was systematically analysed, as well as its reproducibility. Its potential usage of constructing trabecular bone orientation trajectory model was also demonstrated. A novel MR dephaser pulse sequence, named multi-directional sub-pixel enhancement of nonuniform tissue (mSPENT) was designed, implemented and validated. Its feasibility of revealing both the trabecular bone orientation and volume fraction was also demonstrated.

The rest of this report is organized as follows. In Chapter 2, the general background regarding the bone studies, especially trabecular bone, is introduced, including the quantification techniques, the models at organ and microstructure level for skeletal functional study, and the imaging methodologies. In Chapter 3, MR-based bone imaging is broadly discussed. The basic theory of MRI is also listed as it is the background of the following studies. A combined-MR imaging strategy was proposed to study the healthy human knee joint function based on its contact mechanism *in-vivo* at the whole organ level. This methodology will be explained in Chapter 4. A pilot study to demonstrate the feasibility of this method with 6 volunteers will be reported in Chapter 5, leading to six subject-specific right knee joint models. At finer scale, to extract finer scale information of trabecular network, new MR protocols are studied. The feasibility of utilizing diffusion tensor imaging (DTI) in bone on a clinical set-up was first explored in Chapter 6. The objective is to quantify the "trajectory" of trabecular bone orientation, and thus to quantify the anisotropy parameter of the TB network. Its reproducibility was further studied in Chapter 7. In Chapter 8 and 9, a novel MR sequence, mSPENT, was introduced as another candidate. Its theory, the design and simulation are presented in Chapter 8. Experimental results are presented in Chapter 9. Conclusions and future developments are given in Chapter 10.

Chapter 2. Bone and its functional assessment

2.1 Bone anatomy, function and bone diseases

There are two main types of bone: cortical (dense/compact) bone and trabecular (spongy/cancellous) bone (TB) [10] (Figure 3a). The hard outer layer of bone is compact bone, contributing 80% of the weight of a human skeleton. The solid filling the interior of the organ is the trabecular bone. Trabecular bone is predominant in the axial skeleton and near the joints of long bone [10]. It consists of a network of interconnected plates and struts encased within a thin cortex (Figure 3b). This special structure of trabecular bone sustains the given loads with a minimum amount of material whereas cortical bone supports biomechanical loads through the material properties of solid bone. Consequently, the topological (plate-/strut- like) nature of trabecular bone at different locations depends on the biomechanical loads experienced at each particular anatomical site (Wolff's law, 1892 [9]).

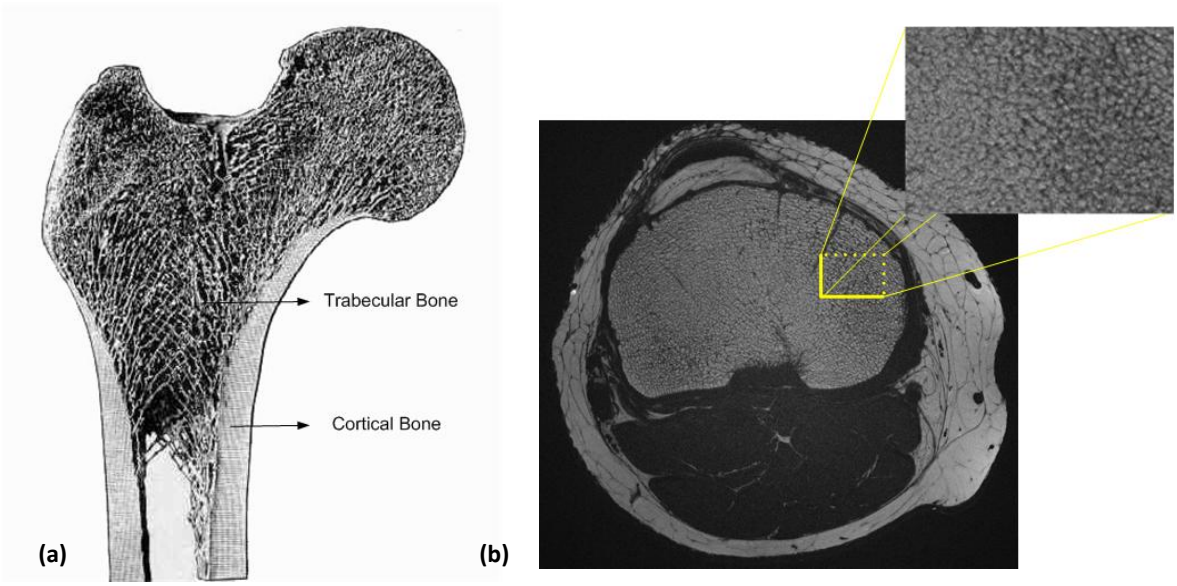

Figure 3. Bone anatomy (a) Coronal plane photo of proximal femur showing cortical bone and trabecular bone. (b) High resolution spin-echo MR image shows the trabecular network by detecting the signal from bone marrow

Bone is not a uniformly solid material, but a composite biomaterial made up of: 1) a mineral component including calcium hydroxyapatite and calcium phosphate (~45% by volume); 2) an organ matrix mainly of type I collagen (~40% by volume); 3) water (~15% by volume) either bound to collagen or residing in the lucuno-canalicular system [7]. This combination confers to bone its unique mechanical properties in terms of tensile and compressive strength and is responsible for the material's viscoelastic properties [11]. Osseous tissue is the primary bone tissue. It has relatively high compressive strength but poor tensile strength. All bones consist of living cells embedded in the mineralised organic matrix that makes up the osseous tissue.

At a grosser level, the features of morphology can help to differentiate and classify the diseased bone. Osteoporosis is a disease of bone that leads to an increased risk of fracture. It is one of the most common bone diseases. Though earlier research focused on the absolute decrease in the volume of bone [12], later investigations realized the importance of bone micro-structure, bone strength and an even broader definition of bone quality [13]. Osteoarthritis (OA, also known as degenerative joint disease) is a progressive disorder of joints caused by gradual loss of cartilage and resulting in the development of bony spurs and cysts at the margins of the joints. It refers to a clinical syndrome of joint pain accompanied by varying degrees of functional limitations and reduced quality of life [14]. Most of the time, the cause of OA is unknown. Risk factors, such as aging, gender, trauma, overuse, genetics and obesity, all make contributions to initiate the process of injury of the joints; then the biochemical process involving the three components of the knee, cartilage, bone and synovial membranes intertwine and damage all the three components eventually [15]. Osteogenesis imperfecta (OI) is a genetic disorder characterized by bones that break easily, often following minimal or no apparent trauma. Currently, eight known types of OI have been reported. The majority are caused by a dominant mutation in a gene coding for type I collagen (types I, II, III and IV), while a type I collagen disorder has not been discovered for OI types V and VI. [16] More recently discovered types VII and VIII are inherited in a recessive manner. Unfortunately, no cure has been found currently, however bisphosphonate therapy has been shown to reduce the incidence of fractures and reverse changes in the spine [17]. Other bone disorders include osteosarcoma, osteomalacia and

osteophytes.

At the micro-scale, the abnormality of bone material composition might help to clarify the skeletal pathologies. “Rickets” in the growing bone and “osteomalacia” in the adult subjects interfere with the ability of mineral ions to be deposited within the collagen “scaffold” yield bone that bend, but not necessarily break. A feature of OI is the abnormal structure or the quantity of collagen fibres. As a precursor of osteoporosis, osteopenia shows an altered coupling of bone formation to its subsequent resorption which leads to the reduction of bone mass. [18]

2.2 Quantitative assessment of bone

One obvious heterogeneous phenomenon of bone material is its hierarchical structure. At the cellular level of this hierarchy (Figure 1), bone cells (i.e. osteoclasts, osteobalsts, and osteocytes, form a connected cellular network) play important roles in bone turn-over: the perturbation of such mechanics will lead to the abnormality of bone formation, both in trabecular and cortical bone. Therefore the structure changes are also sensitive to the pathologies of bone. Studies are undergoing to help define structural parameters in order to assist the prognosis, diagnosis, treatment and its evaluation. Such features can be detected indirectly or quantified directly with post processing methods from geometric models reconstructed from 3D datasets acquired by imaging. In this section, the parameters of interest to assess the bone conditions quantitatively will be addressed and reviewed.

Bone mineral density (BMD) is a measure of bone mass and the current clinical standard to confirm the diagnosis of osteoporosis, estimate the severity of bone loss and to evaluate the treatment [19]. However, in terms of explaining the bone’s mechanical competence, BMD is less powerful and leads to the explanation of 60% among all the cases [20]. Data have shown that by combining the micro-structural parameters, the prediction has been improved greatly [21, 22]. The following will discuss parameters used to describe the bone architecture with a focus on those which quantify trabecular bone architecture.

2.2.1 Cortical bone assessment

At the bone organ level, the cortical bone geometry, the mean wall thickness, and the size of gap between the cortical and trabecular bone have been observed. Non-invasive assessment of cortical bone structure in osteoporosis is typically performed on the basis of X-ray projection radiographs or DEXA [7]. However, such projection-based methods cannot capture the 3D nature of cortical architecture. MR-based cortical bone analysis is difficult due to the short T_2 property of cortical bone. Recently the development of UTE techniques has enabled the detection of signals from tissues like cortical bone, but such techniques still lack clinical applications [23].

At the ultrastructural level, Schneider and his colleagues [24] used synchrotron radiation (SR) micro-CT to study the intracortical porosity. In this study, a hierarchical imaging strategy was exploited to describe the cortical matrix at three levels: organ level, tissue level and cellular level. At the tissue level, the appearance of the cortical bone is similar to that of the trabecular bone network. Thus, a similar morphometry applying to trabecular bone network was used on the gene knockout mouse models. They discovered the pure parameters from organ level, i.e. cortical bone volume and volume density, cortical bone thickness, could not provide a satisfactory explanation of the results from mechanical testing, the combination with tissue level parameters, namely canal volume density, mean canal diameter, and mean canal length, would help to interpret the results from the mechanical testing.

2.2.2 Trabecular bone assessment

Trabecular bone architecture refers to the geometric and spatial properties of trabeculae, which should be observed with a resolution of the order of trabecular bone thickness between 100-150 μm [7]. A variety of methods to quantify and model trabecular bone microstructure have been proposed which may seem confusing. Associated with different measurement systems (i.e. stereology, direct 3D measurement, traditional histomorphometry and ad-hoc 2D measures), these various parameters can be classified as in Table 1 [25].

Table 1 : Often used morphometric parameters [25]

	Stereology	Direct 3D Measurement	Traditional Histomorphometry	Ad hoc 2D Measures
Density[a]	V_V	V_V	BV/TV[b]	----
Surface density	S_V	S_V[b]	BS/TV	----
Trab. Dimensions[c]	star volume	Thickness[d]	MTPT(Tb.Th)[e]	direct measures
	----	MTV[e]	MTPS(Tb.Sp)[e]	----
Anisotropy	MIL[e]	MIL	----	----
	VO[e]	VO	----	----
	SVD[e]	SVD	----	----
Topology	ConnEulor [26]	Euler number	MTPD(Tb.N)[e]	TBPf[e]
(connectivity)	----	β_1	----	N.Nd[e], N.Tm[e]
	----	β_2	----	Nd.Nd[e], Nd.Tm[e]
	----	β_3	----	Tm.Tm[e], TSL[e]
	----	----	----	N.Nd/N.tm[e]

[a] Implicity bone density. May also be used for the marrow phase, V_v represents the trabecular bone volume fraction; [b] Identical to the stereological method, BV means bone volume, TV means tissue volume, BS means bone surface, S_V representes the surface density; [c] Also need for quantification of marrow space dimensions; [d] Volume weighted; [e] For abbreviations: mean trabecular plate thickness (MTPT), trabecular bone thickness (Tb.Th), mean trabecular volume (MTV), mean trabecular plate separation (MTPS), trabecular bone separation (Tb.Sp), mean intercept length (MIL), volume orientation (VO), star volume distribution (SVD), mean trabecular plate density (MTPD), trabecular bone number (Tb.N), trabecular bone pattern factor (TBPf); the following refers to the parameters from the node-and-struct networks [25]: node number(N.Nd), terminus number (Nd.Tm), node to node (Nd.Nd), terminus to terminus (Tm.Tm),total struct length (TSL), node-to-terminus ratio (N.Nd/N.tm)

In trabecular bone, traditional histomorphometry measurements can be classified into dynamic (i.e. observing the bone remodelling) and static measures. The latter can be further divided into two subgroups: stereologically founded measures and model-based measures [25]. The model based method was originally proposed by Parfitt et al. [27] to examine the structural changes that occurred in trabecular bone in ageing and osteoporosis. Parfitt's model assumed that all trabecular bone was organized in infinite parallel plates with mean trabecular plate thickness (MTPT) and mean trabecular plate separation (MTPS) apart. It also assumed that the surface density (S_V) had been determined using eq. 1.

$$S_v = \frac{4}{\pi} B_A = 2I_L \qquad \text{eq. 1 ,}$$

where I_L represents the number of surface intersections per line length and B_A stands for the linear length of the border between trabeculae and marrow per examination area. However, this model relies on S_v being unbiased through being measured by a set of isotropic random lines which is hard to achieve in most of the cases [25].

Stereological methods are based on rigorous spatial statistics of samples. Many techniques that have been developed to interpret the trabecular bone network aimed at estimating volume fraction, surface density, star volume and connectivity. Trabecular bone volume fraction (BVF) $V_v\,(bone)$ is defined as the trabecular volume per reference volume as eq. 2:

$$V_v(bone) = \frac{trabecular\ bone\ volume}{trabecular\ bone\ volume + marrow\ space\ volume} \qquad \text{eq. 2.}$$

The marrow space volume fraction, V_v(marrow), is defined equivalently, and $V_v(bone) + V_v(marrow) = 1$. BVF is also the most commonly used parameter to quantify the trabecular structure. It is considered as a 1st order structure parameter (or sometimes it is said to be the first best local measurement) [28]. Star volume ($\bar{v}_V{}^*$) is defined as the average volume that can be seen unobscured from a random point within a structure, given by eq. 3.

$$\bar{v}_V{}^* = \frac{\pi}{3} l^3 \qquad \text{eq. 3 ,}$$

where l is the average length of an intercept with random orientation through a random point [25]. In the case of trabecular bone, the star volume gives a volume weighted mean of the trabecular/marrow volume "visible" from a random location. Connectivity is a parameter used to describe the topology of bone architecture. The rationale behind this is the etiology of bone loss in the most common form in osteoporosis which causes fenestration of trabecular plates with eventual progression to rods and disconnection of rod-like trabecular elements [29]. However, both histomorphometry and stereological approaches mentioned above are mostly 2D based method. For structure as anisotropic as trabecular bone, a more accurate method should be directly based on the 3D architecture

and measure quantitatively the spatial features from the true architecture.

The 3D methods are developed to perform morphometric measurements in a 3D dataset, e.g. from micro-CT and micro-MRI. They adapt the metrics used in histomorphometry and 2D stereology. The normal procedure is to reconstruct the 3D geometry from the acquired dataset first. Various features are automatically preserved thanks to the imaging technique. Previously discussed parameters can be extracted from this more realistic model. Here, we further divide the commonly used structural characterized parameters into three groups: scale, anisotropy, and topology [7] for the convenience of review in the later paragraph. The rest of this section will review all three commonly used parameters: scale, topology and anisotropy. However, the later study will only focus on scale (BVF) and anisotropy (orientation) to model the microstructure.

Scale

Scale refers to the amount of bone contained in the volume to be observed. The two key parameters are trabecular bone volume fraction (BVF) and trabecular bone thickness (Tb.Th) [7]. BVF corresponds to the bone density in Table 1 and eq. 2. BVF is often computed from binarized images with bone and bone marrow being distinguished. Segmentation is trivial in high resolution images (e.g. micro-CT) since the histogram is bi-modal and global thresholding is good enough to distinguish bone and bone marrow [30]. However, the voxel sizes achievable in MRI *in-vivo* at $SNR \approx 8\text{-}10$ are usually of the order of or greater than the trabecular thickness [7], which coalesces the two peaks in the histogram. To resolve this, different approaches have been tried. Majumdar et al. [31] chose an empirical threshold as a means of standardization by inverting the greyscale of the image and setting a threshold at the intensity corresponding to 50% of the histogram peak. This resulted in deriving a parameter called "apparent trabecular bone volume fraction", app.TB/TV. An alternative approach seeks to evaluate true BVF by computing the BVF maps as greyscale images in which the pixel gray value represents the fractional occupancy of bone, e.g. deconvolving the histogram [32] and edge detection (e.g. convolve the images with a discrete 2D Laplacian operator [33] and morphological operators [34]).

It is considered to be advantageous to enhance the resolution of the acquired images first in order to reduce partial volume effects. Wu et al. [35] modelled the sub-voxel classification of bone MRI images as a Bayesian problem and exploited maximum likelihood estimation in order to enhance the image resolution. Alternatively, Hwang et al. proposed an empirical method named subvoxel processing to reduce the errors brought in by partial volume effects [36]. This technique made two assumptions: 1) smaller voxels are more likely to have high BVF (as they become more completely occupied by bone); 2) bone is generally in close proximity to more bone. The principal strategy is to subdivide voxels first and then to assign voxel intensities to each sub-voxel based on local neighbourhood criteria and strict mass conservation.

Topology [1]

In trabecular bone, the parameter to describe topology is connectivity and shape of individual trabecula. Feldkamp et al. [37] showed that trabecular bone network connectivity can be expressed in terms of its topology characteristics. One such measure is the Euler-Poincare characteristic, χ, given as eq. 4:

$$\chi = \beta_0 - \beta_1 + \beta_2 \qquad \text{eq. 4,}$$

which quantifies network connectedness. The quantities β_0, β_1 and β_2 are the Betti numbers, representing the number of objects, handles and cavities that remain invariant under homomorphic transformation. There are no free-floating trabeculae inside the trabecular bone (which means there is only one subject), neither are there isolated pores for marrow (which means there is no cavity). Therefore, it can be concluded: $\beta_0 = 1$ and $\beta_2 = 0$. So eq. 4 can be simplified as $\beta = 1 - \chi$. Clinically, it is considered that less connected TB network is a symptom for possible osteoporosis, though mechanically connectivity density parameter is shown to have no or very limited value for assessment of elastic properties [38].

[1] The term *topology* in this context refers to the integrity of the trabecular network not the one used in FEM regarding the meshes.

Apart from connectivity, the shape of individual trabecula is also important as the transformation between rod-like and plate-like structures is a hallmark of age-related changes. Therefore, analysis methods that can capture and quantify this process on the basis of 3D images would be highly desirable. Structure model index (SMI) [39, 40] is calculated by means of 3D image analysis based on a differential analysis of the triangulated bone surface. The partial derivative $\partial s/\partial r$, with s and r representing the surface and "radius" of a structural element, is a function of the element's curvature. For an ideal plate and rod structure, the SMI values are 0 and 3, respectively, independent of the physical dimensions. For a structure with bone plates and rods of equal thickness, the value lies between 0 and 3, depending on the volume ratio of rods and plates. However, SMI is less suited for analysis of *in-vivo* images since it requires an accurate surface representation of the structure which is difficult to achieve with the resolution of *in-vivo* clinical images.

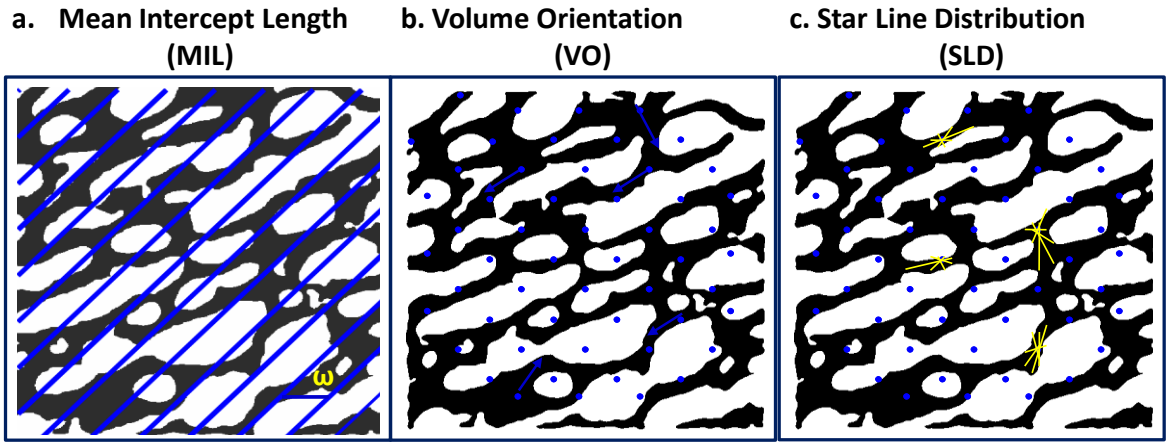

Figure 4. Principles for determining trabecular bone anisotropy: (a) mean intercept length: to count the number of intersections between a linear grid and the bone/ marrow interface as a function of the grid's orientation, ω; (b) volume orientation (VO): a randomly translated point grid is placed on the structure. For each point hitting the phase of interest (bone), the orientation of the longest intercept through the point is determined and this orientation is the local volume orientation for the point (illustrated as blue arrows); (c) start volume distribution and star length distribution: a randomly translated point grid is placed on the structure. For each point, hitting the phase of interest (bone) is determined for several orientations (yellow bars). [47]

Anisotropy: orientation of trabeculae

Trabecular bone models and remodels in response to the stresses to which it is subjected.

Therefore, trabecular bone is inherently anisotropic (Wolff's law). Generally, anisotropy is described by main directions, which are directions perpendicular to symmetry planes in the structure, and by numbers describing the concentration of directions around the main directions. In a typical porous media system as trabecular bone, a fabric tensor is a structure tensor commonly used to provide compact descriptions of architectural anisotropy in the form of a 3×3 matrix [28]. Its biggest eigenvalue gives the degree of concentration around the main direction which is indicated by the corresponding eigenvector. As it is a continuum point property, it is considered as a continuous function of position in the material. Although there is no agreement on the standard of anisotropy measurement, there are several commonly used metrics to quantify anisotropy: mean intercept length (MIL, the mean length between two intersections), volume orientation (VO), and star volume distribution (SVD) (Figure 4).

2.2.3 Anisotropy characterization

Mean intercept length (MIL)

MIL was first introduced in trabecular bone morphometry by Whitehouse [41]. He quantified the deviation from isotropy by showing that MIL between trabeculae varies as a function of test-line direction as eq. 5:

$$MIL(\omega) = \frac{\sum_{i=1}^{N(\omega)} I_i(\omega)}{N(\omega)} \qquad \text{eq. 5 ,}$$

where $I_i(\omega)$ corresponds to the intercept length of the i th line segment measured along the test lines drawn in the direction at angle ω (Figure 4 (a)), and $N(\omega)$ represents the number of all the randomly intercepted segments in that direction (Figure 4(a)). Therefore, MIL quantifies the interface anisotropy of a structure. When plotted as a polar diagram, MIL was found to map an ellipse. Harrigan et al. [42] generalized Whitehouse's 2D observation to three dimensions, showing that anisotropy could be expressed as the quadratic form of a second-rank tensor $\boldsymbol{M}$ (a MIL tensor). Cowin [43] defined a fabric tensor $\boldsymbol{H}$ as the inverse square root of $\boldsymbol{M}$. This modification aligned the principal direction of fabric tensor with that of the elastic tensor, which provided an algebraic formulation of Wolff's law at remodelling

equilibrium.

Volume orientation

MIL is an interface based global measure. Hence, given a structure with very small local anisotropy, e.g. the two-dimensional "Swiss cheese" structure, MIL is not sensitive enough to quantify the anisotropy. Odgaard et al. [44] invented another measure, named volume orientation (VO). It determines the orientation of the longest intercept length through randomly sampled points falling within the bone (Figure 4(b)). The advantage of VO is that it yielded a sample of orientations which may be treated by many statistical methods.

Star volume distribution

VO depends on the typical distribution of trabecular volume around a typical point in bone, but it is difficult to estimate from sections without model assumption. To overcome the possible bias brought by the model assumption of VO, Cruz-Orive et al. [45] invented a new characterizing technique, named star volume distribution (SVD, Figure 4 (c)) and applied it to the analysis of duplex stainless steel. SVD was an extension of star volume as used in eq. 6. They took a random point *x* drawn from a uniform distribution inside a sample to be characterized (in the case of trabecular bone, it can be in either bone or marrow), and then considered a beam of light emanating from *x* in a direction *u* in 3D. Then SVD was the average volume of this beam (modelled as a function of *u* when *x* was inside the phase to be described, $l^3(x,\ u)$ in eq. 6 timing 4π. If the sample consisted of separate phases[2], the point *x* would also sample a phase with a probability proportional to the volume of that phase and SVD ($\bar{v}_V^*$) could be then considered as a volume weighted mean of the mean beam volume within the phase, as eq. 6:

$$\bar{v}_V^* = \frac{\pi}{3} \cdot E_V E_x\{l^3(x,\ u)\},\ u \in unit\ hemisphere \qquad \text{eq. 6,}$$

where $l(x,u)$ was the length of the segment determined by the light beam *x* of direction *u*, and the two operators E_x and E_V are averaging operation: E_x denoted the mean value when *x*

[2] Cruz-Orive originally meant separate particles in [25] when analyzing steel. Here to explain SVD in trabecular bone analysis, separate phases are used inside to mean either bone or bone marrow depending on which is to be quantified.

was inside the desired phase while E_V was the mean value over the volume weighted distribution of particles. If the whole phase is connected, like in trabecular bone, eq. 6 can be simplified as eq. 7:

$$\bar{v}_V^*(x,u) = \frac{\pi}{3} l^3(x,\ u) \qquad \text{eq. 7}$$

Cruz-Orive therefore defined the tensor representation of star volume distribution (Figure 4(c)) [25, 45] as:

$$S = \begin{bmatrix} \sum L_i^2 u_{i1}^2 & \sum L_i^2 u_{i1} u_{i2} & \sum L_i^2 u_{i1} u_{i3} \\ \sum L_i^2 u_{i1} u_{i2} & \sum L_i^2 u_{i2}^2 & \sum L_i^2 u_{i2} u_{i3} \\ \sum L_i^2 u_{i1} u_{i3} & \sum L_i^2 u_{i2} u_{i3} & \sum L_i^2 u_{i3}^2 \end{bmatrix} \qquad \text{eq. 8,}$$

where L_i was the i th star volume component in direction u and the summation was done over all directions that were examined [46].

Odgaard et al. [47] compared the above three anisotropic measurements together with star line distribution (SLD, a variation of SVD, which uses the segment length instead of observing the volume) with the main direction derived from elastic tensors (results from FEM simulation) to provide experimental support for the implicit assumption of the alignment of mechanical and fabric main directions in Cowin's fabric-mechanic relations[3] [48]. They concluded that there were only marginal differences between the results of different anisotropy measures, i.e. surface-based and volume-based. However, SVD and SLD might provide superior architectural measures of the mechanical anisotropy, while VO had difficulties in identifying the secondary and tertiary (third) directions and MIL measure had a relatively significant deviation of 1.4° from the primary direction.

With the development of new imaging modalities, like CT and MRI, techniques are under development for relatively lower resolution images (compared to those used in stereological and histological images). Such algorithms utilize image post processing methods to extract information similar to that obtained using MIL or SVD. Gomberg et al. [49] resorted to digital topological analysis in machine vision in order to quantify structural

[3] For the explanation of Cowin's fabric-mechanic relations, please refer to Section 2.5

orientation. Spatial autocorrelation analysis (using the autocorrelation function, ACF) provided not only directional information on mean marrow intercept length but also a measurement of the orientation dependence of trabecular bone thickness [50, 51]. The trabecular network was treated as a quasi-periodic lattice in ACF. In this lattice, the first peak of the autocorrelation function occurs at the lattice spacing whereas the full width at half maximum of the parent peak is a measure of structural thickness. To give a more local morphometric index, Saha et al. [52, 53] defined the notion of tensor scale. Tensor scale was claimed to include the topological measurement, the volume fraction and anisotropy at the same time. In lower resolution images (plain radiography and CT images), fractal dimensions and greyscale structure tensors are applied and fitted into the correlated model of fabric tensor and elastic property to provide estimations of bone quality by Lynch et al. [54], Yi et al. [55], and Tabor and Rotika [56]. However, almost all the listed methods required image resolution on the order of the trabecular bone thickness (on the order of around 150 μm) which is lower than histological data but still higher than the maximum achievable resolution using a standard clinical routine (around 400 μm) [7].

2.3 Functional modelling

In the context of bone mechanical characterization and modelling, four levels of bone structural organization are commonly distinguished. They are, in order of scale: the whole bone level, trabecular bone level, bone tissue level and bone ultrastructural level [57]. At the whole bone level, bone is considered as a continuous material. Its material property represents the average property of a sampled bone volume. At this level, two types of bone are distinguished: cortical bone and trabecular bone. The structural organization is determined by the bone's external and internal geometry, the bone density distribution and the bone anisotropy. At the trabecular bone level, mechanical properties of bone are determined by its network architecture. For forces in the physiological range, deformations in bone tissue are relatively small, which implies that under this condition, linear FE analysis is usually adequate. It is also known that bone exhibits linear elastic constitutive behaviour for strains in this range. Material properties for linear elastic materials acquired by FE analysis are fully described by the components of a fourth-rank stiffness or

compliance tensor in the generalized Hook's Law [58, 59]. Further down, at the bone tissue level, structural organization is merely determined by the porosity of the bone due to Haversian canals, lacunae and canaliculi. The trabecular tissue that forms the trabecula is built of collagen fibres oriented in the trabecular direction and reinforced with apatite crystal [60]. Finally at the ultrastructural level, by the organization of apatite and collagen that forms the constituents of bone tissue. A typical length scale at these levels is in the range 1-10 μm. [57]

2.3.1 The knee joints and its kinematics

The knee joint is one of the most complex and biggest joints in the human body. Anatomically, two types of articulations may be identified (Figure 5(a)): the tibiofemoral[4] and the patellafemoral articulations [61]. The former is composed of two parts as the two tibial cartilage surfaces are separated from each other by the intercondylar eminence in front and triangular intercondylar areas at the back. It is the more important articulation among the two since it controls the lengthening and shortening of the lower limb. Patellafemoral articulation is responsible for the alignment of the knee joint with the legs. Anatomically, the lateral and medial femur condylars have different shapes which lead to asymmetric behaviour during motion. Being a condyloid variety of the synovial joint type, the knee joint mainly achieves movements at the point of contact of articulations. It is bathed in synovial fluid contained inside the knee joint capsule, whose major function is to reduce the friction between the articulation cartilages during motion. The research interest of this work will focus on the tibiofemoral articulations.

The understanding of the normal knee joint kinematics has been greatly developed in the past years. Previous work using mathematical analysis of the sagittal slices through femur described the axial rotation of the knee as an instant centre of rotation, shifting along a predictable, curved pathway through its range of flexion [62]. The 'four-bar linkage' model was also supported by mathematical analysis when considering the two cruciate ligaments

[4] In some books, it is said that three articulations are contained in the knee joints by considering the two tibiofemoral articulations separately.

as rigid links. This 2D model helped explain the combination of glide and roll that occurs on the articulation surface. However, the "ligament-guide four-bar linkage" model is based on 2D descriptions of motion while the knee joint is actually a 3D structure [63]. Its principle criticism is that it assumes that the flexion and extension axis of the knee joint lies exactly in the sagittal plane, whereas such motion occurs in a 3D space and is composed of rotation, gliding and rolling. Physiologically, three arcs (Figure 5(b)) can be recognized during knee flexion [61]: screw-home arc (from knee fully extending to bending at approximately 20°), functional active arc (from bending at approximately 20° to 120°) and passive deep flexion arc (from bending at 120° to fully bended) [64].

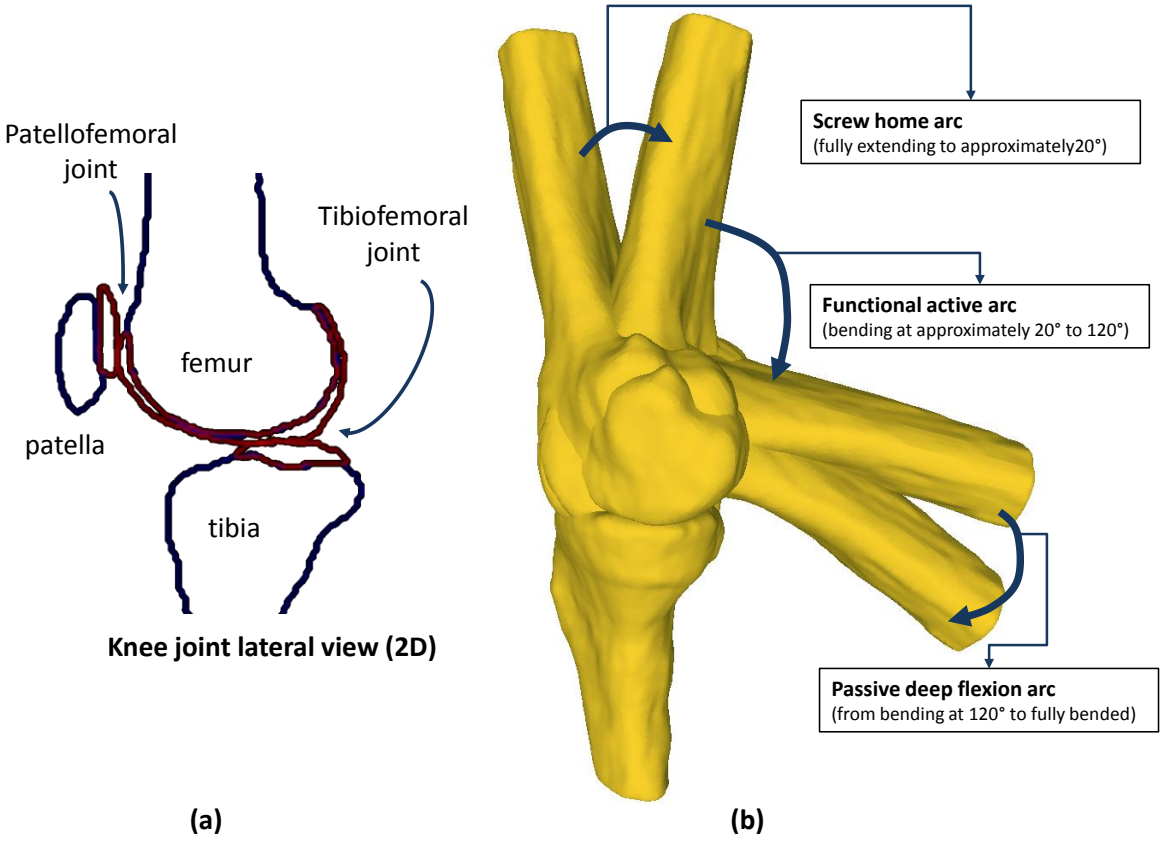

Figure 5. The articulation component of knee joint (a) and its flexion arcs (b) (in sketch).

As indicated by name, the screw-home arc is to describe the termination of the extension of the knee movement phase. The anatomical asymmetric shapes between the medial and

lateral sides within this arc lead to an asymmetric behaviour on either compartment. Morphologically, the medial femoral condyle articulates with the anterior tibia surface through the cartilage, whose surface slope evolves upwards as the knee gradually extends. For the lateral femoral condyle, as the corresponding tibia cartilage surface is flatter, it rolls down over the anterior edge of the lateral tibial plateau and compresses the anterior horn of the lateral meniscus and the termination of the motion is achieved. The motion that occurs within this arc is gliding (i.e. internal rotation) [61]. Within the functional active arc, a mixture of internal and external rotations (i.e. gliding and rotation [61]) takes place. This flexion arc is influenced by neuromuscular control and leads to an "active" flexion. From around 120° of flexion to a fully bending status, the tibiofemoral articulation motion is passive and forced by an external force, e.g. the body-weight; therefore, this arc is named as the passive deep flexion arc. Using MRI, Freeman and his group published a series of their investigation of the knee flexion in terms of the shape and rotational motion of the joints, both on cadavers and on human *in-vivo* under weight-bearing and non-weight-bearing conditions, which provides comprehensive clinical baseline data for normal knee joint [63, 65, 66, 67, 68, 69, 70].

Contact points can be thought of as being able to "mirror" the motion (magnitude and direction) of the bones in the tibiofemoral articulation. Wretenberg et al. [71] investigated the change of the contact point position with the knee joint flexion using a series of static datasets *in-vivo*, with healthy subjects in a supine position and flexing their knee joint at several angles. The aim of their study was to provide baseline data from healthy volunteers and to compare it with pathological cases such as cruciate ligament injury, in order to evaluate the skeletal joint function, i.e. motion and stability. However, the contact of the tibiofemoral articulation actually happens on the cartilage surface, therefore it is more advantageous to locate the contact points on the tibial/femoral cartilage surface instead of bone. To address this, Li and his group [72, 73, 74, 75] combined data from both MRI and 3D fluoroscopy (dual-orthogonal x-ray) in order to investigate the human lower limb kinematics *in-vivo* under weight-bearing condition (e.g. knee joint and ankle during squatting and gaiting). With the high resolution anatomical data acquired from the MR scanner in a supine position, they were able to resolve both femur and tibia cartilage

surfaces with great details. The skeletal motion was recorded first with the 3D fluoroscopy, leading to two x-ray images captured at the orthogonal directions. To map the motion data and the anatomical model, a "virtual" 3D fluoroscopy system was developed, in which the anatomical model could be flexed and projected on to the two x-ray images bearing motion information. By matching the "virtual" projection in this system with the real "projected" images, the anatomical model was considered to achieve a position which recaptures the recorded motion. However, the registering criteria were not clearly addressed. Also trying to resolve both the contact points on the cartilage surface and their motion, we proposed to use a combined MR imaging strategy [76]. In this approach, a quasi-dynamic acquisition was performed in order to record the knee joint motion with a double-donut open access MRI, in whose centre the subjects could stand and flex their knees. A high resolution MR acquisition was done afterwards to acquire the anatomical information of the knee joint. By a dual-registration (i.e. registering the femur part and tibia part separately) from the motion data to the static data, a 6 DoF functional model of the tibiofemoral articulation of the knee joint can be achieved.

2.3.2 Mechanical Properties of bone

It is intuitive to understand mechanical properties of bone using a compressive test (experimental approach). For a comprehensive review of mechanical testing of bone, the reader is referred to Bone Mechanics Handbook [77]. A different methodology for studying mechanical properties of bone is the finite element method (FE method) to back-calculate the bone tissue modulus [78]. In the FE based back-calculation scheme, the apparent elastic modulus of the specimens E_{Exp} is determined first from non-destructive mechanical tests such as uniaxial compression of trabecular bone cubes. Next, this bone sample will be scanned using either a micro-CT/ micro-MR scanner or a serial grinder in order to acquire 3D images to reconstruct the structure model of the sample. This model will then be descritised into a FE model (meshing). Assuming an initial guess of the tissue modulus E_0, the predicted apparent elastic modulus E_{Comp} can be calculated simulating the same boundary conditions as in the experiments. Within the linear elastic assumption, the true trabecular bone tissue elastic modulus E_s can be determined by:

$$E_s = \frac{E_{Exp}}{E_{Comp}} E_0 \qquad \text{eq. 9.}$$

Rietbergen et al. [79] exploited the FE model to determine all the 21 coefficients in the overall stiffness matrix of trabecular bone for the first time. The technique invented in their study was later used to build a database of elastic constants from 141 human cancellous bone specimens [80]. Cowin commented that this work was superior to the previous database as the entire stiffness matrix components were computed without a prior assumption of a particular material symmetry and without an assumption of the direction [60]. Based on this database, Yang et al. [81] showed the human trabecular bone had orthotropic elastic symmetry at the 95% confidence level with anisotropic Hooke's law via the averaging eigenbases analysis of the elasticity tensor by Cowin and Yang [82]. It provided a solution to resolve the complexity of identification of trabecular bone elastic symmetry [60].

2.3.3 Finite element (FE) method to study trabecular bone

The FE method is a numerical method for the solution of equations by approximating continuous quantities as a set of discrete points, often regularly spaced in a so-called grid or mesh. The grid or mesh is composed of simple geometric shapes called elements. These elements are connected to each other at their corner points, called nodes. The differential equations describing the underlying problem are then integrated per element. The finite element discretization leads to a set of coupled linear algebraic equations (usually a very large number) with the unknown parameter defined at the nodal points which can then be determined by solving the set of equations. After solving, the distribution of the parameter can be determined throughout the entire domain by using a suitable set of interpolation functions, usually linear or higher order polynomials.

The FE method of bone is mainly based on the continuum level mechanics, including two types of FE analysis: linear and non-linear. If the strains within the bone tissue exceed physiological values, the small deformation and linear elasticity assumption no longer holds and a nonlinear finite element approach is required to account for deformation-

dependent changes in geometry or material properties.

Both surface meshes and volume meshes are used in FE models of bone. Surface meshes are mostly used in whole bone level modelling where the microstructure of trabecular bone and cortical bone is not considered. Van Rietbergen et al. [83, 84] proposed a FE modelling strategy called the micro-FE method in which the investigated bone dataset was discretized into cubes based on each voxel. In this micro-FE model, they assumed that due to the anisotropy of trabecular bone, each voxel was the smallest heterogeneous volume inside this dataset and each voxel was the statistical average of the materials on a finer scale inside this voxel. Thus volumetrization of the dataset was only about mapping each reconstructed dataset into a cubic volume mesh (e.g., the easiest example is to convert each voxel directly to an element of the final finite element model) and keeping the topology (i.e. the connectedness of the trabecular bone network), the bone volume and the orientation of the network. This method has the advantages of fewer assumptions about the elastic constants thus is almost the most popular algorithm in trabecular bone mechanics property study. However, its limitation is the large-scale computation that it has to handle and the dependence on the resolution of the dataset.

2.3.4 Material property model

The continuum mechanics assumes the material distribution, the stresses and the strains within an infinitesimal material neighbourhood of a material element can be regarded as essentially uniform. When using these models for biological tissues like bone, it is essential to make sure that such an assumption is correct. Down to finer scales, the infinitesimal material neighbourhood of a composite material like bone is not uniform, as can be seen from Figure 6 [85]. However, such uniformity assumptions can still be applied if finer scale material elements are carefully characterized in a systematic and rigorous manner [28]. One key concept in modelling the microstructure for the inclusion in continuum mechanics is the representative volume element (RVE). It is a statistically homogeneous representation of the material in the neighbourhood of **X**, with the characteristic length scale L_{RVE}. In a FE model, each RVE is one element inside the model. Thus at different levels, the correctness of the continuum mechanics model assumption is closely related to the choice of length

scale of RVE and the material distribution inside. [86]

Porosity is the obvious first order parameter to describe the material distribution inside a composite material. In bone, this porosity corresponds to BVF. The best second-order parameter to describe the material property of a composite material is suggested to be anisotropy. It has been discussed earlier in this chapter that several ways can be used to quantify the anisotropy and reconstruct a fabric tensor. The quantification of anisotropy is important in terms of its direct relationship to material symmetry. According to Cowin [28], the quantification of material symmetry by anisotropic parameters play an important role in formulating the continuum mechanics equations (i.e. modelling the shearing components) and simplifying the complex modelling problems by determining the effective material parameters. There are eight types of material symmetries in theory, among which orthotropic and transversely isotropic are of primary interest in bone.

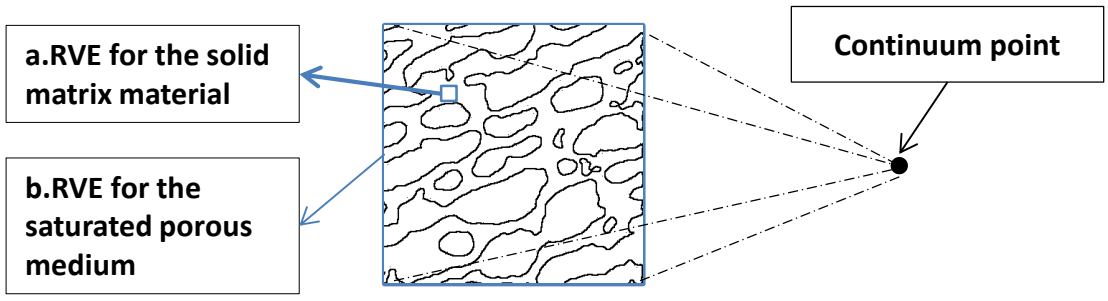

Figure 6. RVE for representation of a domain of a porous medium by a continuum point. It illustrates the selection of RVEs with different sizes: (a). a small RVE (the blue box inside the bone volume) will just contain the solid matrix while a big RVE (the whole bone volume illustrated in this figure) will average over the pores and the bones to represent them as a whole. [85, 86]

2.4 Bone Imaging

In order to understand the microstructure of bone, many imaging modalities have already been reported in the past several decades. This section will mainly cover two imaging methodologies: X-ray based techniques (2.4.1) and MRI (2.4.2), which would be exploited and studied in this research but the reader should be aware that many other imaging

approaches (e.g. ultrasound and positron emission tomography, PET) have also been reported, such as ultrasonic, enhanced backscattering of light, and techniques to acquire histological images. For a comprehensive review, please see [87].

2.4.1 X-ray based methods

The mineral components of bone give a good attenuation contrast when exposed to X-rays, which has thus made micro-CT a precise and validated technique for the micro-architecture reconstruction of bone [57]. The resolution of micro-CT bone images can be very high (10 μm) but when applied *in-vivo* the limitation on radiation dose results in a coarser level at around 200 μm [7]. Therefore, many studies have used micro-CT as an imaging tool either to visualize the TB network or to serve as a ground truth to validate results acquired from the proposed methods, e.g. [52]. Schneider et al. [24] has followed a hierarchical imaging framework including SR micro-CT to observe the mouse cortical bone at several levels to observe morphological changes due to osteoporosis. At a coarser level, dual-energy X–ray absorptiometry (DEXA) measures the mineral component of the bone (bone mineral density, BMD) inside the field of view (FOV). It is the most commonly used bone measurement in clinical settings because most of the osteoporotic changes lead to the decrease of bone mass. However, DEXA cannot differentiate the loss from cortical bone and that from the trabecular bone, and is also insensitive to the structural changes of the internal structures ([76], ch9, page 9-1). To compensate the insufficiency of only considering BMD while evaluating bone mechanical competence, some groups (e.g. Schileo and his colleagues, [88, 89]) used 3D peripheral quantitative computed tomography (pQCT) *in-vivo* instead to acquire the bone architecture and material information and build finite element (FE) models of bone to understand the bone mechanical properties.

2.4.2 MR based methods

Based on the magnetic resonance phenomena, biological tissues can be probed by manipulating the hydrogen spin systems perturbed by various magnetic fields. This section will briefly outline the research of NMR based methods of bone. A more detailed introduction on the basic MR theory and review on studies related to MRI imaging of bone

will be explained and introduced in Chapter 3. Bone is composed of a very small percentage of water and has very short T_2 values (around tens of micro seconds), therefore signals from bone vanish before conventional MR sequences start to receive them. Thus sequences with sufficiently short echo time have been proposed to be used to image bone. Alternatively, the natural MR contrast between bone and its surrounding tissues (e.g. soft tissues and cartilage) can also be exploited to visualise bone microstructure. Both ways seek to visualize TB network directly. On the other hand, the relaxation of MR signals in the TB region is dependent on the spatial distribution, i.e. micro-architecture, and the amount of trabecular bone present, i.e. bone volume [90]. According to the measurement of the MR relaxation properties, it may be possible to estimate the bone quality and differentiate unhealthy cases, such as osteoporosis patients, from healthy subjects [91, 92]. This is the indirect assessment method.

Indirect assessment aims to detect the signatures of bone from MR signals and correlate these with clinical discoveries and mechanical analysis results. However, different relaxation rates were discovered at epiphysis and diaphysis for both fat and water. Wehrli et al. [92] reported the first patient studies (in the vertebral bodies) demonstrating that patients with independently established osteoporosis had prolonged TB marrow $\boldsymbol{T_2^*}$**.** Majumdar et al. [93] conducted $\boldsymbol{T_1}$, $\boldsymbol{T_2}$ and $\boldsymbol{T_2^*}$ experiments at 1.5T on bone specimens. They measured susceptibility mediated effects on marrow relaxation times. It was found that no variation of the estimated $\boldsymbol{T_1}$ and $\boldsymbol{T_2}$ with trabecular density was observed at 1.5T for *in-vitro* data. Yablonskiy et al. [90] quantified $\boldsymbol{T_2'}$ anisotropic effects on BMD measurement in quantitative MR theoretically and provided a physical model for quantitative MR measurement. Both Jergas et al. [91] and Chung et al. [94] studied the relationship between $\boldsymbol{T_2^*}$ and biomechanical properties of bone. They demonstrated that $\boldsymbol{1/T_2^*}$ increased linearly as the elastic modulus increased.

Alternatively, direct MRI assessment utilizes the contrast between the significant signal intensity difference between bone and marrow to extract the trabecular bone structure. Vasilic et al. [95] studied the impact of isotropic voxel size for the structural assessment of trabecular bone network. Biases in morphological studies of the basic structure elements and structural orientation had been revealed by comparing images with voxel size (160

$\mu m)^2 \times 160\ \mu m$ and $(160\ \mu m)^2 \times 600\ \mu m$.

Although bone marrow gives much more signal than bone, pulse sequences devoted to measure the MR signals directly from bone have also been developed, such as ultra-shot TE (UTE) sequence [96] and sweeping imaging with Fourier transform (SWIFT) [97]. Both types of the sequences try to increase the receiving efficiency of the sequence so that the MR signals from bone could be received before it vanishes.

2.5 Heterogeneous multi-scale method (HMM) framework

The multi-level structure of bone implies the biological dependence on multiple scales. It is possible to borrow ideas from the fields of nano-engineering and physics about scale linking to provide a multi-scale modelling technique. Systems, like turbulence, crack propagation [98], and many in nano-engineering (for a review, see [99]) have shown inherence across physical scales. For such problems, modelling on a single scale is either inefficient (e.g. nano-engines do not obey continuum principles because they are too small) or too slow [99], thus multi-scale modelling and computing techniques are introduced. In nanoengineering, multi-scale approaches are grouped into two main categories: information-passing and concurrent [98, 100]. In concurrent multi-scale methods, both the discrete (i.e. finer scale like cellular level and molecular level) and continuum scales (i.e. coarser level, where the continuum principles are still obeyed) are simultaneously resolved. In information-passing schemes, the discrete scale is modelled and its gross response is infused into the continuum scale. Most of the information-passing approaches provide sub-linear computational complexity but the quantities of interest are limited to or defined only on the coarse scale.

Models of bone remodelling have benefitted from multi-scale modelling [101, 102, 103, 104]. Cowin et al. [101] developed a consistent mathematical theory for load adaptive bone remodelling in accordance with the theory of adaptive elasticity. In Cowin's theory, bone has a characteristic equilibrium configuration represented by a particular shape and density distribution. It is assumed that for normal external loading conditions a typical equilibrium state of stress and strain in the bone is obtained. A deviation from this equilibrium state is

the driving force for an adaptation in shape (external remodelling) or bone density (internal remodelling) back to the equilibrium state. Mullender et al. [105] later developed the 3D version. The relationship between bone morphology (i.e. fabric and BVF) and mechanical properties (i.e. elasticity) has been revealed in many studies [48, 106, 107] at continuum level (i.e. both trabecular bone level and the whole organ level). It has been discussed both by theoretical derivation [48, 106] and experiments results [80, 81, 84] that it is possible to predict the trabecular bone elastic properties from its morphological appearance. Such models are becoming increasingly relevant as the resolution levels of 3D scanning techniques approach the size of trabeculae [84].

2.5.1 Relationship between morphology and mechanical properties

The notion of fabric tensor plays an important role in relating the morphological parameters to the strength of bone. This concept arises in several efforts to characterize the solid microstructure of an elastic porous material. Oda [108] introduced the concept of a fabric ellipsoid, as an ellipsoid determined by the three dimensional distribution of the normals to the tangential contact planes about a point. Cowin [106] pointed out that the fabric ellipsoid was equivalent to a symmetric second rank tensor. Later together with his colleagues, Oda [107] proposed that, for granular materials, the fabric ellipsoid was the second best measure of the microstructure in granular materials after porosity. Whitehouse et al. [41] made the observation concerning the quantitative morphology of trabecular bone structure. They showed that when MILs within the solid bone matrix were plotted in a polar diagram as a function of direction across a specimen section, the polar diagrams produced ellipses. This observation is analogous to the fact that the three dimensional distribution of grain contact normals about a point in a granular medium can be represented by an ellipsoid [106]. Harrigan and Mann [42] observed that in three dimensions these mean intercept length ellipses in trabecular bone would be ellipsoids and could be represented by a second rank tensor. Cowin [48] further combined the concept of fabric tensor and continuum mechanics and derived the algebraic relationship between the second rank fabric tensor and the fourth rank elastic tensor. This derivation provided the mathematical basis for the relationship between bone elastic properties and bone micro-architecture. This theoretical model was proven later using micro-FE techniques by Odgaard et al. [46]. However, the limitation of

this relationship is that it assumes the material property is isotropic and his model is limited to continuum level at a coarser scale [109].

2.6 Summary

A multi-scale based method should be potentially helpful in both research and clinical applications. We are motivated by the hierarchical structure of bone and its functional adaptation. Ideally, we would like to build a model that could inversely predict the finer scale behaviour with information achievable clinically. However, most of the modelling involving finer scale information, i.e. on the order of tissue level or even finer, mainly uses *in-vitro/ ex-vivo* data, while the *in-vivo* data only serve the modelling above the tissue level. Therefore, we aim to bridge these scales from both imaging and modelling aspects. Looking at the hierarchical structure of bone, from both the pathological and functional point of view, resolution is a key for a more comprehensive understanding. In this chapter, the methods regarding characterizing bone, especially trabecular bone (TB) micro-structures and functionalities are reviewed. While traditionally only bone volume parameters are used to estimate the TB mechanical properties, such as its elastic property, it has been demonstrated by many studies that its micro-architecture parameters play a very important role in explaining the elastic properties of bone measured experimentally and can greatly improve the estimation. Therefore, several micro-structure parameters are introduced, with a focus on the anisotropy characterisation. This characteristic organization has been commonly considered as a result of the natural remodelling process of bone. Therefore it might be considered as a parameter to bridge the cellular scale biological process of bone and its tissue scale mechanical properties as discussed later in this chapter. Although several methods have been proposed to quantify structural anisotropy, most of them rely on a 3D visualisation of TB structure, which is difficult to achieve in a conventional clinical environment. Therefore, new imaging techniques towards going beyond the resolution penalty are extremely welcome. In the next chapter, MR imaging technology is discussed as a possible solution to address this issue.

Chapter 3. MRI and its application in bone

Imaging plays an essential role in understanding the microstructure of bone. As introduced in Section 2.4, many different imaging modalities has already been reported to be used to provide quantification of trabecular bone functionality and micro-structure. Although X-ray based methods are more commonly used clinically due to the contrast brought by the mineral component of bone, there is an increasing interest in MR based methods of bone imaging, thanks to its non-invasive, non-ionising nature and the ability of acquiring real 3D volume. A more important property of the MRI technique is the idea of visualizing the biological tissues through the magnetic properties of the spin systems (an atomistic level property) inside the tissues. From this point of view, it is naturally a "multi-scale" imaging approach, which reveals the micro-scale behaviours through a macro-scale measurement. However, a single MR acquisition approach cannot retrieve valuable information from all the scales, especially for *in-vivo* imaging. Its resolution penalty [7] suggests the assistance from other imaging modalities in case information from a micro-scale is necessary. This chapter will first introduce the basic theory of MRI (Section 3.1). The second part of this chapter will briefly review the MRI protocols that have been used to study bone (Section 3.2), including conventional protocols such as those exploiting the T_2^* properties of TB and the direct visualization of TB micro-architecture, using spin diffusion (DTI) or dephasing (SPENT) to extract information on TB architecture parameters, and sequences which are able to collect signal directly from bone.

3.1 Basic theory of MRI

This section is presented to expose the basic concepts necessary for a better understanding on DTI and mSPENT work in the later chapters.

MR imaging of biological tissues (e.g. humans and animals) is based on the ability to manipulate the spin (a quantum property of fundamental particles) system by the combination of magnetic fields, and then to detect the bulk precession of the hydrogen spins (i.e. the net magnetization) in water, fat and other organic molecules of the tissues.

The rest of this section will briefly introduce the basic theory of MRI from several aspects: the magnetic resonance phenomenon of a single spin; the net magnetization and the generation of MR signals; k-space and its sampling; and the basic sequences. Both classical mechanics and quantum mechanics are needed to help to understand the behaviour of spins. In this section, we mainly focus on the explanation based on the knowledge of classical mechanics. As the detailed MRI theories have already been discussed and summarized many times in several classical books [110, 111], here only a general introduction will be given as a theoretical prescription for the imaging techniques addressed later in this thesis.

3.1.1 A single spin and the spin magnetization vector model

All the fundamental particles, such as electrons, protons, and neutrons, share a quantum property, called "spin". It is the rotation of a charged particle about a principal axis, therefore it is also termed magnetic angular momentum or angular momentum, $\vec{J}$. Without any further disturbance, the spin stays in an equilibrium state. The angular momentum $\vec{J}$ and the magnetic moment $\vec{\mu}$ are linear correlated (eq. 10) and their ratio is another important constant, called gyromagnetic ratio, γ:

$$\vec{\mu} = \gamma \vec{J} \qquad \text{eq. 10}$$

While being immersed into an external static magnetic field $\overrightarrow{B_0}$, spins tend to align with the direction of $\overrightarrow{B_0}$. The classical description of the $\vec{\mu}$'s motion can be understood as a simple magnetic dipole moment (i.e. magnetic moment for simplicity), such as a bar magnet, and precesses around the direction of $\overrightarrow{B_0}$ (Figure 7 (a)). The direction of $\vec{\mu}$ is the spin axis, and it always tends to align itself along the direction of the external magnetic field, $\overrightarrow{B_0}$. Inside $\overrightarrow{B_0}$, it receives a torque τ (eq. 11) , though there is no net force applied.

$$\tau = \vec{\mu} \times \overrightarrow{B_0} \qquad \text{eq. 11}$$

Now recalling knowledge in classic mechanics, when applying a nonzero total torque onto a magnetic moment $\vec{\mu}$, it will undergo a rotation, whose angular velocity depends on the torque. Just as a force is given by the rate of change of the momentum, a toque is given by the rate of change of the angular momentum. Together with eq. 11 and eq. 10, the equation to describe a single magnetic moment motion (Figure 7(a)) is thus as in eq. 12:

$$\frac{d\vec{\mu}}{dt} = \gamma\vec{\mu} \times \overrightarrow{B_0}, \qquad as\ \tau = \frac{d\vec{J}}{dt} = \vec{\mu} \times \overrightarrow{B_0} \qquad \text{eq. 12}$$

It can be considered as a simplified version of the Bloch equation which will be introduced later in the next section. eq. 12 also indicates that the magnetic change, $d\vec{\mu}$ is perpendicular to the plane of $\vec{\mu} \times \overrightarrow{B_0}$. Let θ denote the angle between the spin/dipole $\vec{\mu}$ and the main magnetic field $\overrightarrow{B_0}$, according to the geometric presentation shown in Figure 7(a), $|d\vec{\mu}| = \mu \sin\theta\, d\Phi$. From eq. 12, we also have $|d\vec{\mu}| = \gamma\left|\vec{\mu} \times \overrightarrow{B_0}\right| dt = \gamma\mu B_0 \sin\theta$, $B_0 \equiv \left|\overrightarrow{B_0}\right|$.[5] Thus, the angular velocity ω_0 can be derived by equating the two expressions above (eq. 13):

$$\omega_0 = \left|\frac{d\Phi}{dt}\right| = \gamma B_0 \qquad \text{eq. 13}$$

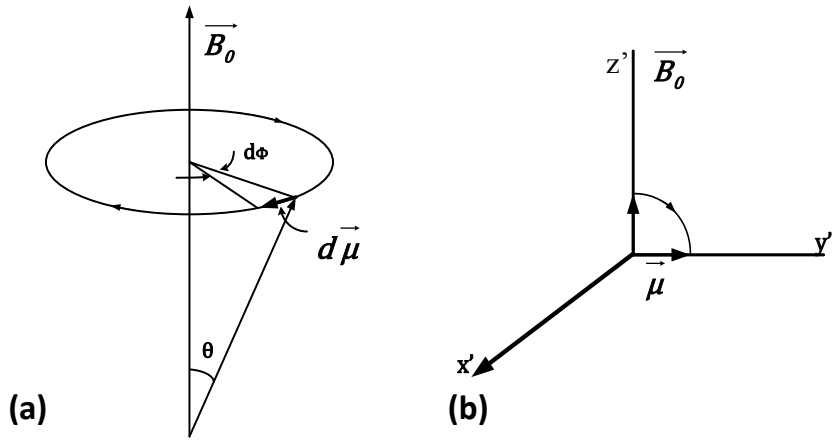

Figure 7. Sketch of the interaction between a magnetic moment with a static magnetic field. (a). Clockwise precession of a proton's spin about a static magnetic field. In this geometric sketch, the motion of a spin/ dipole ($\vec{\mu}$) inside an external magnetic field $\overrightarrow{B_0}$ is presented. At the time *dt*, in the transverse plane, the angle of $\vec{\mu}$ rotates is *dΦ*, the angle between $\vec{\mu}$ and $\overrightarrow{B_0}$ is θ. (referenced and reproduced from [111] page 3) (b). Illustration of the effect of an r.f. pulse on the individual magnetic moment $\vec{\mu}$ in a rotating frame ($x'y'z'$). The frame is rotating about $\overrightarrow{B_0}$ at the Larmor frequency. In this frame, there is no observed precession about $\overrightarrow{B_0}$.

[5]the rest of this chapter, such expression is used for all the vector/ directional variables: an upper arrow indicates a variable is directional, and its magnitude is expressed without the upper arrow

This formula is also called Larmor precession formula and ω_0 is termed Larmor frequency. From the quantum mechanics point of view, it relates to the energy transition of a proton spin between the two energy levels: "spin-up" (parallel to $\overrightarrow{B_0}$) and "spin-down" (anti-parallel to $\overrightarrow{B_0}$). Without enough energy, the spins would resist to the original state without doing anything. This is to say the external magnetic field $\overrightarrow{B_0}$ needs to be big enough to polarise the spins. When the spins precess at Larmor frequency, ω_0, they are said to be "on resonance". Therefore, eq. 13 is also the condition for spins to be "on resonance".

3.1.2 Excitation and relaxation of spins, Bloch equation

Whether the individual spin aligns parallel or anti-parallel to $\overrightarrow{B_0}$ cannot be decided easily. However, a macroscopic measurement as the difference between the total number of 'spin-up' and 'spin-down' within a sample is possible. This directional quantity is also called net magnetization, $\vec{\mathrm{M}}(\mathrm{t})$. Another related useful concept is the spin isochromat, which is a cluster of spins with the same phase [111]. It is actually the spin isochromats that MR techniques manipulate and the net magnetization in tissues that they measure. If the external static magnetic field keeps the same, the net magnetization would stay at a state without any changes. In order to relate the distribution of the spins to their spatial locations, MRI uses two types of spatially and temporally varying magnetic field: the transverse magnetic field, $\overrightarrow{B_1}(t)$, generated by varying radiofrequency (r.f.) pulses to tip the spin system to a new direction θ (Figure 7(b)) and the gradient magnetic fields ($\vec{G}_{x_1}$, $\vec{G}_{y_1}$, $\vec{G}_{z_1}$, where $\overrightarrow{x_1}$, $\overrightarrow{y_1}$, and $\overrightarrow{z_1}$ correspond to the frequency, phase and slice encoding directions) to assist to localise the magnetic signals. In this section, the excitation and relaxation procedure of spins are introduced.

Recalling Section 3.1.1, the act of adding an oscillating, $\overrightarrow{B_1}(t)$, perpendicular to $\overrightarrow{B_0}$, for some period of time would make the spins leave the initial direction and orient at a new angle θ (Figure 7(a)). This perpendicular magnetic field is generated by r.f. pulses, whose frequency has to be the same as the Larmor frequency ω_0 in order to meet the 'on resonance' condition. The angle (θ) that r.f. pulses can tip the spins from their original orientation to another depends on the time duration of r.f. pulses being added. The

relationship is as eq. 14. The angle θ is therefore termed as flip angle.

$$\theta = |\gamma B_1| t \qquad \text{eq. 14}$$

The magnetization vector, $\vec{\mathrm{M}}$(t) can be decomposed into two perpendicular vector component, a transverse component $\vec{M}_\perp$ (on x-y plane, also noted as $\vec{M}_{xy}$) and a parallel (to $\overrightarrow{B_0}$) component $\vec{M}_\parallel$ (can also be noted as $\vec{M}_z$, as it is along the $\vec{\mathrm{z}}$ axis of the main magnetic field). After the r.f. pulses are applied, the spins appear with a coherent transverse magnetization, $\vec{M}_\perp$. However, once the r.f. pulses are switched off, the spins start to realign with the main magnetic field $\overrightarrow{B_0}$ via the exchange of energy between spins and its surrounding environment (lattice). This process is characterized by two time variables, the spin-spin relaxation time T_2, and the spin-lattice relaxation time T_1 .

In the longitudinal plane, the change of $\vec{M}_\parallel$ reflects the interaction between spin and its surrounding environment, and termed spin-lattice/T_1 relaxation. It is described by the equation as eq. 15.

$$\frac{d\vec{M}_\parallel}{dt} = -\frac{(M_0 - M_\parallel)}{T_1} \qquad \text{eq. 15.}$$

The solution of this equation (eq. 15) is that of an exponential return to the equilibrium position.

$$M_\parallel(t) = M_0 + (M_\parallel(0) - M_0) \cdot exp\left(-\frac{t}{T_1}\right) \qquad \text{eq. 16}$$

In the transverse plane, the coherence is lost gradually (i.e. a phase dispersion) as spins composing of $\vec{M}_\perp$ would exchange energy between each other which causes spins obtaining different phases (i.e. dephase). This process is called T_2 relaxation. The dephasing of spins causes the decrease of $\vec{M}_\perp$. The rate of this change can be described as eq. 17:

$$\frac{dM_\perp}{dt} = -\frac{M_\perp}{T_2} \qquad \text{eq. 17,}$$

The solution to this equation indicates the development of $\vec{M}_\perp$ follows an exponential decay

as indicated in eq. 18.

$$M_{\perp}(t) = M_{\perp}(0) \cdot exp\left(-\frac{t}{T_2}\right) \qquad \text{eq. 18}$$

However, the loss of transverse coherence may not only rise from the interactions between spins, but may also result from the local field inhomogeneities [90]. This dephasing, characterized as $T_2^{'}$, is temporal invariant and reversible in case the local field inhomogeneity is also time invariant. The combination of T_2 and $T_2^{'}$ is measured in MRI, and termed as T_2^*.[6] As T_2^* is sensitive to the spatial variations, it may also be possible to exploit T_2^* as a signature to distinguish the spatial variation caused by the 'abnormal' spatial variation such as the 'over'-broadening in trabecular bone of the osteoporosis patients. Such technique will be reviewed briefly in Section 3.2.1.

Looking at the spin dynamic globally, it is the combination of the above two relaxations and spins' self-precession. The net magnetization in a sample ($\vec{M}$) is thus the sum of all the magnetic dipoles ($\vec{M} = \frac{1}{V}\sum_{protons\ \ in\ V}\vec{\mu_i}$) and can be written into one vector equation, which is referred to as Bloch equation (eq. 19) [111]:

$$\frac{d\vec{M}}{dt} = \gamma\vec{M} \times \vec{B}_{ext} + \frac{1}{T_1}(M_0 - M_{\parallel})\vec{z} - \frac{1}{T_2}\vec{M}_{\perp} \qquad \text{eq. 19,}$$

where the first part of the equation $\gamma\vec{M} \times \vec{B}_{ext}$ is to describe the non-interacting protons, and $\vec{B}_{ext}$ is the exact magnetic field applying to the spins. As the net magnetization is related to the (effective) proton density ρ,[7] it is therefore possible to reconstruct the proton density ρ within a volume by measuring the signals caused by evolving of magnetization over time [111].

---

[6] Strictly speaking, T_2^* is the combination of T_2, $T_2^{'}$ and T_1. However, in practice, the decay caused by T_1 can usually not be detected while measuring T_2 and T_2^*.

[7] The equilibrium magnetization can be expressed in terms of the proton density ρ_0, which involves the temperature T and the external field B_0. Thus an effective spin density ρ can be introduced, which is proportional to ρ_0. For a detailed explanation, please refer to Chapter 6 and Chapter 9 in [111].

3.1.3 Measuring MRI signals and k-space

The relationship between MR signals over time, $s(t)$, and the proton density, $\rho(\vec{r})$, within a sample (positioned at $\vec{r}$) can be expressed in eq. 20 , where Φ_0 is the phase at the initial state and the $\Phi(\vec{r},t)$ is the accumulated phase over time t and ω is the Larmor frequency, which is a function ($\omega(\vec{r},t)$) of the evolution time and position [111]. eq. 20 also implies that the MR signals (in the time domain, also called k-space) and proton density (in the real space, also called imaging space, or frequency domain) are in a dual space, mapped by the Fourier transform (FT) operation.

$$s(t) = \int d^3r\, \rho(\vec{r}) e^{-i(\Phi_0 + \Phi(\vec{r},t))},$$

$$\Phi(\vec{r},t) = -\int_0^t dt' \omega(\vec{r},t) \qquad \text{eq. 20}$$

The goal of imaging is to correlate the measured signals with the spatial locations of various sources. Towards reconstructing meaningful images from the measured MR signals, these signals need to be localised and to be sampled accordingly. To achieve this, spatially linearly varying magnetic fields are exploited in order that the magnetization signal can be encoded based on their spatial locations. In a Cartesian space, the sampling procedures correspond to the three important encoding steps: slice encoding ($\overrightarrow{z_1}$), phase encoding ($\overrightarrow{y_1}$) and frequency encoding ($\overrightarrow{x_1}$), where ($\overrightarrow{x_1}$, $\overrightarrow{y_1}$, $\overrightarrow{z_1}$) are the three orthogonal axes defining a slice of imaging volume.

When r.f. pulses with bandwidth $BW_{rf}\,(=\delta f)$ and carrier frequency f_0 are switched on, all the spins whose resonant frequency are within BW_{rf} will be all excited. In this case, for a uniform static magnetic field, no spatial selection is made and the correlation between signals and tissue spatial locations is not obvious. Slice encoding is to excite spins only inside a given plane. It works by applying a *slice encoding* gradient, $\vec{G}_{z_1}$ ($G_{z_1} = dB_{z_1}/dz_1$) while r.f. pulses are on, so that only the spins within that plane are on resonant. $\vec{G}_{z_1}$ acts in the normal direction $\overrightarrow{z_1}$ of the plane and leads to a magnetic field ($\vec{B}(z)$) linearly changing along $\overrightarrow{z_1}$. The Larmor frequency is thus shifted to ω_{slice} (eq. 21).

$$\vec{B}(z) = \overrightarrow{B_0} + G_z\vec{z} \;\rightarrow\; \omega_{slice} = \gamma\vec{B}(z) = \gamma \cdot \left(\overrightarrow{B_0} + G_z\vec{z}\right) \qquad \text{eq. 21}$$

The slice encoding gradient can be understood as a sampling window of the MR signals. The slice thickness (Δz) is determined by BW_{rf} and the gradient strength of $\vec{G}_{z_1}$ and the slice position is determined by the carrier frequency of the r.f. pulse and the gradient strength (eq. 22) (Figure 8).

$$\Delta z = \frac{BW_{rf}}{\gamma G_z}, \qquad z_{slice} = \frac{\omega_{slice} - \gamma B_0}{\gamma G_z} \qquad \text{eq. 22,}$$

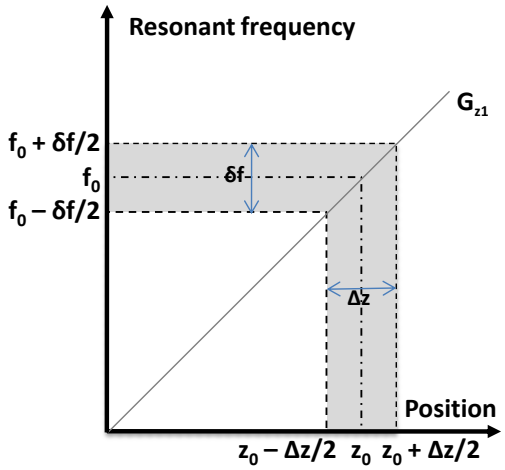

Figure 8. Slice encoding illustration: G_{z1} is the applied slice selection gradient. The two axes represent the resonant frequency and the sampling position. If the excitation bandwidth is δf, the slice thickness is Δz. f_0 is the central frequency and z_0 corresponds to the slice centre.

After selecting the 'on resonance' plane, the sampling process continues to localise the phase of the spins inside the plane. This is through the *phase encoding* procedure which adds a phase encoding gradient $\vec{G}_{y_1}$ during a fixed time period (i.e. the phase encoding gradient lobe) while the magnetization is in the transverse plane. With $\vec{G}_{y_1}$, a linear variation of the phase (i.e. the angle formed by the transverse magnetization vector with respect to some fixed axis in the same plane) is introduced within the excited plane. By varying the phase gradient strength, different amount of phase variation can be generated (the time to apply the phase gradient is fixed for all the phase encoding procedure). It is equivalent to applying a linear phase shift to the magnetization in the phase encoding direction. The overall phase shift applied is a factor of 2π.

The *frequency encoding* is the last step to localise the signal and applied together with the signal readout. It also uses a linearly changing gradient $\vec{G}_{x_1}$ to create a spatially varying magnetic field. This magnetic field assigns unique Larmor frequency to every spin isochromat at a distinct location. The signal detected is the vector sum of the effective magnetization of all the spins in the object. It is conventional to combine the two orthogonal components of the magnetization into a complex number: $M_\perp = M_x + iM_y$, which leads to a complex MR signal readout.

The concept of k-space is introduced for a clearer quantitative expression of the above signal localisation procedure. At a given time t, the encoding position (k_{x_1}, k_{y_1}) in a Cartesian k-space is determined by the history of the applied gradients in both the phase and frequency directions (eq. 23). In the other words, the gradient can also be viewed as the speed of the sampling in k-space.

$$k_{x_1}(\mathrm{t}) = \gamma \int_{\mathrm{t}_0}^{t} G_{x_1}(\mathrm{t}')\, dt' = \gamma G_{x_1} t, \qquad k_{y_1}(t) = \gamma \int_{\mathrm{t}_0}^{t} G_{y_1}(\mathrm{t}')\, dt' = \gamma G_{y_1}\, t \qquad \text{eq. 23}$$

Therefore, in the absence of relaxation effects, the k-space 2D signal equation at the sampling time *t* is:

$$S(k_{x_1}, k_{y_1}, t) = \iint \rho(x_1, y_1) exp\left(i2\pi\left(k_{x_1}x_1 + k_{y_1}y_1\right)\right) dx_1\, dy_1 \qquad \text{eq. 24,}$$

where $\rho(x_1, y_1)$ is the proton density at the position (x_1, y_1) of the real space, and $S(k_{x_1}, k_{y_1}, t)$ is the MR signal received at time *t*. Thus the proton density of the object can be obtained by the inverse FT:

$$\rho(x, y) = \frac{1}{2\pi} \iint S(k_x, k_y, t) exp\left(-i2\pi\left(k_x x + k_y y\right)\right) dk_x\, dk_y \qquad \text{eq. 25.}$$

Although eq. 24 is continuous, in practice the MR signal sampling process in k-space is discrete and thus governed by Nyquist sampling criteria [111]. Consequently, the spatial extent of an image, namely "Field of View" (FoV), needs to fit the size of the object in order to sample the object without aliasing. The step size $(\Delta k_{x_1}, \Delta k_{y_1})$ between two successive sampling positions in a standard Cartesian k-space thus needs to meet the relationship as in eq. 26, where L_{x_1} and L_{y_1} are the FoVs along the frequency and phase

encoding directions respectively, $N_{x_1} \times N_{y_1}$ is the image matrix size and $(\Delta x_1, \Delta y_1)$ is the size of each pixel in the image (i.e. the resolution):

$$1/\Delta \mathrm{k}_{x_1} \equiv L_{x_1} \equiv FoV_{x_1} = N_{x_1}\Delta x_1, \qquad 1/\Delta \mathrm{k}_{y_1} \equiv L_{y_1} \equiv FoV_{y_1} = N_{y_1}\Delta y_1 \qquad \text{eq. 26.}$$

Consequently, the maximum k-space shift (k_{max}) has the following relationship with the image resolution:

$$k_{x_{max}} = 1/\Delta x_1, \qquad k_{y_{max}} = 1/\Delta y_1 \qquad \text{eq. 27}$$

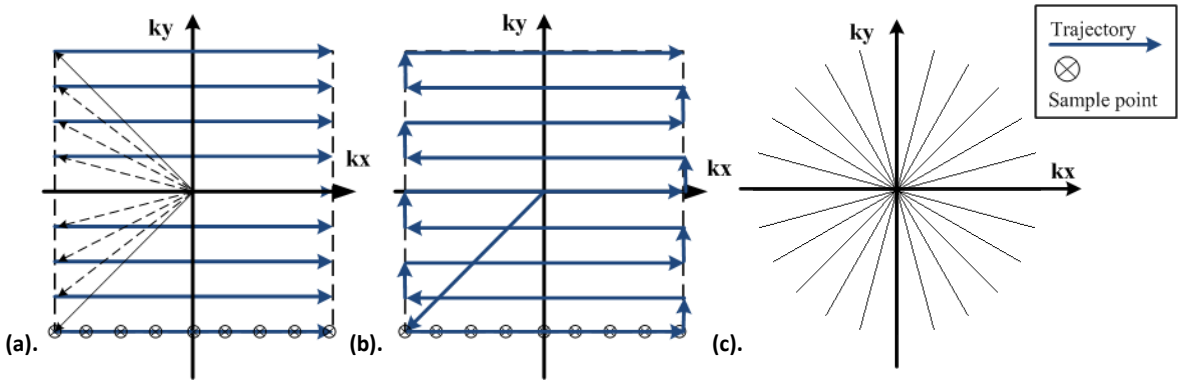

Figure 9. Examples of k-space trajectories: (a) a linear Cartesian k-space trajectory; (b) the k-space trajectory for EPI sequence; (c) a non-Cartesian k-space trajectory example: radial trajectory (indicated by black lines).

The path to sample k-space is plotted as k-space trajectory (Figure 9). The previously explained signal localisation method follows a Cartesian k-space trajectory, where the coordinates of each k-space point is expressed in a Cartesian space (e.g. Figure 9(a, b)). The overall acquisition time is related to how long it takes to sample the whole k-space. Thus to sample k-space more efficiently, one can try to reduce the time spent on travelling in all the points on k-space. Efficient k-space trajectory examples include echo-planar imaging (EPI, Figure 9(b)) and a radial k-space trajectory (Figure 9(c)).

3.1.4 Basic sequences

In this section, two basic sequences related to the works in this research are briefly introduced [112]: spin echo (SE) sequence and gradient echo (GRE) sequence.

The spin echo sequence

A standard SE sequence (Figure 10) is based on the application of two r.f. pulses: a 90° r.f. pulse followed by a 180° r.f. pulse. With the first r.f. pulse, the magnetization of the sample is tipped down to the transverse plane, and starts to dephase after it is switched off. Then the following r.f. pulse (with twice the amplitude of the 90° pulse) is applied at a time TE/2 to rotate the dispersing spin around an axis in the transverse plane so that the dephased spin isochromats would refocus at a later time, such as at TE. This refocused magnetization leads to a signal peak (i.e. an echo) at the time TE and which is the desired MR signal.

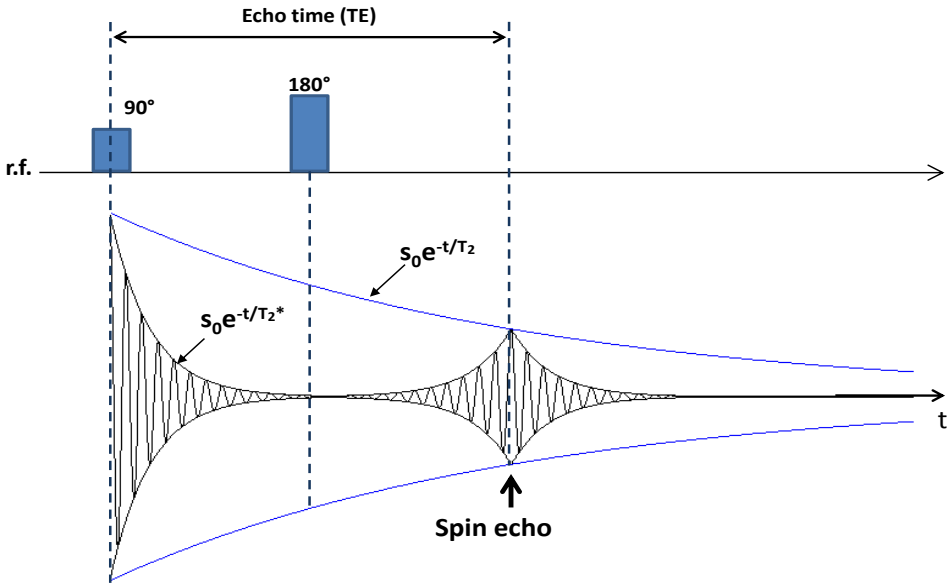

Figure 10. A schematic of spin echo sequence graph with the corresponding signal decay (s_0e^{-t/T_2^*}) and the signal decay envelope (s_0e^{-t/T_2}).

The gradient echo sequence

The GRE sequence (Figure 11) is a class of pulse sequences primarily used for fast scanning. Without the r.f. refocusing pulse as in SE sequence, to create an echo, GRE uses gradient reversal on the frequency-encoding axis ($\overrightarrow{x_1}$). It first dephases the spin isochromats with a frequency-encoding prephasing gradient and then rephases them with an opposite polarity.

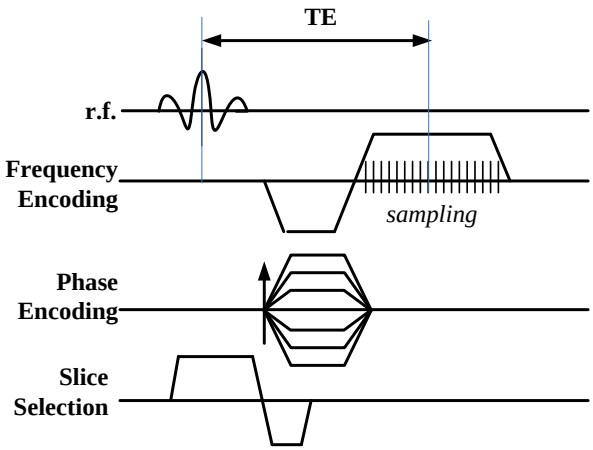

Figure 11. A typical gradient echo sequence graph

3.2 MR imaging of bone

At present, most applications of MRI in bone exploit the signal coming from bone marrow to understand the status of bone, or more specifically, trabecular bone. These conventional MR imaging methods, as introduced in Section 2.4.2, can be divided into two categories, indirect assessment and direct visualization [113]. The former exploits the fact that near the boundary of two physical phases with different susceptibility, spatial inhomogeneity in the static magnetic field leads to an alteration in bone marrow relaxation time, T_2^*. Although this technique was considered as a surrogate measure of BMD, its application is currently considered investigational. The latter strives to increase the resolution as much as possible so that trabeculae become visible and a visualization of the micro-architecture of trabecular bone (TB) can be achieved. Further quantification of the architecture of TB network, as in histology and on micro-CT data, becomes possible, as well as finite element analysis of mechanical status. However, the *in-vivo* resolution penalty prevents this method from becoming a commonly used clinical method [7]. Both of the two techniques characterize bone status using MR signals from bone marrow due to the extremely short T_2 properties of bone (Table 2). Recently, studies started to investigate other sequences as alternative choices for *in-vivo* bone MR imaging, such as diffusion sequences (e.g. DTI), dephase techniques (sub-pixel enhancement of nonuniform tissue (SPENT)), and sequences that measure signals from bone directly. This section reviews the various reported MR related studies of trabecular bone, using conventional protocols such as SE and GRE types of sequences (Section 3.1.4), DTI (Section 3.2.2) , SPENT (Section 3.2.3), and UTE and SWIFT (Section 3.2.4).

3.2.1 Conventional methods

Indirect assessment takes advantage of susceptibility effects whereby the trabecular bone alters the adjoining marrow relaxation properties in proportion to its porosity and structure and thereby provides information regarding the trabecular bone network. An estimate for the signal loss ***S*** at an echo time ***TE*** for a gradient echo experiment is obtained through the empirical expression [90]:

$$S(TE) \propto exp(-R_2^* \cdot TE)\ , with\ R_2^* = 1/T_2 + R_2^{'} \qquad \text{eq. 28.}$$

In eq. 28, $R_2^{'} = \gamma \Delta B$ (γ is the gyromagnetic ratio) is a contribution to the signal relaxation rate from the local field inhomogeneity. Two basic phenomena affect the NMR signal formation in the presence of external static field inhomogeneity: one is from the difference in local frequencies that magnetic moments of different nuclei experience, which leads to reversible spin dephasing and signal loss; the other is caused by diffusion, the translational motion of spins, which results in a loss of phase memory and irreversible signal loss. [111] Indirect assessment utilizes the former case, the characteristic relaxation time T_2^* $(= 1/R_2^*)$ of marrow and correlates it with bone density and spatial structure of trabecular bone [30].

Table 2: Approximate mean T_2s of some short T_2 tissues and tissue components (adult clinical results estimated for 1.5T [96])

Tissue or tissue component	***Mean T_2***
Ligaments	4-10 ms
Achilles' tendon	0.25 and 0.7 ms, 1.2 ± 0.2 ms, 0.52 ms (88%) and 4.8 ms (12%), 7 ms
Knee menisci	5-8 ms
Periosteum	5-11 ms
Cortical bone	0.42 – 0.50 ms
Dentine	0.15 ms
Dental enamel	70 µs
Protons in water tightly Bound to proteins / Protons in proteins	10 µs

While indirect detection methods can provide useful information on both BVF and structural orientation, it requires measuring the T_2^* properties of the objects at different angles with the main magnetic field, which is impractical. Therefore, the direct visualization of 3D TB network would be preferable. Among all the imaging parameters, resolution is the most critical, as the mean thickness of human trabecular bone is between 80-150 μm [7] which is just around the highest resolution that *in-vivo* MRI can achieve. Wehrli et al. [7] concluded that in practice, the resolution achievable *in-vivo* is entirely governed by SNR. They formulated the relationship between SNR and other imaging parameters, including voxel size $(\Delta x, \Delta y, \Delta z)$, the dependence on pulse sequence $f(\rho, T_1, T_2, T_2^{'}, TR, TE)$, data sampling time t_s, the numbers of samples collected in the three orthogonal directions N_x, N_y, N_z and the number of signal averages N_{av} as:

$$SNR \propto \Delta x \Delta y \Delta z \times \left(N_x N_y N_z N_{av} t_s\right)^{\frac{1}{2}} f(\rho, T_1, T_2, T_2^{'}, TR, TE) \qquad \text{eq. 29.}$$

eq. 29 entails a clear SNR penalty. Various *in-vivo* pulse sequences have been developed in order to achieve as high resolution as possible. The most commonly used three types are gradient echo (GRE), spin echo (SE) and balanced steady-state free precession (b-SSFP). Due to the anisotropic nature of trabecular bone network, isotropic voxels are preferable to anisotropic ones. Normally, the in-plane pixel size is easy to be isotropic, while isotropy in slice-encoding direction is difficult to achieve *in-vivo*.

3.2.2 Diffusion MRI

Trabecular bone consists of a 3D network formed by two phases: the trabeculae and the marrow filled in the pores. This highly heterogeneous network can also be considered as a particular porous media system. Capuani et al. [114] analyzed this link and applied the long-term established diffusion NMR method in porous media systems (i.e. the flows inside the pores of such systems [115]) to perform DTI of bone on the calf distal femur. A PGSTE (pulsed gradient stimulated echo, [110, 116]) was equipped on both a 7T (Bruker Biospec) and a 9.4T (Bruker Avance) scanners. Both fractional anisotropy (FA) and mean diffusivity (MD) were calculated to indicate anisotropic diffusion in different types of tissues of the femur (e.g. fat, cartilage and trabecular bone). Although they concluded that DTI was a

potential tool in the study of bone architecture and the geometrical organization of anisotropic porous systems, they only illustrated DTI as a novel contrast mechanism in bone without any further application or quantification regarding the relation to its mechanic properties. Hatipoglu et al. [117] sought for the possibility of using ADC in red marrow (red marrow in lumbar vertebrae) for the diagnosis of osteoporosis. By comparing their results with that measured by DEXA on 240 lumbar vertebrae (L1-L4) from 51 subjects, they reported the decrease of the water diffusion ADC on the osteoporotic or osteopenic group.

The mixed composition of bone marrow definitely adds complication when observing diffusion in trabecular bone by MR. While some studies focus on understanding the water diffusion inside bone marrow, some groups seek to utilize the diffusion of fat. Ong et al. [118] used a PGSE pulse sequence to measure ADC of fat. Their results showed that the fat signal is slow enough to be considered as a static regime at diffusion times of tens of milliseconds. Therefore, it is reasonable to choose a low b-value (< 1000 $s \cdot mm^{-2}$) with conventional clinical protocols to observe water diffusion inside bone marrow. Considering the ability of diffusion tensor imaging to derive orientation, we showed that the feasibility of using DTI to measure human TB orientation *in-vivo* with a clinical scanner in Chen et al. [119]. NMR diffusion measurements on trabecular bone are indeed rare. Sigmund et al. [120] analyzed the complexities of MR diffusion measurement in trabecular bone. According to their argument, the small accessible diffusion lengths (10-100 μm) compared with the average pore size (0.2-1 mm) was the strongest factor to affect the limited contrast in conventional diffusion MR imaging. Other factors included the shorter relaxation time and smaller diffusivities, as well as the aforementioned complicated composition of bone marrow.

3.2.3 SPENT

While MR relaxometry method remains investigational and the direct measurements have very high requirements of resolution, an alternative innovative MR sequence by dephasing spins inside each voxel has been proposed by Yiannakas et al. [121]. The sequence, named subpixel (subvoxel) enhancement of nonuniform tissue (SPENT), is reported to be able to

measure subvoxel information by adding an extra gradient in the classical spin echo sequence. The use of this extra gradient allows the creation of a 2π phase dispersion across each voxel so that the spins disperse again after the refocusing r.f pulse (Figure 12). Such dispersion causes the cancellation of the spin vectors within a voxel, which is zero in case of voxels containing homogeneous tissues but is non-zero for voxels with non-uniform structures. This extra gradient lobe was shown to be possible to be applied on any of the three encoding directions (i.e. frequency, phase and slice encoding directions) to create the dephasing prone to that direction.

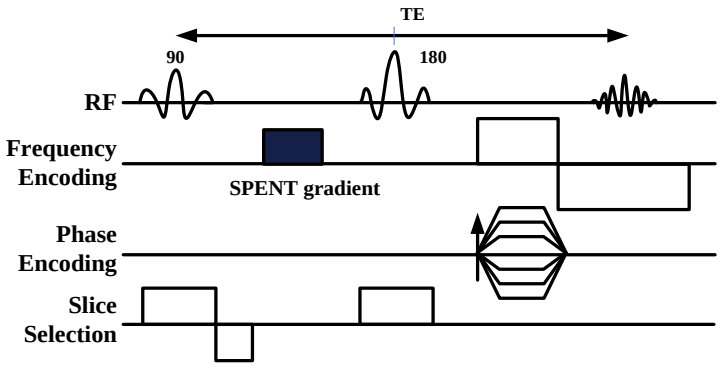

Figure 12. The SPENT pulse sequence as presented in [121]

In their study, Yiannakas et al. [121] performed the SPENT sequence on a group of 30 human trabecular bone samples *in-vitro* and demonstrated that the SPENT measurement of voxel nonuniformity (with an isotropic voxel size) is highly correlated to BMD given by DEXA ($R^2 = 0.95, \mathrm{p} < 0.0001$ for the summation of SPENT measurement on x, y and z direction). Another highlighted feature of this method is its nature of being directional specific. It was also shown in the study that the SPENT measured values along the y direction were higher by 3% than that on x direction (the measurement was performed in isotropic pixels with x direction along the trabecular bone orientation). This anisotropic appearance matches the anisotropic feature of trabecular bone, which hints that SPENT might also be potentially powerful to measure trabecular bone orientation.

Based on this clue, we (i.e. the author and her collaborators) sought to use the SPENT sequence as a probe to measure the local trabecular bone orientation through a tensor based

method [122]. This involved an extension of the original x-SPENT and y-SPENT to arbitrary directions. In order to make it easier for a future clinical adaptation of the sequence, we used a conventional k-space grid instead of a radial trajectory. We initially obtained the arbitrary direction SPENT measurement by rotating the imaging plane. This consequently rotated the SPENT gradient whose orientation was in an angle with the original imaging coordinates. Although the results were interesting and encouraging, the chemical shift caused by the fat components of the bone marrow was a big problem when changing the imaging plane orientation. To complement this problem, we proposed a further modification to the original SPENT sequence in [76], which contained simultaneously added SPENT gradients on both frequency and phase encoding direction. The overall strength of the two gradient lobes is equal to that to create the 2π phase dispersion across each voxel. The overall SPENT gradient orientation with reference to the in-plane imaging coordinates is thus determined by the ratio between the strengths of the two gradient lobes. With promising results shown in a chicken femur sample, we also validated the sequence ability to resolve structure orientation in a pineapple sample.

3.2.4 Other imaging protocols

Tissues such as bones, cartilage, ligaments, and tendons have very short T_2 (Table 2 [96]). Their MR signals decay rapidly, and thus little or no signal is detectable by the time conventional MR systems begin to receive. This very fast transverse relaxation motivates the idea to reduce TE in a pulse sequence. UTE techniques use half RF excitations with radial mapping from the centre of k-space [23, 96]. These UTE sequences have TEs about 10 to 20 times shorter than the shortest clinically achievable sequences. Tissues with a majority of very short T_2 components such as bone (Table 2) can thus be visualized as high signal areas in images. Such information can be genuinely complementary to conventional sequences such as fast spin echo imaging, EPI and diffusion-weighted imaging which detect long T_2 components [7].

Robson et al. [123] imaged phosphorous in cortical and trabecular bone *in-vivo*. The complex structural differences between the crystals of bones and of pure hydroxyapatites were hypothesized to reflect the metabolic history of the bone. A potential use of

phosphorous imaging was then proposed by Robson et al. [124] in order to provide a further insight into the status of bone. Four hundred patients were scanned using clinical UTE imaging to detect tissues with short T_2s (i.e. bone and other connective tissues). Using a method based on a UTE sequence, Techawiboonwong et al. [125] quantified bone water concentration *in-vivo* in human cortical bone. As most of the water is stored in the pores of cortical bone, this technique, according to Techawiboonwong, can be considered as a probe for cortical bone porosity which provides a unique insight into osteoporosis.

Sweep imaging with Fourier transform (SWIFT) is another MR pulse sequence to facilitate probing the tissues with very short transverse relaxation time [97]. In SWIFT, the frequency-modulated r.f. pulses are used with simultaneous acquisition so that the acquisition speed is significantly improved. Idiyatullin et al. [97] demonstrated the sensitivity of SWIFT to spins with very short T_2 properties by testing the sequence on a sample of bovine tibia.

As a complement to DTI, intermolecular multiple-quantum coherences (iMQC, or distant dipolar field DDF) measures have been proposed as a method for probing material microstructure. Bouchard et al. [126] reported an algorithm to reconstruct the geometry of porous media systems using the bulk intensity of the distant dipolar field from a correlated spectroscopy revamped by asymmetric z gradient echo detection (CRAZED, [127]) NMR pulse sequence. Capuani et al. [128] used a multiple spin echo (MSE, CRAZED-type) sequence to study bone ex vivo. The discrete drops on signal intensity which appeared on a half cycle of magnetization helix were hypothesised to show the characteristic pore sizes. The MSE weighted contrast mechanism was reported in this study. They later performed both MSE and DWI (x, y, z directions) experiments on a 1.5 T SIEMENS scanner and concluded that parallel information about proton diffusion and proton dipolar correlation distance along different directions might be obtained [129].

3.3 Summary

As we are interested in revealing information from as fine a scale *in-vivo* as we can, some new imaging methods have to be investigated. Here, MRI plays a fundamental role due to

its non-invasive and non-ionizing nature, and its ability to encode the spin spatial distribution which is directly related to the tissue structure and material properties. In this study, both the stationary spin system (e.g. conventional T_1-weighted MRI, SPENT) and the dynamic spin system (i.e. diffusion) are exploited to investigate the trabecular bone network. It has been widely agreed that bone micro-architecture plays a significant role in determining the bone mechanical properties; therefore the MRI techniques are to provide descriptors of trabecular bone micro-structure information, in this case, porosity and anisotropy. Although there is a 40% water component (with 15% free water) inside bone tissue, the T_2 decay of bone is too fast to be captured in conventional MRI. The methods that we are currently investigating, DTI, SPENT and T_2-weighted, all capture the signal from bone marrow.

Chapter 4. Combined MR imaging for knee joint function at the macro-scale

At the macro-scale, we focus on the kinematics of the human body, in particular, the knee joints. The knee permits flexion and extension of the lower limb, as well as slight rotations medially and laterally. Being the main support of the weight of the whole human body, the knee joint is vulnerable and much easier to suffer from both acute injury and the development of osteoathritis (OA). While the failure of handling the mechanical stress may be a risk factor leading to OA [15], it is important to know where these forces are applied. Hence, where the contact occurs during the knee flexion is of great value to assist the understanding of the knee degeneration. Also, as a compound synovial joint, the pattern of the contacts through the full arc of knee flexion may be a signature of the knee joint motion and can contribute to a more comprehensive understanding of the knee joint function.

In this chapter, a combined magnetic resonance (MR) imaging strategy is proposed to investigate individual's knee functionality quantitatively under weight-bearing condition. High resolution MR data were acquired first to reconstruct the subject-specific anatomical model. A dynamic MR acquisition was obtained afterwards to record the motion of knee joint. A dual-rigid registration was applied to retrieve the knee joint motion, leading to a 6 degree-of-freedom (DoF) knee functional model. Using this model, the tibiofemoral contact mechanism was studied and analysed in both 2D and 3D. A mathematical definition of contact points of cartilage surfaces is given by modelling these surfaces as manifolds. We believed that such subject-specific motion of contact points on cartilage surfaces of femur and two tibia plateaus can provide valuable insights for clinical applications such as knee replacement surgery.

4.1 Introduction

Insights about knee contact mechanism, especially subject-specific information, is of great importance in understanding the knee function, the joint forces and its impact on abnormalities such as joint degeneration. These contacts happen on the surface of the

articulation cartilage when the knee bends at different angles. As explained in Section 2.3.1, the special arrangements of the knee joint indicate that the knee joint contact mechanism is not only dependent on the anatomical location, but also related to its physiological environment. This feature requires the techniques to measure subject-specific contact mechanism *in-vivo* under body-weight-bearing conditions.

Although extensive studies have been conducted on the knee motion and relate its contact patterns to pathologies [66, 72, 73, 74, 75, 130, 131, 132, 133, 134], accurate measurements and quantitative analysis of the human knee joint contact mechanism remains challenging technically. One major technical difficulty is the data acquisition method. While video capture can record a global motion of the full leg within a large field of view (FoV) at a high temporal resolution, it mainly uses skin markers with inevitable errors caused by the movement of fat between the skin and muscles. Bone pins (e.g. Arndt et al. [135]) were proposed to avoid such errors however the serious invasiveness level of this approach is now against research ethics in many countries [136]. Also, the video motion capture techniques cannot reveal the internal structure of the knee joint; therefore this technique is limited as a global measurement. The X-ray based approach, such as Roentgen stereophotogrammetric analysis (RSA), fluoroscopy and computerised tomography (CT), is also widely applied due to its ability of capturing both real-time/near real-time *in-vivo* motion and the anatomical information. In some cases it requires a 3D reconstruction from 2D images which might lead to an inaccurate result as there is overlapping (e.g. fluoroscopy). Magnetic resonance imaging (MRI) has been introduced in the past decades to study knee kinematics, with its specific feature of visualizing cartilage and other soft tissues as well as the bony structures. Cohen et al. [133] assessed the three-dimensional accuracy of MRI for measuring the cartilage geometry of human cadaveric knee joints (*in-vitro*) and young volunteers (*in-vivo*). Freeman and his group [66, 67, 68, 69] conducted a series of comprehensive studies on the knee function by MRI. Li and his group [72, 73, 74, 75] has used a technique which combines the capability of two imaging modalities, dual orthogonal fluoroscopy and MRI. The anatomy information was obtained by static MR acquisition and dual orthogonal fluoroscopy was exploited to record the motion in real-time.

Apart from acquiring data *in-vivo*, analysing contact itself is not easy. Knee contact is believed to be closely related to how the forces are applied onto the cartilage surface, which potentially affects the knee degeneration at multiple scales. Therefore, defining the area in contact and locating the contact centre might help to identify the forces and patterns of cartilage degeneration. Contact mechanisms have been studied vastly both clinically [66, 67, 68, 69, 71, 70] and experimentally [72, 73, 75, 133]. Clinical contact analysis is mostly a 2D quantification, based on defining the contact point visually and measuring its distance to anatomical landmarks such as ipsilateral posterior tibial cortex [67]. Although important discoveries [63, 64, 70] have been made, which have revolutionized the understanding of knee joint motion from the traditional ligament guided "four-bar linkage model" [130], this 2D method is not sufficient to capture the complete 3D information, such as the sliding between the tibia and femur during flexion which is an out-of-plane motion. Thus 3D contact quantification would be preferable. Experimentally, the contact areas are defined by measuring the inter-node distance on smoothed meshes [133, 137, 138]. Cohen et al. [133] constructed their geometric model via a b-spline surface fitting method, and detected the patellofemoral contact areas by locating regions with the vertex to surface distance smaller than a given threshold (0.5 *mm*, around the spatial resolution of a voxel). Morooka et al. [138] built a surface separation map between each point of tibia and femur bony surfaces extracted from their joint X-ray and CT model, and defined a contact region with a surface separation of less than 6 mm. They defined the centroid of each contact area as the contact point in 3D.

4.2 Material and Methods

4.2.1 Data acquisition: a combined MR imaging method

A pilot study with the right knee joints of 2 volunteers (1 male, 24 years old and 1 female, 25 years old, without any known knee abnormality) were scanned using a combined MR imaging strategy as proposed in Chen et al. [119]. It is composed of a dynamic MRI acquisition as a knee motion recorder and a static high resolution MRI acquisition as a knee anatomical imager. The volunteers were first scanned with a 0.5 T double doughnut interventional MR system (Signa, General Electric, WI, USA) in order to record knee

flexing at different angles β under body-weight bearing for kinematic information (*dynamic datasets*). During the acquisition, the subjects were leaning against a vertical wooden frame (body-weight bearing condition) while their knee joints were in the sensitive spot of the imaging system. The flexing angles were visually decided by an experienced radiographer (as vis. angle β) and recalculated when contact points were analyzed (see Section 4.2.4). The whole experiment was to capture the moments from human squatting. The acquisition procedure (2D multi-slice FSPGR sequence, T_1 weighted) was sufficiently fast and covered the whole knee joint volume: from lateral to medial, 1 angle per volume, acquired in sagittal plane, acquisition matrix 256×256, 20 slices, in-plane resolution 1.1×1.1 *mm*, slice thickness 4.5 *mm* with 0.5 *mm* gaps (more details in Appendix A1). The anatomical information of the same knee joints (*static datasets*) was acquired afterwards with a 1.5T MR scanner (GE Signa HDx), while the two volunteers were lying supine. A much higher resolution 3D dataset (T_1 weighted, acquired in sagittal plane, matrix size 512×512×120, in-plane resolution 0.3×0.3 mm^2, slice thickness 0.7 *mm*) was acquired after one week on both volunteers. The protocol was tuned to enhance bone and cartilage, so that the knee motion can be measured more accurately. Thus the different tissue types, i.e. bone and cartilage, could be distinguished. This enables to reconstruct the real surface geometry of both femur and tibia cartilage. B_1 field inhomogeneity which may affect the segmentation of knee structures were removed on the scanner console using the GE built-in software Phased array UnifoRmity enhancement (PURE, [139]).

4.2.2 Anatomical modelling: segmentation and 3D reconstruction

Structures of interest (i.e. femur, tibia, and their cartilage) in this study were segmented on both static and dynamic datasets through a semi-automatic approach using MITK (Mint Medical GmbH, Heidelberg, Germany [140]). Contours of each structure were first delineated every 3 or 4 slices in the sagittal plane using their region growing method. Interpolation in the sagittal plane was then applied between these slices to generate contours of different structures on those unsegmented slices. 3D surface geometrical information was extracted by reconstructing the 3D models of knee from the segmented static datasets, with in-house software written in MATLAB.

The initial meshes were then smoothed using Poisson surface reconstruction, in order that the knee joint model especially the cartilage articulation surface geometry is well defined [141]. In practice, the implementation of MeshLab (Visual Computing Lab-STI-CNR [142]) was used. The Poisson reconstruction method formulates the surface mesh reconstruction procedure as a spatial Poisson problem; therefore the advantage of Poisson system being resilient to the presence of noise can be exploited. A 3D indicator function χ_M (defined as 1 inside the model, and 0 outside the model) of a solid object M is first computed by solving a Poisson equation: $\Delta\tilde{\chi}_M = \nabla \cdot \vec{\boldsymbol{V}}$. The term $\tilde{\chi}_M$ is the smoothed function of χ_M. The vector field $\vec{\boldsymbol{V}}$ is the smoothed surface normal field, generated from the input point set *S* (stored as an octree) convolved with a Gaussian filter $F_o(q)$ and weighted with eight nearest neighbours using a tri-linear interpolation:

$$\vec{\boldsymbol{V}}(q) \equiv \sum_{s \in S} \sum_{O \in N_D(s)} \alpha_{o,s} F_o(q) s.\vec{\boldsymbol{N}} \qquad \text{eq. 30,}$$

in which q is a point on the indicator function χ_M, s is a sample point inside *S*, $\mathrm{N_D(s)}$ is the set of eight neighbouring nodes at an octree depth of D closest to s. The term $\vec{\mathbf{N}}$ is the inward-facing normal, pointing from the space outside the 3D solid *M* to the inside. $\{\alpha_{o,s}\}$ is the set of the tri-linear interpolation weights. The Poisson equation is solved by minimizing the distance between the sample points and the indicator function, using a least square method. In the end, the surface model of χ_M is obtained by extracting an appropriate iso-surface using an adapted version of marching cubes [143].

In this case, the input oriented point sets are the contour vertices of the segmented datasets. The procedure of solving the Poisson equation and extracting the surface description function is a mesh smoothing process. As the Poisson system solves the problem globally using a local hierarchy, it has advantages over using smoothing filter alone but still retains the surface detail well enough [141]. The cartilage and its hosting bony structures were reconstructed together, to avoid the algorithm over-smoothing the cartilage edges which invokes very big curvatures (cartilage is very thin on its surface edges). The parameters defined in MeshLab for this analysis are: octree depth 10, solver divide 6, samples per node 1, and surface offset 1.

4.2.3 Functional modelling: motion retrieval and mapping

Kinematics modelling was performed on the segmented datasets (i.e. the masks) through an intensity-based rigid registration [144]. Each volume of the dynamic study is considered as one frame of the squatting motion. To retrieve every volunteer's knee motion model, each of their motion frame (*moving images*) was registered to the high resolution static dataset (*reference images*). The two bony structures together with their attached cartilage, i.e. the femur and its cartilage (femoral data), and the tibia and its cartilage (tibial data), are both considered as rigid bodies. As these two rigid bodies have different shapes and surrounding tissues and hence endure different forces, they are subject to different motions during the knee flexing procedure. To resolve this problem, a dual-rigid registration strategy, similar to that used in [145] was applied in order to project the recorded motion back to the anatomical model, where the two rigid bodies are registered separately. A standard sum-of-squared-differences (SSD) metric was used as the cost function (the similarity measure), leading to a non-linear least-squares problem. A third party optimizer in MATLAB was used to find the optimal solution of this problem iteratively following a Gauss-Newton scheme using a multilevel approach [147]. The segmented anatomical data were first down-sampled to a volume with 1 mm^3 isotropic voxel resolution, while the segmented motion data volume (i.e. femoral and tibial data masks) at each motion frame were up-sampled in the slice direction in order to achieve the same voxel resolution. The vis. angle β was used as an initial guess for the rotation of the femur. Then the two datasets were aligned approximately using a user interface which allowed the users to tune the alignment along the x, y, z axes of the data volume. The resulting data volume (i.e. after initialization) was the input for the registration procedure. The dual-rigid registration procedure led to two different transformation matrices at each knee flexing frame for femoral and tibial data respectively, leading to a 6 DoF knee joint model. The registration was performed by home-made software written in MATLAB (R2010b, The Math-Works, Natick, Massachusetts, USA).

4.2.4 Contact mechanism: planar and volumetric analysis

The tibiofemoral contact mechanism was analyzed on the cartilage surfaces on both 2D

sagittal profiles of knee joints and the 3D functional model. To identify the change of contact points (CP) against of the angles of knee flexion, the reference system was set to be the anatomical system formed by the geometric median axis of tibia (tibia median axis, TMA) and femur (femur median axis, FMA) in the 3D functional models. The knee flexion angle, also named the f-angle θ, indicates the actual flexion between the two bones (Figure 13a). It is defined as the angle that is needed to rotate TMA towards FMA until they become overlapped or parallel to each other. Anti-clockwise direction was considered to be the positive direction. The measurement of flexion angle was performed based on the registered 3D knee joint models in MITK ([140]).

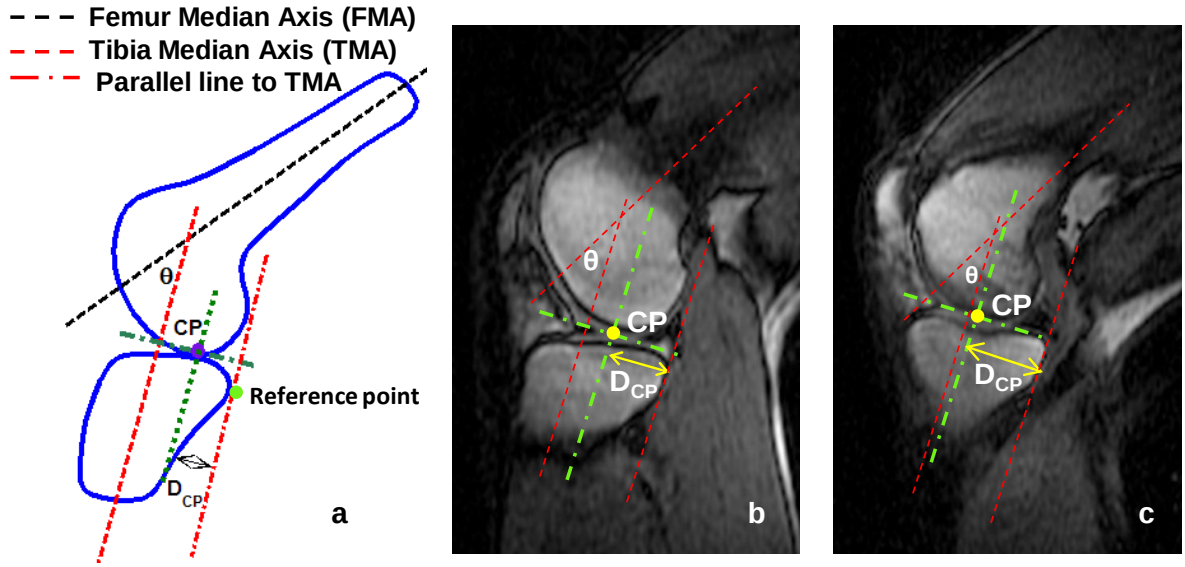

Figure 13. Contact analysis in 2D. a. Reference coordinates for contact analysis. The angle θ between the femur and tibia median axis is the final knee flexion angle. CP is the contact point. *DCP* is the distance from CP to the tibia median axis. b.: Contact analysis on one volunteer's mid-lateral profiles in the sagittal plane; c.: Contact analysis on one volunteer's mid-medial profiles in sagittal plane.

2D contact mechanism was first studied on the sagittal profiles of the mid-medial (MM) and mid-lateral (ML) slices through every motion frames (Figure 13). A motion frame is an acquired knee volume of the dynamic datasets. Mathematically, contact exists if two curves or surfaces Σ_1 and Σ_2 have consecutive regular points in common. The general definition of *contact* and *tangent* as in differential geometry is as follows [148, 149]:

Definition 1 (*Contact*): *Let two smooth manifolds Σ_1, Σ_2 have a regular point P in common (Figure 14). Take a point A on $\Sigma_1$near P and let AD be its distance to Σ_2. Then, Σ_2 has a contact of order n with Σ_1 at P, when for A approaches P ($A \to P$) along Σ_1, $lim\frac{AD}{(AP)^k} = \delta$,*

$$\delta = \begin{cases} finite(\neq 0), & k = n+1 \\ 0, & k = n \end{cases} \qquad [AD = o((AP)^k)\ for\ k = 1, 2, \cdots\cdots, n].$$

AP is not necessarily a straight segment however when *A* approaches *P*, the ratio of the arc length ℓ and the corresponding chord length connecting two points *A* and *P* (i.e. the Euclidean distance) on a curve approaches a unit w[8].

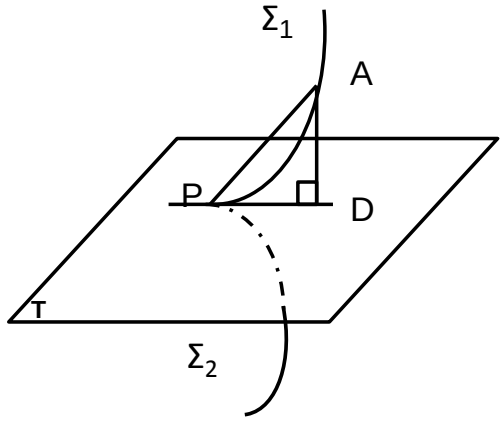

Figure 14. Definition of contact and tangent: $\Sigma_1$and Σ_2 are two smooth curves. P is a contact point between: $\Sigma_1$and Σ_2. AP is a chord of Σ_1, and PD is the tangent line of : $\Sigma_1$and Σ_2 . AP ⊥ PD. PD is inside the space **T**

Definition 2 ***(Tangent):*** *Given a curve or surfaceΣ_1 , the tangent at a point P, $x_P \in \Sigma_1$(*Figure 14*) is defined as the first derivative of x_P. $t = dx_P/d\ell$ is the unit tangent vector, where ℓ is the arc length.*

After the reconstruction procedure, both surfaces are smoothed. Therefore, it is reasonable to assume that both surfaces are analytical manifolds. Adapting Definition 1 and 2 to analyse knee contacts, if a point *P* on the femur cartilage surface mesh Σ_1 is in contact with the tibia cartilage surface mesh Σ_2, the tangent vectors of this point to Σ_1 and Σ_2 are inside

[8] For proof of this statement, please refer to [149] on page 7

the tangent space of both surfaces and they are collinear. Thus the Euclidean distance from P to the tibia cartilage surface mesh Σ_2 is zero and the Euclidean distance from P to the femur cartilage surface mesh Σ_1 is also zero. Therefore, in practice, contact points can be located by searching the nodes of Σ_1 whose distance to the nodes of Σ_2 is approaching zero or smaller than a given tolerance value [150] (in this study 0.5 *mm* is used as the threshold). The node- to-node distance is calculated based on Qhull [151], using the built-in function in MATLAB.

To understand the knee kinematics, a further analysis on how contacts change against the flexion of knee is performed based on observing the motion of the contact point (CP), as the centre of the contact regions. For 2D analysis, the contact region is a curve segment and the CP is the midpoint of the segment. For 3D analysis, the contact region is a bounded surface and the CP is the centroid of this surface. The motion of CP in 2D is traced by the distance of CP (D_{CP}) against the reference frame. It is defined as the Euclidean distance from CP to the line passing ipsilateral posterior tibial cortex and parallel to the projection of TMA onto the selected image. Therefore the relative movement of CP while knee flexing from angle θ_k to θ_{k+1} in 2D can be computed as the difference of D_{CP} at different flexing angle β (Figure 13):

$$\Delta \mathrm{D}_{\mathrm{CP}}^{\mathrm{k,k+1}} = D_{\mathrm{CP}}(\theta_{k+1}) - D_{\mathrm{CP}}(\theta_k), \quad k = 1 \cdots n-1 \qquad \text{eq. 31}$$

In 3D, the contact point was estimated as the centroid of the contact area of the tibial cartilage surface mesh. The contact area was extracted using a region growing algorithm for surface mesh segmentation as explained in [152], implemented in MATLAB.

4.3 Results

4.3.1 Modelling and data acquisition

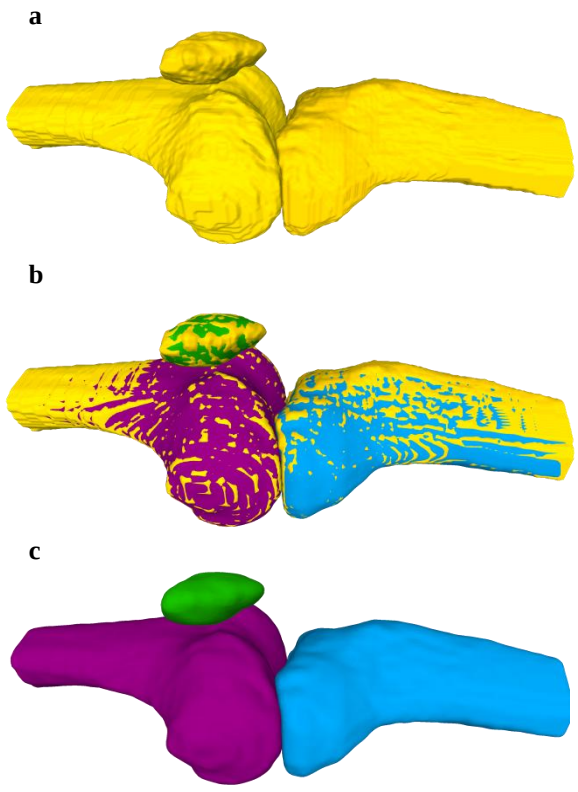

Figure 15. 3D anatomical model generated from Poisson reconstruction. a. 3D model before applying Poission reconstruction; b. Surface reconstruction difference: with (green for patella, blue for tibia and violet for femur) and without (golden colour) Poisson reconstruction; c. 3D anatomical model: Poisson reconstruction.

Examples of dynamic images are shown in Figure 13(b-c). Structures of interest, e.g. cartilage and bone can be well recognized. Anatomical models generated by Poisson reconstruction are illustrated in Figure 15. In Figure 15(a), the anatomical model reconstructed directly from smoothed contour sets shows obvious bumps and steps between slices (caused by the size of the slice thickness). However, in reality these structures are much more regular. These bumps and slice steps are clearly reduced after extracting the surface model from the oriented point sets formed by the contour vertices by Poisson reconstruction (Figure 15(b)). Differences between the two reconstructions are shown in Figure 15(c) by superposing the two models. The original model is coloured gold while the Poisson model is coloured with green, blue and violet for patella, tibia and femur respectively. The registration result is illustrated in Figure 16. The evaluation of the registration of both volunteers will be presented in Chapter 5 together with all the other volunteers included in knee kinematics study.

4.3.2 Subject-specific contact analysis

Table 3 lists either volunteer's displacement of contact points in mid-medial and mid-lateral planes under different angles of knee flexion. In the experiment of volunteer 1, 3 knee flexion angles were studied. The vis. angles β are 5°, 45°, and 90°. The corresponding f-angles θ are 16.4°, 49.5° and 74.3°. The displacement of CP (ΔD_{CP}) from β = 5° to 45° and

from 45° to 90° are -1.91 *mm* and 0.46 *mm* in mid-medial plane and 0.74 *mm* and -1.51 *mm* in mid-lateral plane. For volunteer 2, five knee flexion angles were studied, from extension to fully bended (β = 0°, 30°, 45°, 90°, fully bended). The corresponding f-angles θ are -18.6°, 26.5°, 52.4°, 88.3° and 142.1°. The flexion angles covered all three flexion arcs: screw home arc, functional active arc and passive deep flexion arc [63]. The displacement of CP (ΔD_{CP}) of volunteer 2 showed a different pattern from volunteer 1. A bigger displacement of CP has been observed. In the mid-medial plane, from θ_1 to θ_5 CP moved by -0.5 *mm*, 4.4 *mm*, 3.2 *mm* and 2.9 *mm* while in the mid-lateral plane, it moved by 2.7 *mm*, 2.9 *mm*, 3.4 *mm* and 6.6 *mm*.

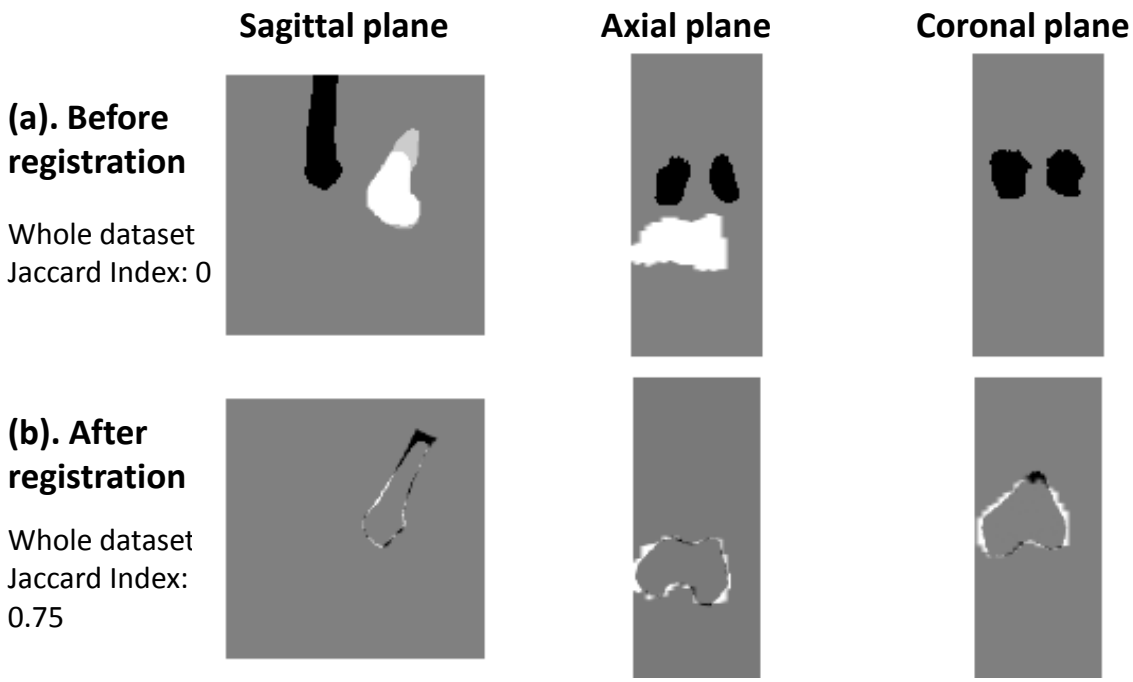

Figure 16. Registration result (femur data from volunteer 1, at vis. angle β=5°). (a) Image difference between the anatomic data and motion data in all the three planes view before registration. In the coronal plane, the two datasets hardly overlap. (b) Image difference after registration with overlapping improved. The Jaccard index (Dice score, [156]) for volunteer 1 at this flexion angle is 0 before registration and 0.75 with registration applied. The Jaccard indices at other flexion angles of volunteer 1 are reported in Table 5, Chapter 5. The un-overlapped part of the femur proximal shaft in (b) in the sagittal plane is caused by a bigger FoV at 0.5T when acquiring motion data than that used for the anatomical data acquisition at 1.5T where the knee coil covers a relative smaller FoV. Un-overlapped part in the other two planes may be due to the oversampling of motion data which has a bigger slice thickness (4.5 mm) as compared to that of anatomical data (1.0 mm).

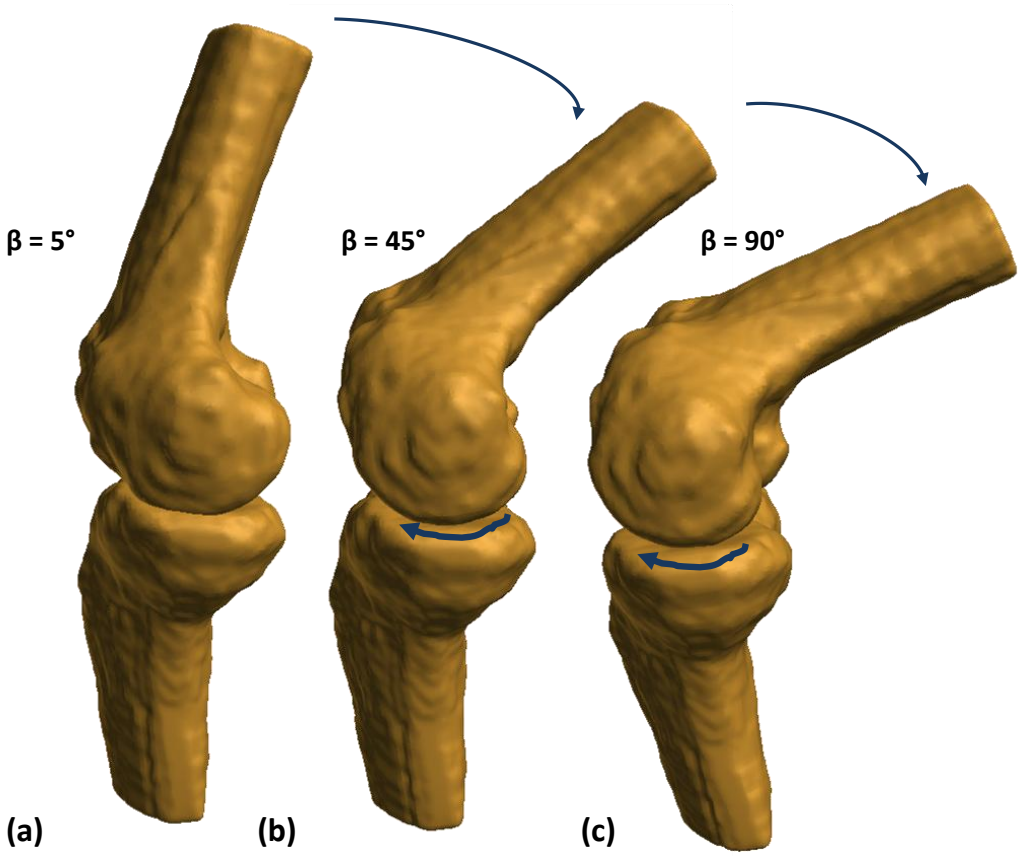

Figure 17. A 3D view of bending knee joint (volunteer 1). From (a) to (c), the visualisation corresponds to vis. angles β at 5°, 45°, and 90°. The deep blue arrows plotted on the tibial plateau indicate the direction of the femur external rotation.

Table 3: Subject-specific motion of contact points against flexing angles (2D)

Volunteer 1 (male, 24 years-old)				Volunteer 2 (female, 25 years-old)				
vis. Angle β	5°	45°	90°	0°	30°	45°	90°	Fully-bended
f-angle θ	16.4°	49.5°	74.3°	-18.6°	26.5°	52.4°	88.3°	142.1°
ΔD_{CP} (mid-medial plane) (mm)	-	-1.9	0.5	-	-0.5	4.4	3.2	2.9
ΔDCP(mid-lateral plane) (mm)	-	0.7	-1.5	-	2.7	2.9	3.4	6.6

Figure 17 illustrates the 3D view of the knee flexion of volunteer 1. From (a) to (c), the

three knee models correspond to knee with the flexion angle β = 5°, 45°, and 90°. It shows very intuitively how the knee joint changed its position while bending at the three angles. The squatting motion is to 'shorten' the lower limb (i.e. lower the absolute height of human body and reduce the absolute distance from the hip joint to the ankle joint). To achieve this motion, in the anterior-posterior direction, the femur condyles and tibia head moved for a big distance. The external rotation of femur can be noticed by comparing the orientation of the medial femoral condyle in Figure 17(c) and (a), (b). However, very little rotation can be spotted on tibia. The rolling motion that is reported to occur during the knee bending motion can also be easily noticed by looking at the distinct directions to where the femur shaft points.

The out-of-plane rotation which cannot be observed in the 2D contact analysis is revealed by the 3D contact analysis. In Figure 18, the axial views of the knee joint contacting at all the three bending angles (Figure 18 (b-d)) of volunteer 1 are shown with the non weight-bearing position as a reference (Figure 18(a) the anatomical model acquired as the supine position). The contact points allocated as the centre of the contact areas were spotted as green points on the cartilage surface of femur condyle. Possible contact trajectories are qualitatively shown as the pink lines going through the contact points.

4.4 Discussion

The combined MR imaging method provides a methodology for understanding the knee motion in a more accurate and detailed manner. The workflow of subject-specific contact analysis may be composed of 3 steps: data acquisition, modelling (parameterization) and analysis & validation (Figure 19).

In the data acquisition step described in this chapter, a combined imaging approach has been proposed to resolve three technical limitations caused by using only one imaging technique. It reveals tremendous anatomical details in both static imaging and dynamic imaging, especially soft tissues; being non-invasive and non-ionizing; and the reliability as in comparison with skin markers. Although using the interventional MR to understand knee

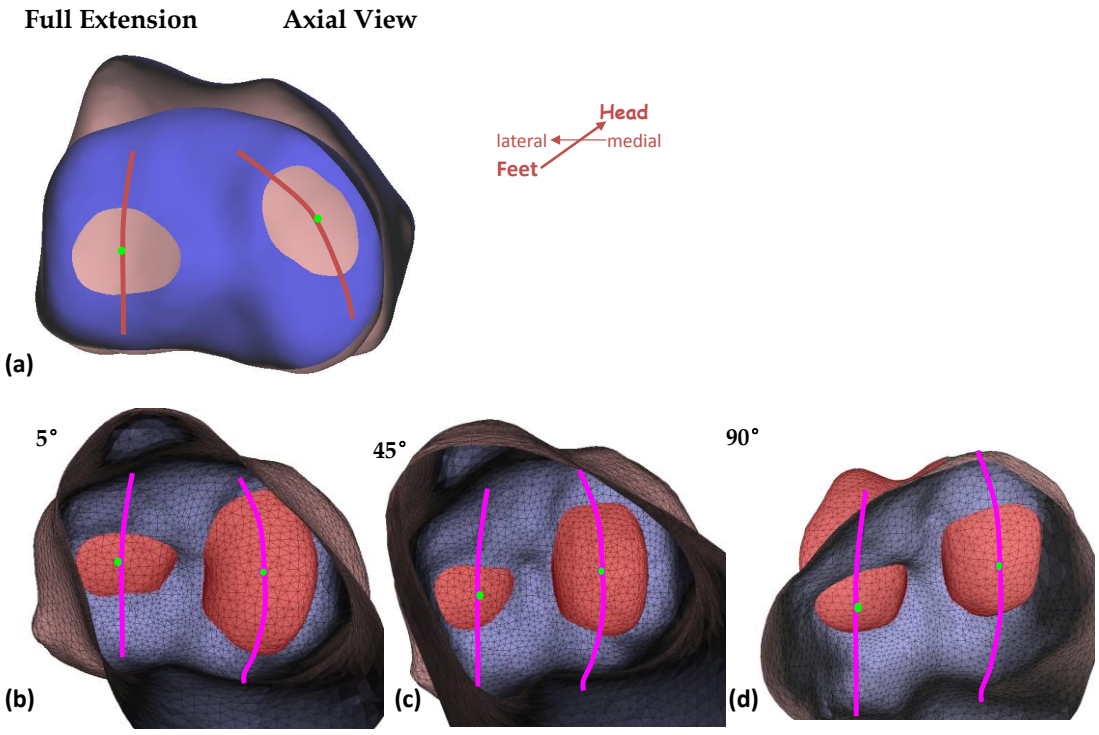

Figure 18. Illustration of locations of contact points of the tibiofemura articulations in volunteer 1 (axial view with contact points projected on the femur head) (a). the contact points on the located at the supine position, non body-weight bearing condition, model derived the static high resolution MR acquisition; (b-d). the locations of contact points at body-weight bearing condition, models derived from the registered motion data. The viewing angle is from distal to proximal (i.e. from the feet to the head). The FoV of this figure is from "inside" the tibia, coloured blue. The outside of the bones are coloured in brown. The contact areas are highlighted in red in (b-d). The contact points are delineated in green points and the pink/ red lines are qualitatively illustrated as possible contact trajectory.

kinematics has been previously proposed by Freeman's group [66, 67, 68, 69, 63] and Johal et al. [153], they mainly utilised the motion data only to understand the knee kinematics and analysed the tibiofemoral contact pattern in 2D without incorporating any three dimensional models as that has been proposed in this chapter. The disadvantage of MRI methods for motion study is mainly its relative small FoV compared to the ability of video camera and X-ray based method such as fluoroscopy. However, there is no doubt that MRI as other imaging modalities suffer from the partial volume effects, thus the lower bound of measurement error is on the order of the resolution. Hence, from the data acquisition point

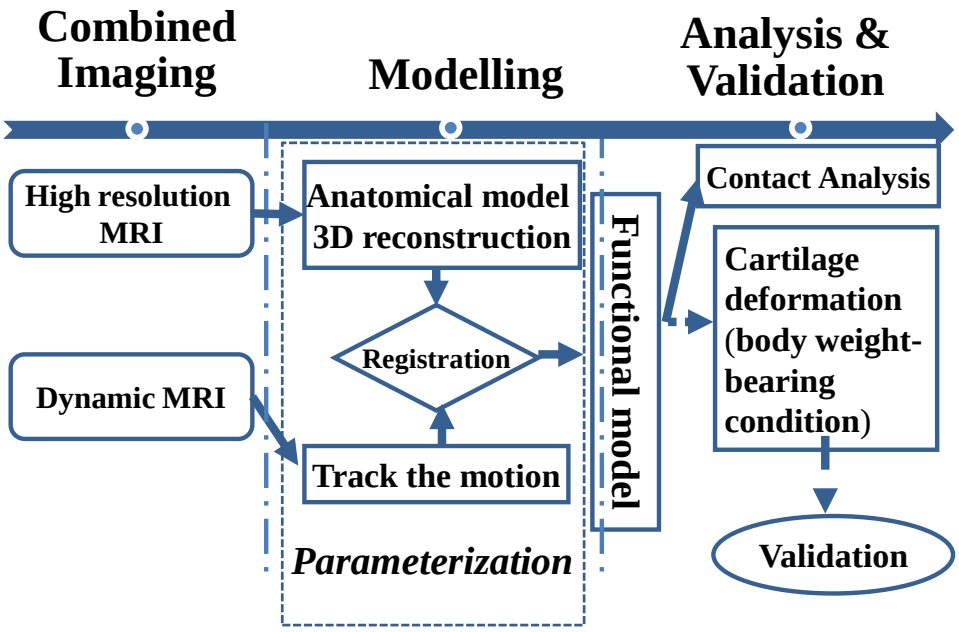

Figure 19. The workflow of subject-specific knee joint contact analysis.3 steps can be summarized: *data acquisition* (left block), *modelling* (middle block), and *quantification & validation* (right block). The arrowed dash lines indicate that the parts are not included in this work (the validation here refers to a validation with a gold standard, e.g. experimental validation based on cadavers, as proposed by Cohen et al. [133]).

of view, the improvement of hardware's temporal and spatial resolution is critical to improve the measurement. Temporal-resolution-wise, the application of cine sequence with a spiral trajectory [154] has achieved a frequency of 35 frames per second on a 0.5T MR scanner. In terms of spatial resolution, the dynamic MRI acquisition system only has a magnetic field strength of 0.5T, which is a major limitation to the data resolution. A 1.5T interventional MR system will surely provide higher quality data using the current acquisition protocol. And for the static data acquisition, a 3T MR system may provide a better understanding of the soft tissues deformation such as ligaments and tendons. It would certainly be a big step forward for a comprehensive understanding of knee kinematics.

Our modelling process by using Poisson reconstruction leads to a mathematical parameterization of the knee joint geometry. This attempt maybe leads to generation of a more realistic subject-specific model and may increase the reliability and reproducibility of the measurements of knee contact mechanism accordingly. Instead of only smoothing the

surfaces by interpolation as in [133], the point sets of the cartilage surfaces are modelled as a Poisson equation which has been shown to be more resilient to noise [141]. This also enables us to consider all of the cartilage surfaces as manifolds mathematically, leading to a mathematic definition of contact points in 2D and 3D. By considering femur and tibia separately, a knee functional model of 6 DoF is achieved. Therefore, instead of understanding knee kinematics globally by considering the median axis of each structure, the modelling is more localized which leads to a more accurate analysis. The last part of this workflow is validation which is currently a difficult task and also an open question in the field. One reason is that it is very difficult to determine how much force is actually applied to the articulation surfaces *in-vivo*.

The finer scale at which it is possible to observe cartilage deformation is $0.2\ mm$ [155]. This is much higher than the resolution of our dynamic data, $1.1\ mm$, therefore the cartilage deformation can be ignored in this work. Consequently the tibia, and femur, together with their hosting cartilage are considered as rigid bodies. Functionally, the femoral part of the knee joint is constrained by the hip joint at the proximal end, which is a ball-and-socket type of joint; whereas the tibial part of the knee joint is constrained by the distal tibiofibular joint at the distal end, which is a syndesmosis type of joint and provides smaller range of movement than the ball-and-socket type hip joint [61]. Moreover, the surrounding soft tissues (e.g. muscles, tendons and ligaments) of femur and tibia are also organized differently. Hence, their motion patterns cannot be the same. Accordingly, it is necessary to consider the motion of femoral and tibial rigid bodies independently. Although the registration is applied separately, the linear nature of the image transformation operation allows adding the two corresponding matrices together to derive the final knee joint displacement. As the magnetic field inhomogeneity is very big in the motion data (due to the open access nature of the scanner), we applied our registration based on the masks instead of the original images. The exploited registration method is based on voxel intensity and considers rigid transformation only, therefore the segmentation errors would not introduce significant errors for the registration procedure, but could affect the localisation of the contact points. This error estimation issues will be extensively discussed in the next chapter with all the included datasets.

Wretenberg et al. [71] proposed to use the scanner coordinate system as the primary coordinates and the anatomical coordinates as the reference frames to measure the motion of contact points (CP). However, exploiting the scanner coordinate system as a reference frame is quite sensitive to the relative motion between the subject's leg and the scanner during the knee flexion movement (e.g. the rotation of femur and gliding between femur and tibia condyles when knee flexes between 30° and 120°, as explained in Section 2.3.1), which causes the inconsistency among CP measurements at various knee flexion angles. Moreover, such relative motion is mainly out-of-plane motion which leads to the inevitable changes of imaging slice locations in the whole knee joint. Although a further step was introduced in order to correct the disagreement between the reference frame and the anatomical coordinate for movements at knee flexing at 30° and 60° by the authors, this 2D-3D hybrid method (i.e. analysing three dimensional information based on 2D slices) cannot completely solve the problem caused by slice location misalignment at different knee flexion angles, which varies from subject to subject. Therefore, instead of setting the scanner coordinates as the reference frame, we utilized the subject's own anatomical frame extracted from 3D models directly. This was considered to be more reliable and robust for the following reasons: firstly, it is subject-specific; secondly, no relative motion occurs while knee is flexing thus no correction is needed to resolve the disagreement between the scanner coordinates and the anatomical coordinates.

The traditional ligament-guided "four-bar linkage" model is flawed as it only provides 2D information while the knee complex itself is three-dimensional [63]. The proposed contact analysis method is based on both 2D and 3D information in order to provide a more comprehensive view for the tibiofemoral articulation kinematics. The contact points might be also modelled as a function of the flexion angles so as to differentiate the healthy knee and diseased knee the contact point trajectory of which would be diverted from averaged normal ones. The insights given by the contact point motion will be discussed in Chapter 5.

4.5 Summary

The combined MR imaging provided an imaging strategy to obtain detailed insight of knee function *in-vivo* under body-weight bearing condition and to resolve the previous confusion

found in the 2D-based "four-bar linkage" model [63]. It shows the relations between knee motion and articulation surfaces inside the knee can be modelled and might be used to differentiate healthy knees from those abnormal ones. The observed contact pattern can provide more detailed insights for diagnosis and therapy. Our current future plans include the automation of all the steps in our proposed method. We want to perform this type of analysis on a larger cohort of healthy subjects. In addition, we aim to analyse some pathological cases in order to determine the sensitivity of the contact pattern as a cursor (or precursor) for abnormality of the knee joints.

The author's contributions in this work are summarized as below (the work described in this chapter has been published in Chen et al. [76]):

1) A combined MR imaging strategy has been proposed, tuned and tested for *in-vivo* subject-specific knee joint functional study under body-weight bearing conditions, in which an interventional MR scanner (double donut system) is used to record the knee joint motion and a conventional clinical MR scanner is used to acquire the high resolution anatomical data.

2) A systematic workflow is designed for 2D and 3D contact analysis on the knee joint. Its function is investigated via tibiofemoral articulation by tracking the contact point position on the cartilage surface against knee flexion angles. In this approach, a new reference system for knee flexion angle has been introduced in order to better describe the flexion angle between the femur and tibia (in comparison with the most commonly used visual determined flexion angle system). A dual-rigid registration method is equipped to map the recorded motion to the anatomical dataset using home-made software programmed in MATLAB.

Chapter 5. Subject-specific study of the knee joint function

In this chapter, the systematic study of knee joint functional study proposed in Chapter 4 has been applied to 4 more individuals' right knees. Subject-specific analysis was conducted and compared on the whole experiment group (together with the 2 volunteer data from the pilot study in Chapter 4). Firstly, knee flexion under multiple angles was recorded with an interventional MR under body-weight bearing conditions. Anatomical models of knee joints were reconstructed from high resolution data acquired statically. Secondly, both 2D and 3D contact analysis were applied on all the knee joints. The subject-specific functional knee joint was modelled based on the location of contact points on articular cartilage surface against flexion angles on the 3D model. A comparison was performed in the end between individuals. The results provide valuable insights to understand knee joint kinematics and could be potentially used for surgical treatments (e.g. knee replacement surgery) follow-up evaluation.

5.1 Introduction

A good understanding of knee joint kinematic is important to improve many clinical applications including follow-up evaluation of ligament reconstruction surgery, designing of artificial knee joint for knee arthroplasty, classification of osteoarthritis, etc [64]. Recent work advanced the understanding of knee kinematics significantly [62, 63]. The traditional 'ligament guided four-bar linkage model' [130] has now been shown to be flawed as it does not consider the 3D geometry [63] and oversimplifies the material of the knee joint as a rigid body since the knee joint is not only composed by bone but also cartilage, and soft tissues including ligaments and meniscus. Therefore, quantitative analysis and subject-specific modelling based on 3D information *in-vivo* would certainly help to gain a more comprehensive and detailed knowledge of knee joint kinematics.

In this work, we studied and quantified the kinematics of knee joint *in-vivo* under body-weight bearing conditions by investigating the tibiofemoral contact mechanism on the

articulation surfaces of 6 volunteers' right knee joints. Data acquisition methods and modelling methods are exploited as proposed in Chapter 4. Each volunteer's knee kinematics was analysed in both 2D and 3D. The contact trajectory was derived based on the position of 3D contact points, and comparison between individuals was made to illustrate possible variations on gender, condition of surrounding supporting tissues (i.e. muscles) and bodyweight. Subject-specific knee joint function was studied on knee flexing angles and contact points. It is believed that the moving pattern of the knee joint would be altered and the contact point trajectory would be changed in case of knee joint abnormality.

5.2 Material and Methods

5.2.1 Subjects and experiment setup

Following the pilot study described in Chapter 4, the right knees of four more volunteers (volunteer 3-6, without any recorded knee joint abnormalities) were scanned using the combined MR protocols as suggested in Chapter 4 to record the knee motion during squatting, using the same experimental protocol: the subjects were standing against a vertical wooden frame and flexing at 5 flexion angles visually decided by the radiographer (vis. angle β). The volunteers were also requested to keep their feet in full contact with the floor (avoid ankle flexion) to reduce the influence of ankle motion to the knee flexion kinematics. The age range of the volunteers is between 24 and 33 years old (27.5±3.5 years). The corresponding f-angles (θ, Figure 13(a)) were measured after the scan. The number of slices in the dynamic MR acquisition was adjusted to fit the size of every subject's knee joint (varying between 18 and 23 slices per angle per knee joint). Prior to the acquisition, the experiment procedure was carefully explained to the volunteers. An interview was added after the scan in case the volunteer wanted to explain to the researcher about some special situations that he considered had not complied with the experimental protocol at the extreme knee joint positions (e.g. the full bending and the full extension). Volunteers were later scanned (after around a week) with the same 1.5 T GE HDx system (Chapter 4) to acquire the 3D high resolution static images.

These datasets were archived together with those from the pilot study; therefore a total

Table 4: Subject-specific contact analysis in 2D: bending angles and relative contact point motion.

	vis. Angle β	f-angle θ	Mid-medial plane (mm)		Mid-lateral plane (mm)	
			$D_{CP\_M}(\theta)$	ΔD_{CP_M}[a]	$D_{CP\_L}(\theta)$	ΔD_{CP_L}[a]
Volunteer 1 (V1)	5°	16.4°	27.2	-	15.7	-
male, 24 years	45°	49.5°	25.3	−1.9	16.5	0.7
old, 68kg, 172 cm	90°	74.3°	25.8	0.5	14.9	-1.5
Volunteer 2 (V2)	full-extension	-18.6°	25.6	-	19.6	-
female,	30°	26.5°	25.1	-0.5	16.9	-2.7
25 years old,	45°	52.4°	20.8	-4.4	14.0	-2.9
53kg	90°	88.3°	17.6	-3.2	10.6	-3.4
160cm	fully-bended	142.1°	14.6	-2.9	4.0	-6.6
Volunteer 3 (V3)	full-extension	-8.4°	27.6	-	20.4	-
Male	30°	26.2°	25.8	-1.9	15.8	-4.7
33 years old	45°	52.6°	27.4	1.6	14.0	-1.7
85kg	90°	87.5°	24.5	-2.8	13.3	-0.8
196cm	fully-bended	125.3°	23.6	-1.0	11.1	-2.2
Volunteer 4 (V4)	full-extension	-3.0°	24.2	-	23.6	-
male	30°	34.1°	21.6	-2.6	20.6	-3.0
28 years old	45°	64.8°	20.6	-1.0	17.2	-3.4
67kg	90°	81.9°	18.5	-2.1	13.9	-3.3
183cm	fully-bended	142.5°	18.9	0.5	9.8	-4.1
Volunteer 5 (V5)	full-extension	-2.2°	25.2	-	20.6	-
Male	30°	31.1°	25.1	-0.1	18.8	-1.7
25 years old	45°	62.5°	24.7	-0.4	15.3	-3.5
85 kg	90°	99.1°	23.8	-0.9	15.3	0
185cm	fully-bended	140.7°	22.6	-1.2	12.1	3.3
Volunteer 6 (V6)	full-extension	-10.2°	24.4	-	19.9	-
Male	30°	12.5°	28.0	3.6	19.8	-0.1
30 years old	45°	54.7°	23.0	-4.9	20.1	0.3
70 kg	90°	118.5°	19.2	-3.9	16.1	-4.0
175cm	fully-bended	151.8°	11.4	-7.8	6.9	-9.2

[a]. Negative distance means the contact points are moving posterior, i.e. towards the tibia cortex.

number of 6 subjects is included for this subject-specific study. Anatomical data from all the volunteers were subsequently examined by a consultant radiologist with a musculoskeletal interest. Among all the 6 volunteers, the first volunteer was only asked to flex his knee at 3 angles, 5°, 45° and 90°; the other 5 volunteers were asked to bend their

knees at 5 angles, 0°, 30°, 45°, 90°, and fully bended. The demographic information on each subject (weight, height, age, and sex) and experimental procedure (i.e. the knee bending angles) are listed in Table 4.

5.2.2 Modelling

Both the dynamic and static data were segmented and reconstructed in a manner as in Section 4.2.2 and validated by an experienced radiologist with tibia, femur, tibia and femur cartilage delineated. Functional modelling as explained in Section 4.2.3 was applied to register the recorded motion data to the anatomical model. The registration was assessed by Jaccard index ([156], as an independent metric from that used in the optimization) for all the six volunteers at every flexion angle since this operation was applied onto the segmented data, thus their similarity can be evaluated by the amount of overlapping. The calculated transformation matrices of each angle were applied to the anatomical model in order to replay the squatting motion at the corresponding angle with a much higher resolution.

5.2.3 The tibiofemoral contact mechanism

The quantification of the contact mechanism is based on following the motion of contact points at each angle. In 2D, the motion of contact points is quantified with the relative distance change (ΔD_{CP}) between the two successive angles among all the flexion angles using eq. 31 on the mid-medial and mid-lateral (sagittal) planes. The overall flexion arc ($\Delta\theta$, eq. 32) is calculated as the Q-angle θ difference between the knee-extension frame (θ_1) and the knee-full-bending frame (θ_N, N=5 in this case). The overall absolute contact point displacement ($\sum_{k=1..N-1} \Delta D_{CP}^{k,k+1}$) on either plane is calculated as the difference between the contact positions at the knee-extension frame ($D_{CP}(\theta_1)$) and the knee-bending frame ($D_{CP}(\theta_N)$)

$$\Delta\theta = \theta_N - \theta_1, \quad \text{eq. 32}$$

$$\sum_{k=1..N-1} \Delta D_{CP}^{k,k+1} = D_{CP}(\theta_N) - D_{CP}(\theta_1) \quad \text{eq. 33}$$

The distance (D_{CP}) between the contact point and the knee joint reference frame on both slice were plotted against the flexion angle (f-angle, θ).

In 3D, the contact points (denoted as CP1) were identified by determining the centroid of each contact region as in Section 4.2.4. The movement of contact points were further annotated on the tibia cartilage surface and connected one by one following an ascending order of the f-angle θ. In order to estimate the error of contact point location analysed by the proposed method, a simulated segmentation error of 1 *mm* (around 1 voxel size in the motion data volume) was introduced using the morphological image operator, erosion. Another set of contact points (denoted as CP2) were then extracted based on the simulated segmentation following the aforementioned procedure. The Euclidean distance between the corresponding points from the two contact point sets (CP1 and CP2) of all subjects were calculated.

5.3 Results

Table 5: Jaccard index (Dice score) of each volunteer at every flexion angle: comparison before registration, after initialization and after registration

		Femur					Tibia				
Vis angle (β)		5°	45°	90°			5°	45°	90°		
V1	before registration	0	0.01	0.12			0	0.02	0.11		
	After initialisation	0.52	0.61	0.49			0.67	0.70	0.70		
	After registration	0.75	0.75	0.75			0.75	0.76	0.81		
Vis angle (β)		E	30°	45°	90°	B	E	30°	45°	90°	B
V2	before registration	0	0	0.1	0.01	0	0	0	0.05	0.04	0
	After init.	0.60	0.66	0.54	0.59	0.60	0.52	0.56	0.65	0.66	0.55
	after reg.	0.77	0.74	0.71	0.67	0.71	0.77	0.78	0.79	0.78	0.75
V3	before registration	0	0	0	0	0	0	0	0.01	0	0
	After init.	0.60	0.70	0.65	0.53	0.51	0.49	0.53	0.57	0.68	0.68
	after reg.	0.70	0.77	0.70	0.62	0.64	0.70	0.72	0.72	0.74	0.76
v4	before registration	0	0.2	0.20	0	0	0	0.24	0.05	0.07	0.04
	After init.	0.43	0.63	0.53	0.56	0.62	0.41	0.53	0.63	0.58	0.54
	after	0.78	0.77	0.77	0.73	0.74	0.70	0.71	0.76	0.7	0.7
V5	before registration	0	0.05	0.27	0.12	0	0	0.32	0.03	0	0
	After init.	0.49	0.52	0.53	0.61	0.70	0.47	0.47	0.52	0.64	0.43
	after	0.69	0.74	0.78	0.70	0.77	0.77	0.78	0.75	0.73	0.69
V6	before registration	0	0.11	0.14	0.20	0.08	0.02	0.14	0.02	0.17	0.24
	After init.	0.47	0.68	0.49	0.52	0.54	0.41	0.48	0.58	0.55	0.61
	after	0.75	0.77	0.73	0.73	0.76	0.79	0.8	0.77	0.76	0.76

No abnormalities were detected on the MR images of volunteers 1-5; however Volunteer 6 had diffuse atrophy of right quadriceps muscles (mainly in vastus lateralis and vastus intermedius). The Jaccard indices (Dice score) between the moving volumes (i.e. recorded motion data) and reference volumes (i.e. high resolution anatomic data) before and after registration all the volunteers is listed in Table 5. After registration, the averaged Jaccard index was improved from 0 to 0.79 (±0.15).

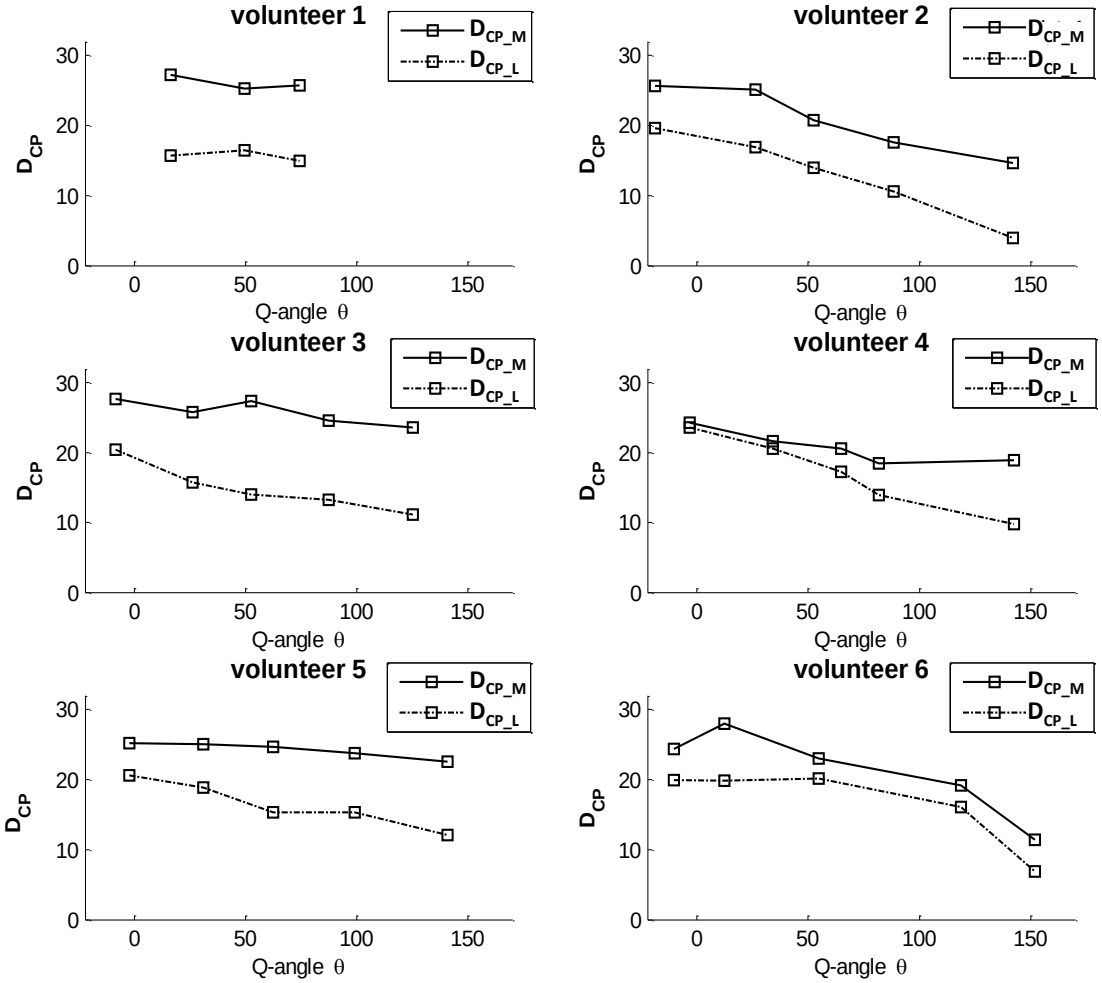

Figure 20. Plot of the position of contact point (D_{CP}, mm) in both mid-medial and mid-lateral planes against the f-angle θ (in degree) of each volunteer (2D)

The 2D contact measurements of all the 6 subjects are listed in Table 4. Although the measured f-angle θ shows some disagreement with the vis. angle β, θ is increasing with β so each dynamic MR acquisition corresponds to a different point of the whole squatting procedure. It is also interesting to notice, when fully extended, the angle between femur and

tibia is not exactly 0°. The median axis of tibia goes slightly in front of that of the femur, resulting in a negative θ.

For volunteer 1, the investigated flexion arc is shorter than the other volunteers. The total investigated arc ($\Delta\theta_{V1} =$) are of 57.9°. The contact point displacement in the mid-medial plane of volunteer 1's knee joint moved first backwards (ΔD_{CP} = -1.9 *mm* (< 0) , toward the ipsilateral posterior tibia cortex) and then forwards; while in the mid-lateral plane, the contact point first moved slightly forward and then backward. The two "forward" displacements are all under the size of a pixel. The overall displacements on both planes are -1.5 mm on the mid-medial plane and -0.8 mm on the mid-lateral plane.

For volunteer 2, on both planes, the contact points moved backwards but with varying magnitude over a total flexion arc ($\Delta\theta_{V2} = 160.7°$). From full extension position to β = 30°, the displacement in the mid-medial plane ($\left|\Delta D_{CP\_M}(26.5°)\right|$ = 0.5 *mm*) was much smaller than that in the mid-lateral plane ($\left|\Delta D_{CP\_M}(26.5°)\right|$ = 2.7 *mm*). The total absolute displacement ($\sum \Delta D_{CP}$) on the mid-medial plane is -11 *mm* while on the other plane, a displacement of -15.6 *mm* occurred.

For volunteer 3, while knee flexing from θ = 26.2° to 52.6°, the contact point almost went back to the starting position on the mid-medial plane (D_{CP_M} (-8.4°) = 27.6 *mm*, D_{CP_M}(52.6°) = 27.4 *mm*) while on the other plane the contact point continued to move backward (from the position at 20.4 *mm* to 14.0 *mm*). The opposite contact point moving direction on the two plane indicates a possible external rotation with the rotation centre lying on the side with less contact point displacement, in this case the medial part of the knee joint. With the knee flexion continued (from θ = 26.2° to 125.3°), the contact points on both planes consistently moved backward, resulting the position change of contact points (ΔD_{CP}) are -2.8 *mm* and -1.0 *mm* on the mid-medial plane and -0.8 *mm* and -2.2 *mm* on the mid-lateral plane. The total displacements of the right knee contact points of volunteer 3 on both planes are -4.04 *mm* on the mid-medial plane and -9.31 *mm* on the mid-lateral plane over a total flexion arc of 133.7° ($\Delta\theta_{V3}$).

In the case of volunteer 4, while θ changed from -3.0° to 142.5°, the contact point shifted

less on the mid-medial plane (ΔD_{CP_M}) than that on the mid-lateral plane (ΔD_{CP_L}) at each flexing step. Especially when the knee changed from bending at θ = 81.9° to the full-bending state, the contact point shifted forward by 4.14 *mm* on the mid-lateral plane, compared to only 0.5 *mm* on the mid-medial plane. The overall displacements on both planes are -5.3 *mm* for the mid-medial plane and -13.8 *mm* over a total flexion arc of 145.5° ($\Delta\theta_{V4}$).

For volunteer 5, the right knee bended from θ = -2.2° to 140.7° ($\Delta\theta_{V5}$). The maximum displacement on the mid-medial plane occurred from θ = 99.1° to 140.7° but just around the size of one pixel. In general, the contact point did not move much in this plane. The motion of contact point was more obvious on the mid-lateral plane. The total displacement of contact points on this plane is -8.5 *mm*, compared to the total displacement of -2.6 *mm* on the mid-medial plane. However, from θ = 62.5° to 99.1° the contact point almost did not move (ΔD_{CP_L} = 0.0 *mm*) with also a small backward shift (ΔD_{CP_M} = -0.9 *mm*). This "static" state on both planes was also observed in volunteer 6.

For volunteer 6, the overall flexion arc investigated is 162.0° ($\Delta\theta_{V6}$). From θ = -10.2° to 54.7°, the contact point moved more on the mid-medial plane than on the mid-lateral plane. Surprisingly, the contact point on the mid-medial plane moved forward and even much beyond the starting position (from D_{CP_M}(-10.2°) = 24.4 *mm* to D_{CP_M}(12.2°) = 28.0 *mm*) while on the other side of the knee joint, the contact point were close to be "static" ((from D_{CP_L} (-10.2°) = 19.9 *mm* to D_{CP_L}(12.2°) = 19.8 *mm*)). An external rotation seemed to take place but with the rotation centre on the lateral part of the knee joint.

The 2D contact point positions of all volunteers are plotted against their bending angles and shown in Figure 20. Each individual's investigated flexion arc and total contact point displacements on both planes are summarised in Table 6. Among the 6 volunteers, the right knee joints of the volunteer 3, 4 and 5 show a similar pattern at the overall contact point displacements: the mid-medial plane contact point shifted around 2-3 times less than that in the mid-lateral plane. The right knee joint of volunteer 2 also shows a relatively bigger total displacement on the mid-medial plane (-11.0 *mm*) and on the mid-lateral plane (-15.6 *mm*) than those of volunteers 3-5, but the difference between the two total displacements is

not as big as the other 3 volunteers. However, volunteer 6 has the same total contact point displacement on both planes.

Table 6: The overall contact point displacements over the investigated flexion arc of all volunteers

		V1	V2	V3	V4	V5	V6
Flexion arc ($\Delta\theta$)		57.9°	160.7°	133.7°	145.6°	140.7°	162.0°
Total contact point displacement $\sum_{k=1..N-1} \Delta D_{CP}^{k}$	Mid-medial plane (mm)	-1.5	-11.0	-4.0	-5.3	-2.6	-13.0
	Mid-lateral plane (mm)	-0.8	-15.6	-9.3	-13.8	-8.5	-13.0

In Figure 21, the tibia (in yellow) of each volunteer is presented in the axial view. The contact points are located on both tibia plateaux in the 3D space and delineated with different colours, with respect to the corresponding f-angles. The contact points are connected to illustrate its moving pathway (the dark blue curves in the figure). The anatomical coordinate used is as shown in Figure 21(g): from right to left, it corresponds to the lateral plane to the medial plane of the right knee joint; and from inwards to outwards of the figure, it corresponds to the direction from foot to head.

In 3D, the knee joint bending at various angles is illustrated from a sagittal view in Figure 22 (volunteer 5). The motion of the whole knee joint is clearly visualised. While bending from β = 30° to 90°, the knee joint was moving interiorly with the tibiofemoral articulation surface almost stayed on the same level. The shift of the whole knee joint from extension position to bending at various angles might be caused by the volunteer moving the foot position to fit the FoV of the scanner better. At the fully bending position however, a lift of the articulation surface could be easily spotted. According to the interview after the scan with the volunteer, he had to raise his ankle to be able to bend his knee joint completely. This is readily recognized in his reconstructed knee function model (at all measured flexion angles) as shown in Figure 22. The mean Euclidean distance between the contact points extracted from the simulated segmentation and actual segmentation is 1.5 *mm*, with a standard deviation of 1.1 *mm*.

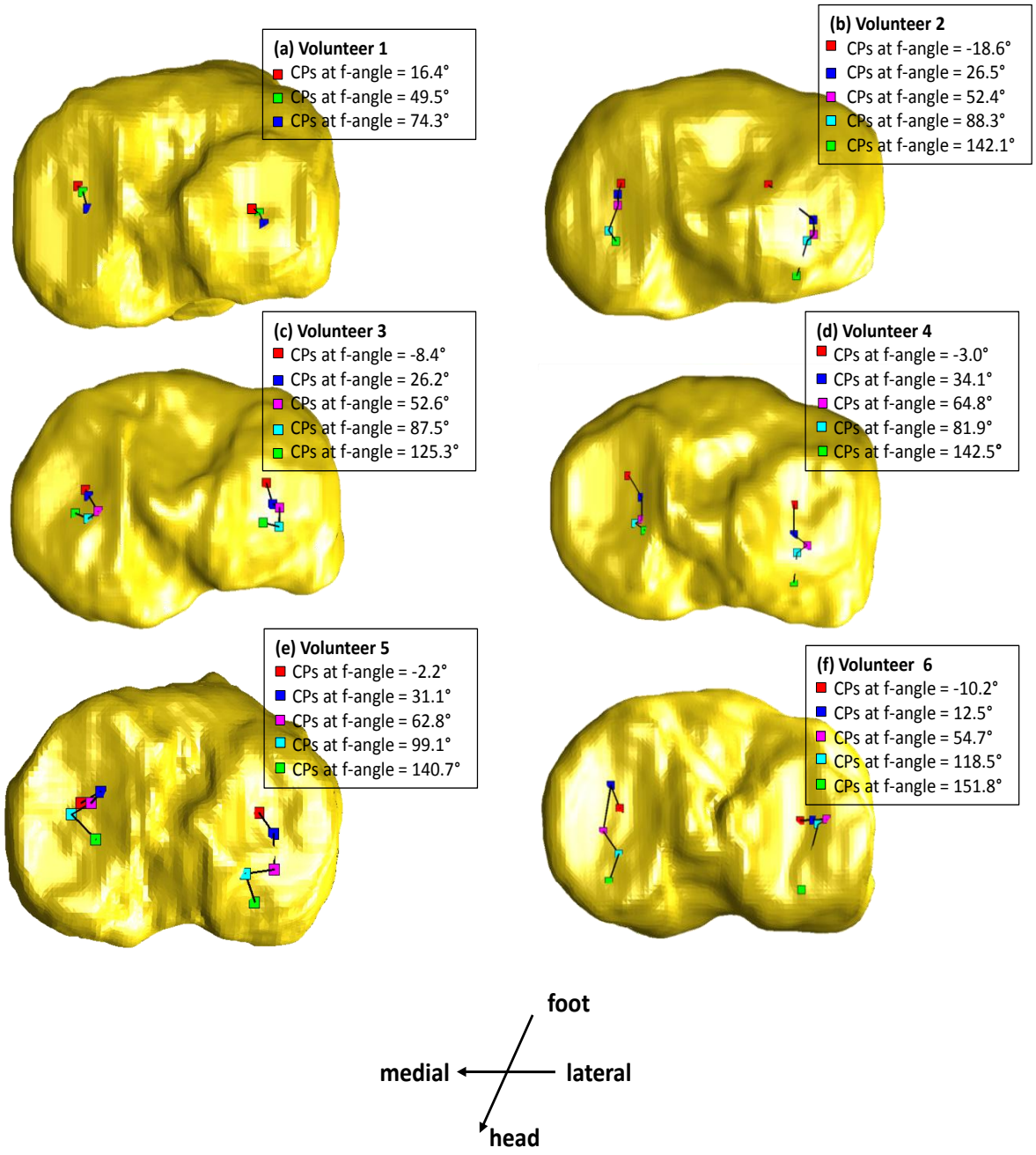

Figure 21 Contact point movement trajectory of every subject (a-f) (against the corresponding f-angles) plotted on the surface of each subject's tibia cartilage (in red). The squared nodes are the identified contact points at the measured bending angles in 3D. (g) the body coordinates

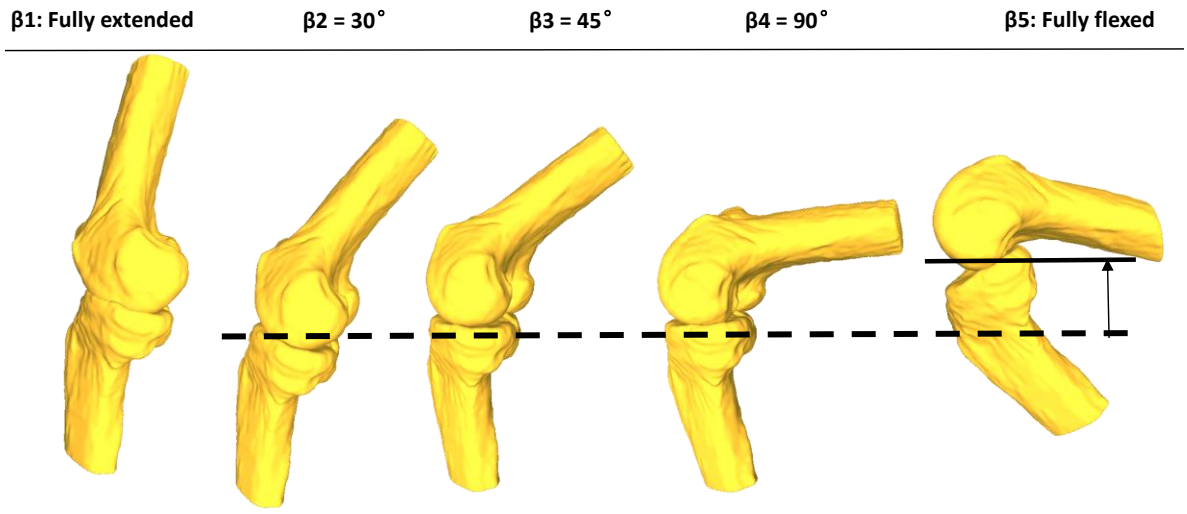

Figure 22. 3D visualisation of the right knee (meshed models) of volunteer 5 bending at each β angles (with corresponding Q-angle values in Table 4). The dashed line indicates the approximate femoral-tibial interface level while volunteer 5 flexed his knee from β_2 to β_4 as compared to that (indicated by the solid line) at angle β_5 by about 2.9 *cm*.

5.4 Discussion

This study aimed to investigate the function of individual's knee joint *in-vivo* under natural physiological condition (body-weight bearing). The knee joint kinematics of 6 volunteers was assessed by quantifying the contact mechanism of the tibiofemoral articulation under body-weight bearing status based on information acquired from MR images. The contact points were tracked on the MR slices and on the 3D registered functional models. The overall flexion arc and overall displacements were quantified. The results were plotted, and were visualized in 3D on how the volunteers' knee joint flexed while they were squatting. An overall dominant posterior motion of contact points was observed in both 2D and 3D on both tibia plateau of all the 6 volunteers, however the magnitude of such displacements varies from volunteer to volunteer and on either tibia plateau of each subjects.

Among all the volunteers, in 2D, volunteers 3-5 showed a similar contact pattern while squatting: less contact point displacement on the medial tibial plateau than the lateral plateau, indicating during the whole flexing process, the medial part of the knee joint played the role as external rotation axis. Volunteer 6 showed a completely different pattern

with more contact point displacement on the medial part of the knee joint than that on the lateral part while he flexed his knee joint from -10.2° to 118.5°. It implies that he was using the lateral part of his right knee as the rotation axis. This difference might come from the later identified shrunk muscle bundles in his right thigh by a radiologist while acquiring the high resolution anatomical image of his right knee. It was considered that these degenerated muscle bundles might have caused the change of his kinematics habit. The complication caused by the degenerated muscle is out of the scope of this study, but the subject reported no pain or any uncomfortable feeling in his everyday life in the past ten years as well as any knee joint abnormality prior to this study. The above findings were further confirmed by the 3D plot shown in Figure 21(c-e). In the medial tibial plateau the contact points were clustered, while in the lateral tibial plateau, they were more spread and approximately followed a simple "curve" (no intersection of itself). In 2D, volunteer 2's contact pattern appeared to be similar to those of volunteers 3-5, but with less displacement on the mid-medial plane than on the mid-lateral plane (5 *mm* more on the mid-lateral plane). This deviation in this volunteer's contact pattern from those of volunteers 3-5 was later enhanced by the 3D plot in Figure 21(b), which clearly illustrates that on the medial tibial plateau, the contact points were more spread and also followed a simple "curve". More surprisingly, the contact point motion on her lateral plateau was within a relatively smaller range, showing a clustering trend especially at the end of the flexion arc. Although the observation of volunteer 2 shows a deviation from volunteers 3-5, the cause of this abnormality was not clear for several reasons: the volunteer is an Asian female who falls into a different race, as well as a different gender group; it was difficult to follow the volunteer's medical history; a more throughout investigation on the muscular-skeletal system of the whole lower limb might be necessary in order to identify whether such deviation is from a physiological abnormality or just a variation of kinematic habit.

The contact point location error is estimated by introducing a segmentation of error of 1mm. This leads to around 20% error, considering that the maximum cartilage thickness in the tibiofemoral articulation is four or five voxels in the lowest resolution of the acquired data (i.e. the motion data). The calculated averaged distance difference of contact point position is (1.5±1.1) *mm* (i.e. within two voxel size), which is acceptable. The determination of the

flexion angles involves the annotation of two anatomical landmarks. This may also lead to observer variation. However, such variation is on the order of several millimetres. The calculation of the flexion angle is based on the femoral and tibial axes. The axes are estimated from line segments derived from the data volume and are on the order of 10 centimetres. Thus the resulting angular difference caused by the landmark annotation variation is not significant.

The registration results were assessed by Jaccard index (Dice score) and were shown to be good (Table 5). Since the 1.5 T anatomical scan was performed using a dedicated knee coil, the FoV coverage was smaller than that of the 0.5 T open access MRI. As a result the masks used for registration only show a partial view of the femur and tibia structures and therefore cannot overlap perfectly after registration (Jaccard index < 1). Other sources of imperfect overlapping include the difference in slice thickness and resolution between the anatomical and motion datasets. The overall knee joint flexion was well described by the 3D visualization, which vividly draws how each volunteers adapted their knee joint level in order to shorten the lower limb to finish a physiological task, e.g. squatting. Sometimes, the volunteers might have to raise their ankle joint position in order to finish the movement leading to a lift of their knee joint level, depending on the flexibility of their lower limbs (Figure 22). At several angles, positive contact point displacements (anterior motion) or quasi-static contact point motion have been identified. Such phenomenon indicates that the knee joint does not simply "roll-back" and agreed with the discussion in the literature [63].

Although extensive studies have been performed on quantifying the contact in order to have more information on the knee joint kinematics, quantitative comparisons with results of other studies would be problematic for the following major reasons. One is due to the various motion recording methods (e.g. *in-vivo* or on cadaver, weight-bearing or non-weight-bearing, MR or other imaging modalities). The second reason is from the differences in methods used to measure the contact points (i.e. the choice of reference system, 2D-slice based or 3D volumetric model based). Li and his group investigated the knee joint contact mechanism comprehensively with body-weight bearing [73, 137]. However their motion recording system is the bi-orthogonal fluoroscopic system and the volunteers were asked to lunge inside the FoV of the system. The resolution of the acquired

motion data is 0.4×0.4×0.4 mm^3, but the 3D volume is mapped with only two orthogonal X-ray images. Wreteberger et al. [71] measured contact movements of 16 volunteers on a supine position. They determined the contact area using four coordinates (the most anterior, posterior, medial and lateral points) located by a radiologist with a controlled intra-observer reproducibility corresponding to the longest contact lines identified on the MR slices (frontal and sagittal view). The centroid of this region was considered to be the contact point with corrections regarding the curved nature of the cartilage surface. Although great efforts were put into using geometric equations to quantify the contact points in this study, the determination of the contact area itself was actually in an empirical manner.

In this study, we modelled the contact point position as a function of the knee flexion angle (f-angle θ), and projected the knee joint motion onto the tibia articulation cartilage surface. When the pattern of knee joint motion changes (e.g. altered external rotation axis), this trajectory might also change. Thus it might be a potential cursor of knee joint abnormalities. Although volunteer 6 with abnormalities in his thigh muscles showed interesting opposite contact displacement pattern from the most of other volunteers, it is still too early to conclude that the location change of contact point could be used clinically. Before any actual clinical applications, large group studies with a dense sampling of points over the knee flexion arc are definitely needed to establish a model of contact point motion trajectory with normal volunteers. The contact analysis of knee joint also plays a potentially important role due to its importance of studying the cartilage stress, which is a plausible cause of increased bone stress. The elevated cartilage stress is also believed to play a role in the long term cartilage degeneration.

It is also important to mention that this study investigated the knee joint function under body-weight-bearing conditions, which is the main source of the everyday forces applied onto the knee joint. Therefore, the contact point location and knee flexion direction measured in this way may potentially be used to determine the everyday force magnitude, its distribution and even its distribution onto the underneath bone structure. According the bone remodelling principle as indicated by Wolff's law [9], the trabecular bone orientation aligns with the applied everyday forces, which is an essential factor of effecting bone mechanical competence. Thus, the proposed imaging strategy and the analysing procedure

also provide a methodology for quantifying the force input of bone remodelling along the time axis. Moreover, such experimental setup allows the investigated kinematics in the current study to be closer to the natural physiological manner than most of the knee joint kinematics investigation using MR, which acquired the knee motion data using a loading machine with the subjects lying in the supine position [157, 158]. The advantage of such experimental settings is that the forces applied to the knee joint are relatively easy to be controlled and to be measured, thus enabling cartilage stress quantification following the contact analysis. However, since the force is not applied in a natural physiologic manner and the subjects are often strapped with the loading machine, the induced muscle activity is therefore different from its everyday activity and the measured surface kinematics may not reveal the subject's moving habit [155].

Apart from muscles which might affect the knee joint kinematics behaviour, other tissues such as ligaments and tendons, as well as meniscus also affect the knee joint function. The future work is also to investigate the knee joint function regarding these soft tissues. To visualize these structures, a high resolution acquisition with higher SNR is needed as these tissues are very small and have relatively fast T_2 properties (Table 2). A pilot study has been performed in order to visualize anterior and posterior cruciform ligaments (ACL and PCL), fibular collateral (lateral collateral or long external lateral) ligament and medial collateral ligament (Figure 23).

5.5 Summary

A Subject-specific study of the right knee joint of 6 volunteers has been performed. In particular, the tibiofemoral articulation kinematics was investigated under the weight-bearing condition. Rich information has been acquired through the previously proposed combined MR imaging methods and the 2D and 3D contact analysis. The contact analysis zooms the observation of the human lower limb kinematics from the whole leg into the articulation cartilage surface. Motions, such as gliding and external rotations which are difficult to recognize using skin markers with video-cameras, are expressed at a relative finer resolution.

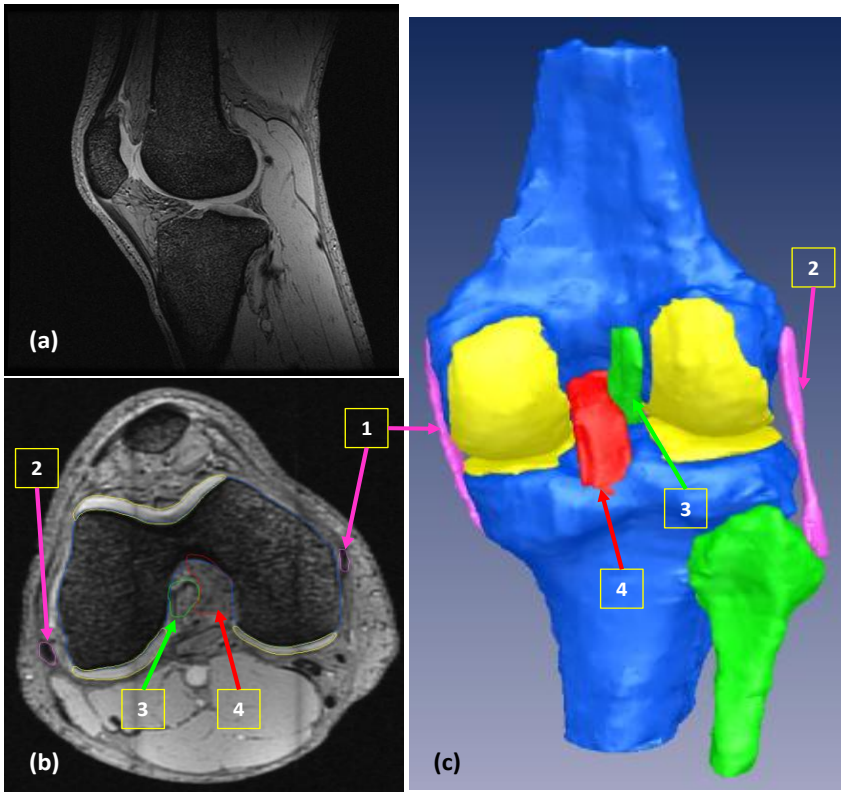

Figure 23. High resolution acquisition of right knee joint (volunteer 4) using 3D MERGE (multi-echo recombined gradient each) sequence on a GE scanner (protocols see Appendix A.2). (a) one image slice of the 3D volume; (b) axial view of the data with 4 ligaments delineated: 1. Fibular collateral ligament, 2. Medial collateral ligament, 3. ACL, 4 PCL; (c). 3D visualization of the anatomical model.

One important potential use of contact analysis is to evaluate the stress on the cartilage. Apart from the chronic pain caused from the overloading on the cartilage, it might also be used to estimate the exact direction of the forces being applied to the bone tissues holding the cartilage. The force direction that bone endures every day is said to influence the remodelling of trabecular bone, thus its micro-structure. On the other side, the orientation of trabecular bone network is quite specific in order to react according to the forces it has to endure. In anatomical locations such as femur and tibia, the forces mostly come from the human weight and are along the direction of the long shaft of these long bones. Therefore, the microstructures of trabecular bone inside these organs presents dominate directions along the organs. Together with BMD, anisotropy is considered as a valuable parameter for

the predication of trabecular bone mechanic competence [60]. To extract it, it is necessary to go from the organ level to finer scales. In the following chapters, MR techniques which are specific to looking for reliable measurement of anisotropy information will be introduced.

Chapter 6. *In-vivo* Diffusion tensor imaging of trabecular bone: theory and feasibility

By measuring the intensity decrease due to particles' Brownian motion, diffusion-weighted imaging techniques probe the tissue structure at the cellular level. Though actively used in brain research, diffusion-based techniques have also been extended to the musculoskeletal system, e.g. [114, 119]. Motivated by its powerful ability of tracking the fibre bundles inside the white matter, we hope to investigate the possibility of applying the DTI protocol to the human trabecular bone on a clinical scanner *in-vivo*. It is hypothesized the principal directions of calculated diffusion tensors may correspond to the trabecular bone network orientation. In this chapter, we aim to find the appropriate imaging parameters (TE, gradient pulse duration δ, gradient separation time Δ), and establish a proper protocol of DTI of bone *in-vivo* on a clinical scanner. The last step is to extract the trabecular bone orientation with the information given by diffusion tensors. To compute the trabecular bone orientation, we would follow the principal direction of the diffusion tensors, analogous to fibre tracking algorithms to process brain DTI data. The advantage of this method is that it could provide more direct and local measurement of orientation by restricted diffusion of spins in each voxel compared to the techniques used in stereology and histomorphology (3D information is not well preserved due to the cutting) and post-processing algorithms used in high-resolution MRI (it is very difficult to get isotropic volume resolution from the scanner [95]).

In this chapter, we review and emphasize some theoretical aspects of obtaining and analysing the diffusion tensor (Section 6.1), which are also very important for the later chapters (Chapter 8 and 9) where the same formalism can be applied in the new context defined by mSPENT. The efforts of performing DTI *in-vivo* on human's lower limb with clinical settings are presented in Section 6.2. The behaviour of background noise is further assessed in Section 6.3. The derived quantitative information is shown in Section 6.4 to demonstrate the feasibility of *in-vivo* diffusion imaging of TB. Related work is discussed and summarized in the end (Section 6.5).

6.1 Introduction and background

Diffusion MRI can be considered as the combination of 'static' MR imaging with a contrast scheme which reveals the spectrum of local translational motion [110]. It measures water molecular displacements subject to diffusion within the sample material. In the presence of magnetic field gradients, these originally random motions impart a phase spread to the spin transverse magnetization. This reduction of signal intensity can be modelled and thus provide a unique probe of the underlying tissue structure at a very fine scale.

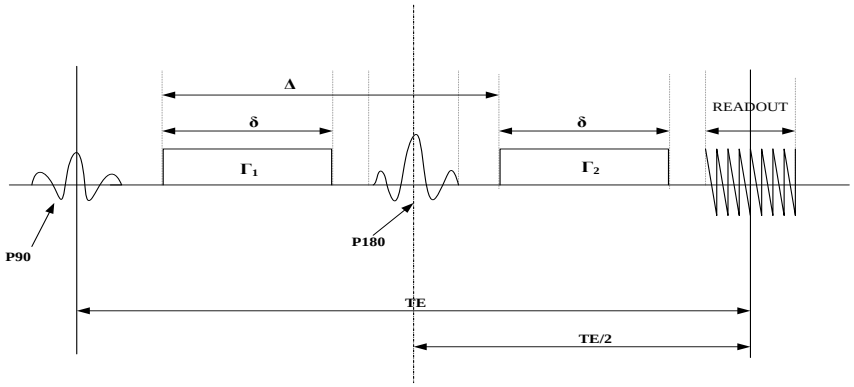

Figure 24. Block scheme for a pulsed-gradient spin echo (PGSE) sequence

6.1.1 Diffusion in MR and its measurement

A powerful tool of diffusion measurement is the spin echo (Figure 24). Hahn [159], Carr and Purcell [160] pointed out the sensitivity of the spin echo to both random and directional motion. Stejskal and Tanner [161] later designed a pulsed-gradient spin echo sequence (PGSE, Figure 24), which is one of the most commonly used in diffusion weighted imaging (DWI) nowadays. This sequence starts with a 90° r.f. pulse (centred at time *t=0*). A bipolar pulse positioned around a 180° r.f. pulse (centred at time $t = TE/2$) is sandwiched between the 90° r.f. pulse and read-out gradient. Right after the 90° r.f. pulse, the gradient pulse Γ offsets the phase of a spin at position r by $r \cdot q$, where $q = \gamma \int_0^\infty \Gamma(t)dt$. $\Gamma(t)$ is the component of the magnetic field gradient parallel to the main magnetic field B_0 at time t and γ is the gyromagnetic ratio of the spins. In practice, the two gradient pulses are approximately rectangular and thus $q = \gamma\delta G$, where G is the gradient strength. Since the

180° r.f. pulse reverts the phase, the second gradient lobe will cancel the phase offset created by the first one for a stationary spin, if a spin moves from position r_1 to r_2 between the pulses, it retains a residual phase offset of $q \cdot (r_2 - r_2) = q \cdot \Delta r$. The magnetic moment of the spin is thus $M \cdot exp(iq \cdot \Delta r)$ at the spin echo, where M is the magnitude of the magnetic moment. Therefore, the MRI signal $S^*(q)$ is the sum of all possible spin displacements, as in eq. 34 :

$$S^*(q) = S^*(0) \int p(\Delta r) exp(iq \cdot \Delta r) d\Delta r \, , q = \gamma \delta G \qquad \text{eq. 34,}$$

where $S^*(0)$ is the signal with no diffusion-weighting gradients and the integral is over all three dimensions (x, y, z) and $p(\Delta r)$ indicates the chance that a single spin moves from position $\boldsymbol{r_1}$ to $\boldsymbol{r_2}$ during the time δ when the gradient is applied. A simple model of $p(\Delta r)$ (the diffusion propagator) is based on Fick's law and random walk [110] as an isotropic zero-mean Gaussian function:

$$p(\Delta r, t) = \frac{1}{\sqrt{(4\pi t)^3 |D|}} exp\left[\frac{-\Delta r^T D^{-1} \Delta r}{4t}\right] \qquad \text{eq. 35,}$$

where D is the self-diffusion coefficient. The self-diffusion coefficient D gives a complete description of particle diffusion in homogeneous and isotropic media (e.g. in a porous media with uniformly distributed permeability and translation invariant in all directions, Figure 25(a)). However, biological tissues are heterogeneous which leads to restricted or hindered diffusion (Figure 25(b-d)). In this case, the measured D is not the absolute value and is termed the apparent diffusion coefficient (ADC). Le Bihan et al. [162] simplified Stejskal and Tanner's equation into eq. 36:

$$S(b) = S_0 e^{-bADC} \qquad \text{eq. 36.}$$

They defined a parameter b (b-value or b-factor) as a function of imaging parameters, i.e. the time for diffusion ($t_{diffusion} = \Delta - \delta/3$), the gradient strength (G) and the length of the gradient pulse (δ), $b = t_{diffusion} \ |q|^2 = \gamma^2 \delta^2 G^2 t_{diffusion}$.

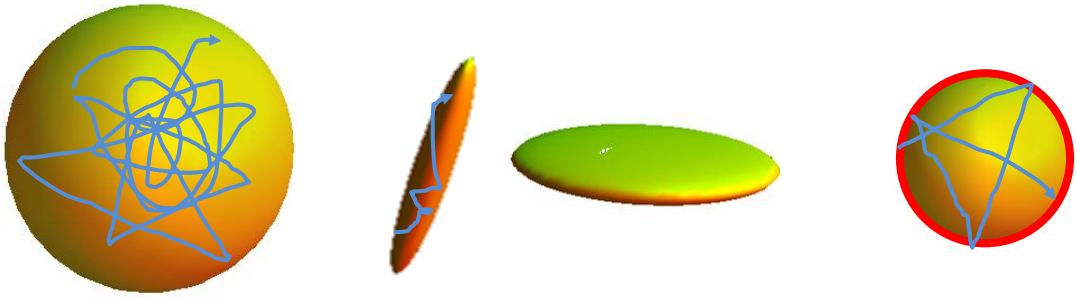

Isotropic diffusion (a) | Anisotropic diffusion (case 1 and 2) (b) (c) | Hindered diffusion (d)

Figure 25. Illustrations of 3D shapes of diffusion tensors in different types of diffusion: (a) an sphere in the case of isotropic diffusion; (b) and (c) are the diffusion tensor shape for cases of anisotropic diffusion, (b) is a linear case tensor and (c) is a planar case tensor [163] ; (d) corresponds to the case of hindered diffusion.

6.1.2 Diffusion Tensor: to describe diffusion as a function of direction

ADC measurement depends on both the diffusion time and the measured direction. In the case of anisotropy, a gradient direction invariant measurement would be preferable to be able to reveal the information about molecular mobility reflective of local microstructure and anatomy. To overcome the disadvantages in DWI, a diffusion tensor imaging (DTI) methodology was first proposed by Basser et al. [164] and has now become one of the standard protocols on clinical scanners. Instead of doing a single ADC measurement in one direction, they applied the same pulsed gradient in several directions (randomly uniform distribution on a unit sphere). The basic tensor model is given in eq. 37, where b is the b-value, $\vec{x}_i$ is the ith gradient direction for ADC measure, $\boldsymbol{D}$ is the diffusion tensor, S_0 is the b = 0 measurement. No advection is assumed in this tensor model therefore symmetry exists in the opposite direction of the applied gradients. Hence, a minimum of 6 gradient directions and one direction with b = 0 measurement are required to build a tensor.

$$S(\vec{x}_i) = S_0 e^{-b\vec{x}_i^T D \vec{x}_i}, \text{ therefore } ln\left(\frac{S(\vec{x}_i)}{S_0}\right) = -b\vec{x}_i^T D\vec{x}_i \qquad \text{eq. 37.}$$

Here, we name the term $S(\vec{x}_i)/S_0$ as the normalized diffusion signal. Each direction $\vec{x}_i$ (x_i, y_i, z_i) corresponds to a measurement of ADC. These ADCs are fitted into a tensor $\boldsymbol{D}$ (eq.

38).

$$\boldsymbol{D} = \begin{pmatrix} D_{xx} & D_{xy} & D_{xz} \\ D_{yx} & D_{yy} & D_{xz} \\ D_{zx} & D_{zy} & D_{zz} \end{pmatrix} \quad \text{eq. 38}$$

Therefore, if expressing

$\bar{x_i}^T \boldsymbol{D} \bar{x_i} = \left[x_i^2, y_i^2, z_i^2, 2x_i y_i, 2x_i z_i, 2y_i z\right] \cdot d$, with $d = \left[D_{xx},\ D_{yy},\ D_{zz}, D_{xy},\ D_{xz},\ D_{yz}\right]'$,

then the diffusion tensor model given by eq. 38 for all directions can be expressed as the form of the linear system:

$$\boldsymbol{A}d = S \quad \text{eq. 39,}$$

where $\boldsymbol{A}$ is the *encoding* matrix, indicating the directions of applied diffusion gradient.

$$\boldsymbol{A} \coloneqq \begin{bmatrix} x_1^2 & y_1^2 & z_1^2 & 2x_1y_1 & 2x_1z_1 & 2y_1z_1 \\ \vdots & \vdots & \vdots & \vdots & \vdots & \vdots \\ x_N^2 & y_N^2 & z_N^2 & 2x_Ny_N & 2x_Nz_N & 2y_Nz_N \end{bmatrix}$$

The right-hand side vector S has the component $-\ln(S(\vec{x}_i)/S_0)$, where S_0 is the non-diffusion-weighted measurement. Thus, the procedure for computing the diffusion tensor is the process of solving this linear system voxel-wise by using a proper fitting algorithm, such as least squares, weighted least squares or sophisticated fitting procedures such as robust estimation of tensor by outlier rejection (RESTORE) [165], which utilizes a reweighted least square regression method iteratively to identify the potential outliers and subsequently exclude them for the diffusion tensor estimation.

6.1.3 Requirements on diffusion gradient directions

Diffusion MRI generally has very low SNR, and also suffers from partial volume effects and artefacts. Studies to improve the information extracted from DTI are undergoing. One effort is for the preciseness of diffusion measurement in MRI. Jones et al. [166] extended previous work to optimize the diffusion measurement from isotropic systems to anisotropic systems. They analyzed the noise propagation related to the calculation of the tensor trace

and applied their optimized scan strategy to a water phantom and human brain. However, their scheme for the gradient orientations assumed the shape of the diffusion tensor was an ellipsoid, which lead to the not-so-generalized tetrahedral direction encoding matrix scheme. Hasen et al. [167] compared several gradient encoding schemes with numerical approaches and Monte Carlo simulation. They concluded that an icosahedra encoding was the optimal for the six encoding directions. Batchelor et al. [168] later theoretically proved the icosahedral directions were the recommended scheme for direction encoding in DTI in order to reduce the noise propagation.

Theoretically, only 6 directions are needed to reconstruct the diffusion tensor. However, due to the corruption of noise, it is necessary to acquire information from more directions in diffusion imaging in order to over-determine this linear system. In order to reduce the noise propagation level when computing the diffusion tensor, we should be careful when choosing the set of gradient directions. The condition number $\boldsymbol{\kappa}$ is proposed as a popular criterion for the choice of directions [166, 167, 168]. In the linear system of diffusion, the encoding matrix A is not a square matrix but with the size M × N (M ≥ N). Therefore, the normal form of the least-square solution of eq. 39, is $d = (A^T A)^{-1}(A^T \cdot s)$. According to Batchelor et al. [168], the inverted matrix $(A^T A)^{-1}$ plays a central part in solving the system. A mean normal matrix $B = A^T A/N$, which is the normal matrix $A^T A$ after being normalized by the number of diffusion directions, was also defined. Errors in s (the right-hand side of eq. 39) will induce errors in the solution. This error propagation is controlled by the condition number $\boldsymbol{\kappa}(A)$ as defined below:

$$\boldsymbol{\kappa}(A) = \|A\|\left\|A^{-\mathbf{1}}\right\| = \sigma_{max}(A)/\sigma_{min}(A) = \sqrt{\lambda_{max}(A^T A)/\lambda_{min}(A^T A)} = \sqrt{\lambda_{max}(B)/\lambda_{min}(B)} \qquad \text{eq. 40,}$$

the ratio of the maximal to the minimal nonzero singular values of A, or the ratio of the maximal to the minimal eigenvalues of the normal/ mean normal matrix. Hence, the condition number $\boldsymbol{\kappa(A)}$ controls the relative error of the solution of the linear system of diffusion as a function of the relative error in the log measurement of diffusion signal on the right-hand side of the system. That is to say:

$$\frac{\textit{relative error in reconstructed tensor } d}{\textit{relative error in } s} \leq \boldsymbol{\kappa}(A) \qquad \text{eq. 41.}$$

The theoretical minimum of the condition number is 1 and is impossible to achieve in experiments. However, by applying a proper gradient direction scheme, it is possible to control this error to a fixed level. It has been shown that $\kappa_\infty = \lim_{N\to\infty} \boldsymbol{\kappa}(A) = \sqrt{10}/2 \approx 1.5811$ being the lower bound. Interestingly, this condition number for the infinity of directions corresponds to the condition number associated with an icosahedron. This means that the gradient direction scheme uniformly distributed on an icosahedron should be chosen.

6.1.4 Quantitative indications of diffusion tensors: parametric maps and fibre tracking

Many metrics have been proposed to quantify the structural and physiological features indicated by diffusion MR and correlated with clinical pathologies. Analogous to the stress tensor in mechanics, Basser and Pierpaoli [169] derived a set of quantitative measurements from the diffusion tensor: mean diffusivity (MD, eq. 42) and fractional anisotropy (FA, eq. 43).

$$MD = \frac{D_{xx} + D_{yy} + D_{zz}}{3} \qquad \text{eq. 42}$$

$$FA = \frac{\sqrt{3\left[(D_{\mathrm{xx}} - MD)^2 + \left(D_{\mathrm{yy}} - MD\right)^2 + (D_{\mathrm{zz}} - MD)^2\right]}}{\sqrt{2\left(D_{\mathrm{xx}}^2 + D_{\mathrm{yy}}^2 + D_{\mathrm{zz}}^2\right)}} \qquad \text{eq. 43}$$

Trace and apparent diffusion coefficient (ADC) are the other two commonly used parametric maps. The definition of trace is the sum of the diagonal elements of the diffusion matrix, thus it is related to the mean diffusivity [169]. Diffusion coefficient is the parameter to describe the relative amount of diffusion and is directional variant. With the conventional diffusion weighted imaging, since it is only defined for one direction and with two *b-value*s, the calculated diffusion coefficient is also named ADC. Clinical studies

sometimes used ADC values calculated from the average of three diffusion measurements taken along the imaging axes (*x, y, z*) [170]. In this work, the latter definition of ADC is used (i.e. MD).

6.1.5 Issues regarding *in-vivo* DTI in bone

The basic material model that we study here is bone, which can be considered as a porous media system (e.g. wood and soil) where diffusion NMR has been widely used to characterize its micro-architecture. Two structural parameters are of primary interest in this research: porosity (first order) and anisotropy (second order). We consider trabecular bone as a porous system [114], but with a more complex fluid filling inside the pores. Similar to T_2-weighted MRI, in DTI, it is still the bone marrow that contributes most of the signal. Two types of bone marrow can be found in the human body: red marrow (consisting mainly of myeloid tissue) and yellow marrow (consisting mainly of fat cells). Red marrow is found in the flat bones, such as the hip bones, breast bones, skull, ribs, vertebrae, shoulder blades and in trabecular bone material at the epiphyseal ends of the long bone. Yellow marrow is found in the hollow interior of the middle portion of the long bone. At birth, all bone marrow is red. With age, more and more of it is converted to the yellow type. Such conversion stops at a steady state of a composition of 50% for either type. DTI tracks the translational displacement of the spins inside the tissue. It is the red marrow residing in the trabecular bone region which contains mainly water component that will give detectable diffusion signals during the pulsed gradients under mostly-used clinical settings. In case the yellow marrow becomes the main components, more powerful diffusion gradients are necessary for the ADC of yellow marrow is found to be three orders of magnitude slower than that of water [118]. Therefore we focus our DTI experiments at places with red marrows, for example, the epiphyseal ends of the tibia.

It is quite difficult to apply DTI inside trabecular bone in general. One reason is the complicated structure of trabecular bone itself. As reported, the thickness of trabeculae is between 80 and 150 μm while the pore size varies between 50 μm and 200 μm [7]. This complexity causes many unwanted signals to interfere with those purely from diffusion. One source of such undesired signals is susceptibility effects due to local change in

magnetic susceptibility. These susceptibility effects cause strong inhomogeneities in the static field which thus generate a background gradient (g_0) and enhance the dephasing of the transverse magnetization, leading to the increasing of relaxation rate. This would seriously affect the PGSE diffusion measurement. This internal gradient (g_0) cannot be corrected as they vary throughout the trabecular bone structure [116]. Chemical shift is another disturbing factor in this case. Protocols have to be carefully tuned to separate the fat and water. Apart from the above effects specific to the trabecular bone, the common MR artefacts, such as geometric distortions, motion artefacts etc, may be enhanced during the *in-vivo* acquisition procedure which is mostly implemented using EPI on clinically available scanners as the signal read-out method. Summing up all of the above, DTI of bone *in-vivo* is a very challenging task.

6.2 Feasibility study

Using anisotropic diffusion within red marrow residing in the pores of trabecular bone, diffusion tensor imaging (DTI) can be potentially exploited as a probe of trabecular bone orientation *in-vivo*. Here, the current results of feasibility study of *in-vivo* DTI on human tibia are presented with experiments on three volunteers. The technique's ability to reveal trabecular network orientation at the micro-scale is also shown by reconstructing diffusion tensors and tracking the dominant diffusion directions.

6.2.1 Subjects and Imaging protocols

Three healthy volunteers (two males and one female, average age 26.5, Table 7), with no recorded lower limb injury, have been scanned in the past two years. Several settings for a proper DTI protocol were proposed and tested on a 3T GE Signa HDx machine. An eight-channel knee coil was placed over part of the knee joint and upper part of tibia. The pulse sequence was chosen to be a dual-echo PGSE preparation with EPI read-out to reduce the eddy currents [171] and the internal gradient effects caused by the big susceptibility difference on the interface between bone and bone marrow [114] (sequence graph see Appendix A.3). In each diffusion tensor imaging experiment, four non-diffusion weighted (b_0) measurements were acquired before the diffusion gradients were applied. In total, 20

diffusion directions (uniformly distributed on a sphere, proposed by the manufacturer) were applied. The data was acquired in the axial plane, with the acquisition matrix 128×128, interpolated to 256×256, in-plane resolution 1.4×1.4 mm^2, and slice thickness 3.2 *mm*. Parallel imaging mode was exploited with an acceleration factor of 2. NEX was set to be 4 in order to achieve an acceptable SNR level. Scan time was about 9 minutes for each DTI acquisition (at *b-value* = 400 $s \cdot mm^{-2}$). The protocol was tuned to set the diffusion time long enough for water molecules to diffuse and short enough to achieve as high SNR level as possible. Consequently, the TE settings vary from each volunteer. High resolution T_2 weighted datasets (using Fast Spin Echo) in the axial plane were acquired before the DTI experiment to give anatomical correspondence. The detailed experiment settings are illustrated in Appendix A.2. The choice of *b-values* was based on the trade-off between the acquisition time and SNR. Imaging experiments with five different *b-value*s (200, 400, 600, 800 and 1000 $s \cdot mm^{-2}$) were first performed on volunteer 1. A *b-value* of 400 $s \cdot mm^{-2}$ was chosen, considering the trade-off between the achievable SNR level and the acquisition time. This multiple *b-value*s acquisition was also for a further observation on the normalized diffusion signal (diffusion weighted signal intensity divided by non-diffusion weighted T_2 measurement) as a function of *b-value*.

Table 7: Volunteer details of the feasibility study

	Age	**Sex**	**Scanned knee (right/ left)**	**Experiments performed in the feasibility study**
Volunteer 1	46	male	left	DTI with multiple b-value acquisitions (b =200, 400, 600, 800 and 1000 $s \cdot mm^{-2}$)
Volunteer 2	20	female	left	DTI with b = 400 $s \cdot mm^{-2}$
Volunteer 3	40	female	right	(1) DTI with b = 400 $s \cdot mm^{-2}$ (2) noise DTI acquisition without r.f. excitation with b = 400 $s \cdot mm^{-2}$

Finally, a "noise-only" acquisition was obtained on volunteer 3 by switching off the r.f. pulses, using the same imaging parameters in order to assess how the background noise behaves in the diffusion tensor under the option of parallel imaging more accurately.

6.2.2 Data processing and analysis

Prior to the diffusion tensor analysis, the DTI datasets were aligned using a home-made software (MATLAB, R2008a) doing a correlation registration to resolve the translational motion caused by the strong diffusion gradients vibrating the patient bed. In the current setting, the knee coil was used and the knee joint was fixed tightly enough, so that the rotational motion in this case was much less serious and thus ignored in this study. The diffusion tensor in each voxel was reconstructed by fitting the log-measurement to the Gaussian displacement model (eq. 37.) by the standard linear regression. A threshold was chosen from the *b-value* = 0 measurement in order to mask out noise before applying the fitting procedure. MD (eq. 42), FA (eq. 43), trace and the principal diffusion directions were calculated voxel-wise from the reconstructed tensors ([169], Chapter 7 in [172]). The diffusion tensors are further plotted in 3D to illustrate the spatial coherence.

In order to illustrate the coherence of the diffusion tensor orientations, we propose to use a ROI-based fibre tracking algorithm such as those methods developed for brain diffusion imaging. The tracking criteria are FA value and curvature threshold (the angle between the principal tensor direction of the current voxel and that of the neighbouring voxels). Linear interpolation was also applied when generating the tracks. In a porous media system as trabecular bone, two phases exist: pore and trabecular bone. These pores are well connected and filled with bone marrows. In this case, it is the trabecular bone that restricts the particle diffusion in certain directions. Consequently, the anisotropic diffusion is thought to happen at the interface between trabeculae and bone marrow. Therefore the principal directions of the diffusion tensors may not only show the dominant particle translational displacements, but may also be related to the orientation of the trabecular bone locally. All the analyses were performed with CAMINO [173] and MATLAB (R2008a, The Mathworks, Natick, MA).The 3D tensor plot is created by fanDTasia library (an open source MATLAB program)[9]. The fibre tracks were rendered with Geomview (University of Minnesota, open source software).

---

9 fanDTasia ToolBox, written by Angelos Barmpoutis, MATLAB central, http://www.mathworks.com/matlabcentral/fileexchange/26997-fandtasia-toolbox

6.3 Noise assessment

The size of trabeculae, the inhomogeneous geometrical arrangement and the complicated composition of bone marrow make the MR imaging of bone not an easy task. For *in-vivo* DT imaging of bone, several questions have to be answered first before applying DTI to derive some quantitative micro-structure information from the data. In this section, background noise of *in-vivo* DTI of human's lower limb is assessed quantitatively. The hypothesis is that image intensities in the regions dominated by noise behave differently from those in the regions with real diffusion signals. To test this, several approaches have been performed. The objective is to assess the origin of the signals detected from the TB region and to compare them with the noise signals.

6.3.1 Plot of the normalized intensity change against increase of b-value

If the intensity change in bone region observed in our experiments was due to the diffusion driven by the diffusion gradients, the signal intensity would decrease as the *b-value* increases according to eq. 37. This has been tested on the data acquired from volunteer 1. The observed *b-vales* are 0, 200, 400, 600, 800, 1000 $s \cdot mm^{-2}$. When the *b-value* setting is changed, the scanner will automatically reset the TE and TR in order to optimize the imaging protocols. Consequently, to observe the intensity change, diffusion signal needs to be normalized with the non-diffusion weighted acquisition of each DTI acquisition to compensate for the possible intensity change caused by different TEs and TRs. Therefore, we observed the relationship between the normalized signal intensity term in eq. 37 and the 5 non-zero *b-value*s.

In detail, the normalized average voxel intensity at each diffusion gradient direction is computed as $\overline{I_{norm}}_{ROI}(x_i) = \bar{I}_{ROI}(x_i)/\overline{I_0}_{ROI}(x_i)$. $\bar{I}_{ROI}$ is the averaged diffusion weighted intensity of voxels inside the ROI at the diffusion gradient x_i. $\overline{I_0}_{ROI}(x_i)$ corresponds to the mean non-diffusion weighted intensity value, which is calculated as the average intensity value of all the four b_0 measurements. Small ROIs (5×5) are arbitrarily chosen in three regions in the same slice, corresponding to muscles, trabecular bone and background noise

respectively. The normalized average intensity ($\overline{I_{norm}}(x_i)$) of each region at each diffusion gradient direction (x_i) is plotted against *b-value*s separately. The overall trend of the intensity change is observed by plotting the mean values in each ROI. The standard deviation (SD) of the normalized intensities $\{\overline{I_{norm}}_{ROI}(x_i), i = 1 \cdots N\}$ is calculated, as in eq. 44. The muscle voxels are used as benchmarks as it has been shown in other studies that diffusion signal was detected under the PGSE DTI protocol (e.g. Lansdown et al. [174]).

6.3.2 Evaluation based standard deviation of ROIs

Another method is to compare the standard deviation (SD) of voxel intensity (eq. 44, where I_i is intensity value of each voxel and $\bar{I}$ is the mean intensity). Three types of ROIs are chosen in noise, muscle and trabecular bone regions respectively in the original diffusion weighted images at each direction of several slices covering the tibia epiphysis part (the ROIs of each tissue type were randomly selected in the regarded anatomical region). The mean intensity values of these ROIs are also computed. In this approach, the intensity differences between bone marrow and trabecular bone are of less concern. However, it should be noted that the ROIs drawn in trabecular bone inevitably contain both marrow and bone, therefore the SD of signal coming from marrow is actually higher than the values given in $SD_{bone}(ROI)$. $SD_{muscle}(ROI)$ is the reference value. $SD_{bone}(ROI)$ and $SD_{noise}(ROI)$are computed to compare with the reference. The comparison is performed on the data from all the three volunteers.

$$SD = \left(\frac{1}{n-1}\sum_{i=1}^{n}(I_i - \bar{I})^2\right)^{\frac{1}{2}} \qquad \text{eq. 44}$$

6.3.3 Evaluation based on the fitted diffusion tensors

Noise appears random in the images while true signal shows coherence with the underlying structures. A vector summation mask is applied (eq. 45) to the principal directions of tensors in the neighbourhood with various size on all the three volunteers' data in order to enhance coherent patterns. In eq. 45, λ_1 is the principal eigenvalue and $\vec{e}_1$ is the principal eigenvector, j refers to any pixel inside the masked neighbourhood). Several sizes (the

tested mask sizes are 3, 5, 7, 9, 11 and 13) of masks have therefore been applied in order to determine the optimal mask size in terms of revealing the structural coherence.

$S_{mask} = \left\| \sum_{j=1\ldots N} \lambda_1^j \vec{e}_1^{\,(j)} \right\|$, N is the number of pixels inside the mask eq. 45

The other interesting values to observe are the negative eigenvalues. It has been addressed in several papers (Jones et al. in [166], Batchelor et al. [168] and Jones and Basser [175]) that in DTI, due to noise, some tensors can have negative eigenvalues. These negative eigenvalues for diffusion tensors in biological tissues are excluded by thermodynamic arguments and are neither mathematically nor physically correct. The diffusion tensors should be positive definite and symmetric. Therefore, it is sensible to investigate the percentage of negative eigenvalues after reconstructing diffusion tensors. On one hand it would give an idea of how much noise has corrupted the foreground region; on the other hand, it would also suggest that if the amount of negative eigenvalues is well below what could be found in the background, some structures must be revealed in the foreground region. It has to be pointed out that the diffusion tensor was reconstructed without the background threshold in order to allow the preservation of voxels with only noise for this type of assessment.

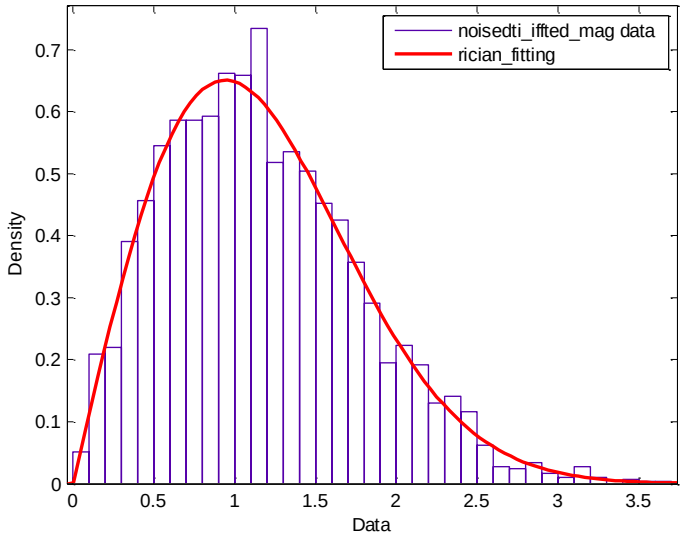

Figure 26. Simulated noise with Rician distribution

The percentage of negative principal eigenvalues (hereafter, the term negative eigenvalue is

used for the negative principal eigenvalue) is compared among 4 types of regions: simulated "noise-only diffusion", background noise region, trabecular bone region and muscle region on all three volunteers. The “noise-only diffusion” experiments were used to provide a series of ‘pure noise diffusion tensors’ in the fashion of Monte-Carlo methods. The noise "diffusion tensor" region was set to be a 4D matrix of size 10×10×*slicenum*×24, in which each “imaging” plane contains 10×10 voxels. The image plane matrix size was chosen to be 10×10 in order to fit the ROI into the other three types of tissue region. The number of “imaging planes” is represented by the parameter *slicenum,* varying from volunteer to volunteer, but is equal to the number of the slices used later while calculating the percentage of negative eigenvalues in other type of tissue ROIs. The whole "acquisition" followed the DTI "protocol": using 4 "non-diffusion-weighted" acquisitions and "diffusion-weighted" acquisition at 20 gradient directions the same as used by the GE scanner. The simulated "noise" k-space was generated by adding independent Gaussian noise on real and imaginary parts. It was then inverse Fourier transformed back to the image space. Only the modulus of the complex number was kept in order to make the noise intensity distribution fit a Rician model [176] (Figure 26). A Monte-Carlo simulation was performed to investigate negative eigenvalues by repeating the experiments 1000 times. The other three types of regions were cropped directly in the actual DTI data. The amount of negative eigenvalues at these regions is calculated as the ratio between the number of negative eigenvalues and the total number of pixels at ROIs chosen arbitrarily in the specific region (i.e. bone, muscle or noise) on several slices which covered as much tibia epiphysis region as possible.

6.3.4 "Noise-only DTI" dataset

A set of "noise-only DTI" data was further acquired with exactly the same DTI after switching off the r.f. transmission channel (this noise-only data acquisition method followed the manufacturer’s instructions [139]) on volunteer 3 to further assess the noise. It needs to be pointed out that this acquisition was performed one month later after the normal DTI acquisition. Therefore, the slice locations were not exactly the same although the radiographer tried to place the coil and FoV as close as possible during the acquisition. It is

fair to assume that the muscle and bone tissues do not change much for this healthy volunteer, and the noise that was concerned in this study was mainly from the human body, therefore it can be considered the measured “noise-only DTI” dataset is able to reflect the noise level in the previous acquisition by applying exactly the same protocol. The goal is to include possible effects that are present in actual experimental data to compliment the insufficiency of the above simulation based study (i.e. “the noise-only diffusion” observation). Such effects include the field inhomogeneity, the coil sensitivity at different locations and the reconstruction method used in images acquired with parallel imaging. Especially, in parallel imaging, the noise varies with the spatial locations, depending on the coil geometry and acceleration factor [177, 178]. Therefore, it is fairer to show the difference between the real signal and the pure noise in the same location. The comparison of the two datasets on volunteer 3 is performed on the reconstructed diffusion tensors in order to illustrate the different behaviours. The noise ROI-based negative eigenvalue ratios were calculated and compared with the bone and muscle ROIs with the "normal" acquisition performed before the r.f. transmission channel was switched off. ROIs of bone, muscle and background (i.e. noise) are chosen arbitrarily in this “noise-only DTI” dataset for the calculation of the negative eigenvalue ratio. The locations of these ROIs were found using the normal DTI scan performed before the r.f. excitation was switched off. The “noise diffusion” parametric maps were also generated for the comparison on the TB region of the epiphysis of the tibia.

6.4 Results

6.4.1 Imaging results

Sampled imaging results of the acquired diffusion weighted images of all the three volunteers’ right tibia are presented in Figure 27(c, f, i). The b_0 data (Figure 27(b, e, h)) are shown next to the DWI images to demonstrate the expected intensity decrease. The b_0 data and DWI data of every volunteer are scaled to the same range. To illustrate the anatomical correspondence, the high resolution T_2 weighted images are also presented (Figure 27(a, d, g)). For each volunteer, the presented images are from the same anatomical location.

6.4.2 Noise assessment

The averaged normalized intensity decreases against *b-value* increase of voxels in bone, noise and muscle regions are plotted Figure 28 (from volunteer 1), with x axis as *b-value* and y axis as the averaged normalized intensity. All directions of all the three regions are observed and shown in Figure 28(a-c). The averaged signal decay from all the directions in all the three regions are also plotted and presented in Figure 28(d). With the signal decay caused by diffusion, the normalized averaged intensity should not be bigger than 1 when *b-value* increases. If diffusion is indeed measured inside the observed voxels, the normalized average intensity should decrease when the *b-value* increases. The curve should follow the pattern of exponential decay as in eq. 36. Specifically, in the muscle ROI, clear normalized intensity decay can be recognized. This plot is considered as our reference and is used to compare with the plot of bone. Inside the bone ROI, a similar pattern can be spotted, however the decay slope is less steep than that of the muscle ROI. In the noise ROI, the normalized signal intensity shows varying behaviours with the increase of b-values (Figure 28(b)). The overall trend of the normalized signal intensities in all the three ROIs are presented in Figure 28(d), with the mean values of the normalized diffusion signal plotted as the points of the curve and standard deviation (SD) displayed as "error" bars at each point.

Table 8 lists the overall mean intensity values associated with standard deviations at chosen ROIs at all diffusion gradient directions in selected slices of bone, muscle and noise on all of the three volunteers. For all the volunteers, both the standard deviations and mean intensity values at the bone and muscle regions are higher than that of the noise ROI. In general, the SD of bone ROIs are approximately more than 5 times higher than that of noise.

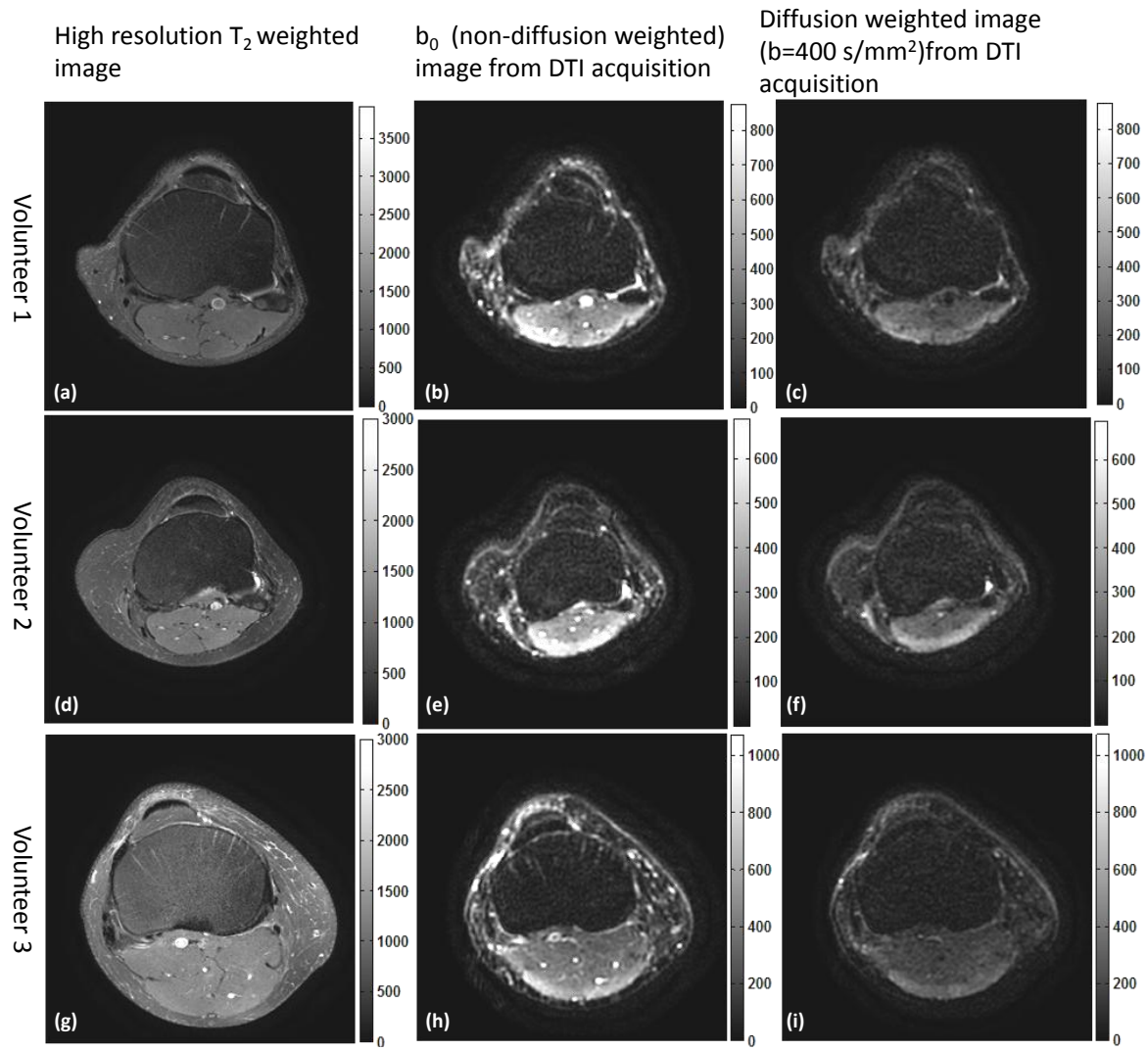

Figure 27. DTI imaging results of the three volunteers. (a-c). slices at the same anatomical location of volunteer 1, from left to right: high resolution T_2-weighted , b_0 and b-value = 400 $mm \cdot s^{-2}$(c) of the DTI data; (d-f) slices from volunteer 2 data at the same anatomical location, corresponding to T_2-weighted, b_0 and b-value = 400 $mm \cdot s^{-2}$ of the DTI data respectively; (g-h) slices from volunteer 3 data at the same anatomical location, from left to right: T_2-weighted, b_0 and b-value = 400 $mm \cdot s^{-2}$ of the DTI data correspondingly.

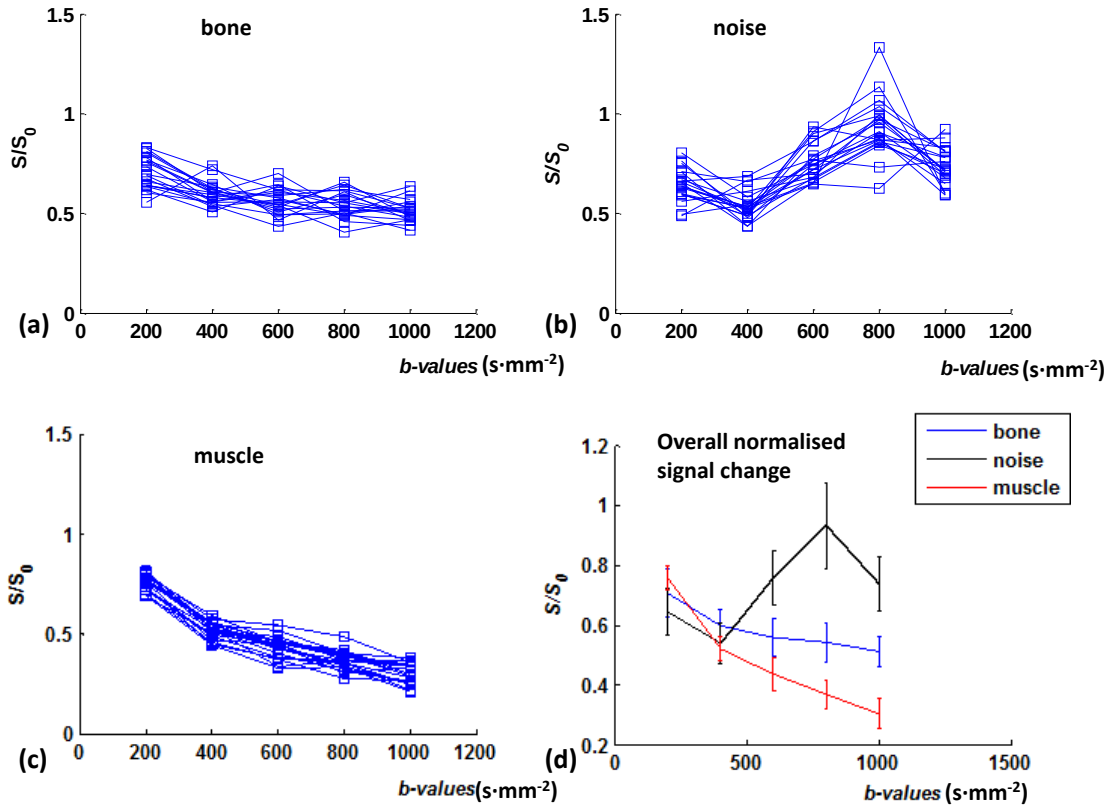

Figure 28. Plots of averaged normalized intensity decay against b-values (*b-values* = 200, 400, 600, 800, 1000 $mm \cdot s^{-2}$) in (a) the bone ROI, (b) the noise ROI, (c) the muscle ROI at all diffusion gradient directions. The averaged normalised signal of all gradient directions in the three type of ROIs are plotted together in (d) with mean (the nodes on the curve) and the standard deviation shown

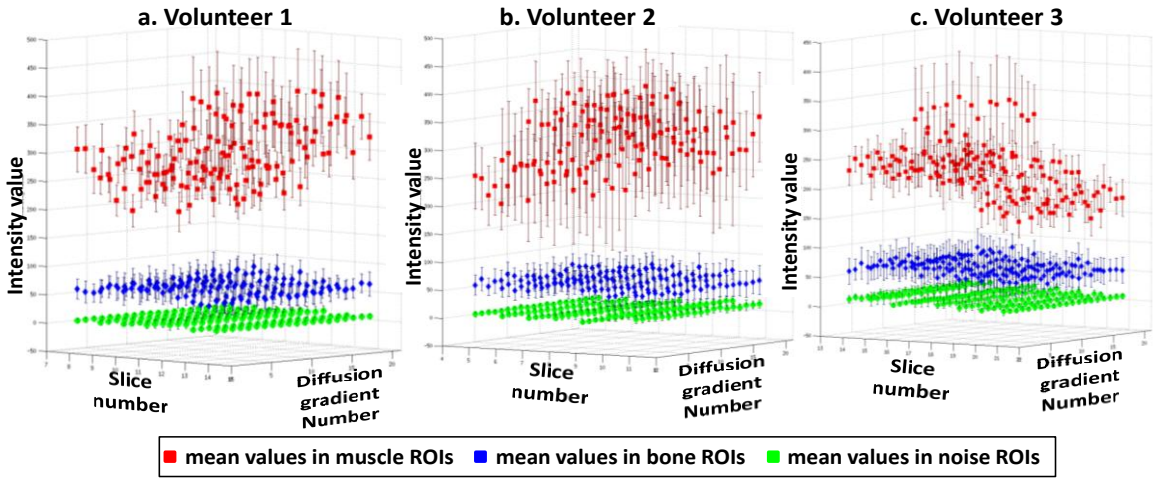

Figure 29. Plot (in 3D) of mean intensity value (nodes) with the associated standard deviation (error bars) in chosen ROIs of bone (blue), muscle (red), and noise (green) at all slices covering the tibia region at each diffusion gradient direction of volunteers 1-3 (from a to c respectively).

Table 8: Mean intensity values with standard deviation in bone, muscle and noise ROIs of all three volunteers on the DW images of the tibia part.

(a). Volunteer 1: measured from Slice 8 to Slice 14

	volunteer 1		
	Noise ROI	Bone ROI	Muscle ROI
Slice 8	7.0 ± 3.8	56.2 ± 18.1	287.3 ± 48.2
Slice 9	6.8 ± 3.4	68.9 ± 24.3	231.9 ± 35.2
Slice 10	6.7 ± 2.9	70.2 ± 22.7	267.6 ± 35.8
Slice 11	9.0 ± 7.4	67.3 ± 21.7	249.3 ± 46.3
Slice 12	10.9 ± 9.1	62.3 ± 19.7	316.8 ± 49.9
Slice 13	6.5 ± 3.7	53.1 ± 18.4	384.8 ± 75.9
Slice 14	8.1 ± 4.2	60.5 ± 19.5	353.0 ± 57.5

(b). Volunteer 2: measured from Slice 5 to Slice 11

	volunteer 2		
	Noise ROI	Bone ROI	Muscle ROI
Slice 5	8.5 ± 4.4	64.3 ± 20.8	244.6 ± 60.1
Slice 6	7.7 ± 4.1	55.7 ± 19.1	248.0 ± 109.4
Slice 7	6.3 ± 3.4	68.3 ± 22.0	358.3 ± 65.4
Slice 8	10.3 ± 7.1	67.6 ± 19.6	358.0 ± 63.8
Slice 9	4.7 ± 2.7	62.0 ± 20.7	342.8 ± 52.6
Slice 10	17.4 ± 9.5	60.6 ± 20.5	310.8 ± 106.4
Slice 11	13.3 ± 7.1	54.6 ± 20.7	314.8 ± 81.2

(c) Volunteer 3: measured from Slice 14 to Slice 21

	volunteer3		
	Noise ROI	Bone ROI	Muscle ROI
Slice 14	11.9 ± 8.0	64.6 ± 22.4	241.5 ± 58.2
Slice 15	11.0 ± 7.2	64.5 ± 24.8	226.1 ± 51.8
Slice 16	12.1 ± 8.4	65.5 ± 23.3	238.3 ± 64.1
Slice 17	11.2 ± 8.2	59.5 ± 22.4	226.3 ± 57.2
Slice 18	12.1 ± 8.9	62.6 ± 23.6	228.1 ± 57.1
Slice 19	12.0 ± 8.6	60.2 ± 22.9	212.9 ± 55.3
Slice 20	13.1 ± 9.2	64.4 ± 24.3	240.7 ± 55.8
Slice 21	11.9 ± 8.5	61.9 ± 23.7	213.5 ± 51.3

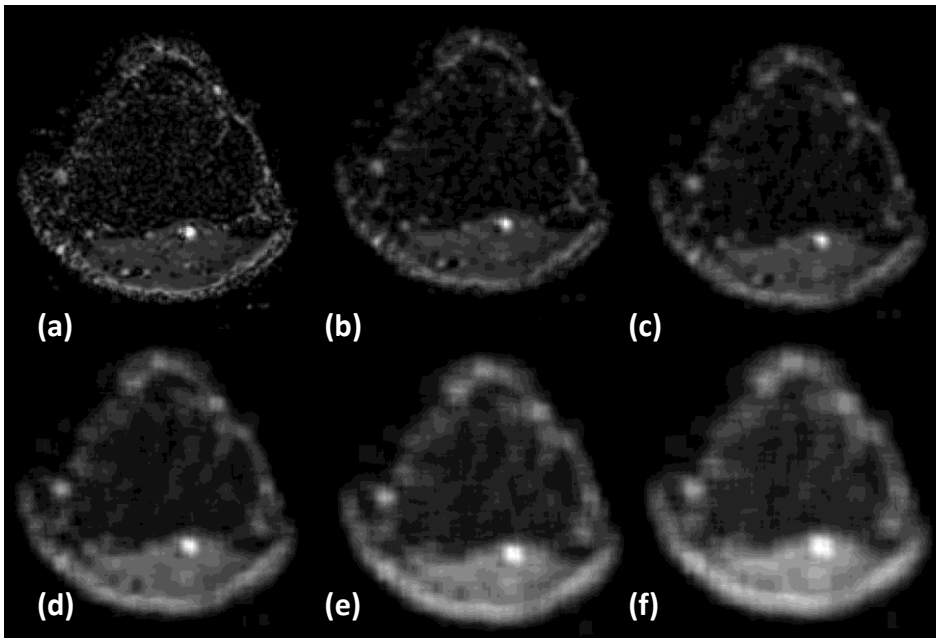

Figure 30. Vector sum results with varying mask size: from (a) to (f), the applied averaging window size of diffusion tensor principle direction vector is 3, 5, 7, 9, 11 and 13 respectively

In the vector-summation evaluation, masks of 6 different sizes (vector averaging window sizes are 3, 5, 7, 9, 11 and 13 respectively) were applied to the whole data volume (sample results in Figure 30). It appears that a 5×5 mask gives the best result in terms of structure coherence as it eliminates the background noise but also keeps most of the internal features not too blurred at the same time. Compared to the background noise region, although very blurred when *mask* is as big as 13, the bone voxels are still visible while the background voxels are completely black.

Noise from both simulated diffusion dataset and from noise-only acquisition (*b-value* = 400 $m \cdot s^{-2}$) was considered when comparing the percentage of negative eigenvalues (NE) with ROIs in bone and muscle regions. Table 9 shows the negative eigenvalue percentage at each type of ROIs of all volunteers. The NE percentages are expressed with the mean and the standard deviation of the ratio of NEs of all the measured slices.

Table 9: Percentage of negative eigenvalues in different types of ROIs of the three volunteers (b = 400 $mm \cdot s^{-2}$)

(a) With real DTI datasets (volunteer 1-3)

	Simulated noise 'diffusion'	Noise ROI	Bone ROI	Muscle ROI
Volunteer 1	10.29% ± 2.87%	5.00% ± 5.01%	2.30% ± 1.79%	0%
Volunteer 2	9.57% ± 2.23%	5.71%±1.98%	1.14% ± 1.07%	0%
Volunteer 3	9.12% ± 2.70%	7.76% ± 3.44%	4.00% ± 2.6%	0%

(b) Volunteer 3 : "noise-only" DTI acquisition

Noise ROI	Bone ROI	Muscle ROI
9.75% ± 5.31%	9.12% ± 3.44%	9.88% ± 4.88%

In all the three volunteers, there is no negative eigenvalue in the muslce ROIs. In the bone ROIs, the mean negative eigenvalue ratio are around 4% (with a maximum 3.95% standard deviation) for all the volunteers within a 10×10 region. For volunteer 3, the negative eigenvalue ratio in the "noise-only" DTI acquisition are also calculated. With the pure noise DTI data, a similar percentage of negative eigenvalues are found as for the simulated noise "diffusion" data (Table 9 (b)).

The trace map of the noise only data (Trd_{noise}) and the actual tibia DTI data (Trd_{DTI})) in the trabecular bone region (mask manually cropped from the b_0 data and applied to both trace maps) is presented in Figure 31(a) and (b) repectively. A "jet" colour map in MATLAB is used to illustrate the difference more clearly. The histograms of trace values (normalized with the maximumu trace value of the dataset) within the trabecular bone region of Trd_{noise} (in blue) and Trd_{DTI} (in green) are plotted in Figure 31(c). According to (c), the bandwidth of Trd_{noise} is much more spread than that of Trd_{DTI}. Moreover, the 0 bin of Trd_{DTI} 's histogram contains a distinct number of voxels. This can be contributed by voxels only containing trabecalar bone which does not give any signal at all. Several bins of histograms of both Trd_{noise} and Trd_{DTI} corresponds to negative trace values, indicating the noise corruption to the diffusion tensor systems as discussed in Section 6.3.3 on negative eigenvalues.

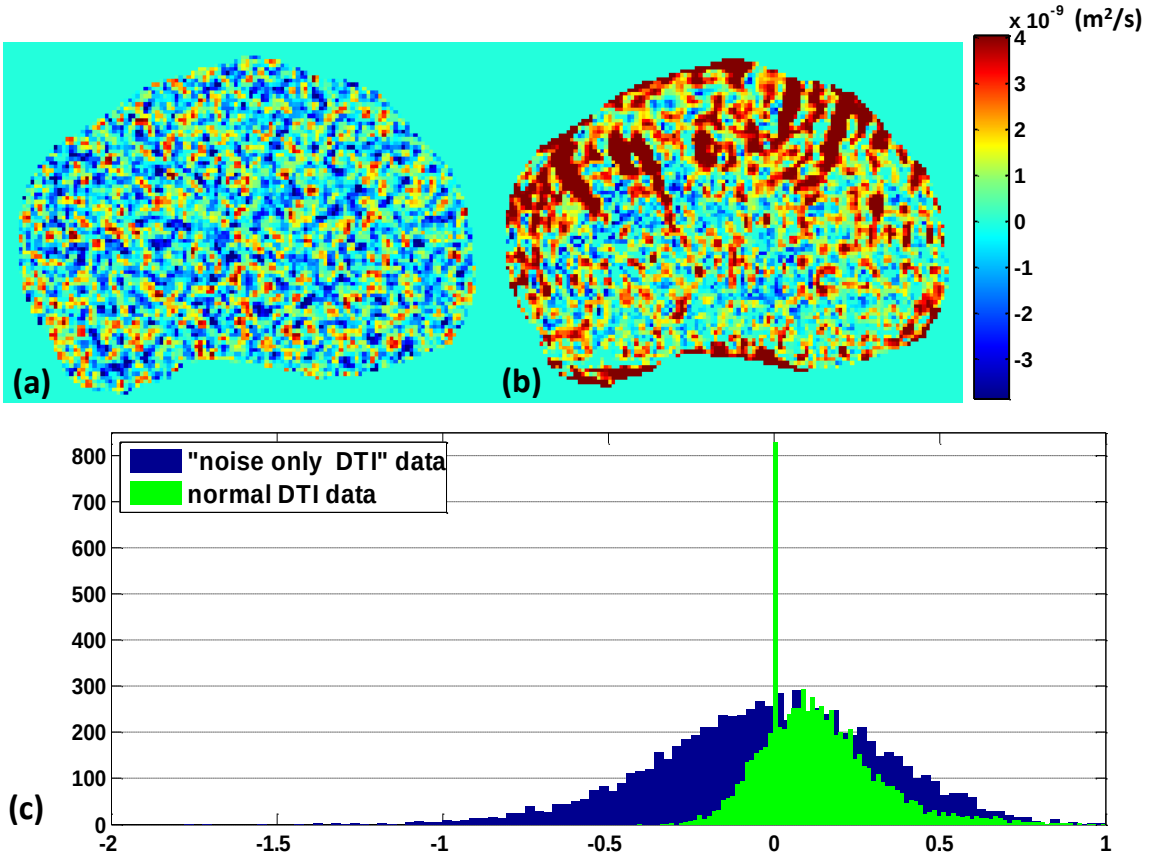

Figure 31. Comparison between "noise only DTI" trace map (a) and the real bone "DTI" trace map (b) of the same slice from volunteer 3. Both images are scaled to the same range. (c) The histogram of the trace values within the trabecular bone region in (a) (blue) and (b) (green). The y-axis corresponds to the number of voxels in each bin, and the x-axis is the normalised trace value (with the maximum trace value within the region).

6.4.3 Quantitative analysis

The calculated mean ADC of red marrow within the ROIs of the three volunteers is

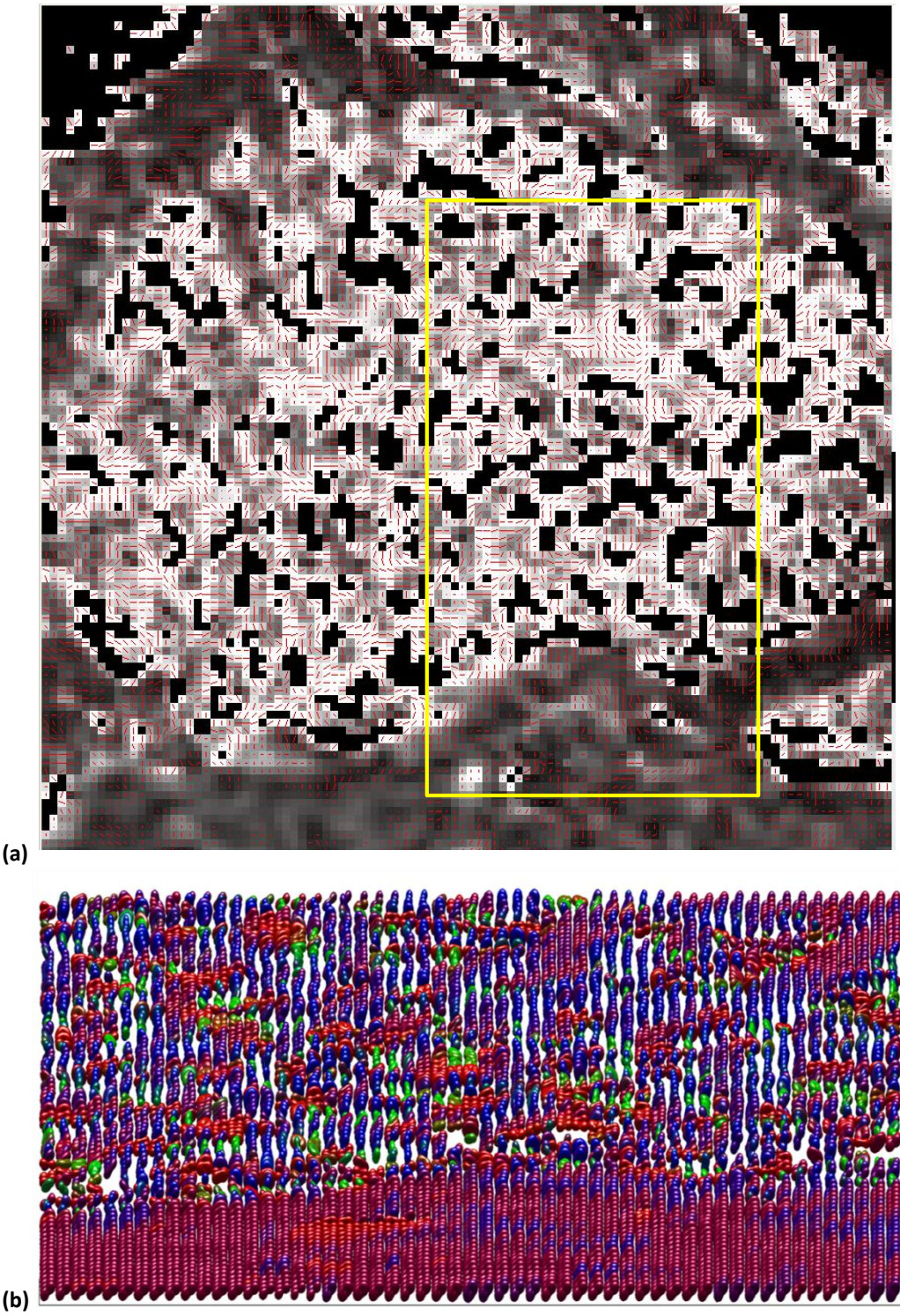

Figure 32. Voxel-wise plots of diffusion tensors (sampled slice, slice 10 from volunteer 1): (a) 2D tensor plot, the red arrow in each voxel oriented based on the principal direction of the tensor and its length is scaled with the projection of the principal direction vector; (b) 3D tensor plot of the ROI (in yellow) of (a). The colour of each tensor corresponds to the principal orientation of the tensor: red for x-axis direction, green for y-axis direction and blue for z-axis direction.

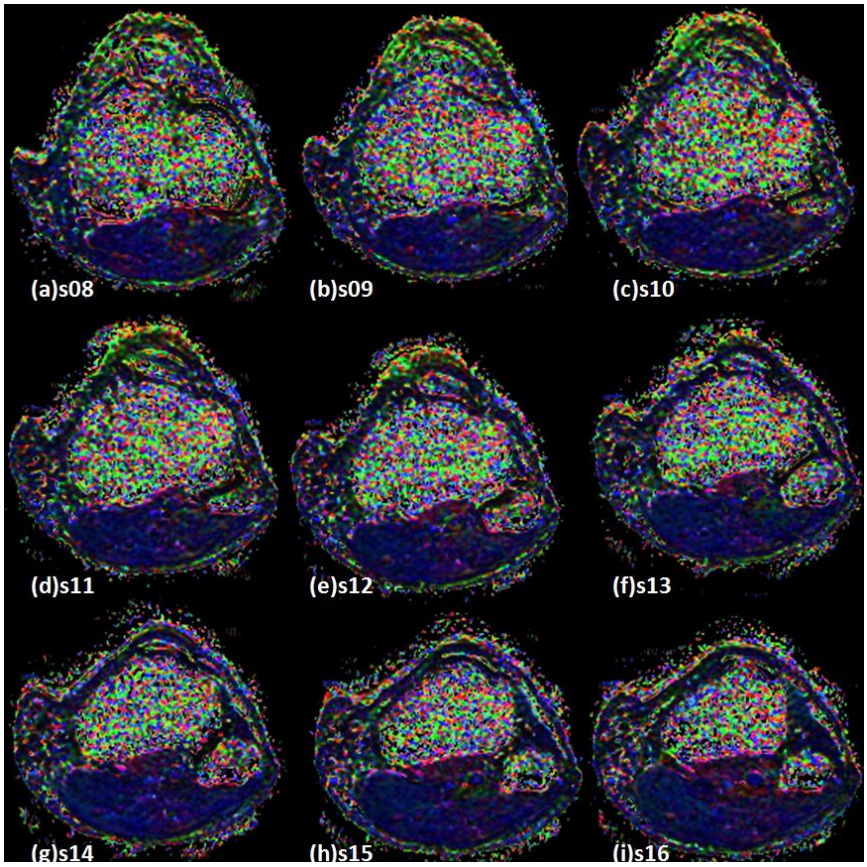

Figure 33. Colour-coded (red for x direction, green for y direction, blue for z direction) principal orientation of diffusion tensors weighted by FA maps of volunteer 1 at b-value =400 $s \cdot mm^{-2}$. From (a)-(g), images corresponds to slice 8 to 16 in the imaging volume, running from the tibia plateau towards the ankle.

$0.6\times10^{-9}\,m^2/s$ while the muscle mean ADC of the three volunteers is $1.6\times10^{-9}\,m^2/s$ and the diffusion of fatty yellow marrow is much slower ($(1.8 \pm 0.1)\times10^{-11}\,m^2/s$, as reported by Steidle et al. in [179]). The principal tensor orientation of the sampled bone regions is shown in Figure 32. In the chosen TB region, 2D red arrows are plotted in each voxel along the projection of principal direction of the diffusion tensor on the imaging plane. The length of each red arrow is scaled with the magnitude of the projection (to the imaging plane) of each eigenvector. The 3D tensor plot of a region (indicated by a yellow box) are plotted (in the form of spherical harmonic functions) and presented in Figure 32(b), in order to illustrate the spatial arrangement of the tensors. The figure plane was rotated around the x axis of the image in order to provide a better visualization angle. Nine slices of volunteer 1

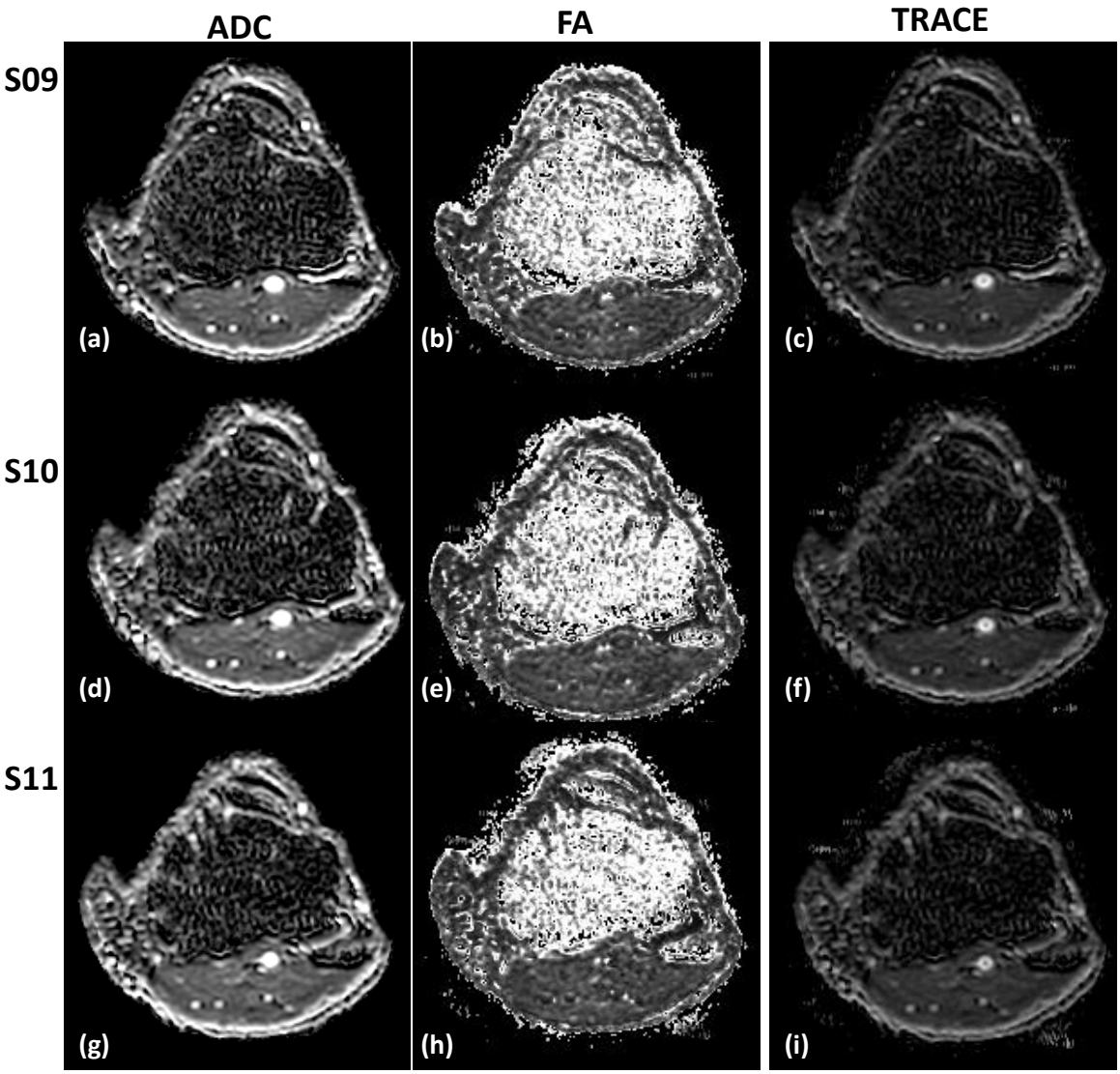

Figure 34. Examples of parametric maps of volunteer 1 at the tibia epiphysis: (a-c) ADC, FA and trace of slice 9; (d-f) ADC, FA and trace of slice 10; (g-i) ADC, FA and trace of slice 11

from the upper extremity of the tibia (~20 *mm*) with the presence of TB are selected and presented in Figure 33. The voxel-wise eigensystem of each slice (i.e. the principal direction weighted by FA values at each voxel) is presented in colour in Figure 33. The same colour map is used for both the 3D tensor plot and the FA weighted eigensystem image. It corresponds to the tensor orientation: red for the x axis (RL), green for the y axis (AP), blue for the z axis. The examples (slices containing the tibia epiphysis from volunteer

1) of parametric maps (ADC, FA and trace) are shown in Figure 34. From top to bottom, the parametric maps of Figure 35 shows the examples of the "fibre" tracking result from all volunteers with *b-value* = 400 ($s \cdot mm^{-2}$). The seeding ROIs were placed as close as possible to the tibia head. The tracks are coloured with red for x axis right to left), green for y-axis (anterior to posterior), and blue for z-axis (the slice encoding direction). The reconstructed tracks show a trend of following the orientation of the trabeculae which is along the tibia (the long blue fibre tracks). Recall Wolff's law, the direction of trabecular bone (TB) is related to the remodelling process which is affected by the force that TB endures. In tibia, this force is normally from the body-weight, which is along the direction of the leg.

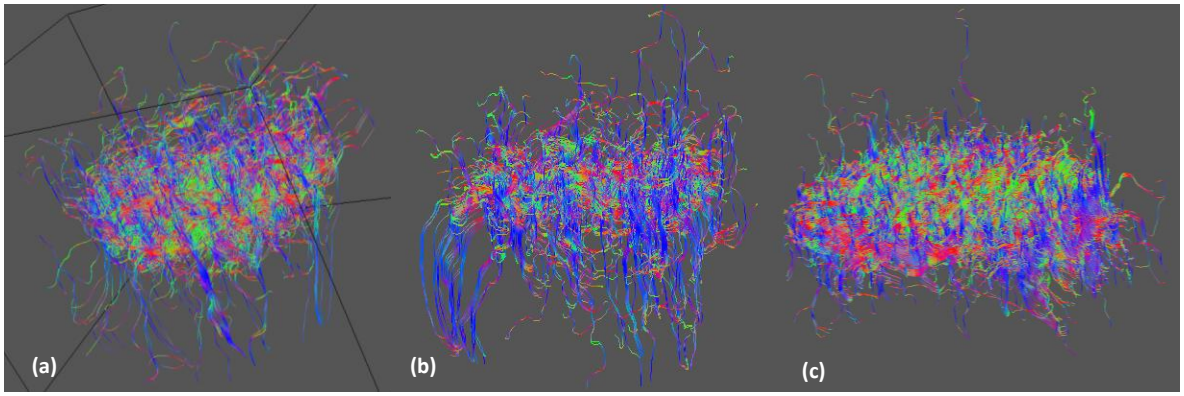

Figure 35. Tibia trabecular bone "orientation trajectory" represented by diffusion tensor "fiber tracks" with data from (a) volunteer 1 (b) volunteer 2 (c) volunteer 3.

6.5 Discussion

The results of the *in-vivo* DTI to human tibia study have been presented. The feasibility of the *in-vivo* diffusion tensor imaging of trabecular bone has been demonstrated. A set of noise assessment was performed first with the aim to verify the origin of the signal detected in the trabecular bone region. Considering the trade-off between acquisition time and SNR, a *b-value* of 400 $s \cdot mm^{-2}$ was chosen for the *in-vivo* DTI protocol of human's tibia. Following the settings, the protocol was performed on 2 more volunteers (volunteer 2 and 3) recruited for this study. Anisotropy indices and ADC values were computed from the diffusion tensors voxel-wise. Based on the coherence of the diffusion tensor orientation, the

tibia trabecular bone "orientation trajectory" was retrieved using a standard fibre tracking algorithm normally used for the brain DTI analysis. Such investigation is indeed rare as DTI at the moment is mainly used for neurology and is being extended to understand the muscles but not for the skeletal system. The technique's ability to reveal trabecular network orientation at the micro-scale are also discussed and demonstrated by reconstructing diffusion tensors and tracking the dominant diffusion directions. As DTI probes the particle motion at a cellular level, it could be used as a direct measurement of trabecular bone orientation, compared to those post processing based methods e.g. to measure fabric tensors from data reconstructed from high resolution MRI data *in-vivo*.

Up to now the application of diffusion MR on bone marrow investigation is mainly limited to using ADC as a parameter to detect lesion or distinguish it as benign or malignant [180]. As the microstructure of trabecular bone contains orientation information which is believed to correlate with the bone mechanical competence [46], it may be advantageous to make use of the informative anisotropy measurement contained in DTI, which has not been explored enough. In the DTI of bone marrow study reported by Capuani et al. [114], the preliminary results on DTI of bone marrow (calf femur) *ex-vivo* using a PGSTE sequence on a pre-clinical scanner were presented. However, they only demonstrated the different behaviour of diffusion in fat, cartilage and trabecular bone marrow and commented briefly on the potential of using DTI to reveal the microstructure of TB. No further experiment on utilizing the tensor orientation was performed. Although they did not describe the composition of the bone marrow in the calf femur epiphysis, the different diffusion behaviour between fat and bone marrow were shown. It is, however, sensible to consider that such difference may be due to the free water components inside the red marrow (the existence of red marrow in the femur epiphysis [181]). This part of the femur contains a number of free water molecules which diffuse faster than marrow. To our knowledge, the in-plane resolution ($1.4\times1.4\times3.2\ mm^3$) achieved by our bone DTI protocol is also superior to published protocols in musculoskeletal systems (Lansdown et al. [174], Steidle et al. [179], Sinha et al. [182]).

The implementation of the dual-echo PGSE sequence on the GE scanner is spectral-spatial selective [139], which pre-select the water molecules (i.e. inside the red marrow) to be on

resonance (page 153-164, section 5.4 in [112]). The systematic noise assessment provides evidence to confirm this assumption. Although decaying slower than water inside muscles, the measured normalized averaged bone marrow intensity decayed with the increase of the applied *b-values*. The decaying trend of bone ROI slows down after *b-value* = 600 $s \cdot mm^{-2}$, compared to that of the muscle ROI. However, there is not enough data to say whether such behaviour is due to any particular effects. The randomness of the noise is well shown by the data in Figure 28 (b, d). Apart from increasing with the *b-value*s, the normalized intensity value of noise is bigger than 1 at many directions. The results of these ROI based methods are further confirmed by the real "noise-only DTI" dataset acquired with exactly the same DTI protocol, where the difference between a noise-only trace map and a trace map containing real diffusion signal was revealed and visualised more clearly. The acquired diffusion weighted data on all the three volunteers also show clear intensity attenuation between the b_0 acquisition and the DWI image.

It is also interesting to notice how the tensor oriented around the signal-void voxels (i.e. the pores) which are thought to be trabecular bone (TB). In the 2D tensor plot (Figure 32 (a)), the projection of the principal directions appears to change the orientation around the pores. The coherence of the tensor orientation is further shown by the fibre tracks of volunteer 1 (Figure 35 (a)). Although there is no fibre inside tibia physically, these derived fibres may represent the orientation trajectory of the trabecular bone which is just next to the bone marrow. The blue fibres are mainly distributed on the edges of the investigated volume, while the red and green fibres are bounded tightly in the central part of the volume. Compared to volunteer 1's TB "fibre" network, TB "fibre" network of volunteer 2 contained denser blue fibres in the volume edges. This difference may be caused the varying micro-architectural organization between the two volunteers. It might also be related to the age difference between volunteer 1 and 2 (volunteer 1 was 20 years older than volunteer 2).

Although the results from the current study are quite encouraging, there is certainly a long way from applying DTI derived "orientation" for actual clinical applications, such as estimating the bone fracture risk. From the clinical point of view, although extensive study has been performed in the biomechanics community on trying to relate trabecular bone orientation to bone mechanical behaviour, it is still an open question due to the difficulty of

measuring TB orientations *in-vivo* on a conventional hospital set-up. Therefore, there is not enough clinical evidence of correlating the anisotropy parameter derived directly from actual (OA or OI) patients to the diagnosis scoring. Technique-wise, issues concerning improving the acquisition protocols have to be considered. Although the reported protocols on a clinical scanner do provide promising results, issues such as chemical shift, EPI ghost artefacts and geometric distortions, field inhomogeneity, patient motion and low SNR still exist. In the protocol, dual echo PGSE-EPI (single-shot) sequence is chosen with partial Fourier acquisition and a parallel imaging model (acceleration factor = 2). The reason to choose such a setting is to reduce the time to traverse the k-space in order to reduce the amount of the induced EPI distortion. The frequently switching diffusion gradient is normally very strong that vibrates the patient table. Although we tried to put the knee coil as tightly as possible to the subject's knee joint to reduce big motion (e.g. raising the leg when being stimulated by the diffusion gradient), tiny motion is inevitable. Gradient system heating also causes a slight shift of the images over time. Similar cases have been reported in brain diffusion but the motion correction is not easy. In the current work, correlation registration on the b_0 images is exploited to align the data. In the future, by using the raw k-space data, an improvement on data alignment might be achieved.

Another big technical concern is to understand the diffusion behaviour of bone marrow better. Overall, bone marrow is a complicated mixture and its composition changes with anatomical locations (Chapter 1, page 3 in [183]). Although its ADC values have been measured in spine bone marrow, its diffusivity has not been thoroughly studied yet at various TB locations in human body with a DTI protocol. The last consideration is to evaluate the diffusion of bone marrow indeed captures the shape of the whole microstructure. If we consider the trabecular bone sample contains two phase, bone and bone marrow, the assumption can stand. At the moment, there is not enough data to solidly support such assumption. To prove this, the first step is to perform an *ex-vivo* experiment with a trabecular bone segments whose marrow is completely removed and replaced with pure water. This could provide a baseline for the water-diffusion-retrieved TB network. Then the bone marrow can be simulated by mixing a fatty compound (e.g. olive oil) and pure water as suggested by Bernard et al. [184].

Local contrast in magnetic susceptibility gives rise to inhomogeneity in the static magnetic field and deleteriously affects a PGSE measurement [110]. It is suggested that the unwanted attenuation may be significantly reduced by a pulsed gradient stimulated spin echo (PGSTE) [110, 185]. Another advantage of PGSTE sequence is that magnetization is preserved during the gradient pulses and stored along the longitudinal direction during the diffusion time, which also provides the opportunity to observe the long-term diffusion in order to probe the microstructure [116] more accurately and in group studies. However, the drawback of PGSTE sequence is its long acquisition time.

In this study, although the feasibility of applying DTI in human tibia *in-vivo* is demonstrated, more experiments are certainly needed for validation, reproducibility and to improve the resolution. The calculation of the trabecular bone orientation may also be improved by more sophisticated fitting procedures for diffusion tensor reconstruction. The next step is to examine the reproducibility of this protocol in order to allow a study including a specified patient group.

6.6 Summary

In summary, the goal of multi-scale imaging is to capture information from the micro-scale which provides parameters for modelling across scales. Bone can be considered as a porous media system. Accordingly, porosity (i.e. BMD) and orientation (i.e. anisotropy) are the two parameters of interest to model the micro-structure of bone for its mechanical property evaluation, applying for both trabecular bone and cortical bone (as explained in Section 2.2). It is true that such information can be quantified with higher accuracy in histological images; however the applied quantification is not easy to be transferred to *in-vivo* imaging.

This chapter discussed the current progress of using DTI to measure the trabecular bone orientation. It shows qualitatively good agreement with what is expected at the epiphysis end of the tibia. The future work is: to improve the resolution and SNR, and to perform more experiments to show the reproducibility of the protocol. It would also be more plausible if some patient data can be collected as a comparison with the healthy volunteers.

The author’s contributions are summarized below:

The feasibility of *in-vivo* red-marrow diffusion tensor imaging on human tibia epiphysis with a clinical scanner is demonstrated for the first time to our knowledge. The protocol is tuned locally on a 3T GE scanner. A series of noise assessment has been performed in order to validate the origin of the signal (i.e. whether the red marrow diffuses). By using the diffusion tensor analysis, *in-vivo* orientation "trajectory" of marrow distribution is rendered for the first time which can be used to reflect trabecular bone orientation "trajectory" model in such a two-phase porous media system.

Chapter 7. *In-vivo* DTI of trabecular bone: Reproducibility study

The reproducibility of the established *in-vivo* protocols proposed in the previous chapter was assessed on volunteer 1 and 3 by repeating the protocol several times. The diffusion coefficient measurements and the derived anisotropic measurement are compared among acquisitions of the same volunteer. A further investigation was taken by changing frequency encoding directions to examine the robustness of the protocol. The reproducibility of the experiments was further interpreted using Bland-Altman (BA) plots. The above efforts aim to identify the possible problems and to improve the protocol.

7.1 Methods and Subjects

7.1.1 Subjects and experiments

The same volunteer group for the feasibility study (Table 10) was used for this reproducibility study. The intra-subject inter-scan reproducibility was examined on the right knee joint region of volunteer 1 and volunteer 3 on the same scanner (GE Signa Hx 3T) repeatedly twice for volunteer 1 and 3 times for volunteer 3 for a short-term inter-scan reproducibility study of the previously established protocol. The same protocol and knee joint coil were used for the acquisition. For the two volunteers, both were scanned repeatedly on the same day without any repositioning of the coil, and only one calibration scan was performed before all the acquisitions.

Another reproducibility study (intra-subject, inter-protocol) was performed, aiming to investigate whether the diffusion measurement resist with changes in imaging protocol or not; if not, what might be the cause to affect the measurement. In this study, volunteer 1 and volunteer 2 were scanned with switched frequency encoding direction (from right-left to anterior-posterior, corresponding to the imaging volume) on their left knee joints. Other imaging parameters were the same for each volunteer. Both studies did not involve a repositioning of the coil. This reproducibility study was performed on the same day for the two volunteers after the feasibility study reported in Chapter 6 was conducted, which was

before the intra-subject reproducibility study on the same protocol.

Table 10: Volunteer details of reproducibility studies

	Age	Sex	Scanned knee (right/ left)	Experiment type	Number of repeated times
Volunteer 1	46	male	right	Intra-subject inter-scan	2
			left	Intra-subject inter-protocol	2
Volunteer 2	20	female	left	Intra-subject inter-protocol	2
volunteer 3	40	male	right	Intra-subject inter-scan	3

7.1.2 Data processing and statistical analysis

DTI datasets were processed offline using CAMINO [173] and MATLAB (R2008a, The Mathworks, Natick, MA). All DTI datasets were aligned by registering all the diffusion weighted images and the second, third and fourth b_0 scans to the first set of b_0 datasets. This was done by pre-processing all DWI data (histogram matching with the b_0 image and thresholding at 3% of the maximum image intensity) and then applying a sum-of-squared differences registration of the pre-processed (binarized) images. The registration only searched for in-plane translations (to correct for drifts in the images due to patient motion or gradient heating). The resulting transformation matrices were applied to all the DWI data. As no repositioning of the coil was involved during the whole study and the knee joint was fixed very tightly inside the knee coil, rotational motion was not observed and only translational motion was considered which required no realignment of the diffusion tensor after the registration of DWI datasets. Diffusion tensors were fitted voxel-wise with the registered datasets separately using the routines introduced in Chapter 6 (Section 6.2.2). Trace and FA, as well as the principal eigenvector (PEV) were computed for the comparison among the DTI datasets on the same volunteer with the same protocol.

In the intra-subject inter-scan reproducibility, the reproducibility of diffusion parameters, trace and FA, were examined with a ROI-based analysis. Arbitrary ROIs were manually chosen on the same slices covering the tibia region with two tissue types, bone and muscle, of each registered DTI dataset for the comparison. The size of the ROIs was set to be 10×10 (i.e. 1.4×1.4 cm^2) in order to fit all the ROIs into the same tissue type in all the analysed slices. The mean and standard deviation of FA and MD are calculated within the ROIs. To investigate the principal eigenvector (PEV) orientation reproducibility, the voxel-

wise angular differences (DA_{PEV}) of the PEV orientation between every two DTI datasets of the same volunteer were compared on the whole bone region which was manually segmented for that purpose. DA_{PEV} is computed through the dot product between the PEVs of the same voxels, using eq. 46.

$$\mathrm{DA_{PEV}}\,(\mathrm{j,k,z}) = \cos^{-1}\left(\frac{\mathrm{PEV_A}\cdot\mathrm{PEV_B}}{\|\mathrm{PEV_A}\|\cdot\|\mathrm{PEV_B}\|}\right) \qquad \text{eq. 46,}$$

where PEV_A and PEV_B indicate the principal eigenvectors at the voxel with the same location $(j,\ k,\ z)$ from DTI datasets A and B respectively. In the end, the difference angle was re-oriented so that the difference was within the range $[0,\ \pi/2]$. The intra-subject inter-protocol reproducibility was processed and analysed with the same routine introduced above. It is necessary to point out that the intra-subject inter-protocol study was performed prior to the inter-scan study.

A Bland-Altman (BA) test was applied to assess the agreement of trace (i.e. diffusivity measurement) and FA between the different acquisitions of the same volunteer in the reproducibility study.

7.2 Results

7.2.1 The intra-subject inter-scan reproducibility

In the intra-subject inter-scan reproducibility study, the ROI based FA and trace comparison of volunteer 1 and volunteer 3 are shown in Figure 36. The mean (the nodes in Figure 36) and standard deviation (the length of the error bar is $2 \times SD$) of trace and FA in both bone and muscle ROIs are plotted against the slice number. Dashed lines are drawn in each figure to show the lower bounds of possible trace values and the upper bounds of FA. From the figure, the ROI based FA and trace values, in the muscle region of both volunteers show reasonably good agreement on the analysed slices from both datasets. In the analysed ROIs of the muscle, the maximum mean value differences in trace and FA are 2.1×10^{-10} m^2/s (in slice 13) and 0.05 (in slice 18) respectively for volunteer 1, and 3.6×10^{-10} m^2/s (in slice 20) and 0.07 (in slice 17) respectively for volunteer 3. In the bone ROIs, the

mean values of both trace and FA also show relatively good agreements, however the standard deviations are much bigger than those of muscle ROIs. The maximum mean value differences in trace of bone ROIs were found in slice 18 with 5.5×10^{-10} m^2/s for volunteer 1 and in slice 18 with 7.2×10^{-10} m^2/s for volunteer 3, while the maximum mean FA differences are 0.06 in slice 12 for volunteer 1 and 0.1 in slice 15 for volunteer 3. The big variation could be partially explained by the voxels containing only or mostly trabecular bone which do not give any signal. This high variability implies that the measured diffusion parameters in the bone ROIs are less reliable and may be corrupted by noise.

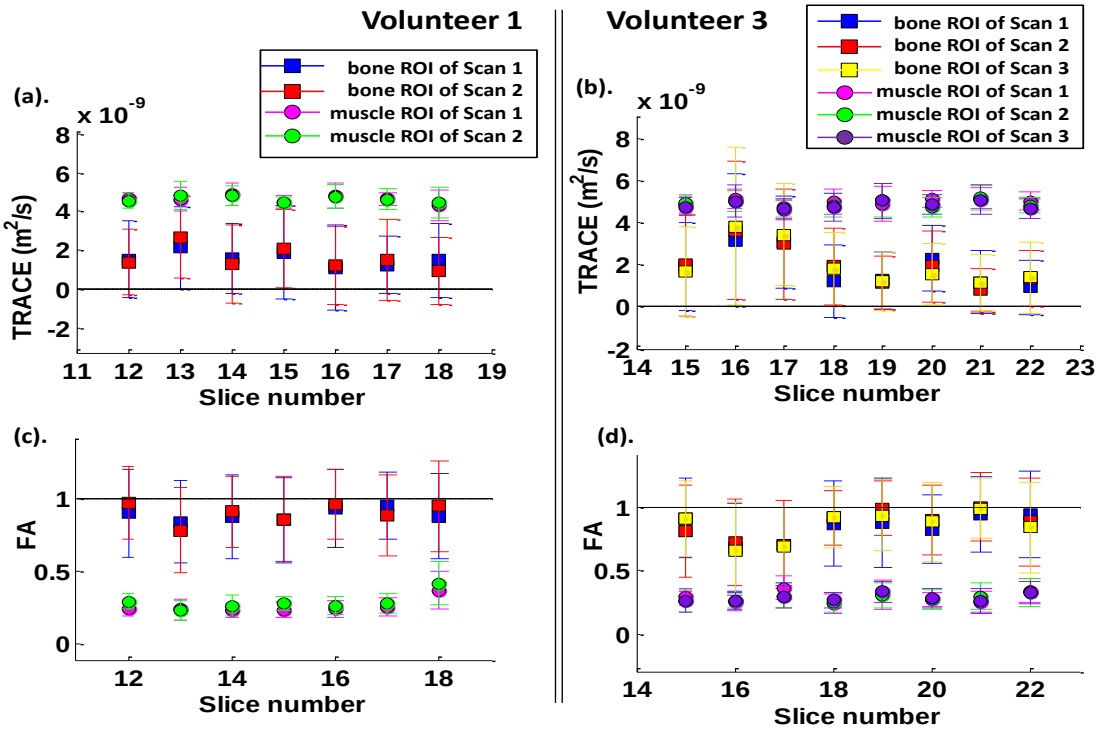

Figure 36. Intra-subject inter-scan trace (a-b) and FA (c-d) comparison of volunteer 1 (a and c) and volunteer 3 (b and d). For volunteer 1, two scans were performed. For volunteer 3, three scans were performed. The dashed lines in each plot indicate the physically meaningful range of the corresponding values: trace = 0 (lower bound of trace) and FA = 1 (upper bound of FA).

The voxel-wise angular difference (DA_{PEV}) between acquisitions of the two volunteers is presented as the histogram of the angular difference distribution ($DA_{PEV} \in [0, \pi/2]$) in Figure 37. Only two acquisitions have been performed on volunteer 1 (v1) in the inter-

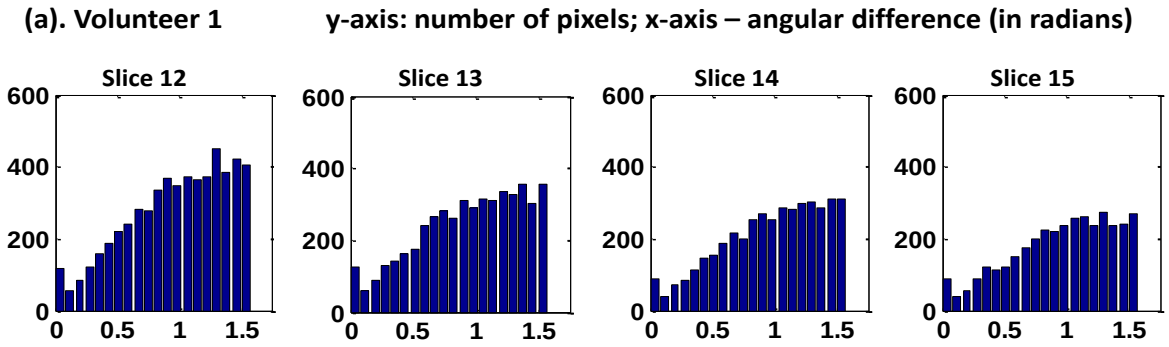

Figure 37. (a) Histogram of the voxel-wise angular difference of the principal eigenvector orientations of the two repeated acquisitions in the whole trabecular bone region (sampled results in slices 12 -15) of volunteer 1 at the tibia bone (covering the tibia head).

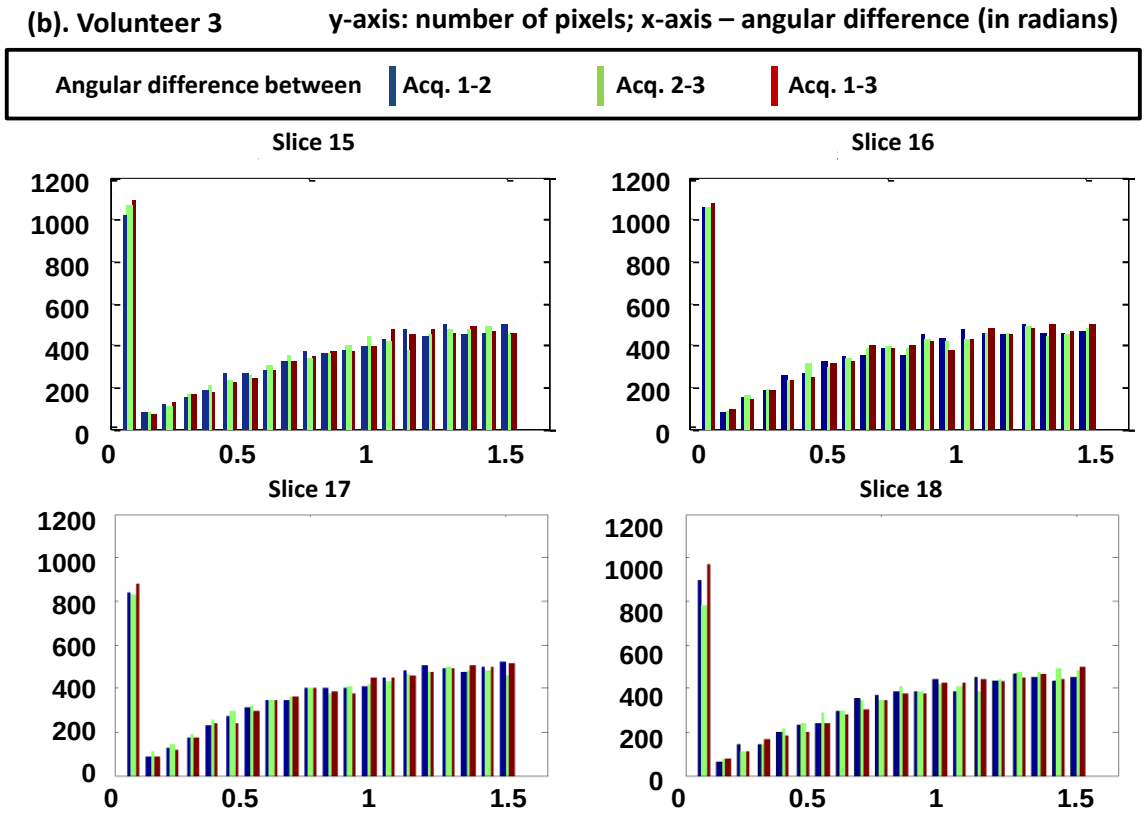

Figure 37. (b) Histogram of the voxel-wise angular differences of the orientation of principal eigenvectors of the three repeated acquisitions in the whole trabecular bone region (sampled results in slices 15 -18) of volunteer 3 (covering the tibia head). The y axis corresponds to the number of voxels, and the x-axis corresponds to the angular differences in radians. For each bin of the histogram, three bars are plotted, corresponding to the differences between every two scans: blue for Acq. 1-2, green for Acq. 2-3, and red for Acq. 1-3.

subject inter-scan study. It can be seen that only a small percentage (2.1%-2.5%) of DA_{PEV_v1} is around 0, indicating that most of the reconstructed diffusion tensor systems were not reproduced in the repeated acquisition, except in this small percentage of voxels corresponding to the peak on the far-left of the histogram. Three datasets were acquired on volunteer 3 (v3), leading to three comparisons: Acq. 1-2, Acq. 2–3 and Acq.1–3 (Figure 37(b)). The number of very low DA_{PEV_v3} (≈ 0) are 10.8% - 14.7%, 10.7% - 14.4% and 11.4% - 13.7% for the above 3 comparisons from slice 15-18. In all the three comparisons of volunteer 3, around 30% of the angular differences in the analyzed slices are less than $\pi/6$, compared to the 18% in the case of volunteer 1. Voxels in trabecular bone region with low angular difference (DA_{PEV}<0.08 in radians) among Acq. 1, 2, and 3 of volunteer 3 are shown in Figure 38.

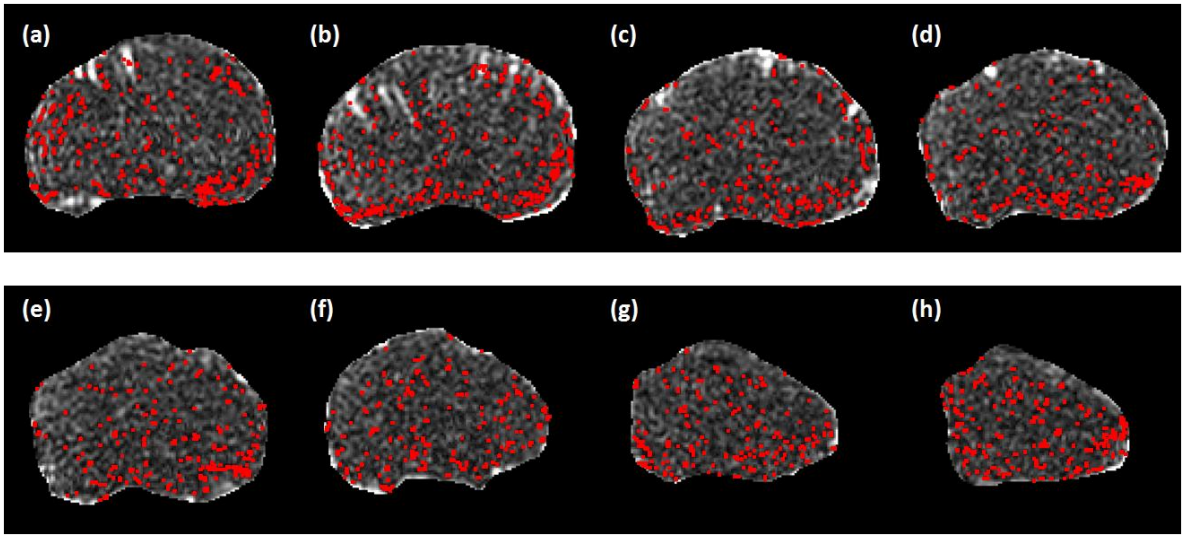

Figure 38. Voxels (red points) with low (< 0.08 in radians) angular difference between diffusion principle directions of Acq.1-3 of volunteer 3's tibia head region in the intra-subject intra-protocol study were plotted on top of the b0 images in the corresponding slices: from (a) to (h) corresponds to slice 15 to slice 22, whose ROI-based trace and FA comparison between scans are indicated in Figure 36.

The results of the Bland-Altman analysis of trace and FA of volunteer 1, and trace of volunteer 3 (comparison of Acq. 1 and Acq. 3) of voxels in the ROIs (the same as those used in Figure 36) in the inter-scan reproducibility study are illustrated in Figure 39. The mean of the paired difference, its upper and lower correlation bounds are also indicated.

However, the BA test failed in the intra-subject inter-protocol reproducibility study, indicating the diffusion measurements were not reproduced when changing the phase encoding direction.

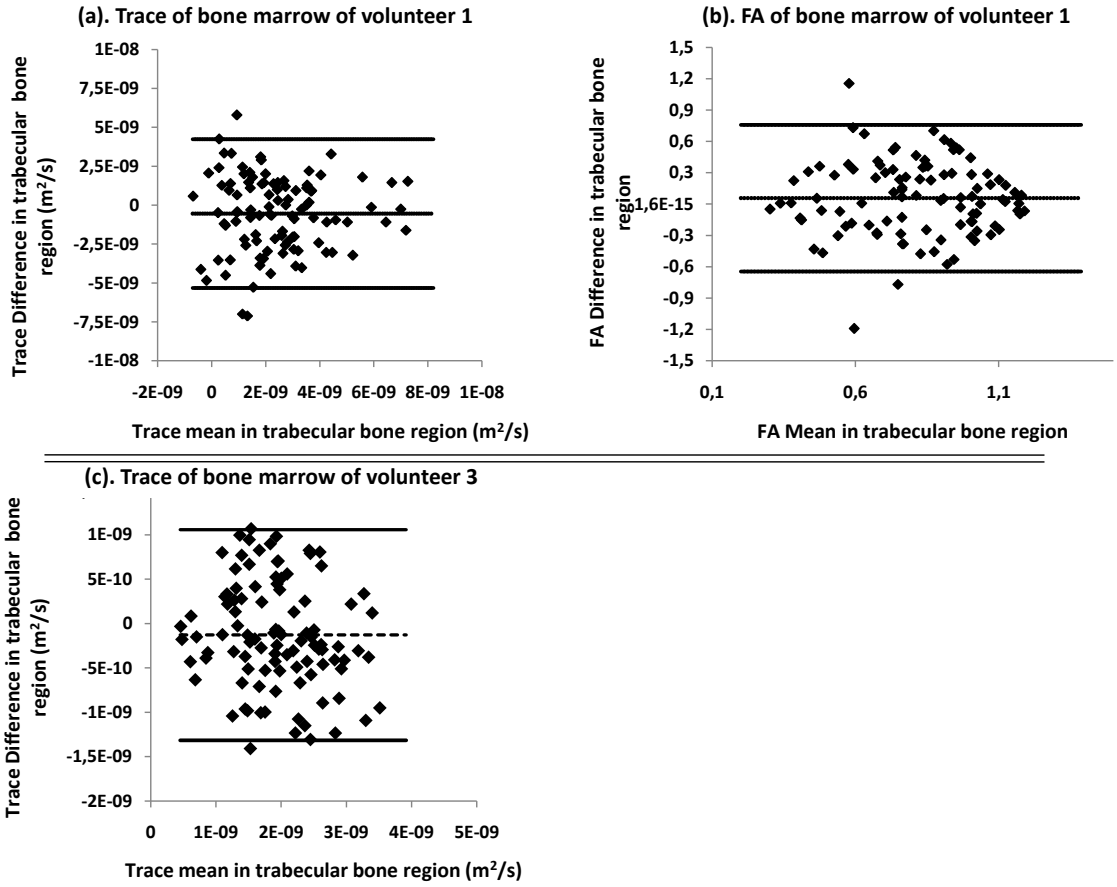

Figure 39. BA plots of the intra-subject inter-scan reproducibility study: (a) trace and (b) FA of bone marrow voxels in the ROIs of volunteer 1; (c) trace of bone marrow voxels in the ROIs of volunteer 3's Acq. 1 and Acq. 3 (the voxels are from the same ROIs as used in Figure 36).

7.2.2 The intra-subject inter-protocol reproducibility

In the intra-subject inter-protocol reproducibility study, the ROI based FA and trace comparison of volunteer 1 and volunteer 2 are shown in Figure 40. In general, for both volunteers, the diffusion parameters of muscles show reasonably good agreements. The maximum differences on the trace and FA values are 1.1×10^{-10} m^2/s on slice 15 and 0.1 on slice 15 for volunteer 1, and 2.9×10^{-10} m^2/s slice 7 and 0.05 slice 11 for volunteer 2. For the

bone ROIs, the mean values of the two successive acquisitions on both volunteers show some agreement in the figure, but the corresponding standard deviations are much bigger than that of the muscle ROIs. The FA values in all bone ROIs showed possibility of falling outside the physically meaningful range. The maximum mean differences of trace for the bone ROI are found in slice 10 ($1.8 \times 10^{-9}\ m^2/s$) for volunteer 1 and in slice 8 ($4.6 \times 10^{-10}\ m^2/s$) for volunteer 2. For mean difference of FA, the maximum values are 0.25 for volunteer 1 in slice 10 and 0.09 for volunteer 2 in slice 10. The voxel-wise angular difference analysis on the principal eigenvectors (DA_{PEV}) is shown in Figure 41, by plotting the histogram of the distribution of DA_{PEV} in the bone region only. It can be seen that the amount of low DA_{PEV} (≈ 0) is quite low for both volunteers in all the slices that were

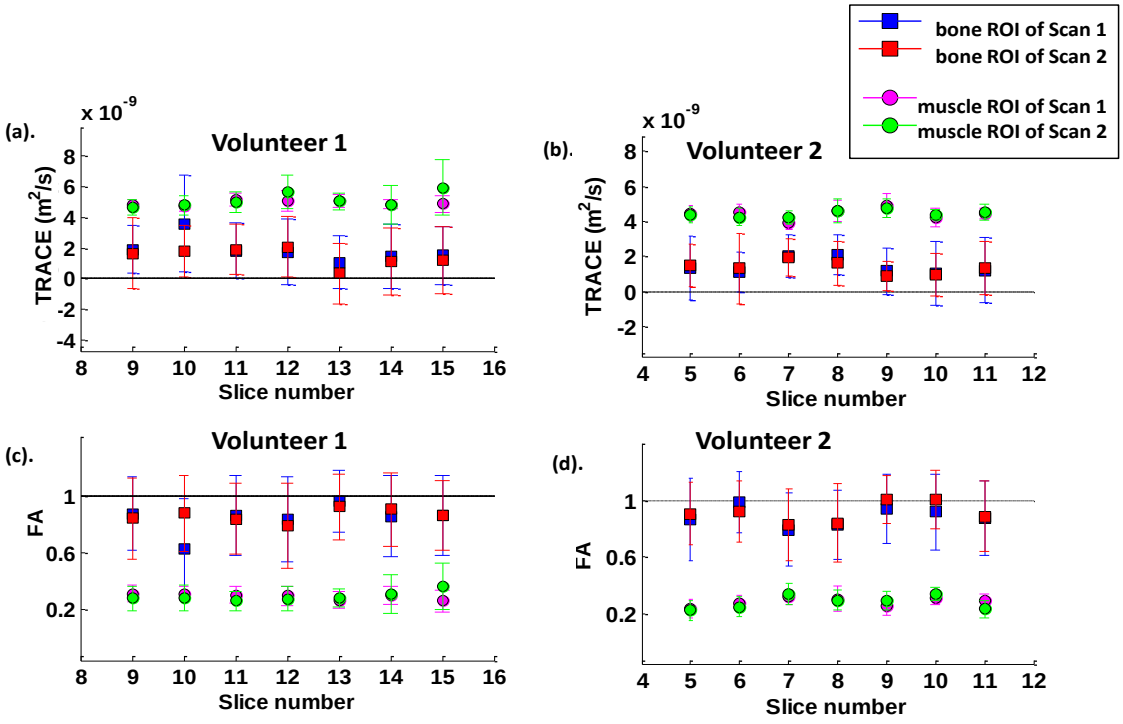

Figure 40. Intra-subject inter-protocol trace (a-b) and FA (c-d) comparison of volunteer 1 (a and c) and volunteer 2 (b and d). The black dash lines in both trace figures indicate the level of trace = 0 (m2/s); the black dash lines in both FA figures indicate the level of FA = 1. The magneta (scan 1) and green (scan 2) nodes and error bars indicate the values of muscle ROIs. The blue (scan 1) and red (scan 2) nodes and error bars indicate the values of bone ROIs.

analysed (1% - 1.97% for volunteer 1 and 1.23% - 2.67% for volunteer 2). About 16% of DA_{PEV} for volunteer 1 is found to be smaller than $\pi/6$, and about 17% for volunteer 2.

7.3 Discussion

In this study, the reproducibility of the previously proposed *in-vivo* red-marrow diffusion tensor imaging on tibia is investigated on three volunteers. This preliminary study involves two sub-reproducibility intra-subject investigations: inter-scan and inter-protocol. For each investigation, two volunteers are involved. Quantitative measurements of each volunteer are compared based on ROIs for the diffusion parameters, FA and trace. The principal eigenvectors are compared angularly on the voxel by voxel basis.

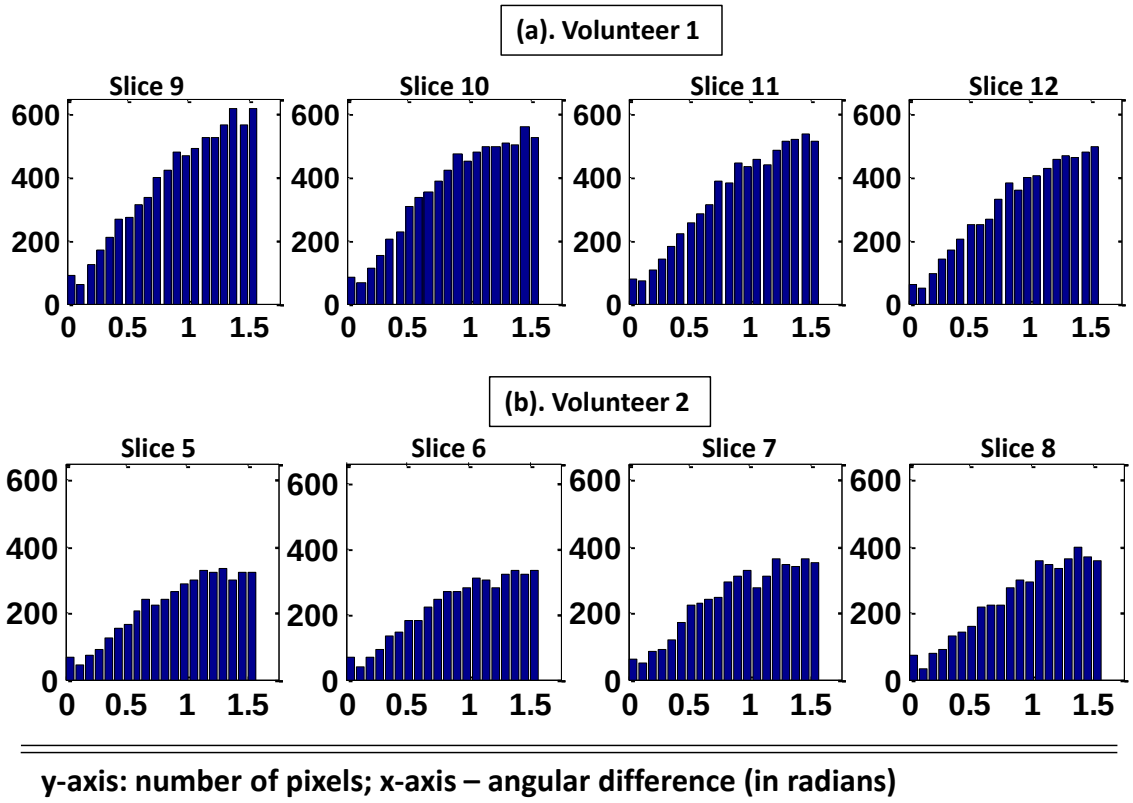

Figure 41. Histogram of the voxel-wise angular difference of the principal eigenvector orientation in the intra-subject inter-protocol study (slices from the tibia bone) of volunteer 1(a) and volunteer 2(b).

According to the current analysis results in both observations, the previously proposed protocol may be able to give a reliable diffusion measurement on muscles but showed

limited agreements in the bone region for both investigations. In terms of the diffusion parameter measurements (i.e. FA and trace), the encouraging fact is that the mean values show reasonable agreements in the inter-scan study, however, the mean values are less consistent in the inter-protocol study. The standard deviations in the ROI based comparison in the bone region are much bigger in all the bone ROI regions than that of the muscle ROIs. It also needs to be pointed out that after changing the frequency encoding direction from the original R-L (right to left) direction to A-P (anterior to posterior), the geometric distortion caused by the EPI sequence changed as well. This might have been one reason that had led to a less consistent measurement even in the muscle voxels, compared to the scans that used exactly the same protocol. In the voxel-wise angular comparison in the bone region, for all the comparisons, there are a huge percentage of big difference angles, which implies only a small percentage of the reconstructed diffusion tensors (up to 15% in the intra-scan study, about 1% to 3% in the intra-protocol study) can be considered reproducible in all the studied cases.

There may be several effects that cause the big instability in the bone region diffusion measurement. One is the noise: not only due to the low SNR in the red marrow, but also due to the choice of parallel imaging in which the image centre has the lowest SNR with the acceleration factor of 2 [177, 186]. Another source of the noise may be due to the magnetic susceptibility difference between bone and bone marrow. Another effect is that the bone region is a mixture of bone and bone marrow, which have different magnetic properties thus lead to different diffusion behaviour. With the current protocol, bone itself does not contribute any signal to the image intensity, thus should lead to a zero diffusion measurement itself. A third cause is the partial volume effects as the trabecular bone is a tiny structure as previously introduced in Chapter 2. The current resolution is 1.4×1.4 mm^2 in plane with a slice thickness of 3.2 mm which is quite coarse compared to the average trabecular bone thickness. Partial volume effect correction is not considered in the current study. A fourth cause is the motion artefacts. Three types of motion occur during the scan according to our observation: 1) flow artefacts caused by the arteries passing through the imaged volume; 2) the vibration of the patient bed caused by the strong diffusion gradients; 3) the imaged object drifting caused by the gradient heating. The flow artefacts

occasionally entered the bone region which corrupted the images. In our analysis, motion artefact has been greatly reduced by the registration program. In the case of strong vibration, the edges of the object were ghosted in the middle of the image, which is hard to be solved by a post-processing-only method. As the knee is quite fixed inside the used knee joint coil, the rotational motion is less severe than that in brain DTI, in which the brain coil provide a relative bigger space to move. The above motion artefacts together with the susceptibility effects, on the other hand, significantly complicate the task of partial volume correction, especially for the drifting and vibration motion. The above considerations need to be taken into account to improve the protocol in the next step.

Apart from the complicated problem listed above and the currently unreliable measurements, another disadvantage of this technique is that the acquisition time is relatively long: the echo time is relative long as it needs to include the diffusion gradients and enough time for diffusion (around tens of milliseconds), and the TR also needs to be long to wait for the magnetization to be recovered (around 8000 ms). This also obscures the practical application of the spin-echo PGSE experiment *in-vivo* in a clinical environment to achieve high SNR and high resolution. It would be more appreciated if the imaging could provide the tensor orientation in a faster manner with a much higher resolution. Thus SPENT could be a very good candidate for this task as it is another sequence which is sensitive to structure inhomogeneity inside each voxel. It is well-shown [121] that by SPENT, BMD values acquired along different directions were different, with the z-direction (the slice thickness 1mm corresponding to z-direction, in plane resolution 234×234 μm^2 corresponding to x, y-directions) indicating the biggest BMD of all three. Interestingly, there was also a small difference between x-BMD and y-BMD, showing that along y direction, there was more bone than along x direction. This direction specific information could be explained by the function adaptation of bone: the x direction is along the trabecular bone orientation and thus along the direction of the force direction that the femur endures. It thus provides a clue of the possibility of building a tensor by adding three more directions, given the fact that the anisotropic appearance of trabecular bone network organization could be mapped onto an ellipsoid [27, 41] and formulated as a fabric tensor [42, 48]. The work of extending SPENT to derive the orientation information through a

tensor based method will be presented in Chapter 8 and Chapter 9.

7.4 Summary

The reproducibility of the proposed protocol in the feasibility study of DTI in trabecular bone of human tibia was investigated in this chapter. Two sub-investigations are considered: intra-subject inter-scan and intra-subject inter-protocol studies. With the current small subject group, the former study showed reasonable reproducible measurements in terms of the mean values of the diffusion parameters, trace and FA in both muscle and bone ROIs in the slices covering the tibia region, though the standard deviation of bone DTI measurement is big; the latter study are less consistent. The voxel-wise angular comparison on the principal orientation of the diffusion tensor in the bone region showed most of the derived principal orientations were not reproduced in the successive measurements, although a small percentage of voxels (15%) gave reproducible measurements in the datasets of volunteer 3. The possible causes of the poor reliability are analysed. Apart from improving the diffusion sequence itself, an alternative pulse sequence may potentially be helpful for the quantification of the trabecular bone network anisotropy, which will be introduced in the following chapters.

Chapter 8. Multi-directional sub-pixel enhancement of non-uniform tissue (mSPENT): theory and simulation

The recently proposed SPENT sequence can provide direction specific information based on the sub-voxel structural uniformity of a sample [121] with relatively high resolution. Analogous to diffusion tensor imaging, given a voxel with a local anisotropic structure (e.g. trabecular bone), it may be possible to apply SPENT at multiple directions and to build a tensor to characterize the orientation of sub-voxel micro-structure. In this chapter, a generalization of the original SPENT sequence is proposed. It extends the original pulse sequence into a series of arbitrary direction measurements. This modification allows the measurement of structural inhomogeneity in each voxel at various directions in order to map them into an ellipse/ellipsoid model. Thus a structure tensor, alike the fabric tensor in traditional stereology (Section 2.2.3), can be derived. It can be further decomposed into an eigensystem, whose first eigenvectors (associating with the biggest eigenvalues) correspond to the dominant orientation of the underlying tissue micro-architecture contained in the voxel.

The rest of this chapter investigates the multi-directional SPENT technique (mSPENT) regarding the following issues:

1) The voxel-wise tensor system that mSPENT utilizes to analyse the tissue microstructures. Local structural orientation can be derived from the reconstructed structural tensors by eigen decomposition. Mean inhomogeneity, relative anisotropy, and fractional anisotropy of the 2D mSPENT tensor system are defined as the structural indices.
2) The theoretical link between the information content measured by mSPENT and the high frequency region of k-space.
3) The optimal imaging settings, i.e. SNR and number of SPENT gradient directions are studied based on simulated mSPENT data. In this simulation study, two questions are to be answered: what is the minimum SNR required to derive trustable structural parameters; what is an optimal gradient scheme in terms of measuring the structural local orientation.

8.1 Introduction

According to Wolff's law [9], the bone remodels itself along the direction of the forces it endures, which leads to a dominant direction in trabecular bone (TB) micro-structure. This anisotropic appearance can be quantified using a set of direction dependent measurements of the trabeculae distribution. Several commonly-used quantification methods were proposed in stereological analysis, including mean intercept length (MIL), volume orientation (VO), and star volume/line distribution (SVD/SLD) (Figure 4) [47]. In such methods, the basic idea can be understood by considering some phase B contained inside a big sample volume A. While sectioning, if the probability of the sectioning (i.e. testing lines) hitting B at arbitrary directions is the same, the distribution of B would be homogeneous; otherwise, its distribution would be heterogeneous. In case of a heterogeneous distribution, when the B distributes along a certain direction, the probability of intersection at certain direction(s) would be much higher than at other directions, B is said to be anisotropic. In particular, if plotting the measurements of TB volume projected at each direction against the angle of a certain direction in a polar coordinate system, the shape of the distribution can be fitted into an ellipse [41] or an ellipsoid [42]. This 'structural' ellipsoid can be expressed mathematically as a second rank tensor, namely a fabric tensor (as discussed previously in Section 2.2.3). It has been proven both theoretically [48] and experimentally [81, 82] that this fabric tensor is correlated with the elastic properties of TB. Tassanni et al. [187] recently compared four models and showed with mechanical tests that if combined with BMD measurement, it could improve the prediction of TB mechanical competence.

However, it is always challenging to extract the trabecular bone micro-architectural orientation information *in-vivo* due to its small size. Most reported methods (as discussed in Section 2.2.3) depend on the direct visualization of the bone microstructure and thus the resolution of the acquired data becomes a key factor to the efficacy of these methods. The required resolution, as discussed by Wehrli [7], should be around the order of the trabecular bone thickness and is normally difficult to be achieved *in-vivo*. This resolution penalty makes the models proposed in the biomechanics community to assess the mechanical

competence of TB not easy to be directly applied *in-vivo*. However, an *in-vivo* anisotropy measurement would be more than welcome as the fine scale structural information of trabecular bone is very limited in clinical applications such as osteoporosis, and the current clinical standard, BMD measured by DEXA, is lacking for specificity and sensitivity. The diffusion of bone marrow might be one way to address the derivation of trabecular bone orientation. While the utilization of the bone marrow relaxometry ($1/T_2^*$) is still under investigation, the recently proposed SPENT sequence [121] might be a surrogate due to its ability to measure BVF and its sensitivity to the spin density distribution measurement within each voxel.

The principle of SPENT might be better understood by looking at the magnetization distribution (Figure 42). Different levels of magnetization distribution inside one voxel can be recognized when 'looking' at it with different resolution and at different directions. There are two main factors to describe the distribution of the spins: the overall density of the spins (or the net magnetization) and how they distribute. For example, in both Figure 42(a) and (e), the spins distribute uniformly but the overall spin density in each case is clearly different; while in Figure 42(b) and (e) the net magnetization is the same but the distribution are very different. Also in Figure 42(b), at the vertical direction the spin distribution is homogeneous while at the horizontal direction, a significant inhomogeneity can be recognized.

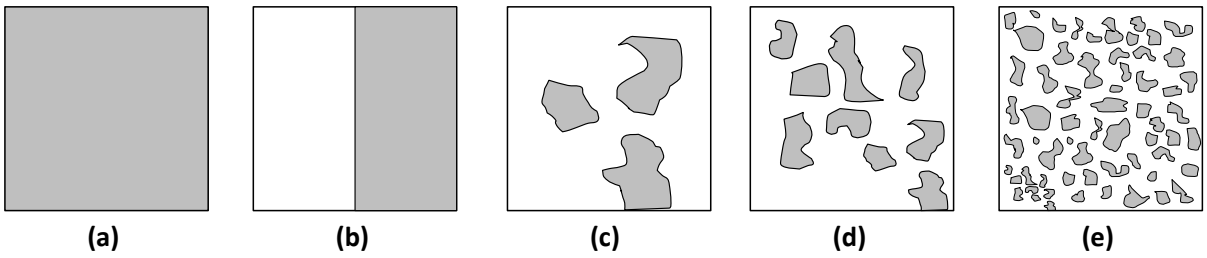

Figure 42. Different levels of magnetization distribution inside one pixel: (a) a homogeneous 2D pixel that contains a uniform magnetization distribution and no structure; (b) a pixel containing a distribution of magnetization that is completely uniform in the vertical direction, but is highly non-uniform in the horizontal direction; (c) if zooming out but keeping the pixel size around the order of the structure size, the magnetization distribution is still non-uniform but appears a different orientation compared to (b) ; (d) while zooming out a bit more, the inhomogeneity is less obvious but can still be recognized; (e) in the end, the magnetization distribution is homogeneous although the pixel contains many small structures.

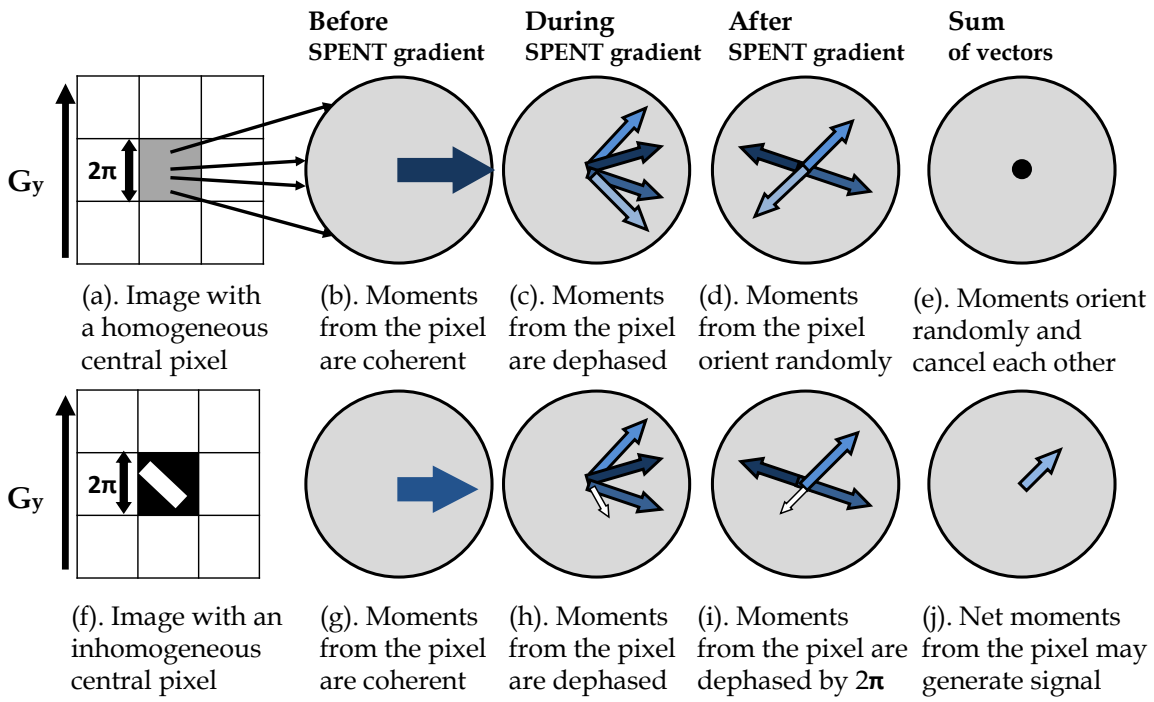

Figure 43. Illustration of the principle of SPENT. In the case of a homogeneous central pixel (a), the magnetic moments (spins) are synchronized before the SPENT gradient, $\vec{G}_{SPENT}$ is applied (b). The coherence is lost after adding $\vec{G}_{SPENT}$ and the spins start to dephase (c). In the end, under the function of $\vec{G}_{SPENT}$, the spins completely lose their coherence and orient randomly (d). Thus the vector sum of the magnetization is zero (shown as a black dot). For an inhomogeneous central pixel with a signal void rectangle region coloured white (f), before $\vec{G}_{SPENT}$ is added, spins inside the pixel are also coherent (g) but the net magnetization is smaller than those in (b). With $\vec{G}_{SPENT}$ the spins start to dephase (h) and orient randomly (i) as in (d). However, due to the spatial inhomogeneity, the vector sum may be nonzero thus could lead to a MR signal.

To make signal intensity sensitive to spin distribution inside a voxel of an image, SPENT adds an extra gradient (namely SPENT gradient, $\vec{G}_{SPENT}$) to the traditional spin echo sequence, which leads to a 2π phase dispersion across each voxel. This 2π dephase has a different impact on a uniform voxel and an inhomogeneous voxel. A qualitative description of the progression of the transverse magnetization within either voxel is illustrated in Figure 43. Recalling the spin echo sequences, after the 180° refocusing r.f. pulse, the spins are synchronized so the magnetization in each voxel (Figure 43(a, f)) is the summation of

all the spins (Figure 43(b, g)). When the SPENT gradient is applied, the spins would lose their coherence (Figure 43(c, h)) and start to dephase (i.e. fan out). In this case, if a voxel is spatially homogeneous (Figure 43(a)), at the end of the 2π dephasing, the vector sum of the spins would cancel each other, leading to a nulled net magnetization (Figure 43(d, e)); on the contrary if a voxel is spatially inhomogeneous (Figure 43(f)), the distribution of the spins cannot be isotropic either (Figure 43(i)). Thus there would be a net magnetization residual in this voxel (Figure 43(j)). Therefore, only the nonuniform voxels are visible.

This direction dependent feature of SPENT technique motivated our idea to exploit it to derive the orientation parameter for quantifying the structural information. The way that SPENT technique manipulates the spin system in each voxel is as if a sample point is uniformly distributed on a lattice and the spatially varying gradients are the probes to project the spin density related to structure information at the corresponding direction. The aforementioned approaches (e.g. MIL and SVD) in stereology exploit testing lines or sample points to project the distribution of the object of interest along a certain direction. Therefore, if SPENT measurements were applied at sufficient directions around the object, it would be possible to map the measurements to an ellipse model in 2D or an ellipsoid model in 3D, which leads to a tensor expression. The orientation of this tensor represents the dominant tissue distribution, thus relates to the orientation of the underlying tissue. The orientation information of TB, combined with bone density which can also be quantified using SPENT [121], may lead to a model which provides an improved prediction of bone fracture risk as demonstrated in [80, 187].

In this work, a 2D multi-directional SPENT series is designed to apply SPENT at arbitrary directions (Section 8.2.1 and Section 8.2.2). The tensor based analysis method to derive orientation information is introduced (Section 8.2.3). The theory of dephasing behind mSPENT is discussed (Section 8.3.1) and a mSPENT simulator is developed. In the end, a simulation study is performed to demonstrate the efficacy of mSPENT regarding its measurement on structure inhomogeneity and the optimal imaging parameters to extract TB-related structural information (Section 8.3.2 and 8.3.3).

8.2 Theory of multi-directional SPENT (mSPENT)

This section addresses the principle ideas of mSPENT: the tensor model it exploits; the 2D modified mSPENT pulse sequence; the quantitative tensor analysis by looking at the decomposed eigen systems. The tensor reconstruction and analysis have been programmed into a homemade software, SPENT toolkit programmed in MATLAB (see Appendix B).

8.2.1 The structure tensor, T

The ellipse model of TB orientation discovered by Whitehouse [41] can be written as:

$$T_{11}x^2 + T_{22}y^2 + 2\,T_{12}xy = S \qquad \text{eq. 47,}$$

where S is the amount of the objects of interest inside a sample at a given direction. This can be quantified in many ways, such as MIL and SVD. (x, y, z) indicates the orientation of each measurement[10]. By reformulating eq. 47 into the quadratic form as eq. 48, a second rank tensor **T** (definite symmetric tensor) can be recognized.

$$S = \vec{a}_i{}^T \mathbf{T} \vec{a}_i \text{ , with } \boldsymbol{T} = \begin{bmatrix} T_{11} & T_{12} \\ T_{21} & T_{22} \end{bmatrix}, \text{ and } T_{21} = T_{12} \qquad \text{eq. 48}$$

Therefore as the linear system to compute the diffusion tensor, the above quadratic form can also be simplified into a linear system: $aT = S$.

As in stereological analysis, the actual net magnetisation orientation inside each voxel is perpendicular to the direction of the structure. This is because the unbalanced spins inside each voxel are mainly in the direction perpendicular to the signal void region (Figure 43(f-j)).

Analogous to the gradient direction encoding matrix in DTI (eq. 39), in SPENT we define an encoding matrix, A_{SPENT}, in a similar way. The direction of each SPENT gradient is defined as a unit vector $\vec{a}_i$: in 2D, $\vec{a}_i := (x_i, y_i)$, and ϑ is the angle of the gradient direction (defined in eq. 52). Therefore, A_{SPENT} matrix can be expressed as eq. 49 in 2D:

[10] In this chapter, the symbols (x, y, z) are used to represent the axis of the imaging volume.

$$A_{SPENT} \coloneqq \begin{bmatrix} x_1^2 & y_1^2 & 2x_1y_1 \\ \vdots & \vdots & \vdots \\ x_N^2 & y_N^2 & 2x_Ny_N \end{bmatrix} \quad \text{eq. 49}$$

Therefore, to reconstruct a SPENT tensor **T** and to extract the sub-voxel tissue orientation, the existing SPENT sequence needs to be modified in order that the structural information can be measured at any angle.

8.2.2 The mSPENT pulse sequence

According to Siow et al. [188], in order to create a 2π phase dispersion across a voxel, the strength of a SPENT gradient, G_{SPENT} needs to meet the requirement of eq. 50 :

$$G_{SPENT} = \frac{2\pi}{\gamma t_{SPENT} \Delta r} \quad \text{eq. 50,}$$

where γ is the gyromagnetic ratio, t_{SPENT} is the time duration that $\left|\vec{G}_{SPENT}\right|$ is applied and Δr is the pixel dimension.

To create an arbitrary direction SPENT gradient, we decompose the overall SPENT gradient into two orthogonal SPENT gradients, which corresponds to the SPENT gradients applied in frequency ($\vec{G}_{SPENTx}$) and phase ($\vec{G}_{SPENTy}$) encoding directions. Hence, a mSPENT gradient with an arbitrary orientation is achieved by applying extra gradients on the frequency and phase directions simultaneously but with different weightings in the relationship specified by eq. 51.

$$G_{SPENT} = \sqrt{G_{SPENTx}^2 + G_{SPENTy}^2} \quad \text{eq. 51}$$

The direction of the overall SPENT gradient is then determined by eq. 52.

$$\vartheta = arctan\left(\frac{G_{SPENTy}}{G_{SPENTx}}\right), \qquad \vartheta\epsilon[-\pi, \pi] \quad \text{eq. 52}$$

Figure 44 illustrates the sequence graph of mSPENT in 2D at one direction. To be able to construct a tensor, several mSPENT acquisitions at different directions are needed as in diffusion tensor imaging.

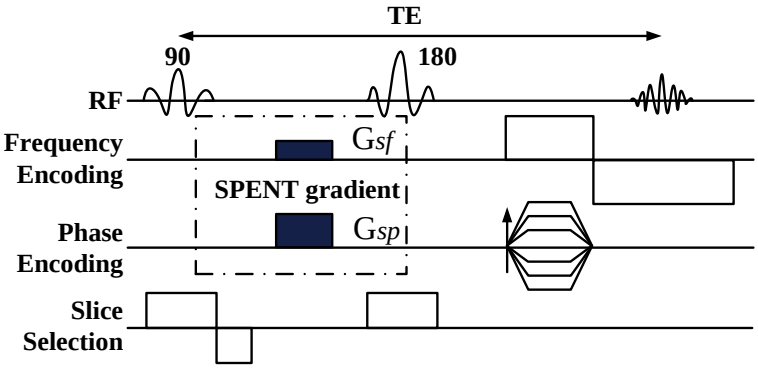

Figure 44. The 2D mSPENT sequence graph at one direction, G_{sf} and G_{sp} correspond to $\vec{G}_{SPENTx}$ and $\vec{G}_{SPENTy}$ respectively.

8.2.3 Extracting of structural features from SPENT tensor

The structure tensor T at each voxel can be reconstructed using a linear regression algorithm to solve the linear system of $aT = S$ as used in DTI. It needs to be pointed out that the right-hand side of this system is the inhomogeneity measurement S which in practice is a normalized quantity calculated by $S = S_{mSPENT\_i}/S_{SPENT0}$ (as used in [121]), where S_{mSPENT_i} is the signal from the *i*th mSPENT acquisition, and S_{SPENT0} corresponds to the non-inhomogeneity-weighted measurement (namely $SPENT_0$, acquired using the same mSPENT sequence and the same imaging parameters with the SPENT gradients off). Prior to the normalization, a background threshold needs to be set to mask out background noise.

Apart from the voxel-wise structural orientation indicated by the principal eigenvectors, other quantitative metrics as used in DTI (Section 6.1.4) can also be proposed here to characterize the tissue microstructure with the mSPENT data. In the quantitative 2D SPENT tensor analysis, the mean inhomogeneity (MI) is defined as the average of the isotropic part of the structure tensor T and is computed as:

$$\mathrm{MI(T)} = \frac{\mathrm{T_{xx}} + \mathrm{T_{yy}}}{2} = \frac{\lambda_1 + \lambda_2}{2} \qquad \text{eq. 53,}$$

where $\mathrm{T_{xx}}$ and T_{yy} are the diagonal elements of the SPENT tensor, T, and λ_1 and λ_2 are the eigenvalues of T, $\lambda_1 > \lambda_2$.

The relative anisotropy can be calculated as the ratio between the standard deviation of the eigenvalues ($SD(\lambda_i)$) and the mean eigenvalues ($\bar{\lambda}$) (eq. 54):

$$RA(T) = \frac{SD(\lambda_i)}{\bar{\lambda}} = \sqrt{2} \cdot \frac{\sqrt{(\lambda_1 - \bar{\lambda})^2 + (\lambda_2 - \bar{\lambda})^2}}{(\lambda_1 + \lambda_2)} \quad \text{eq. 54,}$$

where λ_i is the eigenvalues and $\bar{\lambda}$ is the mean eigenvalue ($\bar{\lambda} = 1/n \sum_{i=1}^{N} \lambda_i$). The fractional anisotropy (FA) is calculated as eq. 55 to measure the fraction of the "magnitude" of the tensor T. As used in DTI, FA of the tensor T ascribes the anisotropic micro-architecture of each voxel.

$$FA(T) = \sqrt{2} \cdot \frac{\sqrt{\left[(\lambda_1 - \bar{\lambda})^2 + (\lambda_2 - \bar{\lambda})^2\right]}}{\sqrt{({\lambda_1}^2 + {\lambda_2}^2)}} \quad \text{eq. 55,}$$

The above three metrics are all quantitative and dimensionless, and also independent of the position and orientation of the laboratory coordinate system as being solely functions of eigenvalues of the tensor system. It needs to point out that the mean inhomogeneity is also a scalar value in the tensor analysis of mSPENT, which is different from the mean diffusivity measurement in DTI. This is because the SPENT tensor is to model the tissue volume distribution inside a voxel which is a scalar itself. The orientation angle (φ, eq. 56) is also defined as the angle between with the principal eigenvector e_1 (e_{1x}, e_{1y}) and the x axis of the image coordinates.

$$\varphi = \arctan(e_{1y}/e_{1x}), \varphi \in [-\pi/2, \pi/2] \quad \text{eq. 56}$$

8.3 Simulation study

8.3.1 mSPENT and dephased MR: a theoretical analysis

The 2π phase wrap created by the SPENT gradient ($\vec{G}_{SPENT}$) can be considered as adding an extra phase accumulation ($\Phi_{SPENT} = 2\pi$, according to eq. 20) to the original phase accumulation at the transverse magnetization plane in SE sequence. The overall phase accumulation is expressed as $\boldsymbol{\Phi} = \Phi_1 + \Phi_{SPENT}$. Therefore, in the corresponding Cartesian k-space, this extra phase shifts the sampling position from the original k-space location (i.e.

(k_x, k_y) the location without the SPENT gradient) by δk (δk_x, δk_y), which leads to a new k-space location, *k*' (eq. 57).

$$k'_x = k_x + \delta k_x \ , k'_y = k_y + \delta k_y, \left(|\delta k| = \sqrt{\delta k_x{}^2 + \delta k_y{}^2}\right) \quad \text{eq. 57}$$

Therefore the signal equation (eq. 58) of mSPENT at a time ***t*** can be derived according to eq. 24:

$$\begin{aligned} S_{SPENT}(k'_x, k'_y, t) &= \iint \rho(x,y,t)\, exp\left(-i2\pi\left(k'_x x + k'_y y\right)\right) dxdy \ \text{(combine with eq. 57)} \\ &= \iint \rho(x,y,t)\, exp\left(-i2\pi\left(k_x x + k_y y\right)\right) exp\left(-i2\pi\left(\delta k_x x + \delta k_y y\right)\right) dxdy \end{aligned} \quad \text{eq. 58,}$$

In eq. 58, the first exponential term $exp\left(-i2\pi\left(k_x x + k_y y\right)\right)$ results from the normal phase ($\vec{G}_y$) and frequency ($\vec{G}_x$) encoding gradients and corresponds to a k-space ($\kappa_{SPENT\,0}$) of the conventional SE sequence (the $SPENT_0$ image). Now consider the iso-centre of this k-space k_0 (O in Figure 45), with $\vec{G}_{\text{SPENT}}$ (according to eq. 23), k_0 is moved by δk to k'_0 (O' in Figure 45) which is the resulting mSPENT k-space (κ_{SPENT}, pink boxed region in Figure 45) centre. The distance between k_0 and k'_0 is $|\delta k|$ (eq. 57, $\left|\overrightarrow{OO'}\right|$ in Figure 45). Although the k-space centre is shifted, the FoV ($L_x \times L_y$) and the sampling stepsize (Δk ($\Delta k_x, \Delta k_y$), determined by $\vec{G}_x$ and $\vec{G}_y$) and the total number of the k-space samples ($N_x \times N_y$) in the SPENT k-space (κ_{SPENT}) is not changed. This implies that mSPENT acquires the information from the outer space of κ_{SE} and leads to a bigger k-space coverage. The trajectory of mSPENT centre O' is therefore a circle as defined by eq. 57, with its iso-centre as O and its radius as δk (the circle coloured in cyan in Figure 45). Therefore the extreme shifts caused by the SPENT gradients occur when the SPENT gradients are applied on the frequency or phase encoding direction.

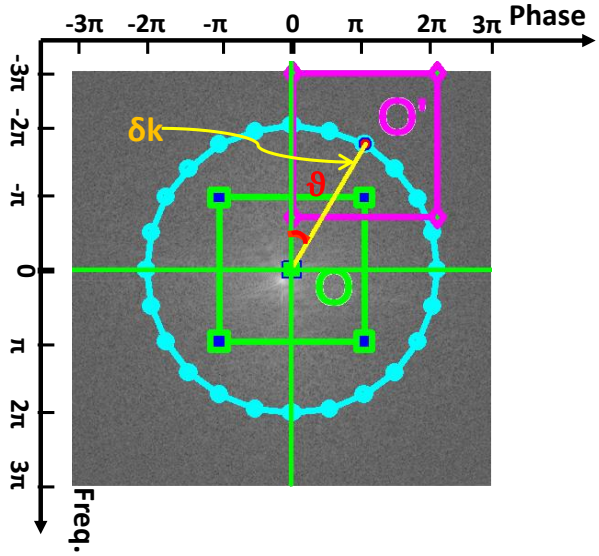

Figure 45. k-space illustration of mSPENT simulation: O is the centre of the $SPENT_0$ k-space (κ_{SE}, region boxed in green). O' is the centre of the mSPENT k-space (κ_{mSPENT}) at the direction of $\overrightarrow{OO'}$ whose orientation is defined by ϑ (eq. 52). The cyan coloured circle is the trajectory of the κ_{SPENT} centre, where the nodes on the circle corresponds to an O' of a mSPENT acquisition with the SPENT gradient oriented with ϑ. The radius of the circle is equal to δk in eq. 57.

In mSPENT, the maximum phase shift created by $\vec{G}_x$ and $\vec{G}_y$ is set to be 2π. With the addition of the 2π wrap created by $\vec{G}_{\mathrm{SPENT}}$, the maximum phase shift against the centre of κ_{SE} is 3π along both the frequency and phase encoding directions to both sides of the iso-centre O of κ_{SE}(Figure 45). Consequently, with a full-circle mSPENT acquisition, the total maximum phase shift is 6π along one encoding direction, leading to an increase of the actual k-space by three. According to the relationship between the image resolution and k-space sampling in eq. 26 and eq. 27, both Δk and FoV is not changed by $\vec{G}_{\mathrm{SPENT}}$, the increase of k-space coverage (i.e. with more sampling points, $N_{hr\_x} \times N_{hr\_y} = (3N_x) \times (3N_y)$) leads to a resolution increase with the factor of 3 at both voxel dimension: $\Delta x_{hr} \times \Delta y_{hr} = (\Delta x/3) \times (\Delta y/3)$, in which $\Delta x \times \Delta y$ is the resolution of $SPENT_0$ and $\Delta x_{hr} \times \Delta y_{hr}$ is the resulting resolution. Therefore, for each mSPENT acquisition, the sampled k-space frequencies correspond to one high frequency region of the k-space (κ_{hr}) of an image whose resolution is three times than that of the one acquired with the same imaging parameters using a SE sequence, namely the $SPENT_0$ acquisition. The centre of this high resolution k-space is overlapped with k_0 (k_{0x}, k_{0y}). The matrix size of the high frequency region in κ_{hr} is equal to that of $\kappa_{SPENT\,0}$, and the centre is thus k'_0 (k'_{0x}, k'_{0y}) and can be calculated by combining eq. 52 and eq. 57:

$$k'_{0x} = k_{0x} + |\delta k| \cdot cos\vartheta, \qquad k'_{0y} = k_{0y} + |\delta k| \cdot sin\vartheta \qquad \text{eq. 59}$$

In eq. 59, the angle ϑ is the angle between the frequency encoding direction and the SPENT gradient direction, in order to make the simulator compile with the definition on the scanner.

According to the above explanation, mSPENT may be also viewed as an extension of the dephased MRI whose theoretical framework has been discussed by Bakkers et al. [189]. This framework indicates that the insertion of additional gradients leads to a shift (an off-centre reconstruction window) in the original k-space which is provided by a more widely (with a higher spatial frequency) and densely (a wider FoV) sampled k-space.

8.3.2 mSPENT simulator

According to the previous analysis, the mSPENT simulation can be realized by applying a group of square reconstruction windows, $w_i(k'_0, \delta k, \vartheta)$, to the high-resolution k-space data $\boldsymbol{S}$ sequentially as illustrated in Figure 46, where $\boldsymbol{\mathcal{F}^1}$ is the inverse Fourier transform. The matrix size of $\boldsymbol{S}$ is $N_{hr\_x} \times N_{hr\_y}$. Its iso-centre is k_0, corresponding to the point O in Figure 45. The window size (δk, as in Figure 46) is constant and needs to meet the following criterion: $\delta k \leq \min(N_{hr\_x}, N_{hr\_y})/3$. The resolution of the generated mSPENT dataset is determined by δk (as the k-space step size Δk is not changed, Section 8.3.1). The parameter $\vartheta = \{\vartheta_i, i = 1 \cdots N\}$, ($\vartheta \epsilon [0, 2\pi]$) is to model the orientation of the SPENT gradient. The centre of the reconstruction window corresponds to the actual mSPENT k-space centre, i.e. O' in Figure 45, and can be calculated from δk and ϑ, using eq. 59. The $SPENT_0$ acquisition is a special case and obtained by applying a reconstruction window at k_0 with the size of δk. Optionally, Rician noise can be added to each mSPENT k-space acquisition (including the $SPENT_0$) separately to simulate the independent noise of mSPENT acquisition at each direction. The SNR of the mSPENT acquisition is calculated as the SNR of $SPENT_0$. The mSPENT simulator is programmed with MATLAB (R2008a, The Mathworks, Natick, MA). This simulator is programmed to produce the simulated 3D mSPENT datasets, which would be used in the simulation study in Section 9.4.2.

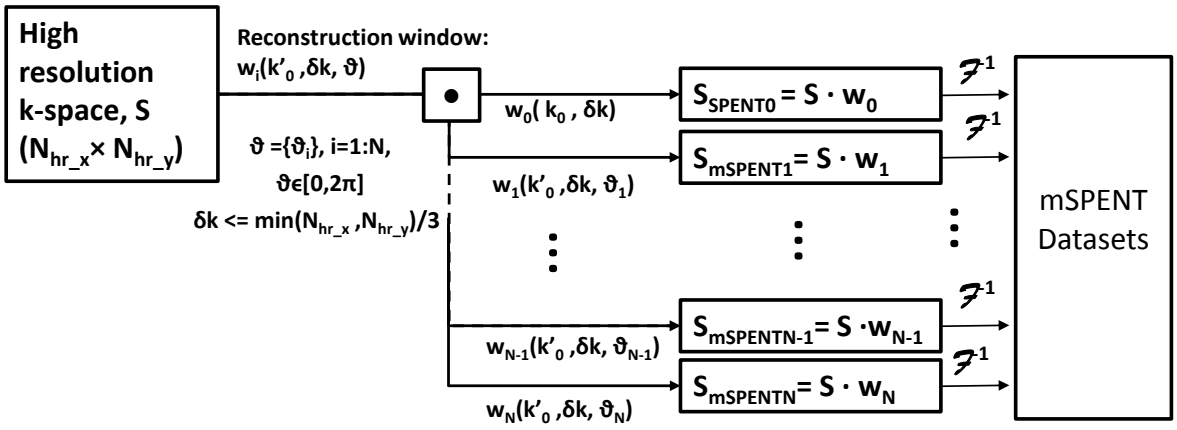

Figure 46. A sketch of the mSPENT simulator

The simulation was run 1) to show the efficacy of mSPENT in terms of acquiring directional information using both the digital phantom and the real k-space data; 2). the SNR requirements needed for mSPENT by adding different noise levels with the imaging parameters; 3) to investigate the number of directions that are required to reconstruct the tensors by varying the number of gradient direction.

8.3.3 Digital phantom and simulation

To achieve the above objectives, a plate model of bone with a known dominant orientation (φ) and BVF (Phantom 1) was first created. Phantom 1 (Figure47(a)) is constructed in the following steps as proposed in [121] to simulate the k-space signal in mSPENT acquisitions: 1) In order to simulate the continuous signal produced by an object, a large image matrix was created at very high resolution within a large FoV, in the centre of which an object (the plate model of bone) was placed. The edge of the central "bone" is smoothed by a Gaussian filter to avoid Gibbs ringing artefacts. 2) The image matrix is then Fourier transformed to retrieve the "ultra-high"[11] resolution k-space data. 3) This k-space data is then sub-sampled both in area (to simulate the signal truncation) and in sampling density (to simulate the discrete sampling procedure). The resulting k-space is the input of the mSPENT simulator. The plate bone model was created with the following parameters, bone

[11] Here, the term "ultra-high" resolution is used to distinguish it from the high-resolution k-space data which corresponds to the input of the mSPENT simulator as explained early in Section 8.3.

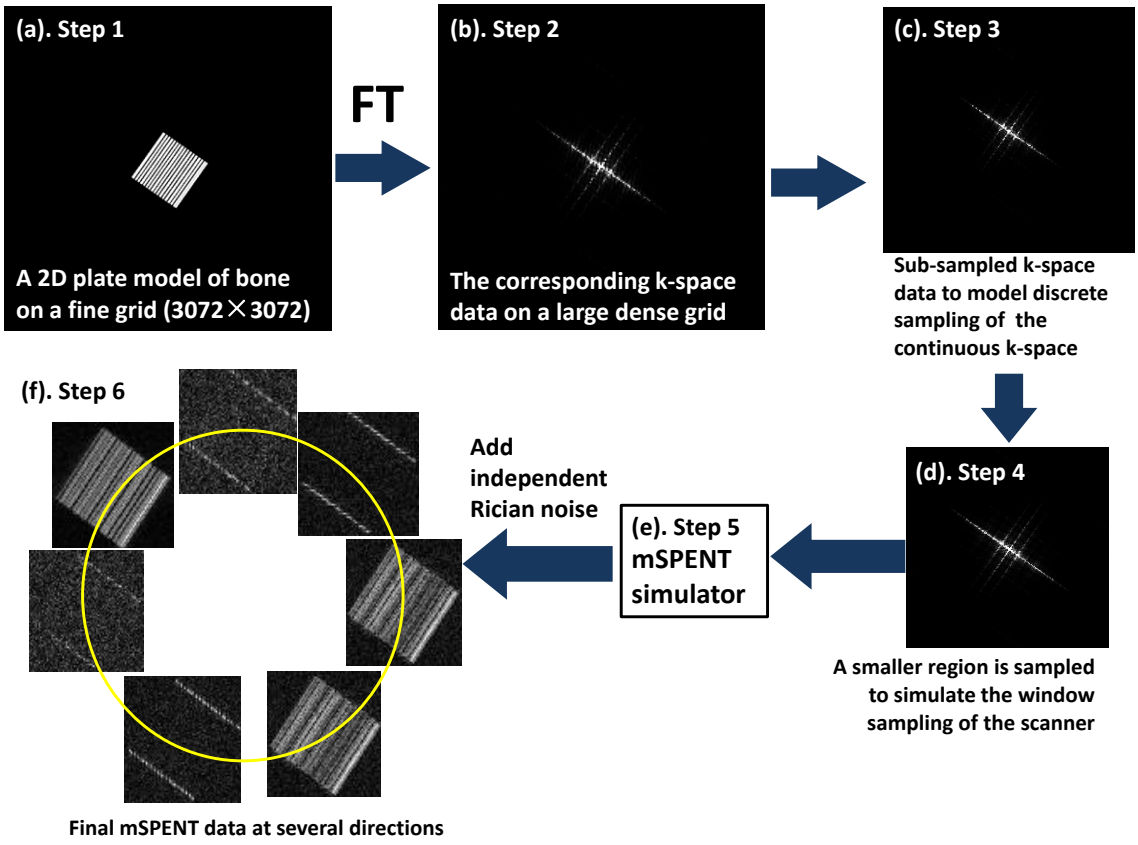

Figure 47. Procedure of mSPENT data generation for the simulation study. (a) Step 1: a large matrix with a bone phantom in the centre is created to simulate a large FoV; (b) Step 2: the k-space of the FoV is created by Fourier transform (FT) of (a) to simulate a pseudo "continuous" k-space; (c). The k-space in (b) is sub-sampled to simulate the discrete sampling procedure of the scanner; (d). Step 4. a smaller region of the k-space data in (c) is kept to simulate the finite sampling of the scanner; (e). The truncated k-space data is input into the mSPENT simulator (Figure 46) both the imaginary and real parts of the data are kept; (f) Rician noise is added to each of the complex mSPENT data matrix created at Step 5 separately, then the magnitude of the complex data is kept which is the final mSPENT data at with the desired SNR level.

volume fraction (BVF) = 41.41%, dominant orientation $\Phi = 55°$ (the angle between the bone strips and the x-axis of the image), bone sample matrix size 512×512, base object FoV 76.8 *mm*, base object matrix size 3072×3072, trabecula thickness 100-350 μm, trabecula separation (pore size) 400-600 μm. The resolution is set to be 100×100 μm^2, on the order of the bone size. The gradient scheme of 64 directions (uniformly distributed on a circle) was used in order to sufficiently sample the outer k-space.

Simulation 1: efficacy of mSPENT and the minimum SNR requirement

In the first experiment, the SNR requirement of mSPENT imaging is examined by generating simulated mSPENT datasets of various SNR (between 1 and 100). Simulated Rician noise (whose distribution is as shown in Figure 26) is added to achieve various noise levels. The amount of added noise is controlled by the SNR in the $SPENT_0$ image, which is determined by eq. 60.

$$SNR = \frac{mean(signals)}{SD(noise)} \qquad \text{eq. 60}$$

In eq. 60, $mean(signals)$ is the mean value of the signals, calculated from the noiseless $SPENT_0$ image; $SD(noise)$is the standard deviation of the to-be-added noise. Given a SNR value, the SD of the noise can be known. Thus the simulated noise can be generated using the method exploited in Section 6.3.3: $noise = SD(noise)*(Re_{noise} + i*Im_{noise})$, where Re_{noise} and Im_{noise} are the real and imaginary parts of the image space signal and generated separately by *randn* in MATLAB to produce pseudo random numbers with Gaussian distribution. The same amount of noise (with the same SD) is then added to the image space data of each noiseless mSPENT image generated by the mSPENT simulator, leading to a complex data matrix. The magnitude of the complex matrix is kept in order to simulate Rician noise. In order to simulate independent noise as in real MR acquisition, for each mSPENT image, Rician noise is added separately.

A gradient scheme with 64 directions was used to generate the mSPENT data in order to make sure the high-frequency region in k-space was sufficiently sampled. For each SNR level, the SPENT tensor was reconstructed and decomposed to retrieve the dominant orientation (i.e. the direction of the principal eigenvector). This orientation is compared to an orientation template (the ground truth). As mSPENT is to measure the inhomogeneity within a pixel/voxel, an anisotropy mask is also created and applied to reject the pixels containing equal ($\lambda_1 = \lambda_2$) or too small first eigenvalues. Pixel-wise comparison was made between the principal eigenvectors (PEV) of the reconstructed SPENT tensor and the created template. The extracted orientation error (between 0° and 90°) at each pixel is considered to be the angular difference between the two vectors using eq. 46. The average

orientation errors of all pixels are calculated at all the observed SNR levels. In total, 17 different SNR levels are considered, ranging from 1 to 100. The average orientation errors are plotted against the SNR levels and shown in Figure 48. It is clearly shown that with the increasing SNR level, the extracted orientation error is decreasing. This decreasing slope is steepest when SNR changes from 1 to 5, leading to the mean errors decrease from 6° to 3.5° at an average speed of 0.8° per SNR level increase. From SNR = 6, the averaged error decreases more slowly and the averaged errors are below 3°. From SNR = 6 to SNR = 10, the error decreases for just 1°.

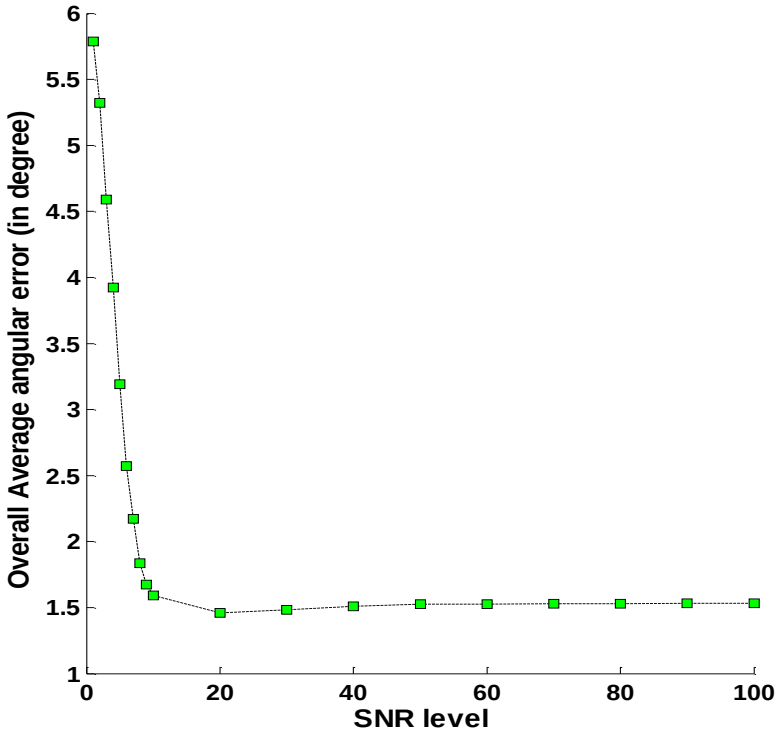

Figure 48. Plot of overall averaged extracted angular error (in degree, y-axis) against the SNR levels (x-axis). The observed SNR levels are from 1 to 10 with interval 1, from 10 to 100 within interval 10.

Simulation 2: the number of gradient direction requirement

In the second experiment, mSPENT data were generated with 25 different gradient schemes (with SPENT gradient number from 4 to 100, with an interval of 4) and 11 levels of SNR (from 5 to 100) in order to observe an optimal settings for the gradient scheme and a SNR

level for 2D mSPENT acquisition. Parameters of Phantom 1 are set to be the same as those in the first simulation. The number of SPENT gradient directions is varied from 3 to 100 (with an interval of 4). The resulting orientation angles from each datasets were compared in a similar way as explained in Simulation 2. The mean of the overall orientation error are plotted against the number of applied SPENT gradients at each SNR level in Figure 49. It can be seen that the mean extracted orientation error is below 2° (± 4.04°) with 7 gradient directions from SNR = 20. For the lower SNR measurements, the mean error is below 2.5° (± 6.67°) with 15 gradient directions at SNR = 10, while at SNR = 5 the mean error is below 4.5° (±10.51°).

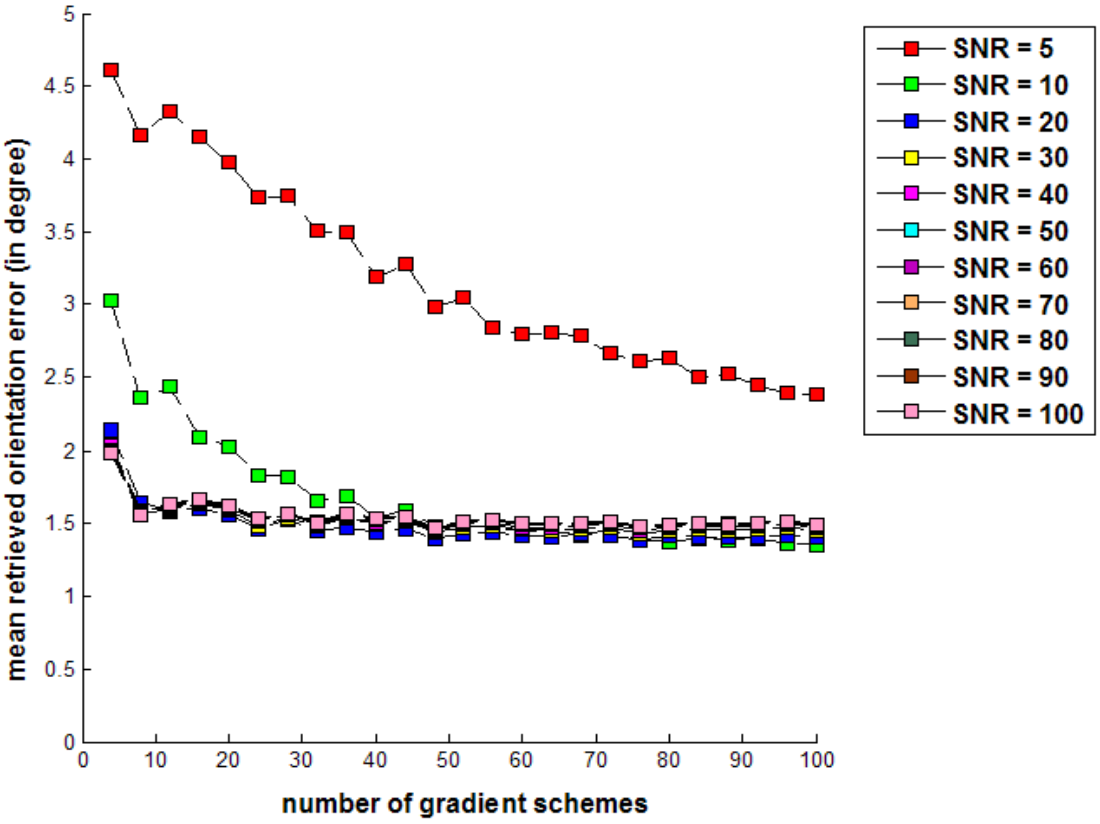

Figure 49. Plot of average extracted orientation errors against different gradient encoding schemes at various SNR levels. The x-axis is the number of applied SPENT gradient directions. The y-axis is the mean retrieved orientation errors (in degree) at each virtual mSPENT acquisition.

8.4 Discussion

The proposed 2D mSPENT sequence modified the existing SPENT sequence in order to measure inhomogeneity at arbitrary directions. It aims to extract meaningful anisotropy indices to assess the tissue microstructure locally and to compensate the global BVF measurement to improve the evaluation of trabecular bone mechanical competence [187]. The generalization is achieved by adding the extra gradients ($\vec{G}_{SPENTx}$ and $\vec{G}_{SPENTy}$) on phase and frequency encoding directions simultaneously instead of placing one SPENT gradient on either direction. The two gradients can be combined orthogonally so that the gradient strength is exactly the same as that of the previous SPENT gradient. The gradient orientation angle is resolved by the ratio between the gradient strength of the two. The dephasing effect caused by mSPENT has been further discussed theoretically. mSPENT leads to a larger k-space coverage whose area is nine times that of SPENT (i.e. 3 times along each direction). The inhomogeneity information it measures is conceptually equivalent to applying a reconstruction window on a high resolution k-space. Based on this, a mSPENT simulator is developed to investigate the efficacy of revealing structure inhomogeneity. The multiple-direction information is assembled through a tensor-based method, analogous to that is used in DTI. The resulting tensor is a structural tensor localized in each voxel. Local anisotropy parameters are quantified: the mean inhomogeneity (MI), fractional anisotropy (FA) and relative anisotropy (RA) and the local orientation angle through the eigensystem of this tensor. These local parameters borrowed from DTI data analysis could be potentially helpful to define locally anisotropy indices. Compared to the conventional stereological methods such as MIL, VO and SVD, the SPENT tensor has an advantage of localizing the tissue properties to the basic element at the microstructure level, and thus bridges the scales between tissue level and the TB network level.

Dephasing is an important concept in MR techniques. The primary use of dephasing is to spatially encode the signals emitted from the spins inside the underlying tissues which make the reconstruction of spin density by inverse Fourier transformation possible. Besides this, other dephasing gradients are also developed to achieve different types of image

contrast to highlight the tissues which originally hide among others and are not obvious enough to be noticed. The projection dephaser is such an example (Section 10.6, pp 357-361, [112]). Barker et al. systematically discussed about the dephased MR technique, with a focus on the projection dephaser sequence [189]. In their discussion, they demonstrated that the application of the dephasing gradient was conceptually equivalent to applying an off-centre reconstruction window in the original k-space (without the dephasing gradient) that was sampled more densely and widely. At this point, it is somewhat similar to the principle of mSPENT. However, they focused on establishing the idea of using an oversampled k-space to study the behaviour of the existing dephaser gradients systematically, in particular the twister gradients (i.e. projection dephaser gradients used in MR angiography, by Dixon et al. [190]), which acts to attenuate signals from larger structures but keeping signals from the smaller features relatively unaffected. Although the paper generally talked about all the possible features regarding dephasing, they did not explicitly explain how to utilize the dephasing inferred information quantitatively. Instead, they considered that further development of dephased MRI was more a matter of well-considered experiment and simulation. From this point, mSPENT might be considered as a "well-designed" experiment of dephasing technique aiming to provide novel quantitative tissue contrast.

The simulation study demonstrates the effectiveness of mSPENT to provide a voxel-wise localised structural orientation measurement based on the inhomogeneity level within the voxel. According to the simulation results, an SNR of $SPENT_0 \geq 20$ is needed to derive a pixel-wise orientation measurement with a minimum 8 SPENT gradients to achieve an error within 6° (2°±4.04°). For lower SNR level acquisition (SNR<5), more densely sampled k-space (about 20 SPENT gradient directions) can compensate the information loss caused by SNR level.

The simulation results are slightly different from what has been reported by Yiannakas et al. [121] and Carmichael [191], where they studied the resolution and SNR requirement for the single direction SPENT to provide a global measurement of BMD. The difference may be caused by the objectives and the applied methodology. In terms of objectives, instead of observing bone volume by the pure SPENT measurement, it is the localised structural orientation that was concerned in this simulation. In terms of methodology, firstly, the

noise was added in a different way in the published work from this work. In [121], the noise was added before cropping the outer k-space patches (i.e. the virtual SPENT data). However in the case of mSPENT, the arbitrary direction mSPENT patch in outer k-space may be overlapped with each other when the gradient number increases. In order to keep the added noise independent from each mSPENT acquisition, noise needs to be added separately to the simulated mSPENT data at each direction. Secondly, in both [121] and [191], the diagonal SPENT data (corresponding to a 45° SPENT gradient) were also generated but were simply considered as the tiles at the four corners after dividing the whole high resolution k-space into 9 small tiles. The resulting k-space centre, however, is then $\sqrt{2}/3$ of the FoV instead of 1/3 of the FoV as the SPENT tiles on the other axes, thus leading to another frequency level corresponding to a dephase angle different from 2π. In our pulse design and simulation study, this has been corrected which allows the extension of SPENT techniques to any arbitrary orientation.

Some questions might be raised on the advantages of mSPENT compared to do a high resolution acquisition directly, as a certain SNR level and mSPENT acquisitions at several directions are needed. The first advantage of mSPENT may be that it allows the signal to be received more efficiently by adding a dephasing gradient. The gradient can be considered as the speed of the k-space sampling, and the SPENT gradient allows the sampling to move more swiftly within a fixed time compared to a conventional spin echo (SE) sequence, thus the receiver can start to receive signal at an earlier point in the FID curve, which leads to higher signal gain compared to the traditional SE sequence. Another advantage is the fact that mSPENT allows the MR scanners to work with clinically achievable resolution but to provide information which can conventionally be obtained from acquisitions with three times higher resolution. However, the debate between a dephasing technique and a high resolution MRI is probably application dependent and needs to be understood with more experiments.

8.5 Summary

In this chapter, a generalization of the previously proposed SPENT sequence is presented.

Our idea is motivated by the published study [121] using SPENT quantifying bone volume fraction (BVF) where a good correlation with BMD was shown by both simulation and experiments. It was also shown that the SPENT measurement was direction dependent. These features lead to using SPENT as a virtual "stereological" probe (Section 2.3) for the extraction of the meso-scale trabecular bone microstructure parameters, in particular, BVF and anisotropy at the same time. A tensor based method is equipped for further analyzing the mSPENT data, where the reconstructed SPENT tensor, **T**, is an analogy to the fabric tensor. The design of a modified SPENT pulse sequence has been presented to allow the SPENT gradient to measure tissue microstructure in 2D at arbitrary direction. A theoretical analysis on how mSPENT can be understood by applying off-centre reconstruction window in the high resolution k-space is also presented. A mSPENT simulator has been developed. A set of simulation were run to investigate how mSPENT performed at various directions; how noise affects the tensor system reconstruction, i.e. what SNR is required; how many gradient direction is sufficient to extract meaning full orientation information of the micro-structure.

The author's contribution in this work includes:

1) A 2D multi-directional SPENT sequence is proposed and designed to apply SPENT at arbitrary directions (Section 8.2.1 and Section 8.2.2). To our knowledge, mSPENT is the only sequence that extracts the tissue structural orientation in a stationary magnetization system.

2) A tensor based analysis method to derive orientation information is introduced and implemented into an in-house software named SPENT Toolkit (Section 8.2.3 and Appendix B).

3) The theory of dephasing behind mSPENT is discussed (Section 8.3.1) and a mSPENT simulator is developed.

4) A simulation study is performed to demonstrate the efficacy of mSPENT regarding its measurement on structure inhomogeneity (Section 8.3.2 and 8.3.3).

Chapter 9. Characterization of Trabecular Bone Orientation using mSPENT

Following the theoretical discussion and methodology introduction in Chapter 8, a series of experiments have been performed with mSPENT in order to evaluate this technique experimentally. This chapter first presents an *ex-vivo* mSPENT acquisition on a chicken femur (Section 9.1 and 9.2). TB structural anisotropy was analyzed using the SPENT tensors as introduced in the previous chapter. To validate the efficacy of mSPENT in terms of revealing the tissue orientation, a pineapple sample was scanned with mSPENT (Section 9.3). Fibre tracks were derived from the pineapple mSPENT dataset using an in-house fibre tracking algorithm adapted from those normally in the brain DTI analysis.

9.1 Experimental setup

The first objective of the experiment is to demonstrate that the designed mSPENT sequence can be used to characterize the trabecular bone micro-structure quantitatively with the tensor analysis method introduced in Section 8.2.3. The second aim is to perform the sequence on biological tissues *ex-vivo*. In the previous study using SPENT as a potential tool for the measurement of bone volume fraction, Yiannakas et al. performed the sequence on human trabecular bone samples with bone marrow removed and immersed into water while scanning [121]. However, in order to introduce the technique for clinical applications in the future, it is necessary to investigate the sequence with bone samples containing bone marrow.

9.1.1 Sample and imaging protocols

A fresh chicken (free-range) femur sample was obtained with its surrounding muscles removed before scanning. The femur was placed inside a Rapid Biomedical Gmbh volume coil with an inner diameter of 26 *mm*. The long shaft of the femur was aligned with the coil and so with the scanner z-direction. It was scanned in the coronal plane on a Varian 9.4T VMRS system. To show the chicken femur anatomy qualitatively, a high resolution image

of chicken femur was acquired first using a SE sequence, in-plane resolution 50 μm, slice thickness 1 mm. Following the anatomical scan, the mSPENT series were performed. A mSPENT series is composed of one SPENT-off acquisition using a normal SE sequence ($SPENT_0$) and several images with the SPENT gradients switched on. Except the SPENT gradient orientation, the whole mSPENT acquisition share the same imaging parameters: acquisition matrix was 128×128, in-plane resolution 200×200 μm^2, slice thickness 500 μm, FoV 25.6×25.6 mm^2, TE 7ms. The image resolution used in this experiment was chosen in order to resolve the microstructure clearly and to demonstrate whether mSPENT can be applied in various directions and used to create a meaningful structure tensor. G_{SPENT} was set to be 11.47 G/cm with duration of 1ms (as calculated from eq. 50,). It was applied in nine directions (uniformly distributed on half a circle with an interval of 22.5°). This experiment was originally designed as a preliminary study on the flexibility of the mSPENT sequence and its potential use and prior to the simulation study to search for an optimal imaging parameter set for mSPENT to produce a best measurement of anisotropy and bone volume fraction (see Section 8.3 for the simulation study).

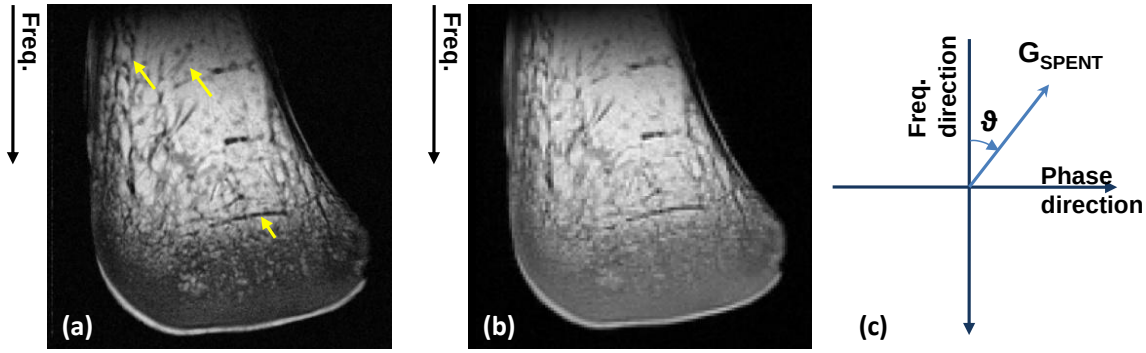

Figure 50. SPENT experiments on a chicken femur: (a). a high resolution acquisition in the coronal plane for anatomical information; (b). a $SPENT_0$ image; (c) the definition of the orientation angle ϑ of SPENT gradient G_{SPENT} (clockwise direction). In (c), the coordinate axis directions correspond to the actual frequency and phase encoding directions in the acquisition, as indicated in (a) and (b).

The tensor analysis of the acquired data is as explained earlier in Section 2.2.3. The acquired mSPENT data was first masked by a background threshold determined from the $SPENT_0$ images. And then each mSPENT image was normalized with the $SPENT_0$. The SPENT tensors were reconstructed using the normalized dataset with a standard linear

regression algorithm. After the reconstruction, the tensors were fed back into the linear system to generate the "expected" mSPENT images in order to evaluate the performance of the ellipse model (i.e. the residual error of the ellipse model fitting). The measured structure tensor, **T,** is further applied with the eigen decomposition to the principal direction of the tissue inside each voxel. Parametric maps (i.e. trace, RA and FA) were computed (eq. 53, eq. 54, and eq. 55) in order to investigate the structural orientation features of the tissue. The orientation angle at each voxel is computed.

9.2 Results

9.2.1 Imaging results

The acquired mSPENT dataset is shown in Figure 51. The SPENT images are presented in the order that it was acquired, and the corresponding gradient orientation angle ϑ was annotated in each acquisition. At each gradient direction, the structural features highlighted in mSPENT images vary with the change of the gradient orientation. As expected, at the gradient orientation ϑ = 0°, the horizontal structures are highlighted while all the pro-vertical features are not visualized (Figure 51 (a)). After the gradient rotated by 22.5° (ϑ = 22.5°), the intensity of the horizontal structures start to fade while some nearby diagonal features start to show up (e.g. yellow arrowed in Figure 51 (b)). At ϑ = 45°, no horizontal structures are shown at all and (Figure 51 (c)). Starting from ϑ = 67.5° to ϑ = 112.5°, vertical-like features gradually appear (Figure 51 (d-f)). However, the three gradient angles did not assign the same contrast to the vertical-like structures in the same region. The white arrowed trabecular bone is best shown at ϑ= 67.5° (Figure 51 (d)) and also visible at ϑ = 112.5°, while at ϑ = 90°, some segments on the trabecula might still be spotted but the whole bar is not recognizable. The feature pointed by the yellow arrow in Figure 51 (g) at ϑ = 135° is quite distinct as it does not appear in any other image of the whole mSPENT series. When the gradient keeps on rotating, the contrasted features start to change from the vertical-like structure back to the horizontal-like structure (Figure 51 (h-i)). Yellow arrows in Figure 50 are overlaid at the same locations as in Figure 51. White arrows are placed in the same location of Figure 51 (d-f) as an example showing that the visibility of orientated structural features changes according to the SPENT gradient direction.

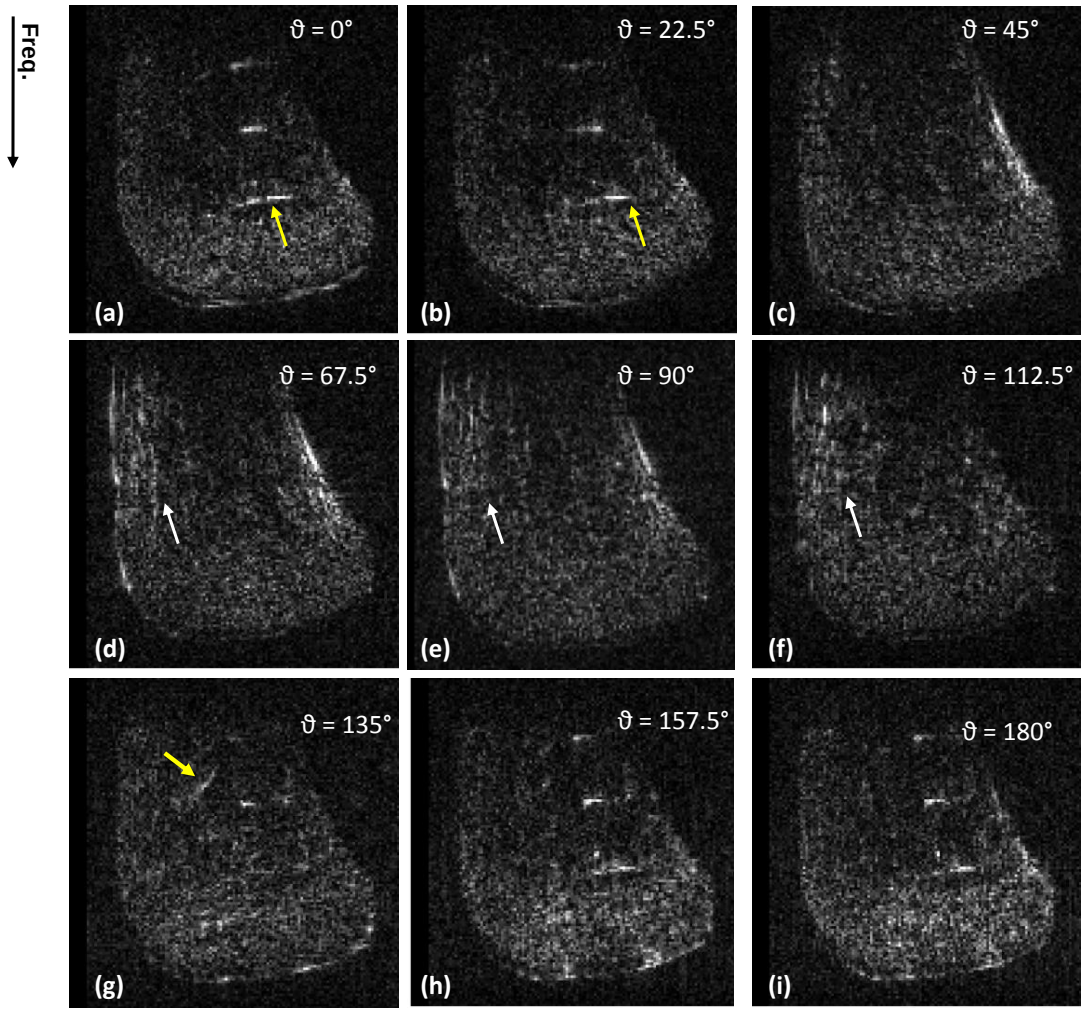

Figure 51. A set of mSPENT acquisitions of a chicken femur. From (a) to (i), the SPENT gradient angle, ϑ = 0°, 22.5°, 45°, 67.5°, 90°, 112.5°, 135°, 157.5°, 180° respectively. Yellow arrows are placed near to the place where highly oriented structures exist as indicated in Figure 50 (yellow arrows in (a)). White arrows point to the same location in (d-f), indicating that orientated structural features appear and disappear as the SPENT gradient orientation changes.

The "predicted" mSPENT data generated from the fitted ellipse model are shown Figure 52 (images on the left of each subfigure). The differences between the acquired images and the virtual data predicted by the tensor model are shown in Figure 52 (images on the right side of each subfigure).

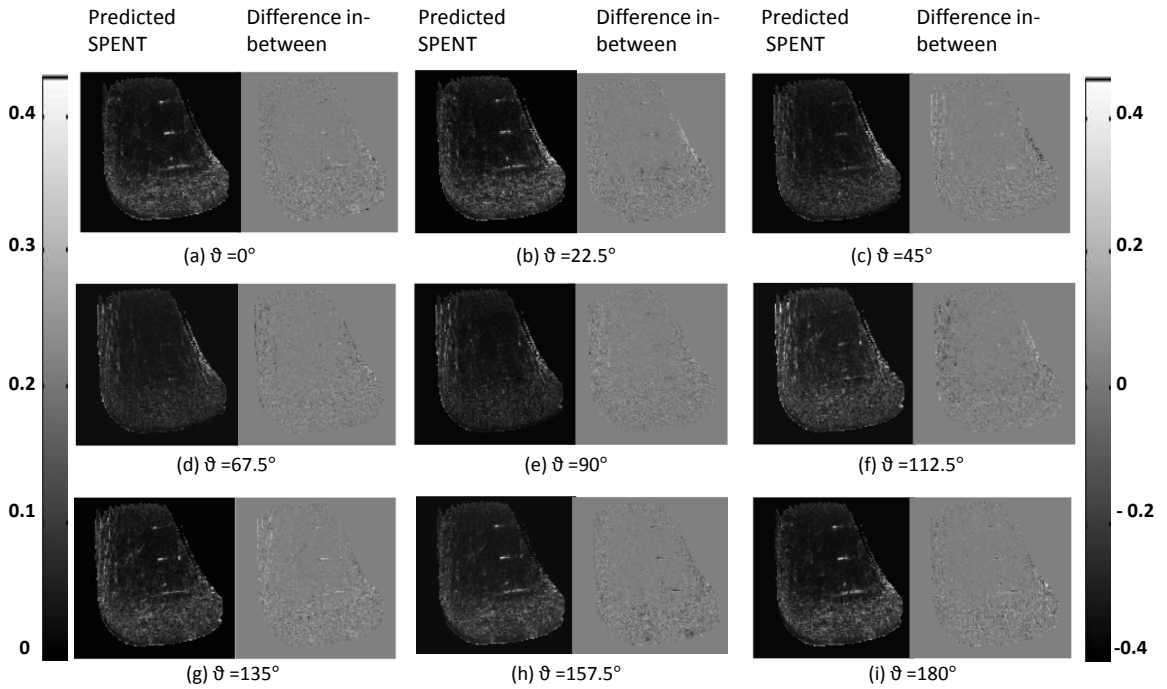

Figure 52 A "virtual" mSPENT dataset (predicted SPENT) generated by the tensor model computed from the acquired 'real' mSPENT acquisition to assess the model and the difference between the predicted SPENT and the original SPENT shown in Figure 51. Predicted SPENT and the difference from the acquired SPENT at all nine directions are presented in (a-g) respectively. In each subfigure, the predicated SPENT is on the left and the difference in-between is on the right. The left colour bar corresponds to the gray scale of the acquired SPENT images, and the right colour bar is to indicate the gray scale of the predicted SPENT images.

9.2.2 Data analysis

The decomposed eigensystems of the SPENT tensors are shown in Figure 53 by plotting the principal eigenvector at each voxel as red arrows on top of the $SPENT_0$ acquisition. The length of the arrow is scaled with the associated eigenvalue of the principal eigenvectors. A region was selected (the green boxed) and further zoomed in to provide a clearer view of the structure orientation (Figure 53 (b)). Two regions are defined in Figure 53: region I corresponds to the shaft of the chicken femur and region II corresponds to the epiphysis of the femur. The trabeculae in region I (Figure 53) are mostly associated with principal eigenvectors orientating across the bone region, indicating the trabecular bone in this region aligning along the femur shaft; while in region II, a good percentage (88.7%) of principal

eigenvectors aligned along the femur shaft (orientation angle $\varphi\epsilon\{[4\pi/9\,,\pi/2]\cup[-\pi/2\,,-4\pi/9]\}$, around 10° deviation from the vertical direction of the image), implying the underlying tissue orientation across the femur.

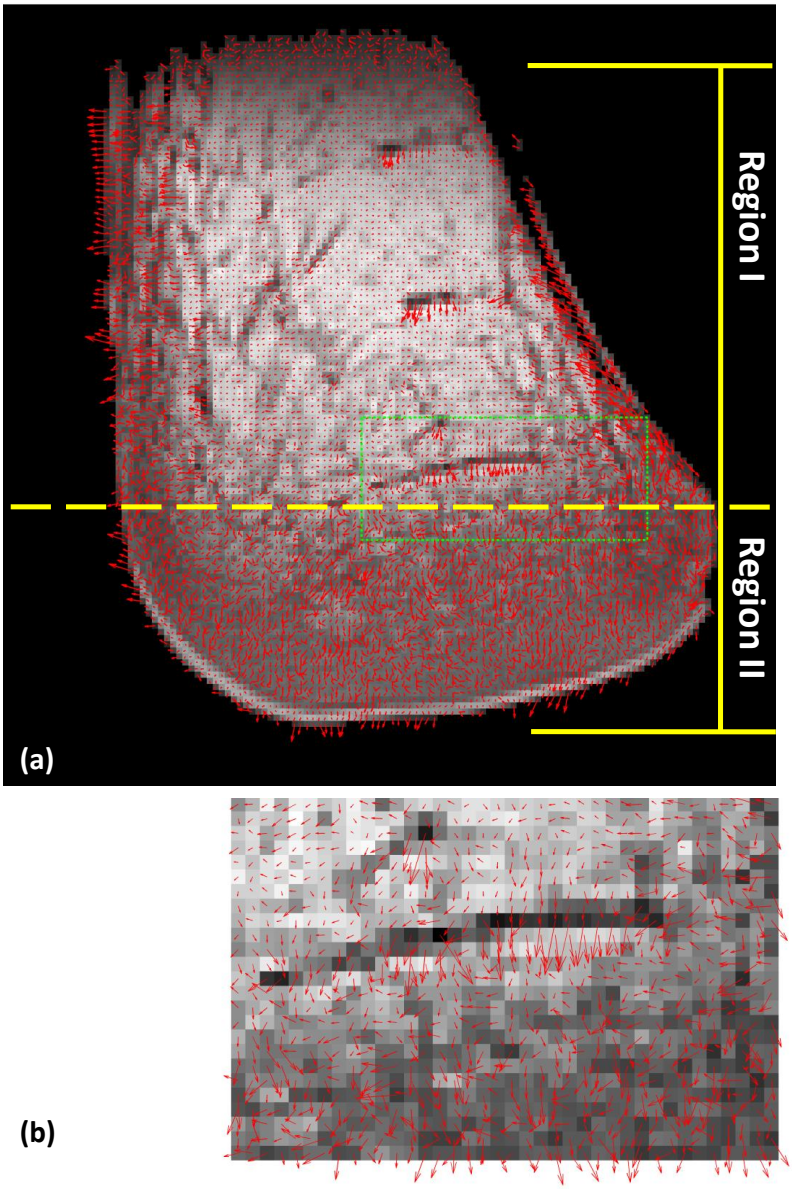

Figure 53. The 2D tensor plot of mSPENT data of the chicken femur: (a).The principal direction of each voxel computed from the tensor model is shown as a red arrow and overlaid on to the $SPENT_0$ image; (b) a region is selected (as pointed out in the green rectangle in (a)) and zoomed in to provide a clearer view.

The parametric maps computed from the reconstructed tensor system are shown with "jet" colour encoding in Figure 54. The MI map (Figure 54(a)) enhances the directional structures and present them more clearly. Both RA ad FA maps provide the anisotropic indices at each voxel.

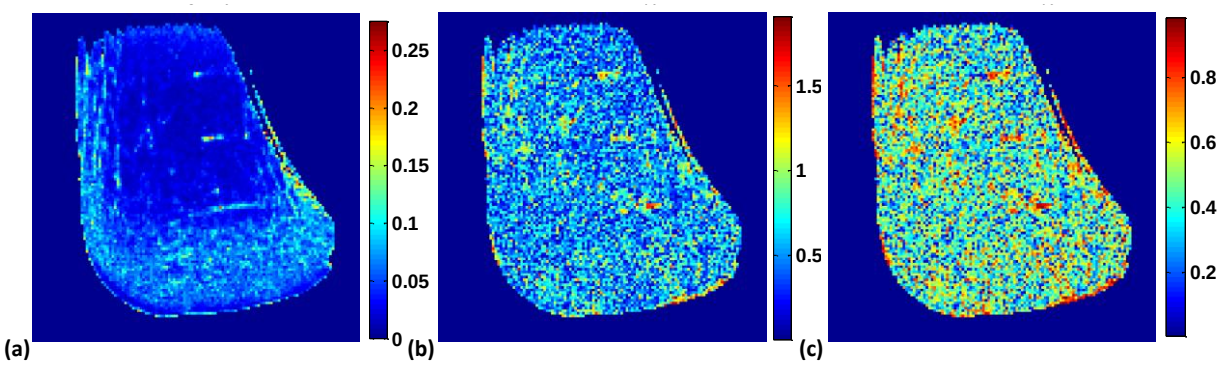

Figure 54. Parametric maps of chicken femur computed from the decomposed eigen system of the generated tensors: (a) the mean inhomogeneity map, (b) the relative anisotropy map, (c) the fractional anisotropy map.

The orientation angles as defined by eq. 56 are shown in Figure 55. A directional HSV colour encoding scheme (Figure 55, on the right) was used to express the colour map.

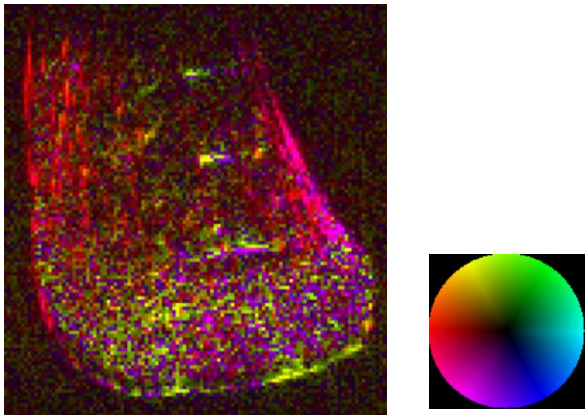

Figure 55. Orientation angle map, with its colour map representing the orientation angle.

9.3 Validation

The objective of this validation is: 1) to show that the structural nonuniformity information

measured by mSPENT at various directions matches the actual structure experimentally i.e. it resolves the actual orientation of the microstructure of the object with the proposed tensor-based method; 2) to investigate how the gradient direction scheme effects the anisotropy measurement. To achieve this, a sample with a known highly orientated internal structure is required; 3) to assess the information content in the high frequency region of k-space, in order to investigate if there exist indeed enough signals for further structural tensor analysis at which mSPENT aim. The following of this section presents the validation experiment performed on a pineapple sample. The SPENT tensor analysis has been performed. A very orientated tensor system inside the sample is revealed. This was the initiative for a SPENT "tractography" study.

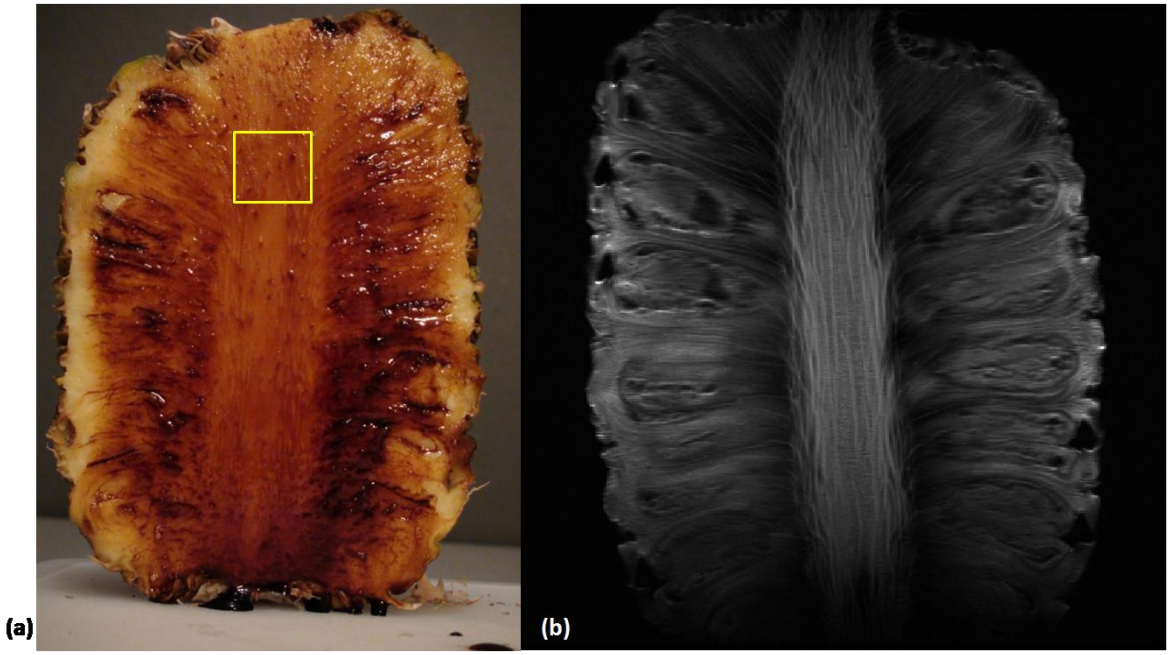

Figure 56. Validation material preparation (a) the internal appearance of a pineapple, stained with Chinese soya sauce. The yellow ROI showed the region where the sample was taken approximately. (b) Illustration of the vascular system (like fibres) inside pineapple under MRI. The image is acquired from a 3T GE Signa HDx scanner, using a conventional 2D FSE sequence, with in-plane resolution 0.293×0.293 mm^2, slice thickness 1.6 *mm*. (This figure is just for the illustration purpose, the shown pineapple is not the one originally for mSPENT validation

9.3.1 A pineapple mSPENT experiment: materials and imaging protocols

The mSPENT sequence was further validated by measuring the microstructure orientation of a sample with known highly orientated structure, in this case a pineapple. Pineapples have very fibrous structures especially in its central axis where the fibres mostly go from one to the other end of the fruit, Figure 56(a)). This can be well visualized in the MR image (Figure 56(b))[12] . Such an internal structure meets the aim of the validation. A sample block (20×14×14.5 mm^3) was cut from the central axis of a fresh pineapple, which is a fibrous stem containing the many vascular bundles supplying the flowers and bracts [192].

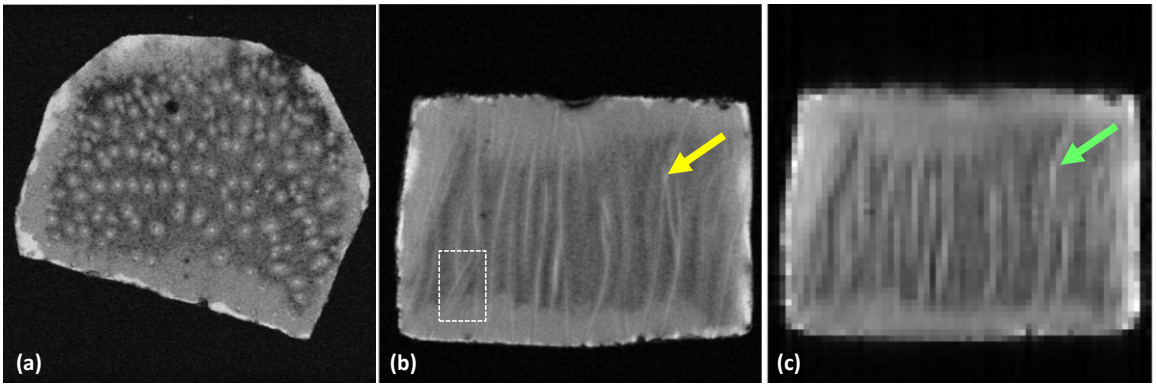

Figure 57. Validation using a pineapple sample: (a) a high resolution acquisition on the cross-section of the pineapple sample, where the white spots correspond to the fibrous vascular bundles [192] in the central core of the pineapple. (b) a high resolution acquisition on the 'coronal' plane, where the white straps (as pointed out by the yellow arrow) inside the sample are the fibres. They mostly oriented vertically with some "diagonal" fibres on the corner (white box); (c) a $SPENT_0$ acquisition on the same location in the same sample, but only with 1/4 of the resolution used in (b). In (c), fibres can be roughly recognized (as indicated by the green arrow) by their orientations are not easy to be understood.

A sample block (20×14×14.5 mm^3) was cut from the central axis of a fresh pineapple (Figure 56(a)). It was scanned in the coronal plane on a Varian 9.4T VMRS system, using a

[12] This pineapple MR image is acquired with a 3T GE HDx scanner, using a FSE sequence. It has to be pointed that the presented pineapple is just for the purpose of illustration and not the same as used for the mSPENT validation.

Rapid Biomedical Gmbh volume coil with an inner diameter of 26 *mm*. High-resolution SE images (Figure 57(a-b)) were acquired first in both axial and coronal planes in order to obtain microstructure information of the sample. The imaging parameters were: in the axial plane, in-plane resolution of 80×80 μm^2, acquisition matrix 512×512, TE= 4 *ms*, TR = 2000 *ms*, slice thickness 1 *mm*; in the coronal plane, in-plane resolution of 80×80 μm^2, acquisition matrix 256×256, TE= 4 *ms*, TR = 2000 *ms*, slice thickness 1mm. The mSPENT data was acquired afterwards at the same location as that of the coronal high resolution SE image, with the same FoV but 4 times lower resolution. The mSPENT dataset were composed of one $SPENT_0$ image and 8 mSPENT images (gradient directions , ϑ_i= {0°, 45°, 90°, 135°, 180°, 225°, 270°, 315°}). The other imaging parameters are acquisition matrix 64×64, in-plane resolution 200×200 μm^2, slice thickness 1*mm*, TE = 7 *ms*, TR = 2000 *ms* and NEX = 1. The SPENT gradient strength is set to be 11.74 *G/cm*, with duration of 1 *ms*. Each mSPENT acquisition took four minutes.

9.3.2 Imaging results

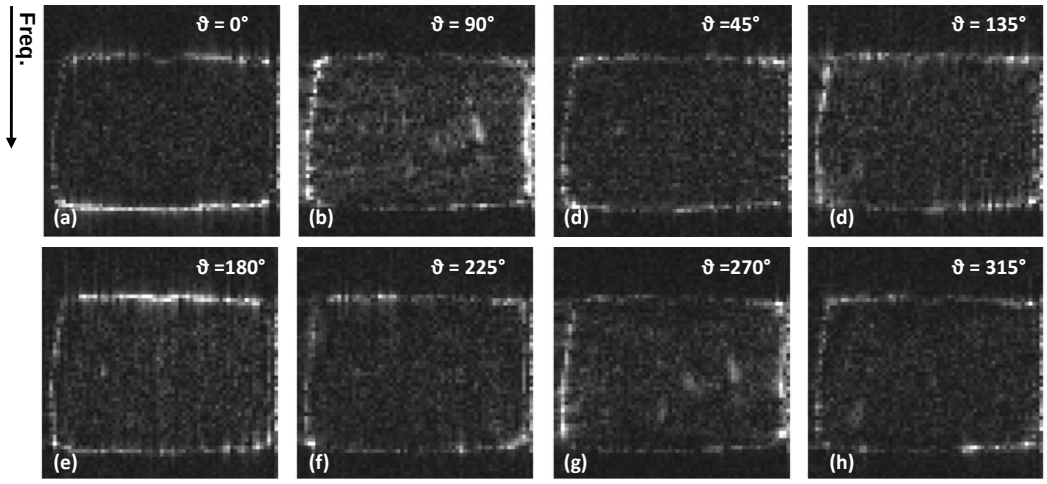

Figure 58. The mSPENT acquisition of a pineapple sample. From (a) to (h), the SPENT gradient angle, ϑ= 0°, 90°, 45°, 135°, 180°, 225°, 270°, 315° respectively. The frequency encoding direction is along the vertical direction of the image.

The acquired pineapple mSPENT data are shown in Figure 58. As shown in the internal structural images of pineapple in Figure 57 (b and c), the pineapple fibres were along the vertical direction in the image but bending with small angles away from the imaging axes. Consequently, with mSPENT gradients at ϑ=0° and 180°, very little signal was gained inside the sample (Figure 58 (a-e)). The closer the SPENT gradients oriented towards that perpendicular direction of the fibre orientation, the more signals were received (Figure 58 (b, g)). Also at ϑ= 135° and 315°, the left bottom corner of the sample are visualized with more signal, which is not observed at other directions. This region corresponds to the diagonally-oriented fibres which can be observed in Figure 57(b) (the boxed region in white).

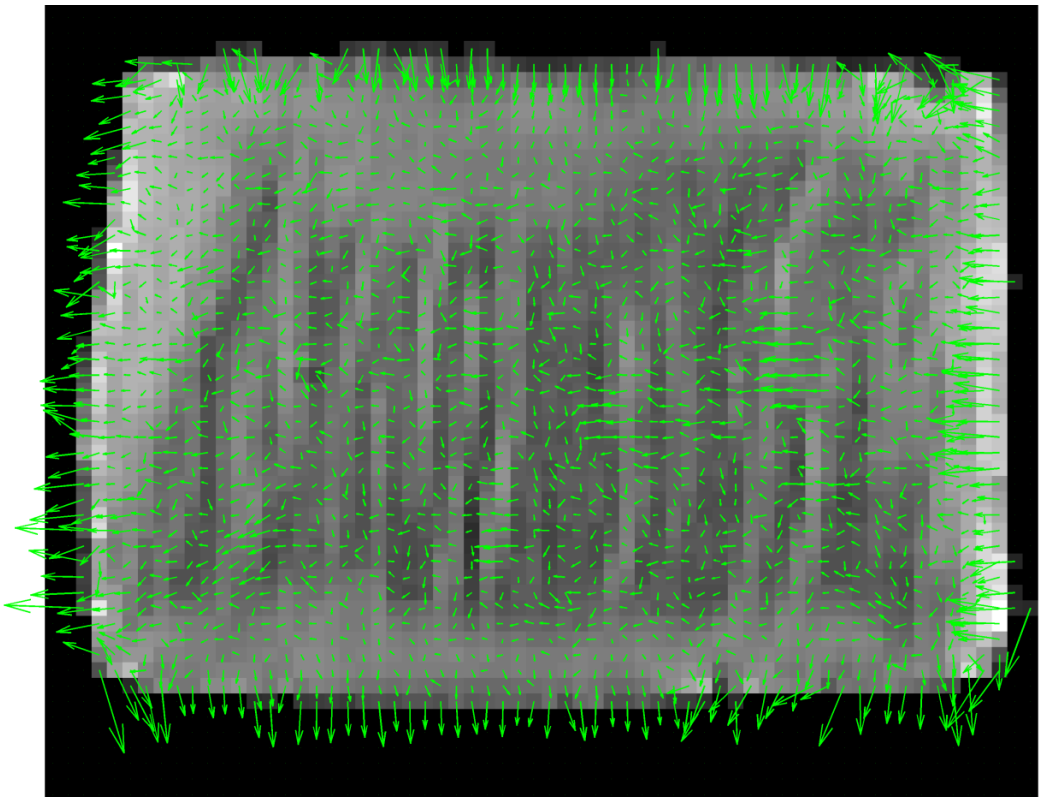

Figure 59. The 2D tensor plot of the pineapple mSPENT data. The principal direction of each voxel is indicated by a green arrow and overlaid onto the $SPENT_0$ image of the pineapple acquisition.

9.3.3 Tensor analysis

Structure tensors at each voxel were reconstructed on the normalized pineapple SPENT

data with background noise masked by thresholding. The eigensystem of the tensors are shown in Figure 59, with its primary eigenvector (i.e. the principal direction) at each voxel plotted as a green arrow and overlaid on top of the $SPENT_0$ image.

The corresponding parametric maps (MI, RA, and FA) were presented in Figure 60. Several regions with high FA/RA values are shown with yellow or red colours, indicating that highly orientated fibres are contained in this region. The corresponding areas in the MI image are visualized with bright blue colours and distinguish themselves from the surroundings. In the 2D tensor plot figure, these high anisotropy indexed regions are also associated with very coherent eigenvector orientations.

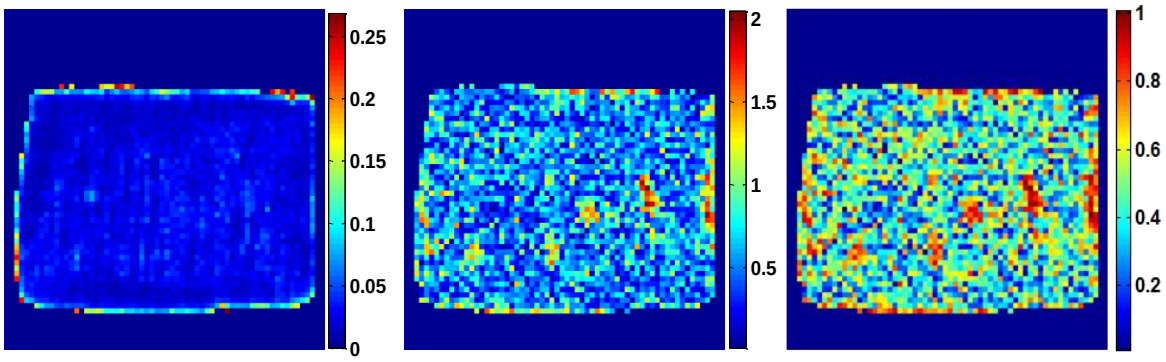

Figure 60. Parametric maps of the pineapple sample computed from the decomposed eigen system of the generated tensors: (a) the mean inhomogeneity map, (b) the relative anisotropy map, (c) the fractional anisotropy map.

9.3.4 The pineapple "fibre" tracks

In the sample, several regions are associated with large anisotropy indices (FA and RA values) where coherent principal directions are also present in Figure 59. This strong coherence of dominant directions motivated the idea of reconstructing the pineapple vascular fibre pathways as in the tractography in diffusion MRI based on the principal directions of the SPENT tensors (e.g. determined streamlines).

In the tractography of the brain, when the orientation of the tensors show strong coherences, it is possible to represent the fibre track as a 3D space curve as a vector $\vec{r}(s)$

parameterized by the arc length, s, of the trajectory [193]. The evolution of $\vec{r}(s)$ can be described using the Frenet equation with the tangent vector $\vec{t}(s)$ (Section 4.2.3, Definition 2):

$$\frac{\mathrm{d}\overrightarrow{r(s)}}{\mathrm{ds}} = \vec{t}(s) \qquad \text{eq. 61}$$

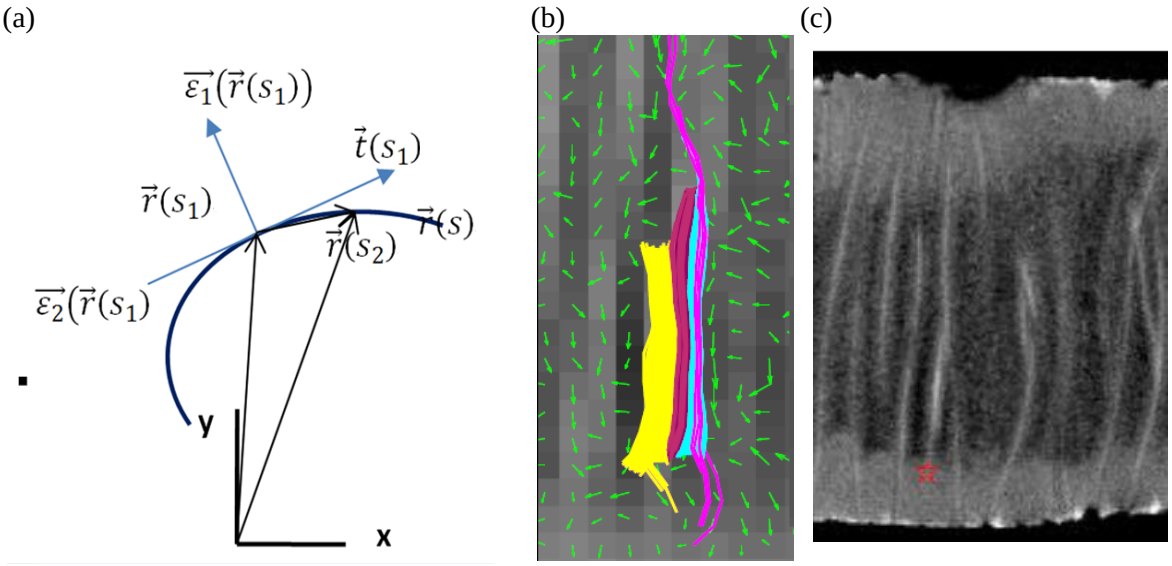

Figure 61. Fibre tracking method for mSPENT data. (a) a sketch representation of a pineapple fibre trajectory as a space curve $\vec{r}(s)$. The local tangent vector $\vec{t}(s_1)$ is identified by the secondary eigenvector, $\overrightarrow{\varepsilon_2}(\vec{r}(s_1))$ at position $\vec{r}(s_1)$. $\vec{r}(s_2)$ is the following position on the curve $\vec{r}(s)$, which can be found using numerical approximation methods, such as Euler or Runge-Kutta method [193] (b) The fibre plot and the secondary eigenvectors weighted by the first eigenvalues starting from a ROI. (c) The corresponding region in the high resolution image as indicated by the small red star.

The assumption of this mathematical framework is that the normalized eigenvector, $\overrightarrow{\varepsilon_1}$, associated with the largest eigenvalue, λ_1, of the diffusion tensor, **D**, lies parallel to the local fibre tract direction [193]. Therefore, if the tangent vector $\vec{t}(s)$ is equated to the unit eigenvector, $\overrightarrow{\varepsilon_1}$, calculated at position $\vec{r}(s)$ as $\vec{t}(s) = \overrightarrow{\varepsilon_1}(\vec{r}(s))$ and combined with eq. 61, the equation of the fibre track trajectory can be obtained:

$$\frac{\mathrm{d}\overrightarrow{r(s)}}{\mathrm{ds}} = \overrightarrow{\varepsilon_1}(\vec{r}(s)) \qquad \text{eq. 62.}$$

The initial condition of this system is $\vec{r}(0) = \vec{r}(s_0)$, which specifies the seeding point of a fibre track.

The tractography of the SPENT tensor system is in a similar regime to the brain diffusion tractography. However, the difference between the two is that instead of indicating the direction along the fibres, the principal direction of the tensor system in SPENT is perpendicular to the assembly orientation of structures inside each voxel. This implies that the principal eigenvector is not the tangent vector $\vec{t}(s)$ but a vector $\vec{n}(s)$ that is perpendicular to $\vec{t}(s)$ at the position $\vec{r}(s)$ (Figure 61 (a)). However, as the eigensystem of the SPENT tensor is an orthogonal system, it is not difficult to find the normalized tangent vector with the knowledge of $\vec{n}(s)$. In a 2D system as the pineapple SPENT tensors, the orientation of $\vec{t}(s)$ is equivalent to the direction of the secondary eigenvector $\overrightarrow{\varepsilon_2}$. Thus the tangent vectors used in the original fibre tracking algorithm can be formed by using the secondary eigenvector weighted by the first eigenvalues $\lambda_1 \cdot \overrightarrow{\varepsilon_2}$. The above algorithm is realized and incorporated in the in-house MATLAB software, SPENT Toolkit (Appendix B.1). The applied fibre tracking parameters are angle threshold 40°, step size 0.5, with bi-linear interpolation method, and the seed ROI sampled with a spacing of 0.2 per voxel. Figure 61(b) shows the extracted fibres (yellow) from a ROI region whose centre is annotated by the small red star shown in the high resolution acquisition of the same slice in Figure 61 (c). The fibres are plotted over the 2D tensor plot (green arrows) of the secondary eigenvectors weighted by the principal eigenvalues. .

9.3.5 Information content in the high frequency region

As discussed in Section 8.3.1, the signal measured by mSPENT is conceptually equivalent to the signal that resides in the high frequency region of a higher resolution MR acquisition. However, doubts might be raised on whether the measured signal is just noise or indeed contains residual spins after the dephasing caused by sub-voxel structural non-uniformity. Since noise is by nature random, with the increasing of the number of signal averaging (i.e. NEX), the real signal at the high frequency region should be preserved while the noise would decrease.

To demonstrate this, an experiment was designed and performed on a 3T GE clinical scanner (the same scanner as used to acquire DTI data in Chapter 6 and 7) with a pineapple phantom. A clinical 2D fast spin echo (FSE) sequence was applied, with 1.6 *mm* thickness, 0.3×0.3 mm^2 in-plane resolution, acquisition matrix 512×512, TR 4540 *ms*, TE 22.86 *ms*. The raw data of this proton-density image was saved in order to get the real k-space data. In Figure 62, the logarithm of the absolute k-space values are shown with colour coding ('hsv' scheme in MATLAB). Circles were placed in the central k-space in order to illustrate the location of "high frequency" region: the regions outside the circles correspond to where the signal detected by mSPENT is from. NEX increases from 1 to 4 (corresponding to Figure 62(a-c) respectively). The intensity ranges of the three images have been scaled to the same interval. The blue straps going across the image are where the real signals are. The background colour goes from cyan (≈4 on the colour map) to green (≈2 on the colour map), implying the reduction of the noise level with the increase of the number of signal average. Most of the blue area (i.e. real signal) is well preserved with the increase of NEX.

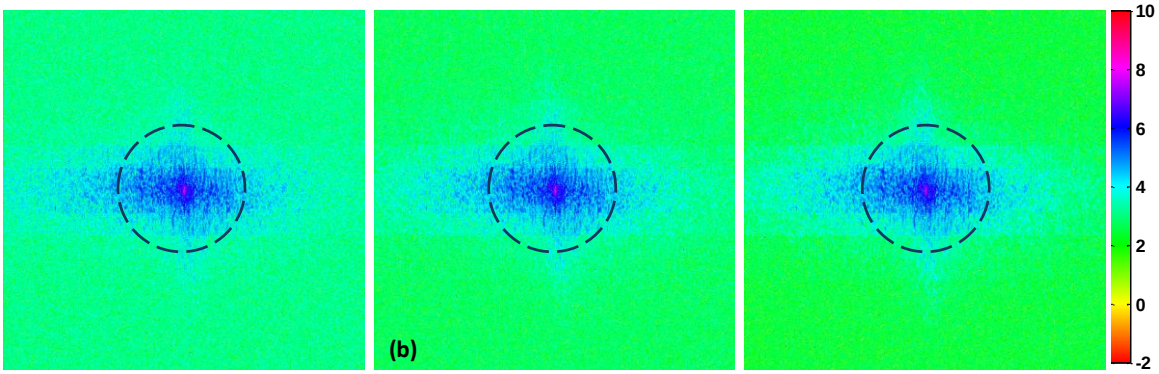

Figure 62. High frequency signal indicating subvoxel inhomogeneity remains with increasing NEX but not the noise signal. (a-c) logarithm of the magnitude of k-space data of one slice in a 2D FSE pineapple acquisition on a 3T GE clinical scanner, with NEX = 1, 2, and 4 respectively. Circles (dark blue) are overlaid on top of each image, to indicate the location of the high frequency region that is approximately the space outside the circle.

Three ROIs were cropped from the regions outside the circle but within the blue strap (i.e. the high frequency region in k-space) on the three images respectively. These regions are considered to contain mainly the real signal as measured by mSPENT. To compare the difference, noise ROIs were cropped outside the circled low-frequency regions and the blue

strap. The mean value and standard deviation of these ROIs are calculated and listed as in Table 11. The size of the ROIs is similar and all bigger than a 20×20 square. The difference of the magnitude data (Rician Distribution [176]) of mSPENT ROI and noise ROI at NEX = 4 were improved from 3.82/3.07 to 3.72/2.74. The difference was test to be significant ($p<0.0001$) by Wilcoxon signed-rank test.

Table 11: Comparison between noise and real high-frequency signal against the change of NEX

NEX	1		2		4	
	Mean	SD	MEAN	SD	MEAN	SD
ROI_{mSPENT}	3.82	0.69	3.67	0.70	3.72	0.71
ROI_{noise}	3.07	0.65	2.79	0.64	2.74	0.64

9.4 Discussion

The proposed mSPENT sequence was successfully performed on a fresh chicken femur *ex-vivo*. As expected, the images acquired at different gradient directions present distinct features. The image contrast changes according to the intrinsic orientation of the structure itself: the voxels containing tissues whose net structural orientation is close to the perpendicular direction of the SPENT gradient direction are more visible on the image. The proposed voxel-wise ellipse model is shown to work well. Although the exploited model fitting method is just the standard least square linear regression, the difference between the actual data and the predicated data using the reconstructed tensor model and gradient scheme is reasonably small (Figure 52). Before the tensor reconstruction, the mSPENT data was normalized first with the $SPENT_0$ acquisition to reduce the field inhomogeneity. The higher the MI value is, the more inhomogeneous the voxel should be. That is to say, those voxels containing highly oriented structures should be more highlighted. This is well shown in the MI map: the bone strips (Figure 50(a), yellow arrow) and the interfaces between bone marrow and the cortical bone all correspond to the hot colours (red) on the "jet" colour map (in MATLAB). Both of the FA and RA maps are presented although they seem to provide similar anisotropy indices mathematically, which one to use in practice needs to be decided in future group studies. Apart from highlighting the locations with a high degree of inhomogeneity, the anisotropy indices indicated by either FA or RA may be used to express

the degree of anisotropy. The characterized dominant TB orientations in the femur shaft and in the epiphysis regions are shown to be different. Such difference is not easy to be recognized even in the high-resolution acquisition, but becomes clearer with the tensor plot. In general, the sub-voxel derived principal direction shows good qualitative agreement with the structures as seen in the high resolution image of the chicken. A relevant problem of the current experiment is that the gradient scheme only covers half of a circle instead of the full circle. The original idea was to utilize the symmetric property of the k-space and to make the acquisition more economical. However, the symmetric assumption in Fourier domain stands when the data in the image domain is purely real. However, this is not the case in reality due to field inhomogeneity and flow artefacts. This problem might be solved by borrowing ideas from the reconstruction algorithm for partial Fourier imaging (Chapter 13, page 292-299, [111]).

The sequence is further validated on a block of pineapple sample to resolve its internal fibrous structure. It has been shown that the characterized principal directions of the tensor correspond well to the internal fibre orientation (Figure 59 and Figure 60). To illustrate the coherence more intuitively, the pineapple vascular “fibre” tracks were extracted based on the principal directions of the tensors. In the low resolution pineapple data (Figure 58(c)), the vessels appear to be straight, like vertical straps going through the core of the fruit, while the fibres are clearly seen as curves wind through the fruit central axis. These features are better expressed with the retrieved fibres. Generally speaking, the validation result is quite encouraging and show quite promising result. The FA and RA maps (Figure 60 (b-c)) appear to provide information complementary to the MI map (Figure 60(a)). Some voxels with similar MI values are associated with higher anisotropy values. This might be due to the fact that MI map gives a quantification of local tissue inhomogeneity and is related to the volume fraction and FA or RA map incorporates the orientation information. The future work is to perform a more comprehensive validation of the mSPENT derived parameters and to compare the derived TB orientation with that measured on the structure, which is lacking in the current study. For the chicken femur sample, such validation can be done by comparing the orientation information to those extracted from the 3D micro architecture TB model reconstructed from a high-resolution micro-CT acquisition. For the pineapple sample,

it may be necessary to use a histology imaging approach. This will be included in the future work of mSPENT.

In the current tensor analysis, the ellipse model is used voxel-wise. Thus the anisotropic quantification is quantified as a local morphometric parameter. It is possible to derive a regional or global descriptor of TB orientation through an averaging window as it is applied by Saha and Wherli [53]. In the conventional stereological analysis, the MIL measured anisotropy is normally a value for the whole sample [41, 42]. This is because traditionally such method targets to describe a sample under microscope but not for the whole bone. For the *in-vivo* applications, a methodology to quantify the local orientation is more preferred. Tassino et al. [187] have shown that methodology respecting both regional TB orientation and local inhomogeneity can improve the accuracy in predicting the mechanical behaviours of bone segments under loading conditions that involves TB. TB orientation trajectory is presented as a function of the principal orientation of the fabric tensor against the z-axis of the analysed slice. The trajectory is like a curve with its tangent as the dominant orientation of the underlying TB, which is similar to the principle idea of fibre tracking. Such a description recalls the arc-like description of the internal structure of human femur, which was originally proposed by the Swedish structure engineer, von Meyer, and later summarized by Wolff [9] to form his law on bone remodelling [194]. Although the original trajectory may be too idealized, it is now commonly agreed that this structural anisotropy is highly related to the bone mechanical properties and influenced by the remodelling procedure of the bone tissues. In this context, mSPENT may play a role in deriving a trajectory model of human's trabecular bone [194], which might carry information, not only on the mechanical property but also on the remodelling history.

The concern whether there would be enough mSPENT signal is investigated by assessing the information content at high frequency regions of k-space data acquired by scanning a pineapple sample using a 3T GE scanner at a high resolution. By increasing the number of signal averaging (from NEX=1 to 4), the real signal is shown to be kept and the difference between the noise signal and the sample signal becomes bigger as indicated in Figure 62 and Table 11. This difference was statistically tested to be significant ($p<0.0001$). Thus, it is reasonable to conclude that mSPENT is able to acquire real signal although it targets at

the same region which hosts more noise than the low-frequency area which is located in the centre of k-space. The fact that with more NEX, the mean values of the noise ROI signal is lower implies that given enough SNR level it is possible to retrieve enough MR signals in the high frequency region. This corresponds to the results from the simulation studies in Chapter 8 that the extracted orientation error decreases while the SNR increases. mSPENT works as a directional specific high frequency pass filter that samples the outer space of k-space, in order to achieve bigger k-space coverage with a conventional lower resolution imaging protocol. This feature is potentially helpful for acquisition environment where there is a resolution penalty, such as on the clinical scanner. On the other hand, this experiment also implies the need to make the best use of mSPENT, there may be a minimum requirement of SNR that provides a more reliable inhomogeneity measurement. It also has to be pointed out that a real mSPENT acquisition is necessary to further confirm the current finding.

Apart from the wish list of the usage of mSPENT, there are still several concerns on utilizing the technical. In the rest of this section, two issues will be discussed in more details: the possible approach to improve the bone fracture risk evaluation *in-vivo,* and the development toward 3D mSPENT. Also, to further demonstrate the power of mSPENT, more experiments and validations are certainly needed.

9.4.1 Potential applications

Although it has been demonstrated by Yiannakas et al. [121] that SPENT achieved good correlation with the current clinical standard bone strength measurement, BMD scanned by DEXA method (R^2 = 0.95, $p<0.001$), it is still a bone density measurement and the information on micro-architecture is still lacking. Moreover, the correlation between the bone density measurement alone (e.g. BMD or BVF) and the Young's Modulus is still low (< 60%) (page 120-134, Section 4.4, [191]). The derived anisotropy indices, i.e. FA and RA, may be potentially useful for clinical quantification. However, the current experiment needs diseased models to demonstrate this usage. It is believed that structural anisotropy plays a role in evaluating the bone mechanical property, the question about how to use the structural anisotropy as a parameter in practice is not answered yet. Moreover, it would be

more convenient for clinical use that a net index is produced from a fine-scale model that gives good evaluation of the desired bone mechanical properties.

A recent study of Tassani et al. [187] proposed a potentially useful model which combines both the bone density parameter and the principal orientation of the TB sample with the objective to improve the TB mechanical property prediction. Four models were compared in terms of the correlation with TB elastic property measured by mechanical testing in their research: 1) BVF only (reference model); 2) BVF projected along the everyday force loading direction (i.e. the specimen axis); 3) BVF along the fabric tensor (i.e. structural tensor) principal orientation (PD); 4) BVF along PD, projected on to the loading direction. These models were also computed with both the global and the local approaches. The difference between the global and the local methods is that the former one expressed the whole sample orientation with one structural tensor, while the latter exploited a sliding window and took into account the structure tensor PD at every step (20 μm along the z-axis of a 4 mm cylindrical sample). The results showed great improvement on the determination coefficients (R^2) of the correlation between the ultimate stress (for the elastic property) and bone architectural parameter comparison. A maximum of 35% determination coefficient increase was observed while changing from model 1 to model 4. An improvement of R^2 was also shown by replacing the global method (up to R^2=0.88) with the local approach (R^2=0.90).

The result of Tassani's study indicates a possible net bone property index with improved accuracy compared to DEXA measured BMD by combining the bone density measurement and its local structural orientation. The input parameters required by this model may be directly acquired by mSPENT. Yiannakas et al. [121] have shown that the SPENT measurement correlates with BMD measured by DEXA. Both the simulation results in Chapter 8 and the experimental results in this chapter further show the potential of mSPENT providing a good anisotropic measurement. This special feature makes mSPENT a good candidate of the surrogate of the current clinical standard method using DEXA. Although the mSPENT technique is motivated by the wish to measure TB orientation, the validation results on pineapple vascular network may provide an idea of applying mSPENT to extract the vascular network of the human body, especially where the vessels are

organized heterogeneously, such as the vascularisation of a tumour.

9.4.2 Towards 3D mSPENT

The structure tensor T in 3D and the 3D mSPENT scheme

As TB network is by nature a three-dimensional architecture, 3D quantification would be more preferable. At the moment, the 3D version of mSPENT tensor analysis has been implemented with the simulated 3D data with the purpose to illustrate the idea. The 3D generalization of the proposed 2D mSPENT is as below:

$$T_{11}x^2 + T_{22}y^2 + T_{33}z^2 + 2\,T_{12}xy + 2T_{13}xz + 2T_{23}yz = S \qquad \text{eq. 63,}$$

$$S = \vec{a}_i{}^T \mathbf{T} \vec{a}_i \text{ , with } \boldsymbol{T} = \begin{bmatrix} T_{11} & T_{12} & T_{13} \\ T_{21} & T_{22} & T_{23} \\ T_{31} & T_{32} & T_{33} \end{bmatrix}, \text{ and } T_{21} = T_{12}, T_{31} = T_{13}, T_{32} = T_{23} \qquad \text{eq. 64}$$

In 3D $\vec{a}_i \coloneqq (x_i,\ y_i,\ z_i)$ and the gradient direction encoding matrix, A_{SPENT}, can be written as (analogous to the diffusion gradient direction encoding matrix in eq. 39):

$$A_{SPENT} = \begin{bmatrix} x_1^2 & y_1^2 & z_1^2 & 2x_1y_1 & 2x_1z_1 & 2y_1z_1 \\ \vdots & \vdots & \vdots & \vdots & \vdots & \vdots \\ x_N^2 & y_N^2 & z_N^2 & 2x_Ny_N & 2x_Nz_N & 2y_Nz_N \end{bmatrix}.$$

Similar to the 2D SPENT simulation, to create a 2π phase wrap for each voxel conceptually, in the case of a cubic k-space volume, the high resolution k-space centre (O) needs to be shifted by one-third of the original k-space (a=$L/3$, FoV = L^3). The distance from the mSPENT k-space centre (O') to O has always to be *a*. That is to say the new SPENT k-space centres are on a sphere with the original k-space centre as the centre, and *a* as the radius of this sphere. A 3D version of the SPENT toolkit was programmed for the tensor reconstruction and eigensystem decomposition in MATLAB as an extension of the previously introduced in-house software SPENT toolkit (Appendix B.). An interface to allow data crosstalk between SPENT toolkit and CAMINO [173] was also written so as to utilize the interactive 3D tensor plot viewer (*pdview* in CAMINO).

Before programming the 3D version of mSPENT sequence on the clinical scanner, it is considered to be beneficial to the later implementation to decide which pulse sequences is the "host" of the SPENT gradients (i.e. which sequence to be modified to add the dephaser gradient lobe). Therefore at the current stage, we investigate the efficacy of the 3D mSPENT tensor analysis, and the appropriate resolution and SNR of a chosen sequence (which is recommended by the vendor to be appropriate for the musculoskeletal system) via simulation.

A simulation study

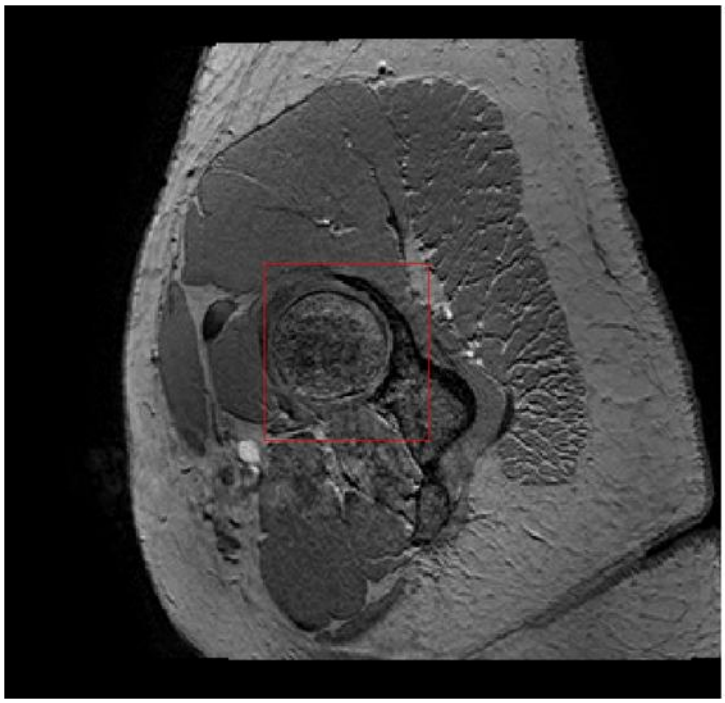

Figure 63. The 3D T_1 weighted MR data of the human hip joint (for the simulation study of 3D mSPENT) with a resolution of 0.7×0.7×0.7 mm^3. The red box is the cropped region to generate the simulated 3D mSPENT data.

In the simulation study, two 3D MRI datasets of a human hip joint *in-vivo* were used. As the 3D tensor fitting procedure in mSPENT is mathematically equivalent to that of DTI except the input measurement is the local structural inhomogeneity instead of the diffusion caused signal decay, the distribution of the mSPENT gradient directions are considered to be advantageous to be distributed uniformly on an icosahedron as in DTI settings (Section

6.1.3, [168]) in order to achieve the minimum noise propagation level while reconstructing the tensors. The gradient scheme used for the simulation of 3D mSPENT is the same as that implemented on the GE[13] scanner for the DTI protocol (as used in the study of Chapter 6).

In the first simulation study, a hollow ball was created to test the algorithm and check the efficacy of tensors to reveal the orientations. It is also to simulate the femur head which is close to the form of a sphere. The inner radius (R_{in}) was set to be 60 (voxels), while the outer radius (R_{out}) was 62 (in number of voxels). Thus it leads to a hollow ball with 2 voxel wall thickness. The high-resolution matrix size was 288×288×288 and resulted in 96×96×96 SPENT matrices. This setting is to simulate the acquisition matrix in the later 3D *in-vivo* dataset of the human femur. To reduce strong ringing artefacts, a Gaussian filter (the variance σ=3) was first applied to the high-resolution dataset. The objective of this simulation was to examine whether the proposed 3D mSPENT algorithm was able to retrieve the underlying tissue structural orientation. The SNR and resolution effects were not studied.

In the second simulation study, two T_1-weighted 3D datasets of human hip joint of the same volunteer (patient data) were acquired on a 3T Philips MR scanner (Achieva, Philips Medical Systems, Best, the Netherlands) using a VISTA sequence (a 3D fast spin echo sequence with variable flip angle) in the oblique plane (Figure 63). The two datasets were acquired with two different resolution settings, both isotropic: 1×1×1 mm^3 (the acquisition matrix 300×298×60, interpolated into 320×320×60, denoted as V_{P1}), 0.7×0.7×0.7 mm^3 (the acquisition matrix 424×425×86, interpolated into 432×432×86, denoted as V_{P2}). The imaged volume was placed with an angle to the body so that the central slices cut transversely across the area where the fractures happened most of the time. As the k-space data were not obtained, the simulation study was based on the frequency space created from the magnitude data by Fourier transform. In order to create the mSPENT data, a cubic volume was cropped first in the original image volume, in which case lead to a set of mSPENT data with volume matrix 20×20×20 at each SPENT gradient

[13] Although the data acquired is from a Philips scanner, we only had access to the GE tensor settings at the time when the study was done.

direction for the dataset V_{P1} and 28×28×28 for the dataset V_{P2}. The objective of the simulation study is to check whether the current resolution settings and SNR is proper for a further group study and whether the sequence is a good candidate to be modified to mSPENT sequence on the clinical scanner. As in the first simulation study, two gradient schemes (one with 6 SPENT gradient directions and the other with 20) were studied. The 3D mSPENT data was generated with the mSPENT simulator (Section 8.3.2). The principal orientation of the structure tensors was computed with the 3D SPENT Toolkit, the principal tensor orientation was visualised by CAMINO.

The results of the simulation

The SPENT tensor was reconstructed using a standard linear regression with least squares. The resulting eigensystem was reformatted to be visualized in *pdview*, CAMINO (Figure 64(a)). The bars inside each voxel indicate the orientation of the tensors. The colour is encoded as red (R) for x-axis, green (G) for y-axis and blue (B) for z-axis. As expected, the principal directions of the SPENT tensors are along the direction of the sphere diameters and approximately norm to the sphere surface.

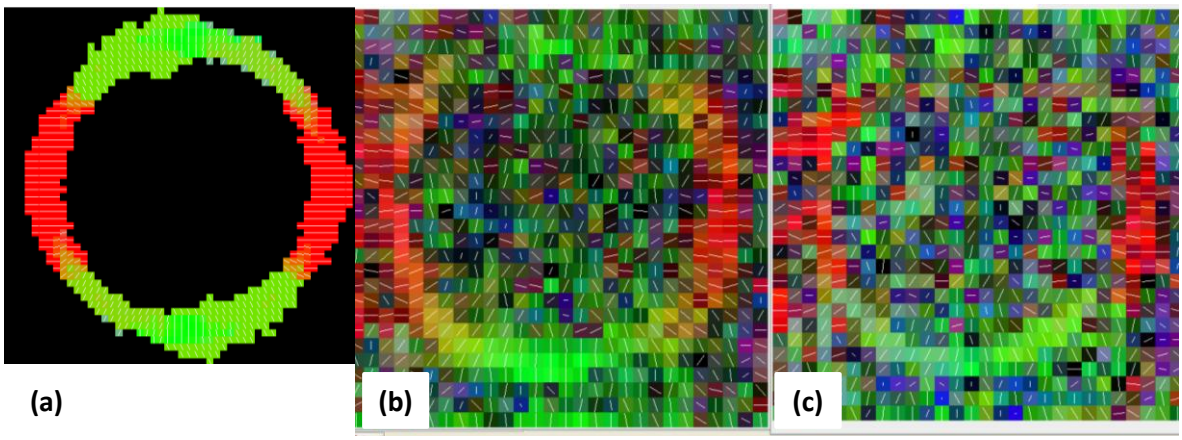

Figure 64. Plots of principal eigenvectors calculated from 3D mSPENT simulation. (a) Result from the hollow ball phantom with 20 gradient directions in the plane of x-y. (b) Result from *in-vivo* human femur data using the second protocol, with 20 gradient directions in the same plane as Figure 63. (c) the simulation results from the same dataset as in (b), with 6 gradient directions. (b) and (c) are the SPENT tensor principle orientation plot from the same slice.

In the second simulation, the principal orientations of the SPENT tensors reconstructed from the simulated 3D mSPENT data using dataset V_{P2} are illustrated in Figure 64(b-c).

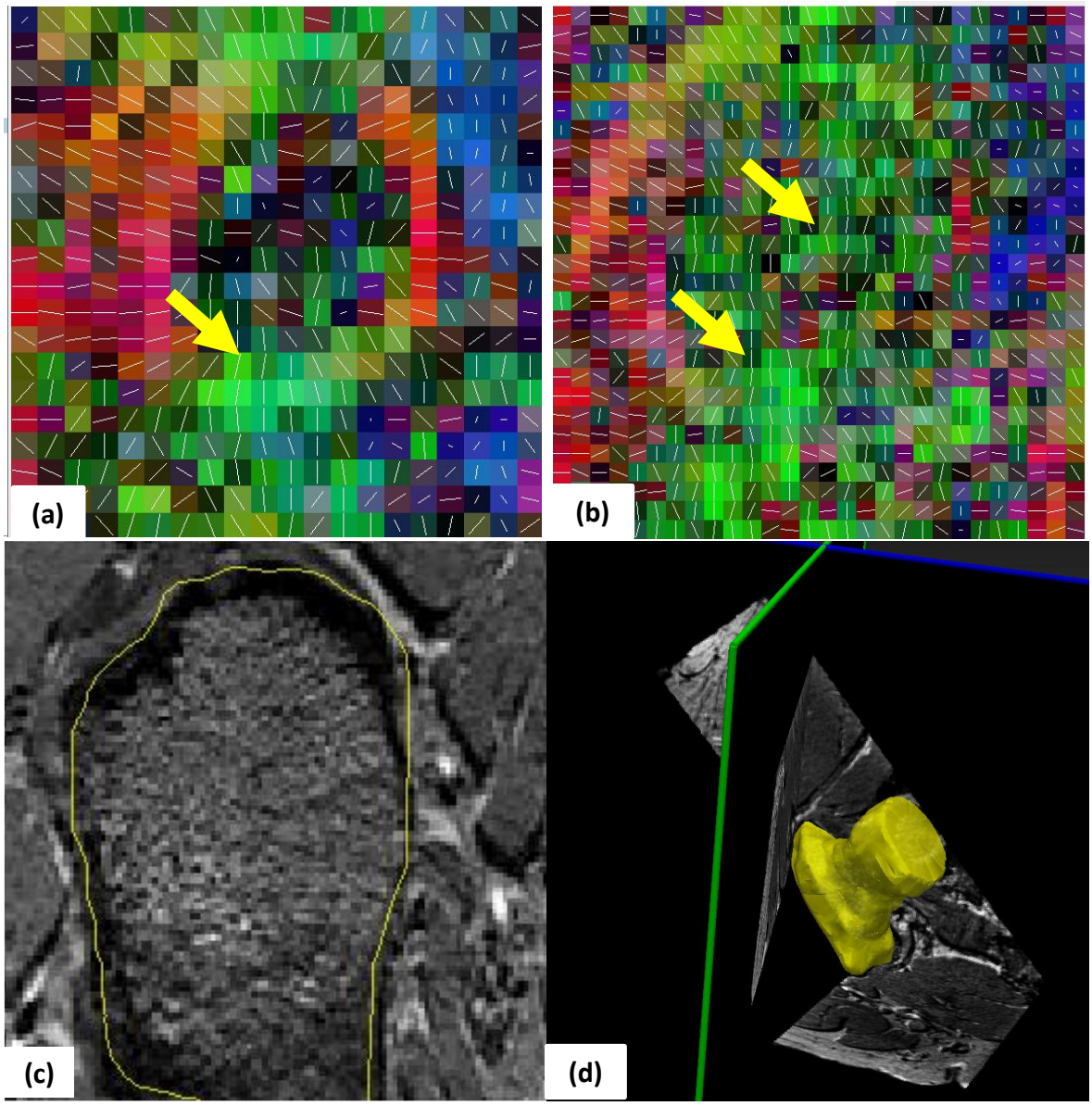

Figure 65. Qualitative comparison between SPENT tensor orientations from simulations with *in-vivo* MRI data of human femur using the two acquisition protocols. (a) Acquisition V_{P1}, resolution 1×1×1 mm^3, (b) acquisition V_{P2}, resolution 0.7×0.7×0.7 mm^3. Both simulations used a 20 SPENT gradient direction scheme. The two slices are roughly on the same anatomical position of the femur (indicated in c, d). Locations with coherent tensor orientations are indicated by yellow arrows in both plots. (c) The corresponding trabecular bone region in the same slice of volume V_{P2} as used in (b) as a reference of anatomical locations. (d) The global orientation of the acquisition with the 3D volume of the acquired femur neck model rendered with volume V_{P2}.

From the shown slice (from the acquisition plane), the principal orientations extracted using

data simulated with 20 SPENT gradient directions appear to be more coherent than those using only 6 gradient directions. The qualitative comparison is made between V_{P1} and V_{P2} in order to decide which settings would be good enough to continue with a group study in the future. As can be seen in Figure 65, the SPENT tensor principle direction plot in (b) is more informative and shows more coherence (yellow arrows) with the tensor orientations. Moreover, in the parts indicated by the yellow arrows, several columns contain more than 10 voxels with almost the same orientation in this slice. As the acquisition is made approximately along the femur neck whose trabecular bone orientation is quite organized and along the arc of the femur neck as described by Wolff's law, this may be a nice qualitative correspondence of the trajectory of the trabecular bone orientation in this position, although more experiments and quantitative validation are certainly needed before the conclusion can be drawn.

Discussion

The current results of 3D mSPENT are quite promising in terms of sub-voxel structural orientation detection. Especially in the second simulation study, the principal direction of the structural tensor shows very high structural coherence inside the femur head (where it is considered to contain highly anisotropic structure along the everyday force direction) with the second imaging protocol (dataset V_{P2}.) using 20 SPENT gradient directions. This also indicates that the SNR and resolution settings with this protocol would be appropriate for a group study involving patients by applying the mSPENT tensor analysis in a big k-space and compare it to the scoring from the measurement from BMD[14]. This preliminary study also supports the chosen VISTA (volumetric isotropic T_2 weighted Acquisition) sequence as a proper candidate to be modified to a 3D mSPENT sequence.

9.5 Summary

In this chapter, the efficacy of mSPENT has been demonstrated *ex-vivo* on a chicken femur. With the inhomogeneity information mSPENT provided, 2D microstructure anisotropy (i.e.

[14] This study is under the evaluation of the local ethic group while this thesis is being written.

orientation) is characterized voxel-wise. The orientation characterization was further validated by applying the methodology to a pineapple sample with an obvious fibre orientation. The results are promising; however more experiments are needed to establish mSPENT as a method to evaluate bone fracture risk *in-vivo*. Future development regarding 3D mSPENT technique is discussed with initial simulation results from a digital phantom and a 3D human femur data. Clinically, mSPENT may be able to provide both the bone volume fraction and the structural anisotropy quantifications at the same time, and eventually lead to an improvement of bone mechanic competence evaluation.

The author's contributions of this work are summarized as below:

1) The mSPENT sequence has been implemented and tested experimentally[15] (*ex-vivo*) on a fresh chicken femur. Specifically, the author's contribution in the sequence development stage was to debug the sequence on the scanner based on her simulation comparison on several k-space schemes for SPENT at arbitrary angle.
2) The mSPENT's ability of measuring tissue orientation has been validated on a pineapple sample.
3) Based on the coherence of the principal directions at each voxel, the internal fibres of the pineapple sample have been extracted.
4) A 3D simulation study of mSPENT has been conducted based on a digital phantom and *in-vivo* human femur data. An optimal mSPENT gradient direction distribution is used which can be directly applied on the clinical scanner. The 3D version of the SPENT Toolkit has been implemented. Preliminary results on extracting human femur trabecular bone orientation are encouraging.

[15] The author's contribution here is to help to tune and debug the sequence on the scanner.

Chapter 10. Conclusions

The lack of information at the finer scales leads to poor evaluation of the bone mechanical competence, which is critical for the prediction of bone fracture. The finer scale information carries important information of the on-going metabolic actions, thus might contain the "first hand" information of abnormalities at its early age.

In summary, the aim of this work has been to develop a multi-scale model-based method, in order that coarser scale information can be understood better via a fine scale model of bone. The idea is motivated by the hierarchical organization of bone and its anisotropic functional behaviour. Ideally, it would provide a new methodology which would be able to provide finer scale information for clinicians with the normal coarse resolution images achievable in clinical environment. This task is challenging for several reasons. Firstly, it is difficult for a single imaging method to provide information at all the scales. With multiple acquisition methods, it is possible but also difficult to acquire fine scale data *in-vivo*. Secondly, passing information across scales is a complicated task as the modelling assumptions on both scales have to be well considered and proper parameters need to be chosen. In the case of trabecular bone, its heterogeneous microstructure brings many problems for *in-vivo* imaging, such as susceptibility effects, and the resolution penalty. How to extract reliable anisotropy quantification of trabecular bone micro-structure is still an open question.

10.1 Key points

This research studies bone tissue at multiple scales. At macro-scale, knee joint motion is studied with in vivo body-weight-bearing observation of knee joint contact mechanism on cartilage surface (Chapter 4 and 5). This allows us to have an insight on the everyday force distribution onto the knee joint and its bony compositions, including femur and tibia. According to Wolff's Law [9], the everyday forces that are applied onto the whole bone organ are thought to be related to remodelling process of the bone tissue, and consequently influence the micro-structure of the bone. In particular the everyday force direction is along

the direction of the trabecular bone orientation [9]. Here lies the underneath link between the knee kinematics study in Chapter 4 and 5, and micro-scale trabecular bone network characterisation tasks as discussed in Chapter 6-9. At the finer level, bone density and anisotropy information determine the mechanical property of bone, thus also provide important insights of the bone fracture risk. Imaging aiming to extract anisotropy information is investigated. The measurement of the everyday forces can help to predict the trabecular bone remodelling, and thus the outcome of the available treatment; on the other side, the trabecular bone microstructure can also help to adjust patients' every day locomotion habit to reduce the risk of the potential fracture. Currently, such across scale investigation on knee joint is not available clinically [4]. In particular, the author's contributions in this multi-scale study are summarised as below:

1) A combined MR imaging strategy has been proposed, tuned and tested for *in-vivo* subject-specific knee joint functional study under body-weight bearing conditions, in which an interventional MR scanner (double donut system) is used to record the knee joint motion and a conventional clinical MR scanner is used to acquire the high resolution anatomical data. Such experimental configuration has the potential of characterising the applied everyday force direction and distribution applied onto the knee joint in-vivo, which influences the underneath trabecular bone remodelling and thus its patterns (i.e. orientation, whose in-vivo characterisation method is discussed in Chapters 6-9).

2) A systematic workflow is designed for 2D and 3D contact analysis on the knee joint. Its function is investigated via tibiofemoral articulation by tracking the contact point position on the cartilage surface against knee flexion angles. In this approach, a new reference system for knee flexion angle has been introduced in order to better describe the flexion angle between the femur and tibia (in comparison with the most commonly used visual determined flexion angle system). A dual-rigid registration method is equipped to map the recorded motion to the anatomical dataset. This leads to subject-specific in-vivo functional knee joint model, which can potentially be used to analyse the locomotion abnormality (as demonstrated on volunteer 6) and to improve the understanding of articular cartilage degeneration.

3) The feasibility of *in-vivo* red-marrow diffusion tensor imaging on human tibia epiphysis with a clinical scanner is demonstrated for the first time to our knowledge. The protocol is tuned locally on a 3T GE scanner (the original protocol is for brain analysis). A series of noise assessment has been performed in order to validate the origin of the signal (i.e. whether the red marrow diffuses). By using the diffusion tensor analysis, *in-vivo* orientation of marrow diffusion is rendered for the first time which can be used to reflect trabecular bone orientation "trajectory" model in such a two-phase porous media system. The reproducibility of this protocol has been evaluated for the further improvement of the protocol.

4) A new multi-directional dephaser MR pulse sequence, named mSPENT (multi-directional sub-pixel enhancement of nonuniform tissue[16]), has been proposed and designed to measure the sub-pixel tissue (e.g. trabecular bone) distribution inhomogeneity and orientation. A mSPENT simulator has been designed for the protocol optimization for imaging parameters such as the minimum required SNR, and the required number of SPENT gradient directions. A tensor-based method is introduced to retrieve the dominant orientation of the underlying tissue. Two indices, mean inhomogeneity and relative anisotropy, have been derived from the SPENT tensors and have been proposed for further tissue quantification. All the analysis have been programmed and incorporated into a home-made software named *SPENT Toolkit*.

5) The mSPENT sequence has been tested experimentally[17] (*ex-vivo*) on a fresh chicken femur. The mSPENT's ability of measuring tissue orientation has been qualitatively validated on a pineapple sample. Based on the coherence of the principal direction at each voxel, the internal fibres of the pineapple sample have been extracted using a fibre tracking algorithm adapted from that used in DTI.

---

[16] The sequence SPENT has been previously published and mSPENT made a significant modification for the original sequence.
[17] The author's contribution here is to help to tune and debug the sequence on the scanner.

10.2 Future work

10.2.1 About the knee joint functional study

The proposed combined MR imaging strategy provided very rich information to understand knee joint bending procedure. The localization of the contact points would be helpful to identify the stress distribution on the knee joint, thus to understand better the cause of the knee joint degeneration, especially in diseases such as OA. The *in-vivo* determination of the forces applied onto the knee joint is still a quite challenging task and is limited by the current technique. However, it has to be pointed out that the temporal resolution of the motion recording using MRI (i.e. the dynamic acquisition) is still poor. The spatial resolution is constrained by the magnetic field strength. In the double donut MRI system the signal sensitive volume is quite limited. This also stops us from exploring other motions and the other joints, such as hip joint or gaiting motion. To improve the temporal and spatial resolution in MRI, as well as to enlarge its FoV, is one of the ultimate goals in the whole MRI society. But some fast acquisition technique such as phase contrast cine sequence with spiral trajectory [154] may be able to reduce the difficulties for real-time motion recording. One reason that made us have chosen to use the open access system is that it allows the subjects to stand thus the natural physiological condition, i.e. body-weight bearing can be well preserved. An alternative solution to improve the spatial resolution might be to choose the conventional clinical scanner and a loading motion to simulate the force that body weight would apply on the knee joint.

In terms of the current subject-specific knee joint functional analysis, the contact point is considered as a key point to study its kinematics. The hypothesis is that the knee joint abnormality can be reflected by the differences between the trend of contacting between the tibiofemoral articulation of the normal subjects and the abnormal subjects. Although only 6 subjects are included in this study, their contact point motion with their knee joint flexion does show a difference among the 3 male subjects with normal knee joint and the 1 male subject with shrunk muscles on the thigh. The female subject's right knee joint also show some deviations from the men's knee joints. However, such variation might be caused by multiple reasons, such as gender, or the anthropological group. In a word, large group study

is necessary in the future to test this hypothesis more quantitatively.

10.2.2 About DTI in trabecular bone

Generally speaking, the bone marrow diffusion is indeed a very challenging task, for the bone marrow itself is quite mixed and the trabecular bone microstructure is very complicated. Although the red bone marrow contains relatively more water molecules, the signal is still not as strong as in locations such as brain where there is much more watery tissue. The attempt to look at the bone marrow diffusion anisotropy started from the knee joint, but not other locations with more clinical interests especially for diseases such as osteoporosis, such as hip joint or ankle joint. The consideration was mainly based on the practical reasons: the knee coil has a better performance on the GE scanner (according to the GE recommendation); the shape of the knee joint is much simpler than the hip joint. The EPI distortion is always a big concern in the clinical DTI protocols. In the current study, we mainly correct the drifting effects due to gradient system heating by aligning the dataset with the b0 acquisition using rigid registration. Additional distortions may come from the chemical shift from fat and the magnetic susceptibility variations (Chapter 16, [112]). Rather than post processing based registration, some improvement can be achieved by applying correction gradients (section 10.1, [112]) which requires the modifications of the pulse sequence.

The advantage of acquiring diffusion tensor data is to understand the orientation of the trabecular bone network *in-vivo* both globally and locally. As discussed in Chapter 2, the trabecular bone orientation (i.e. anisotropy) plays an important role in evaluating its mechanical properties. Previous work on bone marrow diffusion mainly focused on providing quantitative measurements such as ADC or FA which could be used to distinguish the bone marrow types, e.g. benign or malignant. Compared to these diffusion parameters, the orientation measurement implied by anisotropic diffusion may lead to the plot of the whole trabecular bone trajectory at each anatomical location. Before achieving this, it is important to validate the trabecular bone orientation derived from the diffusion tensors. A possible solution might be to start from the *ex-vivo* experiment, and then to compare the orientation models generated from bone sample filled with bone marrow, pure

water, and a mixture of fat and water in varying percentage. As DTI understands the trabecular bone structure by measuring the pore organization, orientation models derived from direct imaging facilities, such as (micro-) CT are also needed as a plausible ground truth. Although the work looks vital, it would help us to identify the various problems that we could face during the real acquisition.

10.2.3 About the mSPENT sequence

Without having to use EPI as the signal read-out, mSPENT might be a good alternative for trabecular bone network quantification as it is based on a SE sequence which produces less geometric distortion. It manipulates the spin system by modulating the dephasing gradients so that the detected signals are mapped to the inhomogeneity information inside a voxel. It has to be pointed out that mSPENT is not a "super" sequence that can see as tiny structure as people would like to. It is also regulated by the principles inside k-space. However, the attraction may be its ability to measure both BVF and anisotropy and provide a net trabecular bone index, through a combined model as proposed in Section 9.4.2. But for sure, more experiments are needed in order to illustrate the principle idea of this method and to use it as a surrogate of DEXA. One initial validation has been made by imaging the internal structure of a pineapple sample. However, in order to further validate the protocol, especially the orientation measurement, more quantitative validation results are needed. An effective approach is to compare the orientation measurement between mSPENT and micro-CT.

The noise issue is a big concern of this sequence as the dephasing signal is low compared to the normal SE signal, thus there is a minimum SNR requirement. Preliminary research has been performed regarding the SNR requirements through both simulation and experimental data. The experiment is not directly on the SPENT data but on high resolution FSE data (Section 9.3.5). Although the original aim is to assess whether the high frequency signal is purely noise or is the actual signal from the tissue, it actually presents the requirement on SNR for the optimal use of the sequence. The resolution requirement is another issue. As shown in Section 8.1, at different levels inside each voxel tissue magnetization show changing degree of inhomogeneity. It has been planned to perform a spectrum study with

varying resolution for mSPENT to observe the behaviour of orientation measurement experimentally. As the imaging resolution is directly linked to the physical scales, the spectrum study will be essentially helpful to know how the information is clustered.

The current version of mSPENT pulse sequence is still 2D and *ex-vivo*. The next step is to extend it to 3D sequence and apply it *in-vivo*. The data processing on 3D mSPENT data has already been demonstrated. The major difficulty is how to modify the sequence as it is not trivial to shift the k-space centre.

10.3 Potential applications

The proposed methods could potentially be grouped together to evaluate the bone mechanical competence of the knee joint from a more patient-specific point of view: the individual's everyday force direction and locations derived using the proposed combined MR imaging strategy might be compared and related to the trabecular bone orientation measured by either DTI or mSPENT and trabecular bone volume fraction, to form a net score globally and locally to predict the fracture risk of the knee joint bone, and to provide advice of reducing such risk by physical training to avoid further destruction in the regions which are weaker. It also has a potential in drug and post-treatment evaluation.

Publications resulting from this work

Peer-reviewed journal papers

B. Chen, T. Lambrou, A. Offiah, M. Fry, and A. Todd-Pokropek, "Combined MR imaging towards subject-specific knee contact analysis," *The Visual Computer*, vol. 27, pp. 121–128, 2011. 10.1007/s00371-010-0535-x.

B. Chen, T. Lambrou, A. C. Offiah, P. A. Gondim Teixeira, M. Fry, and A. Todd-Pokropek, "An in vivo subject-specific 3D functional knee joint model using combined MR imaging," International Journal of Computer Assisted Radiology and Surgery, 10.1007/s11548-012-0801-7 (Online Early View)

Conference proceedings

B. Chen, B. Siow, D. Carmichael, F. Odille, R. Oridge, and A. Todd-Pokropek, "Characterizing tissue microstructure orientation by multi-directional sub-pixel enhancement of nonuniform tissue (SPENT) sequence," in *19th Annual Meeting of International Society of Magnetic Resonance in Medicine (ISMRM*, Montreal), p. 4521, 2011.

B. Chen, P.-A. Vuissoz, A. Offiah, M. Fry, and A. Todd-Pokropek, "Diffusion Tensor Imaging (DTI) as a probe to measure trabecular bone orientation *in-vivo*," in *18th Annual Meeting of International Society of Magnetic Resonance in Medicine (ISMRM*, Stockholm), p. 3198, 2010.

B. Chen, B. Siow, D. Carmichael, F. Odille, R. Oridge, and A. Todd-Pokropek, "Characterization of trabecular bone orientation by multi-directional SPENT (sub-pixel enhancement of non-uniform tissue)," in *18th Annual Meeting of International Society of Magnetic Resonance in Medicine (ISMRM*, Stockholm), p. 793, 2010.

B. Chen, T. Lambrou, M. Fry, and A. Todd-Pokropek, "Combined-MR imaging for functional studies of the knee." in *95th Scientific Assembly and Annual Meeting of Radiological Society of North America*, (Chicago, US), November 2009.

B. Chen, P.-A. Vuissoz, A. Offiah, M. Fry, and A. Todd-Pokropek, "Measure trabecular bone orientation by diffusion tensor imaging.," in *The 5th International Conference on Imaging Technologies in Biomedical Sciences (ITBS): From Physiology and Cellular Biology to Pathology through Imaging*, (Milos, Greece), September 2009.

B. Chen, T. Lambrou, M. Fry, and A. Todd-Pokropek, "Combined mr imaging for anatomical and functional knee joint model," in *International Journal of Computer Assisted Radiology and Surgery (Proceedings of CARS conference)*, vol. 3 of *Suplement 1*, (Berlin, Germany), Springer, June 2009.

B. Chen, M. Fry, T. Lambrou, A. C. Offiah, and A. Todd-Pokropek, "Multiscale modeling and imaging: The challenges of osteogenesis imperfecta.," in *Proceedings of the 12th Annual Conference on Medical Image Understanding and Analysis (MIUA)*, (Dundee, UK), July 2008.

P. Del-Manso, **B. Chen**, M. Fry, and A. Todd-Pokropek, "Multi-scale images of bone and cartilage in joints: a model based approach to incorporate the fine structure information of tissue.," in *International Journal of Computer Assisted Radiology and Surgery (Proceedings of CARS conference)*, vol. 3 of *Suplement 1*, (Barcelona, Spain), p. S365, Springer, June 2008.

Appendix A Imaging Protocols

A.1 Combined MR Imaging protocol

	Dynamic MRI	Static MRI
Manufacture	GE (0.5T Signa)	GE (1.5T Signa)
Sequence name	2D FSPGR (multi-slice)	3D FSPGR
In-plane resolution(mm^2)	1.09×1.09	0.31×0.31
Slice thickness(mm)	5	0.7
Number of averaging (NEX)	1	5
Echo Time (TE, ms)	7.8	3.296
Repetition Time (TR, ms)	16.1	9.219
Pixel Bandwidth	100	244.141
Acquisition Matrix	256×128	384×256
number of slices	20	140
Acquisition Plane	sagittal	sagittal
Flip Angle	60	60
Image matrix size	256× 256	512×512

A.2 High resolution knee joint imaging protocol on 3T

Manufacture	GE (3.0 T HDx Signa)
Sequence name	3D MERGE
In-plane resolution(mm^2)	0.39×0.39
Slice thickness(mm)	1
Number of averaging (NEX)	1
Echo Time (TE, ms)	10.36
Repetition Time (TR, ms)	30
Pixel Bandwidth	100
Acquisition Matrix	320×288
number of slices	144
Acquisition Plane	sagittal
Flip Angle	5
Image matrix size	512× 512

A.3 DTI protocol of *in-vivo* trabecular bone

Volunteer	b-value ($s \cdot mm^{-2}$)	Number of gradient directions	Number of *b-value* = 0 measurement	In-plane resolution (mm^2)	Slice thickness (mm)	Frequency encoding direction	NEX	TR(ms)	TE (ms)	Acq. Matrix	Image volume matrix size
volunteer 1: 46 year-old male	200 [a]	20	4	0.7031 × 0.7031	3.2	Right-Left (R-L)	4	6000	76.8	128 × 128	256×256×23
	400 [a,b]							6000	76.8		
	600 [a]							6200	81.6		
	800 [a]					R-L		6500	85.6		
	1000[a]					R-L		7000	89		
	400					Anterior-posterior (A-P)		6000	76.8		
	400					R-L		6000	76.8		256×256×24
	400					R-L		6000	76.8		
volunteer 2: 20 year-old male	400 [b]	20	4	0.7031 × 0.7031	3.2	R-L	4	6000	76.8	128 × 128	256×256×24
	400 [d]					A-P		6000	76.8		
volunteer 3: 42 year-old female	400 [c]	20	4	0.7031 × 0.7031	3.2	R-L	4	7000	76.8	128 × 128	256×256×29
	400 [c]					R-L		7000	76.8		
	400 [c]					R-L		7000	76.8		

[a] Experiment 1: *b-value* observation, with uniformly distributed gradient directions on a unit sphere [b] Experiment 2: to try to achieve higher resolution and compare with Experiment 1. [c] Experiment 3: with higher resolution and more importantly, the thinner slice thickness and no gap between slices. NEX = 16 is set in order to increase the SNR. [d] Experiment 4: Failed due to too much noise

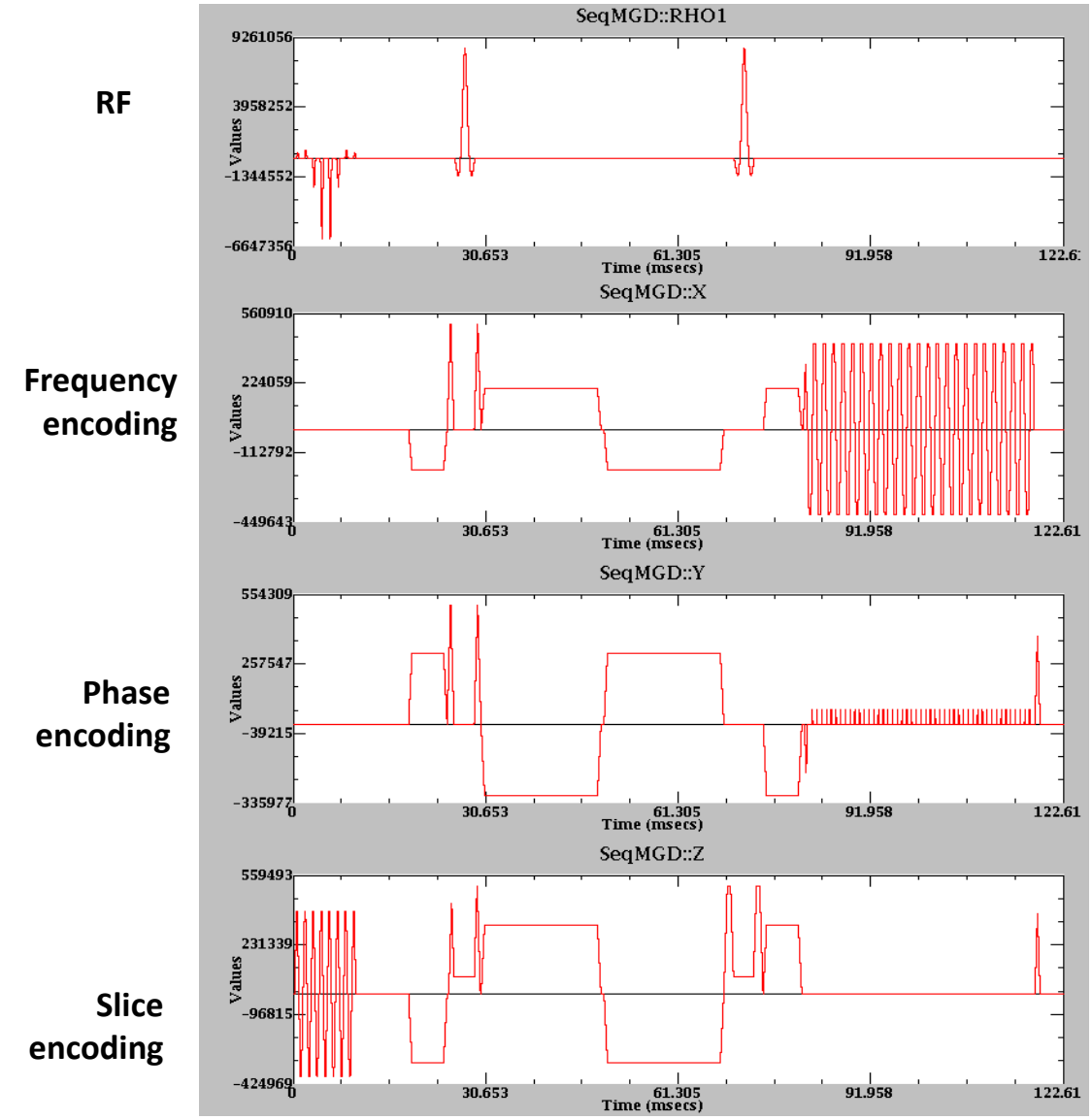

Figure 66. The dual echo-sequence plot on the 3T GE scanner.

Appendix B the mSPENT toolkit

The SPENT toolkit is an in-house software in MATLAB developed specially for analyzing the data acquired by the mSPENT sequence. It currently has two versions: a user-friendly GUI version (Figure 67) and a slightly complicated script version. The current toolkit has several functionalities as below:

1. 3D volume navigator (left column) with the contrast and intensity adjustment.

2. Tensor reconstruction (middle column): As the current sequence is to build a structural tensor based on the inhomogeneity measured in each voxel. The SPENT tensors are reconstructed using an ellipse model (currently mSPENT is still in 2D) as in diffusion tensor imaging (DTI).

3. Eigen system decomposition and parametric maps (middle column): A voxel-wise eigen decomposition is applied. The principal eigenvectors are shown (scaled to the corresponding eigenvalue). Parametric maps including trace, relative anisotropy and fractional anisotropy are computed like in DTI. But physically, it shows the degree of inhomogeneity of the underlying microstructure.

4. Tractography (the right bottom pannel): Streamlines are computed and plotted based on the coherence of principal orientations of these tensors, as tractography used in DTI.

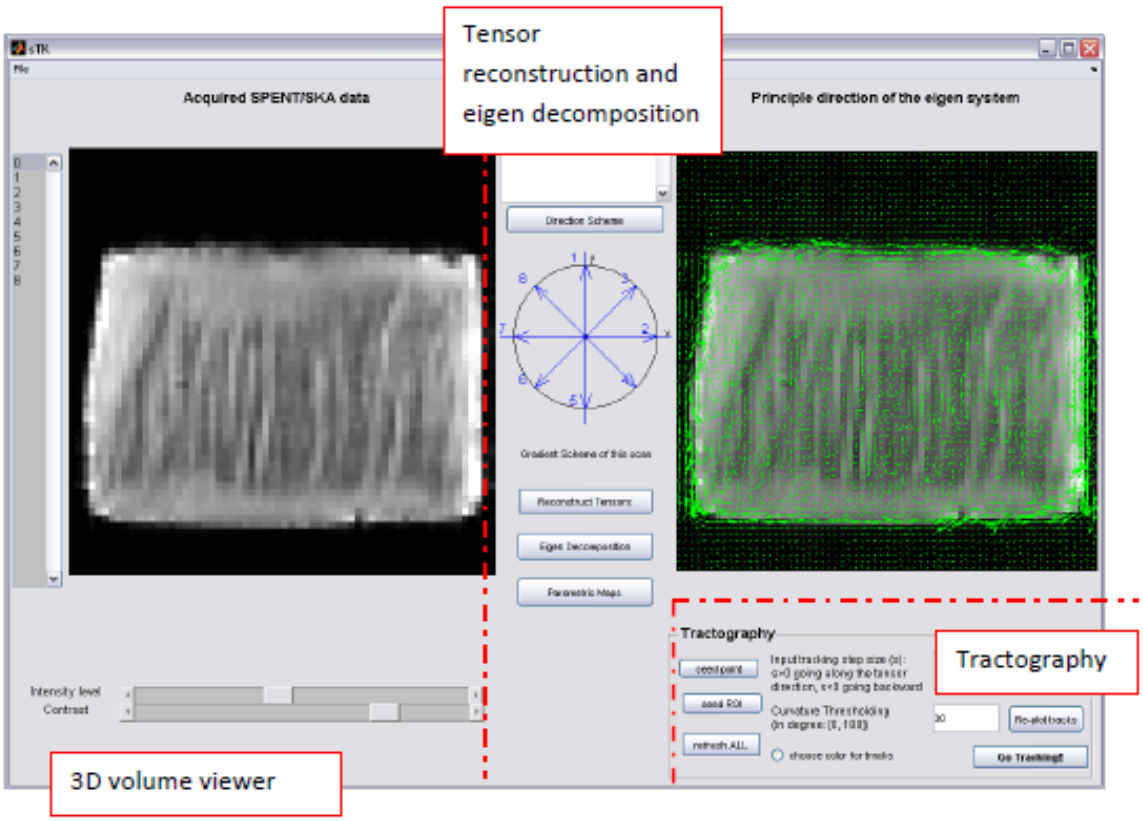

Figure 67. A general view of SPENT tookkit: the left is a 3D viewer of the acquired data

References:

[1] D. T. Campbell, *'Downward causation' in hierarchically organised biological systems*. Macmillan, 1974.

[2] J. Demongeot, J. Bezy-Wendling, J. Mattes, P. Haigron, N. Glade, and J. Coatrieux, "Multiscale modeling and imaging: the challenges of biocomplexity," *Proceedings of the IEEE*, vol. 91, pp. 1723 – 1737, Oct 2003.

[3] J. W. Fenner, B. Brook, G. Clapworthy, P. V. Coveney, V. Feipel, H. Gregersen, D. R. Hose, P. Kohl, P. Lawford, K. M. McCormack, D. Pinney, S. R. Thomas, S. V. S. Jan, S. Waters, and M. Viceconti, "The EuroPhysiome, STEP and a roadmap for the virtual physiological human," *Philosophical Transactions of the Royal Society A: Mathematical, Physical and Engineering Sciences*, vol. 366, pp. 2979–2999, Sept 2008.

[4] M. Viceconti, *Multiscale Modeling of the Skeletal System*. Cambridge University Press, Nov. 2011.

[5] S. Weiner and H. D. Wagner, "The material bone: Structure-mechanical function relations," *Annual Review of Materials Science*, vol. 28, pp. 271–298, Aug 1998.

[6] D. Christen, D. J. Webster, and R. Müller, "Multiscale modelling and nonlinear finite element analysis as clinical tools for the assessment of fracture risk," *Philosophical Transactions of the Royal Society A: Mathematical, Physical and Engineering Sciences*, vol. 368, pp. 2653 –2668, June 2010.

[7] F. W. Wehrli, "Structural and functional assessment of trabecular and cortical bone by micro magnetic resonance imaging.," *J Magn Reson Imaging*, vol. 25, pp. 390–409, Feb. 2007.

[8] W. S. S. Jee, *Bone Mechanics Handbook*, ch. 1.Integrated Bone Tissue Physiology: Anatomy and Physiology, pp. 1(1–68). Informa HealthCare, 2001.

[9] J. Wolff, "Das gesetz der transformation der knochen," *A. Hirschwald*, 1892.

[10] T. Steiniche and E. M. Hague, *Normal Structure and function of Bone*, ch. 3, pp. 59–72. Humana Press, 2003.

[11] F. Linde, "Elastic and viscoelastic properties of trabecular bone by a compression testing approach," *Danish medical bulletin*, vol. 41, pp. 119–38, Apr. 1994.

[12] J. S. Beck and B. E. Nordin, "Histological assessment of osteoporosis by iliac crest biopsy.," *J Pathol Bacteriol*, vol. 80, pp. 391–397, Oct. 1960.

[13] NIH consensus statement, 17(1), page, 1-45, *Consensus Development Conference Osteoporosis prevention, diagnosis, and therapy*, 2001.

[14] London: Royal College of Physicians, "Osteoarthritis: national clinical guideline for care and management in adults." http://www.ncbi.nlm.nih.gov/books/NBK48984/, 2008.

[15] S. Krasnokutsky, M. Attur, G. Palmer, J. Samuels, and S. Abramson, "Current concepts in the pathogenesis of osteoarthritis," *Osteoarthritis and Cartilage*, vol. 16, pp. S1–S3, Oct. 2008.

[16] NIH Osteoporosis and Related Bone Diseases National Resource Center, "Osteogenesis imperfecta overview."
http://www.niams.nih.gov/Health_Info/Bone/Osteogenesis_Imperfecta/overview.asp.

[17] C. Land, F. Rauch, C. F. Munns, S. Sahebjam, and F. H. Glorieux, "Vertebral morphometry in children and adolescents with osteogenesis imperfecta: effect of intravenous pamidronate treatment.," *Bone*, vol. 39, pp. 901–906, Oct 2006.

[18] E. Luccihinetti, *Bone Mechanics Handbook*, ch. 12 Composite models of bone properties, pp. 12(1–19). CRC Press, 2001.

[19] B. Riggs, "Overview of osteoporosis," *Western Journal of Medicine*, vol. 154, pp. 63–77, 1991.

[20] F. W. Wehrli, P. K. Saha, B. R. Gomberg, H. K. Song, P. J. Snyder, M. Benito, A. Wright, and R. Weening, "Role of magnetic resonance for assessing structure and function of trabecular bone," *Topics in Magnetic Resonance Imaging*, vol. 13, pp. 335–355, Oct 2002.

[21] C. H. Turner, S. C. Cowin, J. Y. Rho, R. B. Ashman, and J. C. Rice, "The fabric dependence of the orthotropic elastic constants of cancellous bone.," *J Biomech*, vol. 23, no. 6, pp. 549–561, 1990.

[22] R. Müller, B. F, S. SY, and H. MK, "Mechano-structure relationships in normal, ovariectomized and ibandronate treated aged macaques as assessed by micro-tomographic imaging and biomechanical testing," in *Proceedings of the 47th Annual Meeting, Orthopaedic Research Society, San Francisco, California*, (San Francisco, CA, USA), 2001.

[23] D. J. Tyler, M. D. Robson, R. M. Henkelman, I. R. Young, and G. M. Bydder, "Magnetic resonance imaging with ultrashort TE (UTE) pulse sequences: technical considerations.," *J Magn Reson Imaging*, vol. 25, pp. 279–289, Feb 2007.

[24] P. Schneider, M. Stauber, R. Voide, M. Stampanoni, L. R. Donahue, and R. Müller, "Ultrastructural properties in cortical bone vary greatly in two inbred strains of mice as assessed by synchrotron light based micro- and nano-CT.," *J Bone Miner Res*, vol. 22, pp. 1557–1570, Oct 2007.

[25] A. Odgaard, *Bone Mechanics Handbook*, ch. 14. Quantification of Cancellous Bone Architecture, pp. 14–1. CRC Press, 2001.

[26] H. Gundersen, R. Boyce, J. Nyengaard, and A. Odgaard, "The conneulor: unbiased estimation of connectivity using physical disectors under projection.," *Bone*, vol. 14, pp. 217–222, 1993.

[27] A. M. Parfitt, C. H. Mathews, A. R. Villanueva, M. Kleerekoper, B. Frame, and D. S. Rao, "Relationships between surface, volume, and thickness of iliac trabecular bone in aging and in osteoporosis. Implications for the microanatomic and cellular mechanisms of bone loss.," *J Clin Invest*, vol. 72, pp. 1396–1409, Oct 1983.

[28] S. C. Cowin and S. Doty, *Tissue Mechanics*, ch. 8 Modelling Material Microstructure, p. 239. Springer, 2007.

[29] M. Kleerekoper, A. R. Villanueva, J. Stanciu, D. S. Rao, and A. M. Parfitt, "The role of three-dimensional trabecular microstructure in the pathogenesis of vertebral compression fractures.," *Calcif Tissue Int*, vol. 37, pp. 594–597, Dec 1985.

[30] L. Pothuaud and S. Majumdar, *The Physical Measurement of Bone*, ch. 13. Magnetic resonance imaging, p. 379. Medical Physics and Biomedical Engineering, Institute of Physics, 2003.

[31] S. Majumdar, H. K. Genant, S. Grampp, D. C. Newitt, V. H. Truong, J. C. Lin, and A. Mathur, "Correlation of trabecular bone structure with age, bone mineral density, and osteoporotic status: in vivo studies in the distal radius using high resolution magnetic resonance imaging.," *J Bone Miner Res*, vol. 12, pp. 111–118, Jan 1997.

[32] B. Vasilic and F. Wehrli, "A novel local thresholding algorithm for trabecular bone volume fraction mapping in the limited spatial resolution regime of in vivo MRI," *IEEE Trans Med Imaging*, vol. 24, no. 12, pp. 1574–1585, 2005.

[33] S. N. Hwang and F. W. Wehrli, "Estimating voxel volume fractions of trabecular bone on the basis of magnetic resonance images acquired in vivo," *International Journal of Imaging Systems and Technology*, vol. 10, pp. 186 – 198, 1999.

[34] S. Hwang and F. Wehrli, "A fast method for estimating voxel bone volume fractions from in vivo high-resolution MR images," in *Proceedings 9th Scientific Meeting, International Society for Magnetic Resonance in Medicine, Glasgow*, 2001.

[35] Z. Wu, H. W. Chung, and F. W. Wehrli, "A Bayesian approach to subvoxel tissue classification in NMR microscopic images of trabecular bone.," *Magn Reson Med*, vol. 31, pp. 302–308, Mar 1994.

[36] S. N. Hwang and F. W. Wehrli, "Subvoxel processing: a method for reducing partial volume blurring with application to in vivo MR images of trabecular bone.," *Magn Reson Med*, vol. 47, pp. 948–957, May 2002.

[37] L. Feldkamp, S. Goldstein, A. Parfitt, G. Jesion, and K. M., "The direct examination of three-dimensional structure bone structure in vitro by computed tomography," *Journal of Bone Mineral Research*, vol. 4, pp. 3–11, 1989.

[38] J. Kabel, A. Odgaard, B. van Rietbergen, and R. Huiskes, "Connectivity and the elastic properties of cancellous bone.," *Bone*, vol. 24, pp. 115–120, Feb 1999.

[39] T. Hildebrand and P. Rüegsegger, "Quantification of bone microarchitecture with the structure model index.," *Comput Methods Biomech Biomed Engin*, vol. 1, no. 1, pp. 15–23, 1997.

[40] T. Hildebrand, A. Laib, R. Müller, J. Dequeker, and P. Rüegsegger, "Direct three-dimensional morphometric analysis of human cancellous bone: microstructural data from spine, femur, iliac crest, and calcaneus.," *J Bone Miner Res*, vol. 14, pp. 1167–1174, Jul 1999.

[41] W. J. Whitehouse, "The quantitative morphology of anisotropic trabecular bone.," *J Microsc*, vol. 101, pp. 153–168, Jul 1974.

[42] T. Harrigan and R. Mann, "Characterization of microstructural anisotropy in orthotropic materials using a second rank tensor," *Journal of Materials Science*, vol. 19, pp. 761–767, 1984.

[43] S. C. Cowin, "Wolff's law of trabecular architecture at remodeling equilibrium," *J. Biomech Eng*, vol. 108, pp. 83–88, 1986.

[44] G. H. Odgaard A, Jensen EB, "Estimation of structural anisotropy based on volume orientation. A new concept.," *Journal of Microscopy*, vol. 157, pp. 149–162, 1990.

[45] L. Cruz-Orive, L. M. Karlsson, S. E. Larsen, and F. Wainschtein, "Characterizing anisotropy: A new concept," *Micron and Microscopica Acta*, vol. 23, pp. 75–76, 1992.

[46] A. Odgaard, J. Kabel, B. van Rietbergen, M. Dalstra, and R. Huiskes, "Fabric and elastic principal directions of cancellous bone are closely related.," *J Biomech*, vol. 30, pp. 487–495, May 1997.

[47] A. Odgaard, "Three-dimensional methods for quantification of cancellous bone architecture," *Bone*, vol. 20, pp. 315–328, April 1997.

[48] S. C. Cowin, "The relationship between the elasticity tensor and the fabric tensor," *Mechanics of Materials*, vol. 4, pp. 137–147, 1985.

[49] B. R. Gomberg, P. K. Saha, and F. W. Wehrli, "Topology-based orientation analysis of trabecular bone networks.," *Med Phys*, vol. 30, pp. 158–168, Feb 2003.

[50] S. N. Hwang, F. W. Wehrli, and J. L. Williams, "Probability-based structural parameters from three-dimensional nuclear magnetic resonance images as predictors of trabecular bone strength.," *Med Phys*, vol. 24, pp. 1255–1261, Aug 1997.

[51] M. J. Wald, B. Vasilic, P. K. Saha, and F. W. Wehrli, "Spatial autocorrelation and mean intercept length analysis of trabecular bone anisotropy applied to in vivo magnetic resonance

imaging.," *Med Phys*, vol. 34, pp. 1110–1120, Mar 2007.

[52] P. K. Saha, "Novel theory and methods for tensor scale: a local morphometric parameter," in *Proceedings of SPIE: Medical Imaging* (M. Sonka and J. M. Fitzpatrick, eds.), vol. 5032, (San Diego, CA), pp. 314–324, SPIE, 2003.

[53] P. Saha and F. Wehrli, "A robust method for measuring trabecular bone orientation anisotropy at in vivo resolution using tensor scale," *Pattern Recognition*, vol. 37, pp. 1935–1944, Sept 2004.

[54] J. A. Lynch, D. J. Hawkes, and J. C. Buckland-Wright, "Analysis of texture in macroradiographs of osteoarthritic knees, using the fractal signature," *Physics in Medicine and Biology*, vol. 36, pp. 709–722, June 1991.

[55] W.-J. Yi, M.-S. Heo, S.-S. Lee, S.-C. Choi, and K.-H. Huh, "Comparison of trabecular bone anisotropies based on fractal dimensions and mean intercept length determined by principal axes of inertia.," *Med Biol Eng Comput*, vol. 45, pp. 357–364, April 2007.

[56] Z. Tabor and E. Rokita, "Quantifying anisotropy of trabecular bone from gray-level images.," *Bone*, vol. 40, pp. 966–972, April 2007.

[57] B. van Rietbergen, *the Physical measurement of bone*, ch. 15. Finite element modeling, pp. 477–510. Institute of Physics, 2003.

[58] J. F. Nye, *Physical Properties of Crystals: Their Representation by Tensors and Matrices (Paperback)*. Oxford University Press, USA, 1985.

[59] H. J. Bunge, *Texture analysis in materials science: mathematical methods*. Butterworths, 1982.

[60] S. C. Cowin and S. Doty, *Tissue Mechanics*, ch. 11 Bone Tissue, pp. 341–384. Springer, 2007.

[61] N. Palastanga, D. Field, and R. Soames, eds., *Anatomy and human movement: structure and function*, ch. 3. The lower limb, pp. 356–395. Edinburgh : Butterworth-Heinemann, 2006.

[62] P. N. Smith, K. M. Refshauge, and J. M. Scarvell, "Development of the concepts of knee kinematics.," *Arch Phys Med Rehabil*, vol. 84, pp. 1895–1902, Dec 2003.

[63] V. Pinskerova, P. Johal, S. Nakagawa, A. Sosna, A. Williams, W. Gedroyc, and M. A. Freeman, "Does the femur roll-back with flexion?," *J Bone Joint Surg Br*, vol. 86, pp. 925–931, Aug 2004.

[64] A. Williams and M. Logan, "Understanding tibio-femoral motion.," *Knee*, vol. 11, pp. 81–88, Apr 2004.

[65] S. Todo, Y. Kadoya, T. Moilanen, A. Kobayashi, Y. Yamano, H. Iwaki, and M. A. Freeman, "Anteroposterior and rotational movement of femur during knee flexion.," *Clin Orthop Relat Res*, pp. 162–170, May 1999.

[66] H. Iwaki, V. Pinskerova, and M. A. Freeman, "Tibiofemoral movement 1: the shapes and relative movements of the femur and tibia in the unloaded cadaver knee.," *J Bone Joint Surg Br*, vol. 82, pp. 1189–1195, Nov 2000.

[67] P. F. Hill, V. Vedi, A. Williams, H. Iwaki, V. Pinskerova, and M. A. Freeman, "Tibiofemoral movement 2: the loaded and unloaded living knee studied by MRI.," *J Bone Joint Surg Br*, vol. 82, pp. 1196–1198, Nov 2000.

[68] S. Nakagawa, Y. Kadoya, S. Todo, A. Kobayashi, H. Sakamoto, M. A. Freeman, and Y. Yamano, "Tibiofemoral movement 3: full flexion in the living knee studied by MRI.," *J Bone Joint Surg Br*, vol. 82, pp. 1199–1200, Nov 2000.

[69] J. Karrholm, S. Brandsson, and M. A. Freeman, "Tibiofemoral movement 4: changes of axial

tibial rotation caused by forced rotation at the weight-bearing knee studied by RSA.," *J Bone Joint Surg Br*, vol. 82, pp. 1201–1203, Nov 2000.

[70] M. A. Freeman and V. Pinskerova, "The movement of the normal tibio-femoral joint.," *J Biomech*, vol. 38, pp. 197–208, Feb 2005.

[71] P. Wretenberg, D. K. Ramsey, and G. Németh, "Tibiofemoral contact points relative to flexion angle measured with MRI.," *Clin Biomech (Bristol, Avon)*, vol. 17, pp. 477–485, Jul 2002.

[72] G. Li, J. Gil, A. Kanamori, and S. L. Woo, "A validated three-dimensional computational model of a human knee joint.," *J Biomech Eng*, vol. 121, pp. 657–662, Dec 1999.

[73] L. E. DeFrate, H. Sun, T. J. Gill, H. E. Rubash, and G. Li, "In vivo tibiofemoral contact analysis using 3D MRI-based knee models.," *J Biomech*, vol. 37, pp. 1499–1504, Oct 2004.

[74] T. F. Besier, C. E. Draper, G. E. Gold, G. S. Beaupré, and S. L. Delp, "Patellofemoral joint contact area increases with knee flexion and weight-bearing.," *J Orthop Res*, vol. 23, pp. 345–350, Mar 2005.

[75] A. Hosseini, S. K. V. de Velde, M. Kozanek, T. J. Gill, A. J. Grodzinsky, H. E. Rubash, and G. Li, "In-vivo time-dependent articular cartilage contact behavior of the tibiofemoral joint.," *Osteoarthritis Cartilage*, vol. 18, pp. 909–916, Jul 2010.

[76] B. Chen, T. Lambrou, A. Offiah, M. Fry, and A. Todd-Pokropek, "Combined MR imaging towards subject-specific knee contact analysis," *The Visual Computer*, vol. 27, pp. 121–128, Feb 2011.

[77] S. Cowin, ed., *Bone Mechanics Handbook*. Informa HealthCare, 2001.

[78] X. E. Guo, *Bone Mechanics Handbook*, ch. 10 Bone Mechanics, pp. 10(1–24). Informa HealthCare, 2001.

[79] B. van Rietbergen, A. Odgaard, J. Kabel, and R. Huiskes, "Direct mechanics assessment of elastic symmetries and properties of trabecular bone architecture.," *J Biomech*, vol. 29, pp. 1653–1657, Dec 1996.

[80] B. van Rietbergen, A. Odgaard, J. Kabel, and R. Huiskes, "Relationships between bone morphology and bone elastic properties can be accurately quantified using high-resolution computer reconstructions.," *J Orthop Res*, vol. 16, pp. 23–28, Jan 1998.

[81] G. Yang, J. Kabel, B. Van Rietbergen, A. Odgaard, R. Huiskes, and S. Cowin, "The anisotropic Hooke's law for cancellous bone and wood," *Journal of Elasticity*, vol. 53, pp. 125–146, 11 1998.

[82] S. Cowin and G. Yang, "Averaging anisotropic elastic constant data," *Journal of Elasticity*, vol. 2, pp. 151–180, 1997.

[83] B. van Rietbergen, H. Weinans, R. Huiskes, and A. Odgaard, "A new method to determine trabecular bone elastic properties and loading using micromechanical finite-element models.," *J Biomech*, vol. 28, pp. 69–81, Jan 1995.

[84] J. Kabel, B. van Rietbergen, A. Odgaard, and R. Huiskes, "Constitutive relationships of fabric, density, and elastic properties in cancellous bone architecture.," *Bone*, vol. 25, pp. 481–486, Oct 1999.

[85] S. C. Cowin, "Bone poroelasticity.," *J Biomech*, vol. 32, pp. 217–238, Mar 1999.

[86] S. C. Cowin and S. Doty, *Tissue Mechanics*, ch. 5 Modelling Material Symmetry, pp. 341–384. Springer, 2007.

[87] C. Langton and C. Njeh, eds., *The Physical Measurement of Bone*. Institute of Physics, 2003.

[88] F. Taddei, E. Schileo, B. Helgason, L. Cristofolini, and M. Viceconti, "The material mapping strategy influences the accuracy of CT-based finite element models of bones: an evaluation against experimental measurements.," *Med Eng Phys*, vol. 29, pp. 973–979, Nov 2007.

[89] E. Schileo, E. Dall'ara, F. Taddei, A. Malandrino, T. Schotkamp, M. Baleani, and M. Viceconti, "An accurate estimation of bone density improves the accuracy of subject-specific finite element models.," *J Biomech*, vol. 41, pp. 2483–2491, Aug 2008.

[90] D. A. Yablonskiy, W. R. Reinus, H. Stark, and E. M. Haacke, "Quantitation of T_2' anisotropic effects on magnetic resonance bone mineral density measurement.," *Magn Reson Med*, vol. 37, pp. 214–221, Feb 1997.

[91] M. D. Jergas, S. Majumdar, J. H. Keyak, I. Y. Lee, D. C. Newitt, S. Grampp, H. B. Skinner, and H. K. Genant, "Relationships between young modulus of elasticity, ash density, and MRI derived effective transverse relaxation T_2^* in tibial specimens.," *J Comput Assist Tomogr*, vol. 19, no. 3, pp. 472–479, 1995.

[92] F. W. Wehrli, J. C. Ford, M. Attie, H. Y. Kressel, and F. S. Kaplan, "Trabecular structure: preliminary application of MR interferometry.," *Radiology*, vol. 179, no. 3, pp. 615–621, 1991.

[93] S. Majumdar, D. Thomasson, A. Shimakawa, and H. K. Genant, "Quantitation of the susceptibility difference between trabecular bone and bone marrow: experimental studies.," *Magn Reson Med*, vol. 22, pp. 111–127, Nov 1991.

[94] H. Chung, F. W. Wehrli, J. L. Williams, and S. D. Kugelmass, "Relationship between NMR transverse relaxation, trabecular bone architecture, and strength.," *Proc Natl Acad Sci U S A*, vol. 90, pp. 10250–10254, Nov 1993.

[95] B. Vasilic, J. Magland, M. Wald, and F. W. Wehrli, "Advantages of isotropic voxel size for classification of trabecular bone struts and plates in micro-MR images," in *Proceedings of 16th Scientific Meetings and Exhibitions of ISMRM, Toronto*, 2008.

[96] M. D. Robson, P. D. Gatehouse, M. Bydder, and G. M. Bydder, "Magnetic resonance: an introduction to ultrashort TE (UTE) imaging.," *J Comput Assist Tomogr*, vol. 27, no. 6, pp. 825–846, 2003.

[97] D. Idiyatullin, C. Corum, J.-Y. Park, and M. Garwood, "Fast and quiet MRI using a swept radiofrequency," *Journal of Magnetic Resonance*, vol. 181, no. 2, pp. 342 – 349, 2006.

[98] R. E. Rudd and J. Q. Broughton, "Coarse-grained molecular dynamics and the atomic limit of finite elements," *Phys. Rev. B*, vol. 58, pp. R5893–R5896, Sep 1998.

[99] J. Fish, "Bridging the scales in nano engineering and science," *Journal of Nanoparticle Research*, vol. 8, pp. 577–594, October 2006.

[100] M. S. Shephard, E. S. Seol, and B. FrantzDale, *Handbook of Dynamic System Modeling*, ch. 12. Toward a Multimodel Hierarchy to Support Multiscale Simulation. Chapman & Hall/CRC, 2007.

[101] S. Cowin and D. Hegedus, "Bone remodeling I: theory of adaptive elasticity," *Journal of Elasticity*, vol. 6, pp. 313–326, 1976.

[102] B. van Rietbergen, R. Huiskes, H. Weinans, D. R. Sumner, T. M. Turner, and J. O. Galante, "The mechanism of bone remodeling and resorption around press-fitted THA stems.," *J Biomech*, vol. 26, no. 4-5, pp. 369–382, 1993.

[103] M. G. Mullender and R. Huiskes, "Proposal for the regulatory mechanism of Wolff's law.," *J Orthop Res*, vol. 13, pp. 503–512, Jul 1995.

[104] S. C. Cowin, L. Moss-Salentijn, and M. L. Moss, "Candidates for the mechanosensory system in bone.," *J Biomech Eng*, vol. 113, pp. 191–197, May 1991.

[105] M. Mullender, B. van Rietbergen, P. Rüegsegger, and R. Huiskes, "Effect of mechanical set point of bone cells on mechanical control of trabecular bone architecture.," *Bone*, vol. 22, pp. 125–131, Feb 1998.

[106] M. Satake and S. C. Cowin, "Microstructural continuum models for granular materials," in *Continuum Mechanical and Statistical Approaches in the Mechanics of Granular Materials* (M. Cowin, S. C.and Satake, ed.), p. 162, The U.S.-Japan Seminar on Continuum Mechanical and Statistical Approaches in the Mechanics of Granular Materials, Gakujutsu Buken Fukyu-Kai, Tokoy, 1978.

[107] M. Oda, J. Konishi, and S. Nemat-Nasser, "Some experimentally based fundamental results on the mechanical behaviour of granular materials," *Géotechnique*, vol. 30, no. 4, pp. 479–495, 1980.

[108] M. Oda, "Initial fabrics and their relations to mechanical properties of granular material," *Soil and foundation*, vol. 12, pp. 17–36, Mar. 1972.

[109] T. P. Harrigan, M. Jasty, R. W. Mann, and W. H. Harris, "Limitations of the continuum assumption in cancellous bone," *Journal of Biomechanics*, vol. 21, no. 4, pp. 269 – 275, 1988.

[110] P. T. Callaghan, *Principles of Nuclear Magnetic Resonance Microscopy*. Clarendon Press, 1991.

[111] E. M. Haacke, R. W. Brown, M. R. Thompson, and R. Venkatesan, *Magnetic Resonance Imaging: Physical Principles and Sequence Design*. Wiley-Liss, 1999.

[112] M. A. Bernstein., K. F. King, and X. J. Zhou, eds., *Handbook of MRI Pulse Sequences*. Elsevier Inc., 2004.

[113] F. W. Wehrli, H. K. Song, P. K. Saha, and A. C. Wright, "Quantitative MRI for the assessment of bone structure and function.," *NMR Biomed*, vol. 19, pp. 731–764, Nov 2006.

[114] S. Capuani, C. Rossi, M. Alesiani, and B. Maraviglia, "Diffusion tensor imaging to study anisotropy in a particular porous system: the trabecular bone network.," *Solid State Nucl Magn Reson*, vol. 28, pp. 266–272, Sep 2005.

[115] P.-z. Wong, ed., *Methods of Physics of Porous Media*, vol. 35 of *Experimental Methods in the Physical Sciences*. Academic Press, 1 ed., 1999.

[116] L. L. Latour, L. M. Li, and C. H. Sotak, "Improved PFG Stimulated-Echo method for the measurement of diffusion in inhomogeneous fields," *Journal of Magnetic Resonance, Series B*, vol. 101, no. 1, pp. 72 – 77, 1993.

[117] H. Hatipoglu, A. Selvi, D. Ciliz, and E. Yuksel, "Quantitative and diffusion MR imaging as a new method to assess osteoporosis," *American Journal of Neuroradiology*, vol. 28, pp. 1934–1937, 2007.

[118] H. Ong, A. Wright, S. Wehrli, C. Jones, and F. Wehrli, "Is bone marrow diffusion too slow or too fast for susceptibility-based methods to assess trabecular bone architecture?," in *Proceedings 17th Scientific Meeting, International Society for Magnetic Resonance in Medicine, Honolulu*, p. 1941, 2009.

[119] B. Chen, P.-A. Vuissoz, A. Offiah, M. Fry, and A. Todd-Pokropek, "Diffusion Tensor Imaging (DTI) as a probe to measure trabecular bone orientation in-vivo," in *18th Annual Meeting of International Society of Magnetic Resonance in Medicine (ISMRM)*, p. 3198, 2010.

[120] E. E. Sigmund, H. Cho, P. Chen, S. Byrnes, Y.-Q. Song, X. E. Guo, and T. R. Brown, "Diffusion-based MR methods for bone structure and evolution.," *Magn Reson Med*, vol. 59, pp. 28–39, Jan 2008.

[121] M. C. Yiannakas, D. W. Carmichael, M. J. Farquharson, and R. J. Ordidge, "Subpixel enhancement of nonuniform tissue (SPENT): a novel MRI technique for quantifying BMD.," *J Bone Miner Res*, vol. 24, pp. 324–333, Feb 2009.

[122] B. Chen, B. Siow, D. Carmichael, F. Odille, R. Oridge, and A. Todd-Pokropek, "Characterization of trabecular bone orientation by multi-directional SPENT (sub-pixel enhancement of non-uniform tissue)," in *18th Annual Meeting of International Society of Magnetic Resonance in Medicine (ISMRM)*, p. 793, 2010.

[123] M. D. Robson, P. D. Gatehouse, G. M. Bydder, and S. Neubauer, "Human imaging of phosphorus in cortical and trabecular bone in vivo.," *Magn Reson Med*, vol. 51, pp. 888–892, May 2004.

[124] M. D. Robson and G. M. Bydder, "Clinical ultrashort echo time imaging of bone and other connective tissues.," *NMR Biomed*, vol. 19, pp. 765–780, Nov 2006.

[125] A. Techawiboonwong, H. K. Song, M. B. Leonard, and F. W. Wehrli, "Cortical bone water: in vivo quantification with ultrashort echo-time MR imaging.," *Radiology*, vol. 248, pp. 824–833, Sep 2008.

[126] L.-S. Bouchard and W. S. Warren, "Reconstruction of porous material geometry by stochastic optimization based on bulk NMR measurements of the dipolar field.," *J Magn Reson*, vol. 170, pp. 299–309, Oct 2004.

[127] W. Richter, S. Lee, W. S. Warren, and Q. He, "Imaging with intermolecular multiple-quantum coherences in solution nuclear magnetic resonance," *Science*, vol. 267, no. 5198, pp. 654–657, 1995.

[128] S. Capuani, F. Curzi, F. M. Alessandri, B. Maraviglia, and A. Bifone, "Characterization of trabecular bone by dipolar demagnetizing field MRI.," *Magn Reson Med*, vol. 46, pp. 683–689, Oct 2001.

[129] S. Capuani, G. Hagberg, F. Fasano, I. Indovina, A. Castriota-Scanderbeg, and B. Maraviglia, "In vivo multiple spin echoes imaging of trabecular bone on a clinical 1.5 T MR scanner.," *Magn Reson Imaging*, vol. 20, pp. 623–629, Oct 2002.

[130] H. Zuppinger, "Die aktive flexion im unbelasteten kniegelenk," *Anatomy and Embryology*, vol. 25, pp. 701–764, 1904.

[131] T. Fukubayashi and H. Kurosawa, "The contact area and pressure distribution pattern of the knee: A study of normal and osteoarthrotic knee joints," *Acta Orthopaedica Scandinavica*, vol. 51, no. 1, pp. 871–879, 1980.

[132] A. M. Ahmed and D. L. Burke, "In-vitro measurement of static pressure distribution in synovial joints–part I: tibial surface of the knee.," *J Biomech Eng*, vol. 105, pp. 216–225, Aug 1983.

[133] Z. A. Cohen, D. M. McCarthy, S. D. Kwak, P. Legrand, F. Fogarasi, E. J. Ciaccio, and G. A. Ateshian, "Knee cartilage topography, thickness, and contact areas from MRI: in-vitro calibration and in-vivo measurements.," *Osteoarthritis Cartilage*, vol. 7, pp. 95–109, Jan 1999.

[134] D. R. Wilson, E. J. McWalter, and J. D. Johnston, "The measurement of joint mechanics and their role in osteoarthritis genesis and progression.," *Med Clin North Am*, vol. 93, pp. 67–82, Jan 2009.

[135] A. Arndt, P. Westblad, I. Winson, T. Hashimoto, and A. Lundberg, "Ankle and subtalar kinematics measured with intracortical pins during the stance phase of walking.," *Foot Ankle Int*, vol. 25, pp. 357–364, May 2004.

[136] MRC UK, "Ethics and research guidance." http://www.mrc.ac.uk/Ourresearch/Ethicsresearchguidance/index.htm, 2010.

[137] G. Li, T. H. Wuerz, and L. E. DeFrate, "Feasibility of using orthogonal fluoroscopic images to measure in vivo joint kinematics.," *J Biomech Eng*, vol. 126, pp. 314–318, April 2004.

[138] T. Morooka, S. Hamai, M. Hiromasa, S. Takeshi, H. Hidehiko, F. Benjamin J., I. Yukihide, and B. Scott A., "Dynamic activity dependence of in vivo normal knee kinematics.," *J Orthop Res*, vol. 26, pp. 428–434, April 2008.

[139] GE Medical Systems, *Signa HDx 1.5T & Signa HDx 3.0T Online Help*. General Electronics, 283 rue de la Miniere, 78530 BUC France, 5149698-200 rev 2 ed., May 2006.

[140] Mint Medical, "MITK 3M3." http://mint-medical.de/productssolutions/mitk3m3/mitk3m3/, 2009.

[141] M. Kazhdan, M. Bolitho, and H. Hoppe, "Poisson surface reconstruction," in *SGP '06: Proceedings of the fourth Eurographics symposium on Geometry processing*, (Aire-la-Ville, Switzerland, Switzerland), pp. 61–70, Eurographics Association, 2006.

[142] Visual Computing Lab - STI - CNR, "MeshLab," 2009.

[143] W. E. Lorensen and H. E. Cline, "Marching cubes: A high resolution 3D surface construction algorithm," *SIGGRAPH Comput. Graph.*, vol. 21, no. 4, pp. 163–169, 1987.

[144] D. L. Hill, P. G. Batchelor, M. Holden, and D. J. Hawkes, "Medical image registration," *Physics in medicine and biology*, vol. 46, pp. R1–45, Mar. 2001.

[145] D. I. Caruntu and M. S. Hefzy, "3D anatomically based dynamic modeling of the human knee to include tibio-femoral and patello-femoral joints," *Journal of Biomechanical Engineering*, vol. 126, pp. 44–53, Feb. 2004.

[146] J. C. Lagarias, J. A. Reeds, M. H. Wright, and P. E. Wright, "Convergence properties of the Nelder–Mead simplex method in low dimensions," *SIAM J. on Optimization*, vol. 9, pp. 112–147, May 1998.

[147] E. Haber and J. Modersitzki, "A multilevel method for image registration," *SIAM Journal on Scientific Computing*, vol. 27, pp. 1594–1607, Jan. 2006.

[148] M. Kline, "Note on elementary vector analysis and on an application to differential geometry," *The American Mathematical Monthly*, vol. 43, no. 9, pp. pp. 555–562, 1936.

[149] D. J. Struik, *Lectures on Classical Differential Geometry*, ch. 1. Curves, pp. 1–25. Dover Publications, 1961.

[150] D. Périé and M. C. Hobatho, "In vivo determination of contact areas and pressure of the femorotibial joint using non-linear finite element analysis," *Clinical Biomechanics*, vol. 13, pp. 394–402, Sept. 1998.

[151] C. B. Barber, D. P. Dobkin, and H. Huhdanpaa, "The quickhull algorithm for convex hulls," *ACM Transactions on Mathematical Software*, vol. 22, no. 4, pp. 469-483, 1996.

[152] A. Shamir, "A survey on mesh segmentation techniques," *Computer Graphics Forum*, vol. 27, no. 6, pp. 1539–1556, 2008.

[153] P. Johal, A. Williams, P. Wragg, D. Hunt, and W. Gedroyc, "Tibio-femoral movement in the living knee. A study of weight bearing and non-weight bearing knee kinematics using 'interventional' MRI.," *J Biomech*, vol. 38, pp. 269–276, Feb 2005.

[154] C. E. Draper, J. M. Santos, L. C. Kourtis, T. F. Besier, M. Fredericson, G. S. Beaupre, G. E. Gold, and S. L. Delp, "Feasibility of using real-time MRI to measure joint kinematics in 1.5T and open-bore 0.5T systems.," *J Magn Reson Imaging*, vol. 28, pp. 158–166, Jul 2008.

[155] D. Wilson, J. Feikes, A. Zavatsky, and J. O'Connor, "The components of passive knee movement are coupled to flexion angle," *Journal of Biomechanics*, vol. 33, pp. 465–473, April 2000.

[156] L. R. Dice, "Measures of the amount of ecologic association between species," *Ecology*,

vol. 26, pp. 297–302, July 1945.

[157] V. V. Patel, K. Hall, M. Ries, J. Lotz, E. Ozhinsky, C. Lindsey, Y. Lu, and S. Majumdar, "A three-dimensional MRI analysis of knee kinematics.," *J Orthop Res*, vol. 22, pp. 283–292, Mar. 2004.

[158] C. S. Shin, R. B. Souza, D. Kumar, T. M. Link, B. T. Wyman, and S. Majumdar, "In vivo tibiofemoral cartilage-to-cartilage contact area of females with medial osteoarthritis under acute loading using MRI," *Journal of Magnetic Resonance Imaging*, vol. 34, pp. 1405–1413, Dec. 2011.

[159] E. Hahn, "Spin echoes," *Physics Review*, vol. 80, pp. 580–594, 1950.

[160] H. Y. Carr and E. M. Purcell, "Effects of diffusion on free precession in nuclear magnetic resonance experiments," *Physics Review*, vol. 94, pp. 630–638, May 1954.

[161] E. Stejskal and J. Tanner, "Spin diffusion measurements: Spin echoes in the presence of a time-dependent field gradient," *Journal of Chemical Physics*, vol. 42, pp. 288–292, 1965.

[162] D. Le Bihan, E. Breton, D. Lallemand, P. Grenier, E. Cabanis, and M. Laval-Jeantet, "MR imaging of intravoxel incoherent motions: application to diffusion and perfusion in neurologic disorders.," *Radiology*, vol. 161, pp. 401–407, Nov 1986.

[163] C. Westin, S. Peled, H. Gudbjartsson, R. Kikinis, and F. Jolesz, "Geometrical diffusion measures for MRI from tensor basis analysis," in *ISMRM '97*, 1997.

[164] P. J. Basser, J. Mattiello, and D. LeBihan, "MR diffusion tensor spectroscopy and imaging.," *Biophys J*, vol. 66, pp. 259–267, Jan 1994.

[165] L.-C. Chang, D. K. Jones, and C. Pierpaoli, "RESTORE: Robust estimation of tensors by outlier rejection," *Magn. Reson. Med.*, vol. 53, no. 5, pp. 1088–1095, 2005.

[166] D. K. Jones, M. A. Horsfield, and A. Simmons, "Optimal strategies for measuring diffusion in anisotropic systems by magnetic resonance imaging.," *Magn Reson Med*, vol. 42, pp. 515–525, Sept 1999.

[167] K. M. Hasan, D. L. Parker, and A. L. Alexander, "Comparison of gradient encoding schemes for diffusion-tensor MRI.," *J Magn Reson Imaging*, vol. 13, pp. 769–780, May 2001.

[168] P. Batchelor, D. Atkinson, D andHill, F. Calamante, and A. Connelly, "Anisotropic noise propagation in diffusion tensor MRI sampling schemes," *Magn Reson Med*, vol. 49, pp. 1143–51, 2003.

[169] P. J. Basser and C. Pierpaoli, "Microstructural and physiological features of tissues elucidated by quantitative-diffusion-tensor MRI.," *Journal of Magnetic Resonance, Series B*, vol. 111, pp. 209–219, Jun 1996.

[170] H. G. Hatipoglu, A. Selvi, D. Ciliz, and E. Yuksel, "Quantitative and diffusion MR imaging as a new method to assess osteoporosis.," *AJNR Am J Neuroradiol*, vol. 28, no. 10, pp. 1934–1937, 2007.

[171] T. Reese, O. Heid, R. Weisskoff, and V. Wedeen, "Reduction of eddy-current-induced distortion in diffusion MRI using a twice-refocused spin echo," *Magnetic Resonance in Medicine*, vol. 49, no. 1, pp. 177–182, 2003.

[172] G. H. Golub and C. F. Van Loan, *Matrix Computations (Johns Hopkins Studies in Mathematical Sciences)*. The Johns Hopkins University Press, 3rd ed., Oct. 1996.

[173] P. A. Cook, Y. Bai, S. Nedjati-Gilani, K. K. Seunarine, M. G. Hall, G. J. Parker, and D. C. Alexander, "Camino: Open-source Diffusion-MRI reconstruction and processing," in *Proceedings of the14th Scientific Meeting of the International Society for Magnetic Resonance in Medicine*, (Seattle, WA, USA,), p. 2759, ISMRM, May 2006.

[174] D. A. Lansdown, Z. Ding, M. Wadington, J. L. Hornberger, and B. M. Damon, "Quantitative diffusion tensor MRI-based fiber tracking of human skeletal muscle," *Journal of Applied Physiology*, vol. 103, no. 2, pp. 673–681, 2007.

[175] D. K. Jones and P. J. Basser, ""squashing peanuts and smashing pumpkins": how noise distorts diffusion-weighted MR data.," *Magn Reson Med*, vol. 52, pp. 979–993, Nov 2004.

[176] H. Gudbjartsson and S. Patz, "The Rician distribution of noisy MRI data," *Magn. Reson. Med.*, vol. 34, no. 6, pp. 910–914, 1995.

[177] K. P. Pruessmann, M. Weiger, M. B. Scheidegger, and P. Boesiger, "SENSE: Sensitivity encoding for fast MRI," *Magnetic Resonance in Medicine*, vol. 42, no. 5, pp. 952–962, 1999.

[178] P. Kellman and E. R. McVeigh, "Image reconstruction in SNR units: a general method for SNR measurement.," *Magn Reson Med*, vol. 54, pp. 1439–1447, Dec 2005.

[179] G. Steidle, F. Eibofner, and F. Schick, "Quantitative diffusion imaging of adipose tissue in the human lower leg at 1.5 T.," *Magnetic Resonance in Medicine*, vol. 65, pp. 1118–1124, Apr 2011.

[180] A. Baur, O. Dietrich, and M. Reiser, "Diffusion-weighted imaging of bone marrow: current status," *European Radiology*, vol. 13, no. 7, pp. 1699–1708, 2003.

[181] S. C. Kim, B. R. Krynyckyi, J. Machac, and C. K. Kim, "Patterns of red marrow in the adult femur," *Clinical Nuclear Medicine*, vol. 31, no. 12, pp. 739–741, 2006.

[182] U. Sinha, S. Sinha, J. A. Hodgson, and R. V. Edgerton, "Human soleus muscle architecture at different ankle joint angles from magnetic resonance diffusion tensor imaging.," *J Appl Physiol*, vol. 110, pp. 807–819, Mar 2011.

[183] G. J. Bryan, *Skeletal Anatomy*. Churchill Livingstone, 1996.

[184] C. P. Bernard, G. P. Liney, D. J. Manton, L. W. Turnbull, and C. M. Langton, "Comparison of fat quantification methods: a phantom study at 3.0T," *Journal of Magnetic Resonance Imaging: JMRI*, vol. 27, pp. 192–197, Jan. 2008.

[185] M. Hall and D. Alexander, "A simulation framework for diffusion MRI," in *Proceedings of MIUA*, 2006.

[186] F. Wiesinger, P. Boesiger, and K. P. Pruessmann, "Electrodynamics and ultimate SNR in parallel MR imaging," *Magnetic Resonance in Medicine*, vol. 52, pp. 376–390, Aug. 2004.

[187] S. Tassani, C. Ohman, M. Baleani, F. Baruffaldi, and M. Viceconti, "Anisotropy and inhomogeneity of the trabecular structure can describe the mechanical strength of osteoarthritic cancellous bone.," *J Biomech*, vol. 43, pp. 1160–1166, April 2010.

[188] B. Siow, D. W. Carmichael, J. Riegler, D. C. Alexander, M. F. Lythgoe, and R. J. Ordidge, "Detection of human mononuclear cells labelled with micron-sized iron oxide particles using the sub-pixel enhancement of nonuniform tissue (SPENT) sequence," in *Proceedings 18th Scientific Meeting, International Society for Magnetic Resonance in Medicine, Stockholm*, p. 4942, 2010.

[189] C. J. Bakker, J.-H. Seppenwoolde, and K. L. Vincken, "Dephased MRI," *Magnetic Resonance in Medicine*, vol. 55, no. 1, pp. 92–97, 2006.

[190] W. T. Dixon, L. N. Du, D. D. Faul, M. Gado, and S. Rossnick, "Projection angiograms of blood labeled by adiabatic fast passage," *Magnetic Resonance in Medicine*, vol. 3, pp. 454–462, June 1986.

[191] D. Carmichael, *Speed and Contrast in Magnetic Resonance Imaging*. PhD thesis, University College London, Nov 2003.

[192] M. C. Okimoto, "Anatomy and histology of the pineapple inflorescence and fruit," *Botanical*

Gazette, vol. 110, pp. 217–231, Dec 1948.

[193] P. J. Basser, S. Pajevic, C. Pierpaoli, J. Duda, and A. Aldroubi, "In vivo fiber tractography using DT-MRI data.," *Magnetic Resonance in Medicine*, vol. 44, pp. 625–632, Oct 2000.

[194] S. C. Cowin, *Bone Mechanics Handbook*, ch. 30 The False Premise in Wolff's Law, pp. 30(1–19). CRC Press, 2001.